

THERMAL EXPANSION AND PHASE TRANSFORMATION BEHAVIOR IN THE RARE-
EARTH TITANATE SYSTEM

BY

KEVIN C. SEYMOUR

DISSERTATION

Submitted in partial fulfillment of the requirements
for the degree of Doctor of Philosophy in Materials Science and Engineering
in the Graduate College of the
University of Illinois at Urbana-Champaign, 2015

Urbana, Illinois

Doctoral Committee:

Professor Waltraud M. Kriven, Chair, Director of Research
Professor Jay D. Bass
Assistant Professor Jessica A. Krogstad
Assistant Professor Daniel P. Shoemaker

ABSTRACT

In this work, the thermal expansion behavior in the Ln_2TiO_5 system was explored, and mechanisms behind such behavior were described. The components of the thermal expansion tensor were calculated from the refined d-spacings using the program CTEAS for the cubic, orthorhombic, and hexagonal phases. In the cubic phase, the thermal expansion behavior was found to increase as expected with an increase in thermal vibrations. The orthorhombic phase exhibited an interesting shift from an expanding c-axis to one which contracted. Subsequent analysis of the crystallographic information of the orthorhombic phase revealed that the mechanism behind this behavior was the result of the strained trigonal bipyramidal structure overcoming an energy barrier to become more ideal and relaxed. The thermal expansion behavior in the hexagonal phase was found to be caused by the movement of the axial oxygen in the trigonal bipyramidal structure towards the central Ti cation with increasing temperature.

This information was paired with insights into the volume expansion, structural elements, and geometric units between the orthorhombic and hexagonal phases to describe a potential pathway between two crystallographic cells which have no group-subgroup relationship. The novel pairing of information to describe a reconstructive transformation in this manner is unique and may be a new method to describe such transformations where few tools currently exist today.

Additionally, a new experimental technique was developed to study the phase transformation kinetics between the orthorhombic and hexagonal phases *in situ*. The activation energy of this transformation was found to be 149 kJ/mol. This new technique avoids complications which arise from the study of transformations at high temperatures using thermal analysis methods, and provides increased time resolution of the data improving the calculation of the activation energy.

ACKNOWLEDGMENTS

First, I would like to thank my research advisor Professor Waltraud (Trudy) Kriven. Without her advisement and support none of this would have been possible. In addition, I would like to thank my dissertation committee for their excellent feedback and support throughout the process.

Several individuals have been essential to the success of this work. Most notably are the members of the phase transformations team, both former and current. These included Professor Pankaj Sarin, Doctor Robert Hughes, Doctor Zlatomir Apostolov, Zachary Jones, Steven Letourneau, Andrew Steveson, John Beach, Scott McCoramack, and Daniel Ribero, collectively known as the beamline boys. In addition, I would like to thank other former group members such as Doctor Pathikumar Sellappan and Doctor Christian Espinoza.

Furthermore, I would like to thank my family and several of my closest friends and roommates for their support and friendship. These include Christopher and Michele Seymour, Janine Seymour, Adrian Radocea, Calvin Lear, Ben Eftink, Christoph Baeumer, Laura Rzeha, and Steven Rogers.

Finally, without the support of organizations such as the Air Force Office of Scientific Research, Advanced Photon Source, National Synchrotron Light Source, Spallation Neutron Source, and the Materials Research Laboratory this work would not have been completed.

TABLE OF CONTENTS

CHAPTER 1 INTRODUCTION	1
1.1 Motivation.....	1
1.2 Introduction.....	1
1.3 Limitations of Previous Studies	3
1.4 Synchrotron Radiation	5
1.5 The Debye-Scherrer Diffraction Geometry	11
1.6 Analysis of Data – the Rietveld Method.....	12
1.7 Thermal Expansion in General	15
1.8 Diffusional Phase Transformations in General.....	17
1.9 Objectives and Scope of Research	20
CHAPTER 2 LITERATURE REVIEW	21
2.1 The Rare-Earth Titanates (Ln_2TiO_5).....	21
2.1.1 Introduction.....	21
2.1.2 Polymorphism in the Ln_2TiO_5 System.....	23
2.2 The Rare-Earth Di-Titanates ($\text{Ln}_2\text{Ti}_2\text{O}_7$)	27
CHAPTER 3 SAMPLE SYNTHESIS	29
3.1 Powder Synthesis	29
3.1.1 The Inorganic-Organic Steric Entrapment Method	29
3.1.2 Conventional Solid-State Reaction Method.....	31

3.2	Sample Preparation	32
3.2.1	Thermal Expansion Experiments	32
3.2.2	Phase Transformation Experiments via X-ray Diffraction	33
3.2.3	Phase Transformation Experiments via Differential Scanning Calorimetry	34
CHAPTER 4 EXPERIMENTAL SETUP.....		35
4.1	Beamline Configuration.....	35
4.1.1	The National Synchrotron Light Source	35
4.1.2	The Advanced Photon Source.....	36
4.2	Spallation Neutron Source	38
4.3	The Quadrupole Lamp Furnace	40
4.4	Temperature Calibration	45
4.5	Differential Scanning Calorimetry.....	46
4.6	Dilatometry	47
CHAPTER 5 THERMAL EXPANSION IN THE RARE-EARTH TITANATES		48
5.1	Thermal Expansion in the Low Temperature Cubic Phase	48
5.1.1	Results.....	48
5.1.2	Discussion and Mechanism of Thermal Expansion.....	68
5.1.3	Conclusions.....	72
5.2	Thermal Expansion in the Orthorhombic Phase	73
5.2.1	Results.....	73
5.2.2	Discussion and Mechanism of Thermal Expansion.....	96

5.2.3	Conclusions.....	108
5.3	Thermal Expansion in the Hexagonal Phase	109
5.3.1	Results.....	109
5.3.2	Discussion and Mechanism of Thermal Expansion.....	112
5.3.3	Conclusions.....	114
CHAPTER 6 THE RELATIONSHIP BETWEEN THE ORTHORHOMBIC AND HEXAGONAL PHASES.....		
6.1	The Relationship between the Orthorhombic and Hexagonal Phase.....	115
6.1.1	Results and Discussion	115
6.1.2	Conclusion	126
CHAPTER 7 PHASE TRANSFORMATION KINETICS BETWEEN THE ORTHORHOMBIC AND HEXAGONAL PHASES.....		
7.1	Phase Transformations Kinetics	127
7.1.1	Results and Discussion	127
7.1.2	Conclusions.....	140
7.2	Comparison with Similar X-ray Diffraction Experiments to Investigate Transformation Kinetics	141
7.2.1	Advantages of Described Methods	141
7.2.2	Comparisons with Similar Work	142
7.2.3	Future Method Development	151
7.2.4	Conclusions.....	152
7.3	Improving the Kinetic Model.....	153

7.3.1	Sensitivity Analysis with Time.....	154
7.3.2	Sensitivity Analysis with Temperature.....	156
7.3.3	Sensitivity with Variable Type	158
7.3.4	Analysis of Data.....	159
7.3.5	Discussion.....	164
7.3.6	Proposed Experiments	169
7.3.7	Conclusions.....	170
CHAPTER 8 SUGGESTIONS FOR FUTURE WORK.....		171
8.1	Suggestions for Future Work.....	171
8.1.1	The Rare-Earth Di-Titanates.....	171
8.1.2	Research into Other Reconstructive Systems	171
8.1.3	Improving the Kinetic Model.....	172
REFERENCES		173

CHAPTER 1

INTRODUCTION

1.1 Motivation

A knowledge gap exists in our current understanding of the phase transformation behavior in the Ln_2TiO_5 material system. Previous experimental work, performed *ex situ*, only provides superficial knowledge about the phases present and at what temperature these phases undergo transformations. As an important engineering material in the nuclear and electronic industries it is imperative to understand the relationship between different phases in this system as most of the desirable properties are phase dependent. The study of this material system *in situ* will provide much more information about key thermophysical properties and will shed light on the underlying mechanisms and kinetics of phase transformations. This will be useful for both application as well as basic scientific understanding.

1.2 Introduction

The phase transformation behavior in inorganic materials, particularly in oxides, is poorly understood. There is an ever increasing amount of technology that relies on phase transformations (structural ceramics, actuators, multiferroics, etc). For example, a disruptive phase transformation at 950 °C on cooling and 1170 °C on heating will cause zirconia (ZrO_2), upon cooling, to shatter and render it useless in most materials applications.[1] Garvie et al. reported, while working with the material almost a century after its discovery, transformation toughening in zirconia, describing it as “ceramic steel”. [2] If a sufficient quantity of the metastable tetragonal phase is present in zirconia, an applied stress magnified at the crack tip can cause the tetragonal phase to convert into monoclinic, with an associated increase in volume, as described in Figure 1.[3] This phase

transformation can compress the crack and impede its growth, increasing the fracture toughness.[4] Though zirconia is one of the most well studied transformations in the literature, it is still not fully understood and is a very active area of research – highlighting the significant knowledge gaps which exist in this field of study.[5-9]

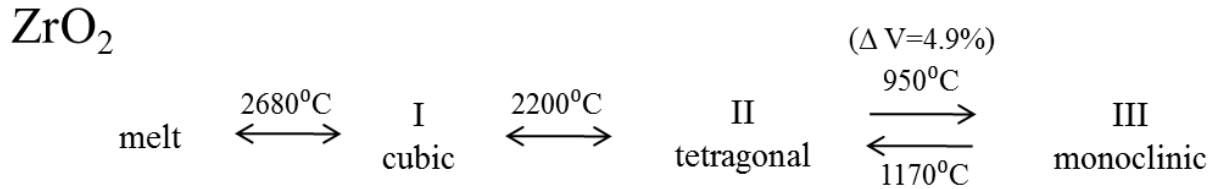


Figure 1. The transformation temperatures and accompanied volume changes in zirconia on heating and cooling.

Most of the desirable properties for the application of phase transformations in ceramics occur at higher temperatures. One reason a large knowledge gap exists in this area of study is due to the limitations of contemporary experimental setups. Previous work relied on *ex situ* studies in which samples were quickly quenched from high temperatures and subsequently characterized. If a sample did transform it was noted, along with the approximate transformation temperature. For the most part, this was sufficient for the development of phase diagrams and characterization of the high temperature crystal structures. However, if a transformation is displacive, having a low activation energy, it may be missed using *ex situ* techniques. In addition, information regarding the thermal expansion behavior and relationship between multiple crystalline phases is not available.

With the advent of computer technologies, advances in detector design, and simplicity of experimental setups, it is quickly becoming more popular to perform these same experiments *in situ*.

1.3 Limitations of Previous Studies

Previous work describing the behavior and properties of ceramics have been measured using essentially an engineering approach. Much of the literature describes conventionally prepared, incompletely reacted ceramics, or those containing grain boundary amorphous phases. These samples were studied by X-ray diffraction, dilatometry, thermal analyses (DTA, DSC), and optical microscopy, without much knowledge of the microstructure, porosity, strain, or presence of microcracks within the material. More recently, studies by electron microscopy (SEM and TEM), have identified important microstructural considerations, such as the critical particle size effect controlling the onset of transformation.[10]

In the past, *in situ* studies were only able to access modest temperatures and needed inert atmospheres or vacuum for higher temperatures. However, in the case of oxides, measurements under vacuum or reducing atmospheres can be erroneous, due to the unsaturated state of oxygen chemistry leading to defects such as oxygen vacancies. A classic example of this is fully or partially stabilized zirconia, where the addition of Ca^{2+} , Mg^{2+} , Y^{3+} or Ce^{4+} cations disturbs the oxygen equilibrium composition in zirconia, necessitating oxygen vacancy defects, and stabilizing the high temperature phases in cubic or tetragonal symmetry.[10]

Crystallographic parameters and thermal expansion coefficients of oxides depend on their level of oxygen saturation, which is a function of their processing conditions as well as experimental measurement conditions. For example, Figure 2 illustrates the need for oxide phase diagrams to

be measured in air. Mullite ($3\text{Al}_2\text{O}_3 \cdot 2\text{SiO}_2$), is white in color as a normal oxygen saturated ceramic, and black or gray when oxygen deficient.[11,12] The phase transformations can be suppressed and the temperature of invariant reactions can be shifted, changing the crystallographic parameters. In an example to illustrate this behavior, samples of mullite were hot pressed under vacuum in a graphite die and appeared black upon densification. Their crystallographic lattice parameters were measured by *in situ* high temperature neutron diffraction to 1600 °C. Due to heating in air, the sample had turned white as they were oxygen saturated. When the *in situ* measurements were repeated, a different set of lattice and thermal expansion parameters were observed, and subsequent cycled measurements indicated that the parameters of the oxygen saturated mullite were then reproducible. The behavior was observed for the crystallographic unit cell volume, which was calculated from the crystallographic axes, each of which was different due to oxygen deficiency. Therefore it is important that the phase transformation behavior, lattice parameters, and thermal expansion properties of ceramic oxides are measured in air.

Other limitations commonly encountered in interpreting earlier studies include incompleteness of reported information or inconsistencies in the units of measurements. The latter, perhaps, is due to the cross-disciplinary appeal of phase transformations as a subject, and is evident from literature reports by chemists, physicists, material scientists, geologists, crystallographers, and metallurgists. Often results presented on phase transformations in material systems are incomprehensible due to insufficient information regarding sample preparation, characterization, purity, or measurement conditions. There is a definite need for simple, yet comprehensive guidelines for reporting phase transformation properties of materials. This will enable

assimilation of widely scattered information on the subject, as well as streamline future efforts focused on transformation behavior in materials.

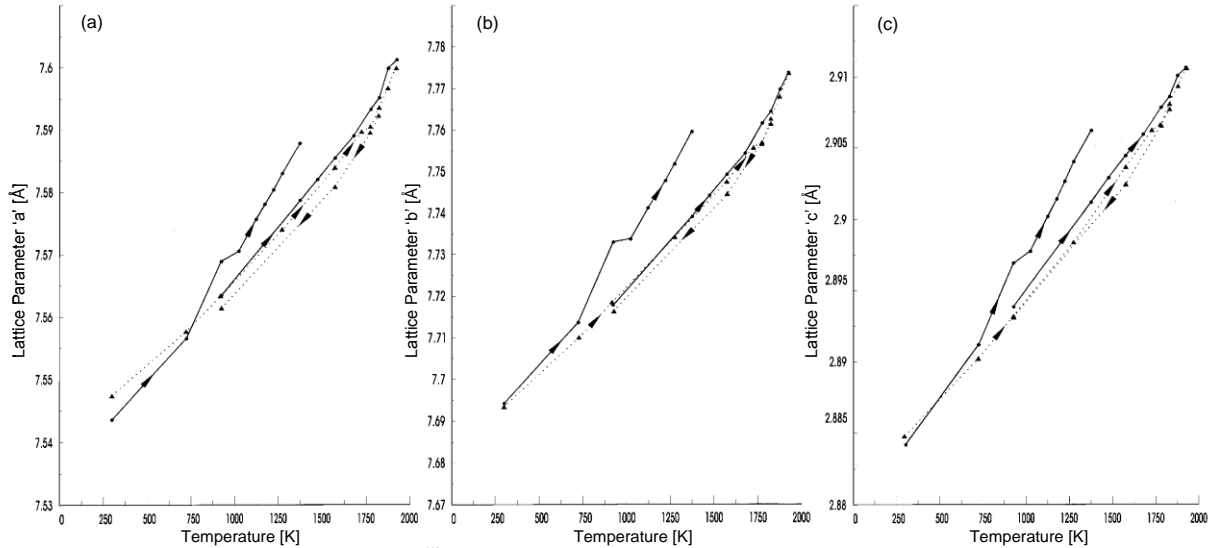


Figure 2. Lattice parameters a, b and c of mullite [(a) to (c), respectively], as a function of temperature. Full circles are experiments on grey mullite, triangles are experiments on annealed white mullite.[12]

1.4 Synchrotron Radiation

Röntgen discovered X-ray radiation in 1895 while studying light emission in evacuated glass tubes. With contributions from Laue, W. H. Bragg, and his son, W. L. Bragg, the importance of X-ray radiation was realized for the determination of the crystal structures of materials. Up to 1912, it was difficult to maintain a reliable X-ray beam from a source. Coolidge, working at the General Electric Research Laboratories, developed a new X-ray tube that worked by accelerating electrons from a filament towards an anode to produce X-rays.[13] The Coolidge tube is the

basis of contemporary X-ray radiation sources and works when an electron is promoted from the inner shell leaving behind a hole. Figure 3 illustrates the concept behind the Coolidge tube. Electrons from higher shells fall to fill this hole, emitting a photon with energy equal to the difference between the two shells, Figure 3 describes this process.[13]

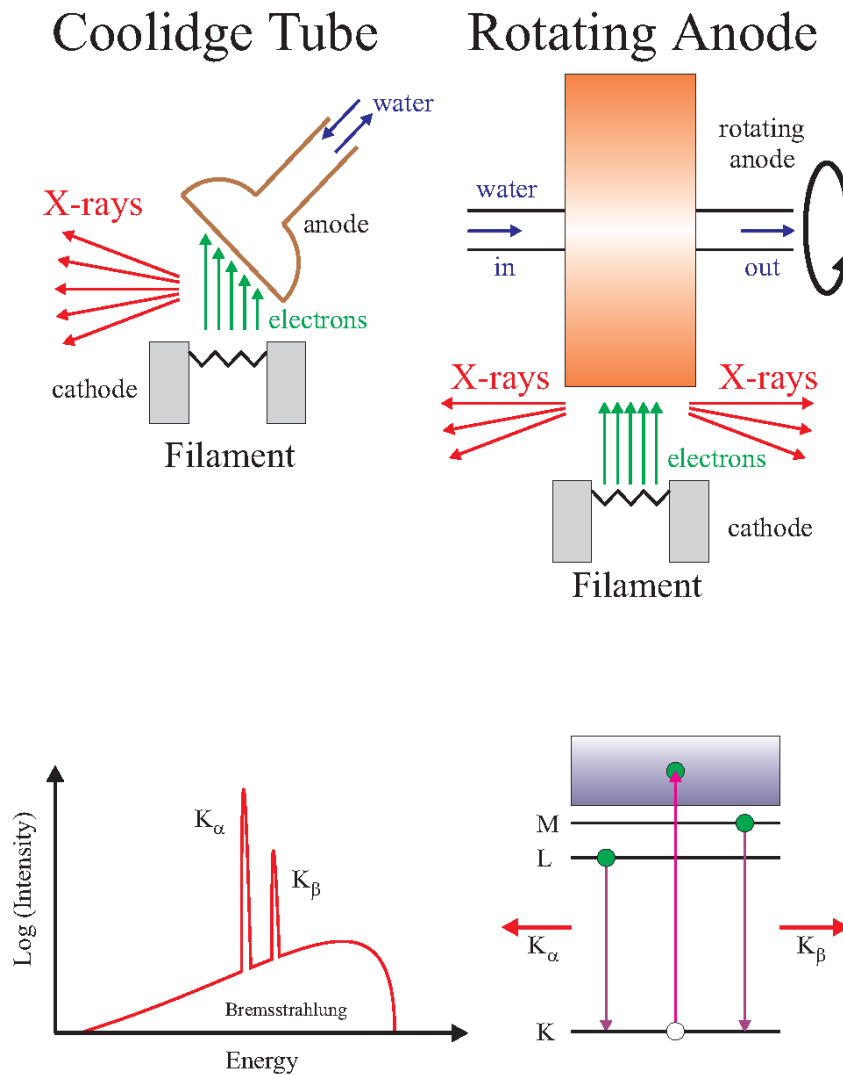


Figure 3. Illustration of different methods of X-ray radiation generation. Depicted here is the traditional Coolidge tube, an early predecessor of the common X-ray generation tubes of today, and a rotating anode, known for producing a large photon flux.[13]

The development of the rotating anode X-ray generation source was an improvement over the Coolidge tube in terms of brilliance, the description of the intensity of radiation through an area given by the equation below:[13]

$$Brilliance = \frac{\frac{photons}{sec}}{(mrad^2)(mm^2 \text{ source area})(0.1\% BW)}$$

Although the brilliance of the beam was improved over the Coolidge tube, rotating anodes still worked on the same principle, and such, suffered the same drawbacks (i.e. $K_{\alpha 2}$ and K_{β} generation, non-polarized, non-tunable wavelength, etc).

Synchrotron radiation was discovered in 1946 by researchers at General Electric.[14] Figure 4 depicts the first image of synchrotron radiation from the General Electric setup. Unlike conventional sources, electromagnetic radiation is generated in a very different manner. First electrons are accelerated to high velocities in vacuum. When accelerated close to the speed of light, the electrons trajectory is modified and bent by a magnetic field. The process of changing the direction of a charged particle (acceleration/deceleration) results in the emission of a photon. These emitted photons have a broad range of wavelengths; see Figure 5 as an example. A single crystal monochromator, usually Si, Ge, or C can be employed to single out a particular wavelength via the Bragg relationship. After which, the X-ray beam can be modified by other optical components (mirrors, slits, filters, etc). Synchrotron radiation is generally used to produce light in the X-ray, UV, or IR range and has significant advantages of conventional laboratory sources. These benefits include: tunable wavelength, minimal divergence, linear polarization, and most importantly extremely high brilliance. The brilliance of synchrotron radiation can be

more than 10 orders of magnitude larger than the best rotating anode. Figure 6 illustrates the differences in brilliance between different sources.[13]

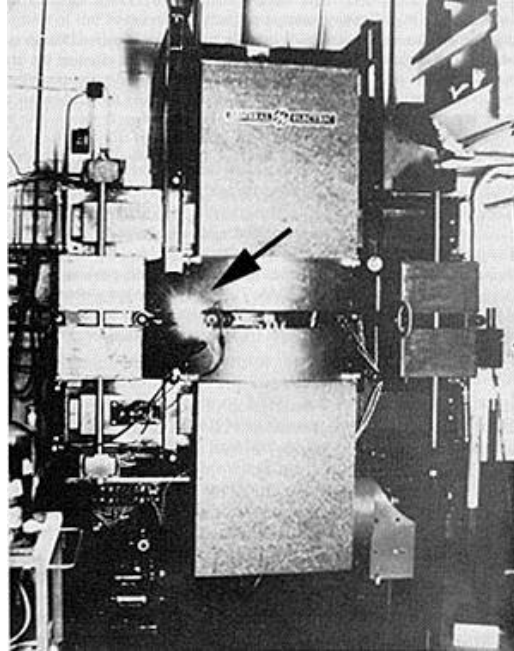


Figure 4. The first image of synchrotron X-ray radiation at General Electric in 1946.

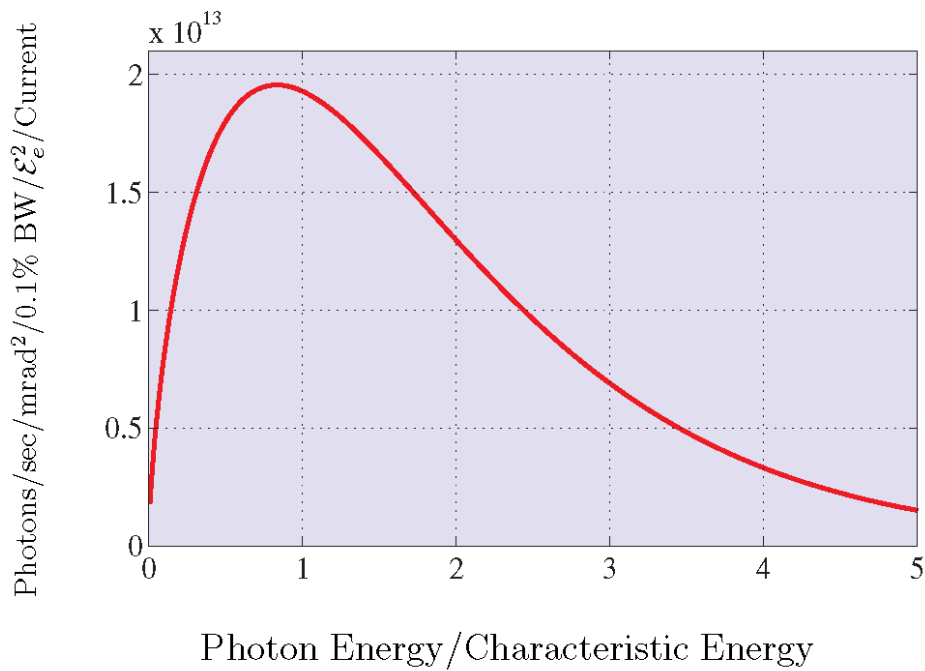


Figure 5. The normalized spectrum of radiation from a bending magnet.

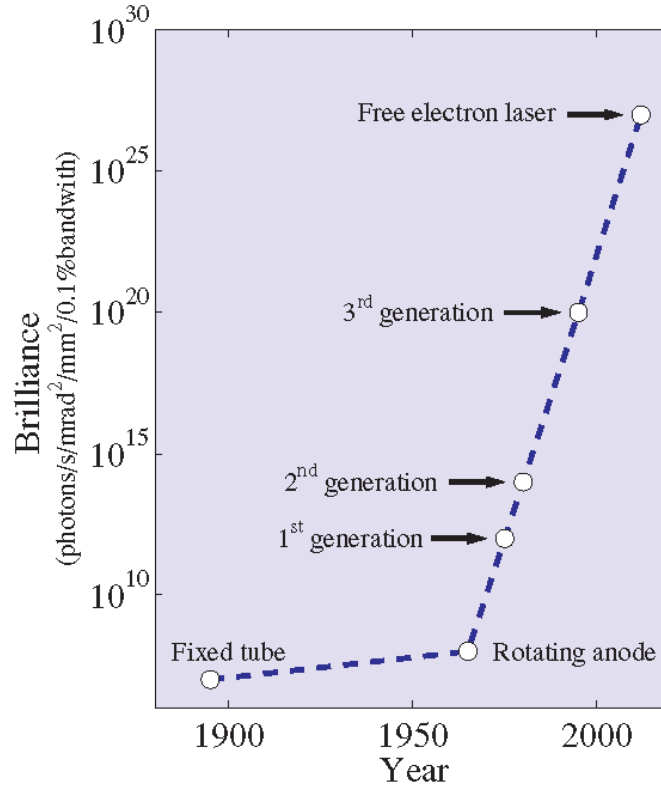


Figure 6. The brilliance of X-ray sources as a function of time.[15]

Synchrotron sources can be characterized by two main criteria: characteristic frequency and opening angle, α , given by the equations[13]

$$E_c = \hbar\omega = 0.665 \varepsilon_e^2 B$$

where, E_c is the characteristics energy, \hbar Plank's constant, ω the frequency, ε_e the energy of an electron, and B the magnetic field of the bending magnet, and

$$\alpha = \frac{1}{\gamma} = \frac{0.511 \text{ MeV}}{E_c \text{ GeV}}$$

where, E_c is the characteristics energy, and γ the opening angle related to the curvature of the electron storage ring.

A typical schematic of an electron storage ring used to produce synchrotron radiation is provided in Figure 7.

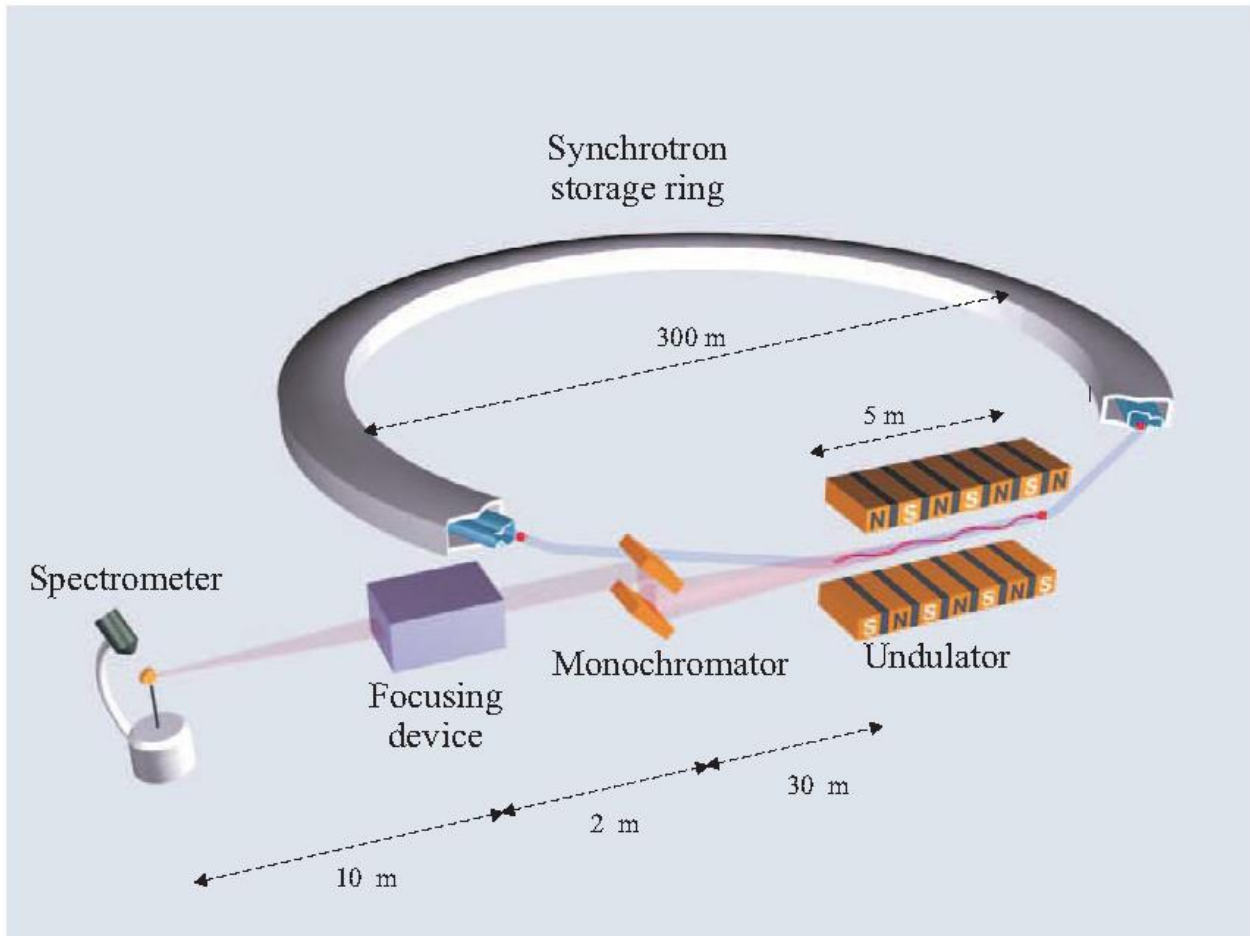


Figure 7. A schematic of a typical X-ray beamline at a third generation X-ray source. Bunches of charged electrons circulate in a storage ring. When the charged particles are bent while traveling around the ring they produce a spectrum of light.

1.5 The Debye-Scherrer Diffraction Geometry

When performing high temperature X-ray diffraction experiments in reflection geometry complications can arise from sample displacement errors. This can be due to sagging of strip heaters at temperature, creating a shift in peak position making thermal expansion measurements erroneous.[16] The uncertainty in peak position, θ , is related to the sample displacement by

$$\Delta 2\theta = -2d \cos \frac{\theta}{R}$$

where, d is the sample displacement and R is the radius of the diffractometer.

This uncertainty can be removed/minimized if the experiment is done in transmission, the most popular of which is the Debye-Scherrer geometry, Figure 8 illustrates this geometry.[16]

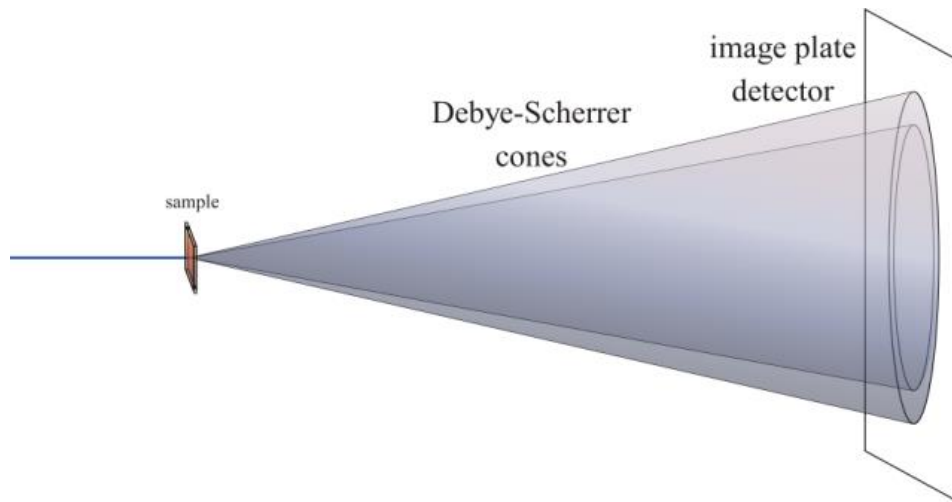


Figure 8. An illustration of the Debye-Scherrer geometry. The rings of intensity are a result of the diffraction of light from planes in the crystalline structure.

In combination with the quadrupole lamp furnace, which has its own positional uncertainties independent of the diffraction geometry (see Chapter 4.3), the Debye-Scherrer geometry

provides unparalleled certainty in peak position minimizing uncertainties in lattice parameters and other refinable parameters.

A disadvantage of this geometry arises from sample absorption, which necessitates the use of very thin samples (less than 0.4 mm in diameter). The mass attenuation coefficient describes the penetration and energy deposition by photons. Ignoring photoelectric absorption edges, it is generally understood that the smaller the wavelength the better the penetration of the photons, and as such, the better the quality of the collected diffraction pattern.[17] However, smaller samples are desired over larger ones as the temperature distribution in the sample is more uniform when heated with the quadrupole lamp furnace.

1.6 Analysis of Data – the Rietveld Method

Hugo Rietveld was a Dutch crystallographer who contributed the single most important quantitative analysis method in the field of crystallography. The aptly named Rietveld method, is a quantitative comparison between a structural model and a diffraction pattern. Though originally developed by Rietveld for the analysis of neutron powder diffraction data, it can be applied to X-ray diffraction data and more.[18,19]

The way that the Rietveld method works is by comparing a profile fitting model with experimental data. First a theoretical diffraction pattern is constructed from a model using the formula for the integrated intensity for each peak

$$I = S|F|^2TMLPA$$

where,

S is the scale factor

F the structure factor = $\sum_0^n f_n e^{2\pi i(hx_n + ky_n + lz_n)}$

T the temperature factor = $e^{\left[-2B\left(\sin\frac{\theta}{\lambda}\right)^2\right]}$

where, $B = 8\pi^2\langle u \rangle^2$

where, u is the root-mean square of thermal displacement

M the multiplicity

LP the Lorentz-Polarization factor = $\frac{(1+\cos 2\theta^2)}{(\sin 2\theta^2 \cos \theta)} [\cos 2\theta^2]$

P the preferred orientation function[20] = $\left[p_1^2 \cos \alpha^2 + \left(\frac{1}{p_1}\right) \sin \alpha^2\right]^{-\frac{3}{2}}$

and A the absorption.

Each point constructed from the model is compared to the experimental data by performing a least squares analysis which is given by

$$R = \sum_{i=1}^N w_i [y(obs)_i - y(calc)_i]^2$$

where, y(obs) is the measured intensity at a point, y(calc) the intensity predicted from the integrated intensity formula, and w the statistical weighting.[21] If the difference between the predicted model and the data is large over all points in a pattern, a change is made to the model (change in lattice parameter, occupancy, peak shape [Gaussian, Lorentzian, and their combinations], etc) and the analysis is performed again. Once the model is minimized and converges, the process concludes.[22] Since the process takes into account all of the structural

information in a model, diffractometer setup and sample conditions, it is very robust in providing accurate results.[23-25]

The R value comes in many different forms to express different numerical representations.[21,26]

$$R_{profile} = \frac{\sum_i |y(obs)_i - y(calc)_i|}{\sum_i y(obs)_i}$$

$$R_{weighted-profile} = \left[\frac{\sum_i w_i |y(obs)_i - y(calc)_i|^2}{\sum_i w_i y(obs)_i^2} \right]^{\frac{1}{2}}$$

$$R_{Bragg} = \frac{\sum_i |I(obs)_i - I(calc)_i|}{\sum_i I(obs)_i}$$

$$R_{expected} = \left[\frac{(N - P)}{\sum_i w_i y(obs)_i^2} \right]^{\frac{1}{2}}$$

where, N and P are the number of observations and parameters, respectively.

Another common statistical measure is the goodness-of-fit, χ^2 . This is given by

$$\chi^2 = \left[\frac{R_{weighted-profile}}{R_{expected}} \right]^2$$

Low values of R and χ^2 (reduced χ^2 in the program GSAS), if properly refined, are desired and indicate a good structural model based on the data.

Several different computer programs exist to perform Rietveld refinements. In this study the General Structure Analysis System (GSAS) and EXPGUI programs were employed for this.[27,28] For a more detailed description of the Rietveld method please consult *Rietveld Made*

Easy by Taylor.[22] An example fit using EXPGUI and GSAS is provided in Figure 9 for Y_2TiO_5 at room temperature with relevant statistical information.

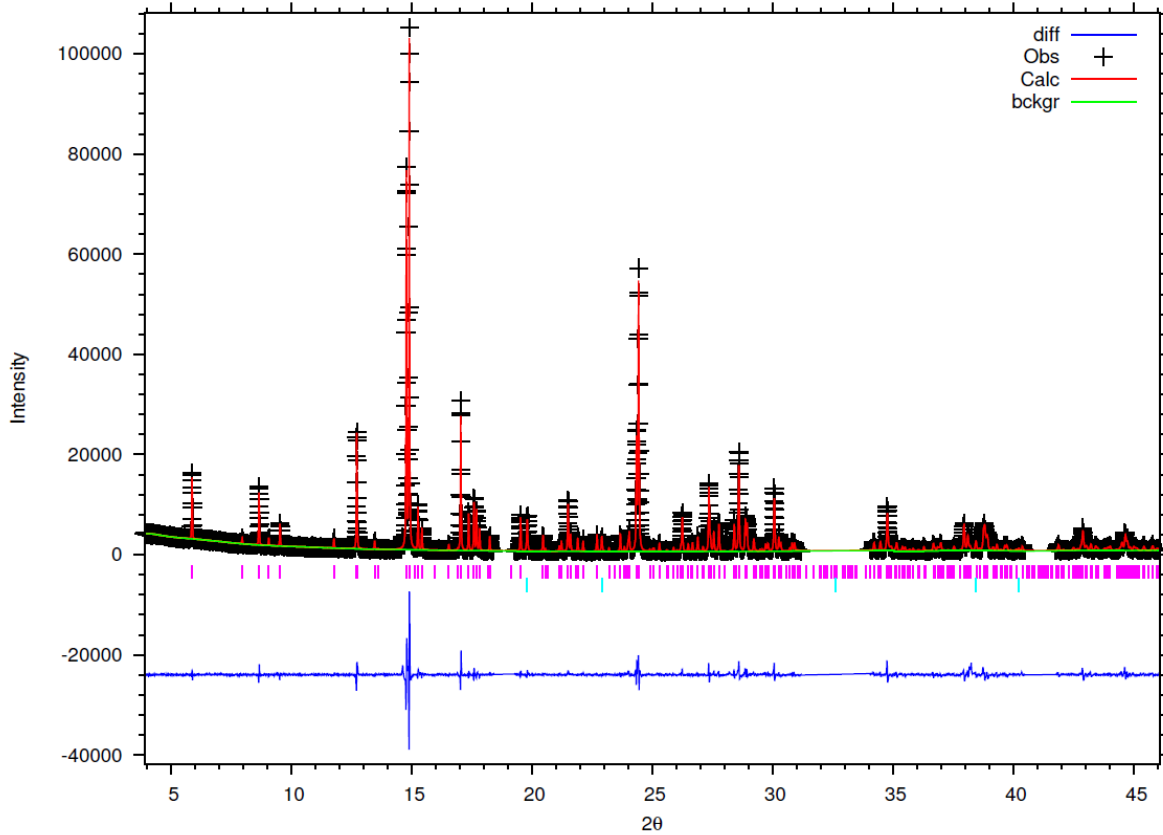


Figure 9. Rietveld fit using EXPGUI and GSAS for Y_2TiO_5 at room temperature. $R_p, \text{fitted} = 0.0837$, $R_p, \text{-bknd} = 0.1123$, and $\chi^2 = 27.64$.

1.7 Thermal Expansion in General

Traditionally the coefficient of thermal expansion is represented by a polynomial equation describing the change in lattice parameter as a function a temperature along each crystallographic axis. Largely due to the fact that thermal expansion is a second-rank symmetric tensor relating strain to temperature, it is becoming increasing popular to describe the thermal expansion of a material in terms of the matrix notation given here:

$$d\varepsilon_{ij} = \begin{bmatrix} \alpha_{11} & \alpha_{12} & \alpha_{13} \\ \alpha_{21} & \alpha_{22} & \alpha_{23} \\ \alpha_{31} & \alpha_{32} & \alpha_{33} \end{bmatrix} dT$$

At any time the number of matrix components can be reduced to six independent parameters due to the inversion symmetry of thermal expansion. These six components can then be further simplified depending on the crystallographic symmetry of the cell. For lower symmetry crystal systems it would be necessary to have six or five components of the thermal expansion tensor for triclinic and monoclinic cells, respectively. Higher symmetry cells such as cubic can be fully simplified to a single component. In crystal systems with orthonormal axes (i.e. cubic, tetragonal, orthorhombic) the thermal expansion calculation can become quite trivial as the thermal expansion tensor components match their respective crystallographic directions (i.e. $\alpha_a = \alpha_{11}$). For lower symmetry cells or cells with non-orthonormal axes (i.e. hexagonal, trigonal, monoclinic, triclinic), the calculation can become more complex. The reduced thermal expansion tensors for an orthorhombic and hexagonal cell are given below. For a more detailed description of thermal expansion, please refer to *Thermal Expansion of Solids* by Taylor.[29]

$$d\varepsilon_{ij} = \begin{bmatrix} \alpha_{11} & & \\ & \alpha_{22} & \\ & & \alpha_{33} \end{bmatrix} dT \quad d\varepsilon_{ij} = \begin{bmatrix} \alpha_{11} & & \\ & \alpha_{11} & \\ & & \alpha_{33} \end{bmatrix} dT$$

The program CTEAS can be used to calculate the coefficient of thermal expansion tensor from high temperature X-ray diffraction data sets. Based on each *hkl* reflection and corresponding d-spacing, CTEAS will perform a least-squares polynomial fit as a function of temperature. The expansion information from each reflection is then recombined and evaluated to fully describe the thermal expansion behavior in a more complete manner, as opposed to conventional methods adopted to calculate thermal expansion.[30,31]

1.8 Diffusional Phase Transformations in General

Generally, phase transformations can be divided into three categories; diffusion-dependent with no change in composition or number of phases present (e.g. melting, recrystallization, etc), diffusion-dependent with a change in composition or number of phases present (e.g. eutectoidal), or diffusionless (e.g. displacive, martensitic). Diffusionless transformations do not break and remake bonds, having low activation energies and can take place on a short time scale.

Diffusional transformations on the other hand require the breaking and remaking of bonds, have larger activation energies, and the transformation process can be sluggish.

Frequently, diffusional phase transformations can be described using a simple nucleation, growth, and impingement model. The new phase can nucleate either randomly (homogeneously) or at defects and grain boundaries (heterogeneously). When there is a sufficient amount of energy such that a supercritical particle size is reached, the formation of the new phase can occur.[32] The classical theory of nucleation describes the kinetics using the Gibbs free energy of nucleus formation, ΔG^* , which depends on the chemical Gibbs free energy per unit volume, the interfacial energy per unit area, and the misfit strain energy per unit volume in the Arrhenius relationship given below,

$$N(T(t)) = C\omega e^{\left(-\frac{\Delta G^*(T(t))+Q_N}{RT(t)}\right)}$$

where, R is the gas constant, T the temperature, C the number of suitable nucleation sites, ω the characteristic frequency factor, and Q_N the activation energy:[33]

After the onset of nucleation, growth of the formed particles occurs. There are two main modes for growth; volume diffusion controlled (where long range compositional changes take place)

and interfacial controlled (where growth determines the immediate area of interface).[32,33] The equation for both models is described by the following,

$$Y(\tau, t) = g \left(\int_{\tau}^t v dt \right)^{\frac{d}{m}}$$

Where, $m=1$ for interfacial controlled growth and $m=2$ for volume diffusional growth, and d is the dimensionality of the growth.

Finally, after reaching a sufficient size, the particles grow large enough to impinge on each other, slowing the rate of transformation of the new phase. As a function of time, the fraction of phase transformed can be plotted. Figure 10 shows a schematic curve which describes this type of phase transformation behavior of nucleation, growth, and impingement.

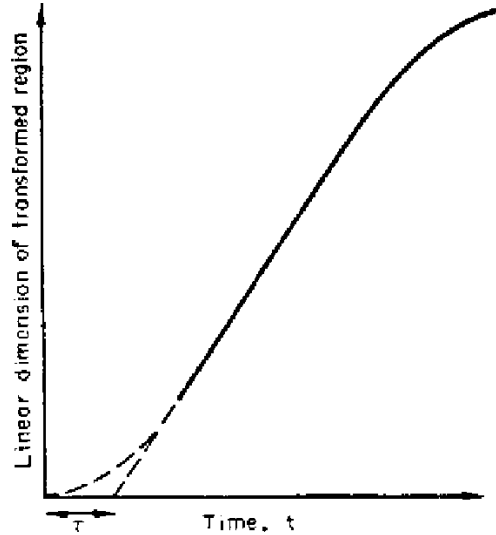


Figure 10. Schematic growth curve for a product region[34]

A simplification of this process was described by the Johnson-Mehl-Avrami-Kolmogorov theory, also known as the JMAK theory.[35-38] The JMAK equation can be written as

$$F(t) = 1 - \exp[-kt^n]$$

Where, t is time, $F(t)$ is the fraction transformed, n relates to the growth mechanism, and k is a rate constant which is derived from the Arrhenius relationship.

This simplification is based on the following assumptions regarding the phase transformation behavior; infinite system size, uniform but random nucleation, growth ends at impingement, spherical particles form, and an interfacial controlled growth mechanism.[39] Although most transformations do not meet the above criteria, the JMAK equation nonetheless can still be applied in many scenarios, and useful information can be inferred.

The kinetics of a transformation can be determined via isothermal and/or isochronal experiments which measure the fractional phase evolution with time. By linearizing the data using the natural log and fitting to the JMAK equation, one can simply back calculate the values for k and n .

Taking the value for k at multiple isothermal temperatures it is then possible to fit the data to the Arrhenius equation to calculate the rate constant and activation energy of the transformation. The value of n can shed light on the type of nucleation and growth which occurred, see Table

1.[34,40,41]

Table 1. Generalized meaning of the Avrami exponent n

Type of Nucleation	n
Random 3D growth	3
Distribution of nucleation site non-random, 1 and 2D	
surface	3
edge	2
point	1

1.9 Objectives and Scope of Research

The goal of this research is to shed light on the phase transformation behavior in the rare-earth titanate system. This was achieved by correlating the thermal expansion behavior, and mechanisms behind such behavior, between two separate and dissimilar crystallographic phases (orthorhombic and hexagonal). In addition, the kinetics of the transformation was evaluated and the key kinetic parameters were determined. The main questions originally posed were:

1. Is the orthorhombic to hexagonal transformation first- or second-order? Does it proceed by a reconstructive or displacive mechanism?
2. What unit cell volume changes and/or shape changes accompany the transformations?
3. What is the thermal expansion in the hexagonal phase and how does it relate to the orthorhombic phase from a continuum mechanics perspective? How does this also relate to the heat capacity?
4. What is the lattice correspondence between the orthorhombic and hexagonal phases?
5. What is the underlying mechanism of transformation between the orthorhombic and hexagonal phases? Can we use our experimental setup to answer this question?
6. What are the kinetics in the transformation between the orthorhombic and hexagonal phases?

At a much higher level, this work is the foundation for future research which may involve the determination of a relationship between two phases which undergo a reconstructive transformation from a crystallographic perspective using the thermal expansion behavior.

Furthermore, this work describes a new method for the analysis of kinetic parameters for a phase transformation which occurs at high temperatures using a thermal image furnace.

CHAPTER 2

LITERATURE REVIEW

2.1 The Rare-Earth Titanates (Ln_2TiO_5)

2.1.1 Introduction

A typical Ln_2O_3 - TiO_2 phase diagram is seen in Figure 11 in the example of La_2O_3 - TiO_2 . Phase transformations have been reported in the 1:1 and 1:2 systems for some of the compositions. No transformations have been as yet reported in the 2:3 compounds.

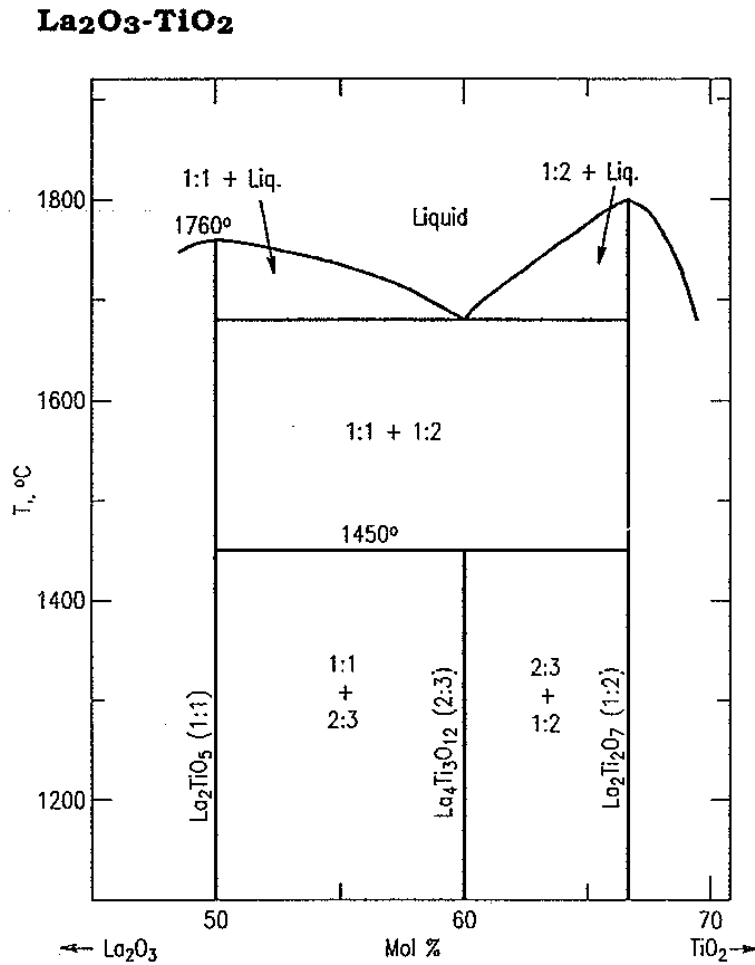


Figure 11. Taken from the NIST Phase Equilibria Diagrams for Ceramists, Vol.XI (1995).

The rare earth titanates have many desirable properties, which make them ideal candidates in several engineering applications. Their high mechanical strength, thermal stability, and robust chemical resistance make them well suited for applications in high temperature environments where structural reliability is critical. For example, boron carbide and boron steels have been popular choices for control rod assemblies in fast breeder nuclear reactors due to their many desirable properties.[42,43] Unfortunately, radiation damage caused by (n, α)-reactions with ^{10}B isotopes results in the formation of helium, causing swelling to occur and cracks to nucleate and grow, resulting in decreased operational lifespans.[44-46] In an effort to find a suitable replacement, engineers have turned to Dy_2TiO_5 and Gd_2TiO_5 , taking advantage of the large neutron absorption cross-sections of the rare-earth cations, good mechanical properties, resistance to chemical attack, simple fabrication, and a low degree of swelling under neutron radiation.[47]

In addition to their high temperature mechanical properties, several of the rare-earth titanates also exhibit special electrical, magnetic, and optical properties. In a study by van Dover, it was demonstrated that a material with a large dielectric constant, k , could be formed by incorporating TiO_2 or Ti into thin films of rare-earth oxides.[48] Having a high electric breakdown field, a low interface trap density, and a small hysteresis and frequency dispersion, Nd_2TiO_5 was studied as an ideal candidate for ion-sensitive field-effect transistors (ISFET). ISFETs are commonly used as microsensors and feature low cost, ease of miniaturization, and low output impedance.[49,50]

Many of the desirable properties of the rare-earth titanates are phase dependent (i.e. the cubic phase performs best under neutron radiation). Much of the existing work on this materials system

has been done *ex situ* via quenching of samples from high temperatures. Although this method is useful, it sometimes fails to capture the true structural behavior at high temperatures.

2.1.2 Polymorphism in the Ln_2TiO_5 System

The rare-earth titanates undergo several polymorphic phase transformations as a function of temperature and size of the rare-earth cation.[51,52] Studies on quenched samples indicate that these compounds exist in the orthorhombic phase for $\text{Ln} = \text{La-Dy}$ and Y and in a cubic phase for $\text{Ln} = \text{Ho-Lu}$. In addition, in certain cases, a metastable cubic phase exists at room temperature before transforming into the equilibrium orthorhombic phase at higher temperatures for Dy_2TiO_5 and Y_2TiO_5 which can only be attained via powder synthesis using sol-gel or related techniques.[51,53-60]

Several studies in the late 70's and early 80's by Petrova, Shamrai, Shcherbakova, Sukhanova, Shepelev, Tiedemann, and Müller-Buschbaum on quenched samples outlined a general phase diagram showing the relationship between phase, temperature, and cation size (Figure 12).

[51,53,55,56,61-63] Equivalently, the temperatures of transformation are listed in Table 2. As described by Figure 12 and Table 2, as cation size decreases, the melting temperature increases. Conversely, as cation size decreases the onset temperature of transition between the orthorhombic and hexagonal phase decreases.

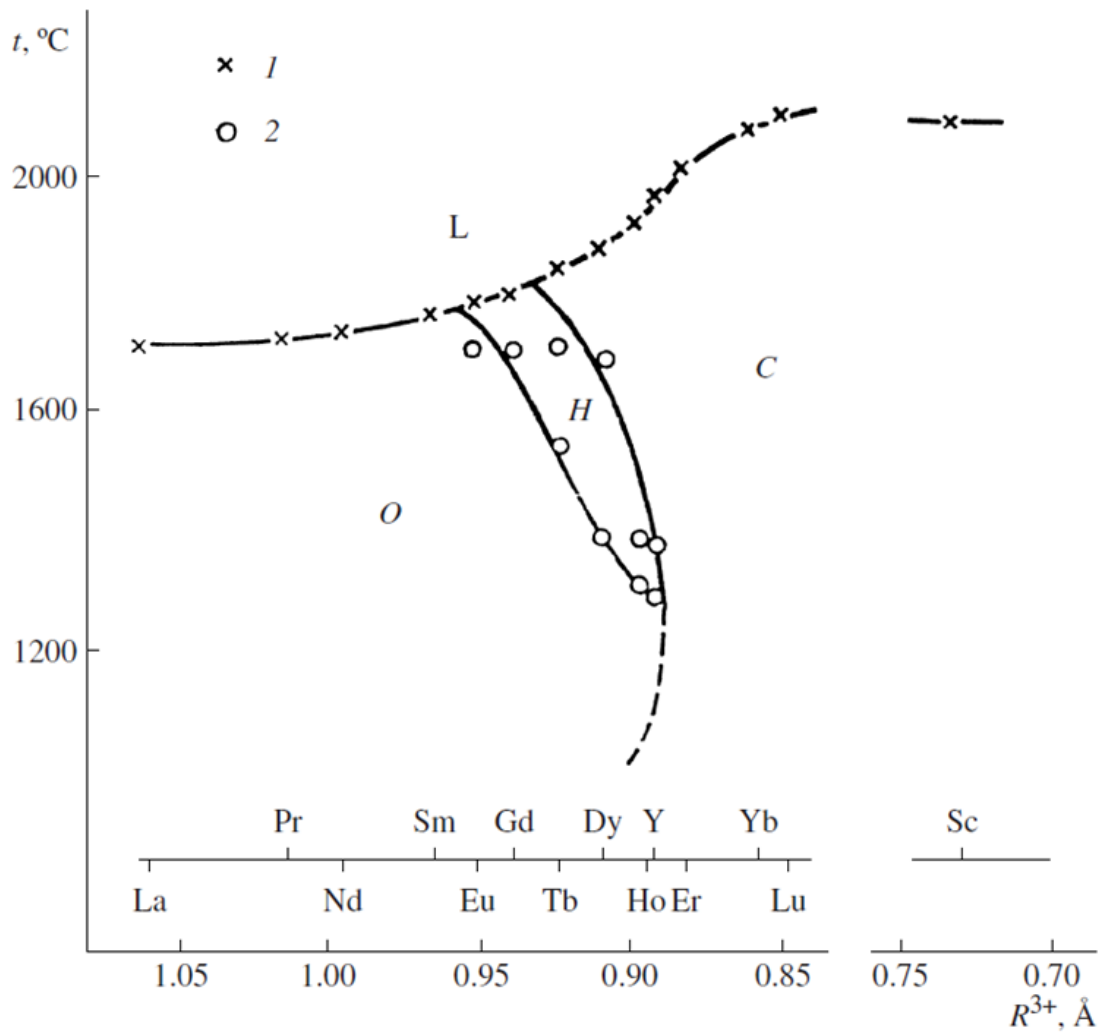


Figure 12. Phase diagram for the rare-earth titanates depicting relevant phases found at varying temperatures as a function of rare-earth cation size. L = liquid, O = orthorhombic, H = hexagonal, C = cubic[51]

Table 2. Transition Temperatures of the Rare-earth Titanates on Heating.[51]

Ln_2TiO_5	Melting Temp °C	Transition Temp °C orthorhombic to hexagonal	Transition Temp °C hexagonal to cubic
La	1710		
Pr	1725		
Nd	1730		
Sm	1765		
Eu	1780	1750	
Gd	1790	1700	
Tb	1850	1520	1700
Dy	1875	1370	1680
Ho	1910	1310	1400
Y	1960	1300	1380
Er	2010		
Yb	2080		
Lu	2100		
Sc	2075		

Since these studies have taken place, a fair amount of work has been done to better characterize the transition temperatures and phases. The cubic phase was once thought to be the pyrochlore structure, related to the geometrically frustrated, magnetic spin ice $\text{Dy}_2\text{Ti}_2\text{O}_7$, and has since been found to be a disordered fluorite structure, one-eighth in size.[64-66] Similar work has also been carried out to solve the hexagonal structure from quenched samples.[56,58-60] A summary of these and other relevant structures can be found in Table 3 and Figure 13.[58,59]

Table 3. Crystallographic Information for the Rare-earth Titanate Phases

Phase	Space Group	Lattice Parameters	Z
Orthorhombic	$Pnam$ (62)	a = 10.361 Å b = 11.229 Å c = 3.716 Å	4
Hexagonal	$P6_3/mmc$ (194)	a = 3.632 Å c = 11.969 Å	2
Cubic (fluorite)	$Fm\bar{3}m$ (225)	a = 5.168 Å	4
Cubic (pyrochlore)	$Fd\bar{3}m$ (227)	a = 10.337 Å	8

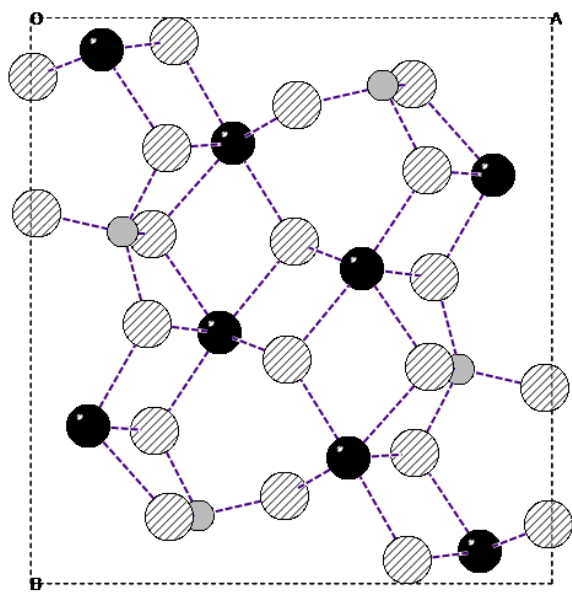


Figure 13(a) Crystallographic structure of the orthorhombic phase for Dy_2TiO_5 . Dy = solid black, Ti = solid gray, O = striped

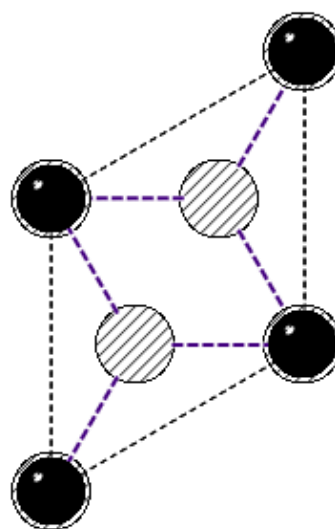


Figure 13 (b) Crystallographic structure of the hexagonal phase for Dy_2TiO_5 . Dy/Ti = solid, O = striped

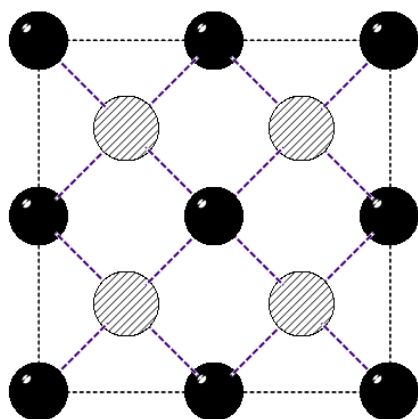


Figure 13(c) Crystallographic structure of the fluorite phase for Dy_2TiO_5 . Dy/Ti = solid, O = striped

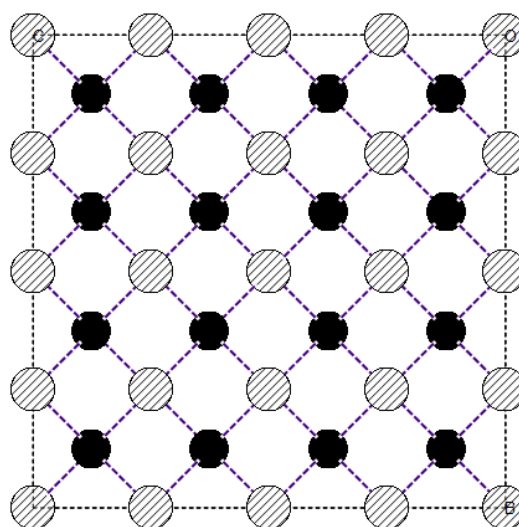


Figure 13(d) Crystallographic structure of the pyrochlore phase for Dy_2TiO_5 . Dy/Ti = solid, O = striped

2.2 The Rare-Earth Di-Titanates ($\text{Ln}_2\text{Ti}_2\text{O}_7$)

Though not the focus of this work, the rare-earth di-titanates are worth mentioning to contextualize this study as well as provide background information for future work in this system.

The rare-earth di-titanates are typically stabilized in the pyrochlore structure for the smaller rare-earth cations ($\text{R} = \text{Eu-Lu}$).^[67] $\text{Dy}_2\text{Ti}_2\text{O}_7$ and $\text{Ho}_2\text{Ti}_2\text{O}_7$ have been well studied for their interesting low temperature frustrated magnetic properties. Both are prototypical examples of spin-ice materials which is a substance that does not have a single minimal energy state, having spin degrees of freedom which prevent it from completely freezing.^[68] Magnetism, the ability of a magnetic charge to behave in the same manner as the more familiar electric charge, is the theoretical basis behind recent efforts to show that a magnetic monopole can exist in a material. Studying the spin-ice nature of $\text{Dy}_2\text{Ti}_2\text{O}_7$, allowed scientists for the first time to prove the existence of a monopole existing inside of a structure.^[69]

Although a significant amount of research has focused on the spin-ice nature of the pyrochlore structures, very little is known about the larger rare-earth cation di-titanates ($\text{R} = \text{La-Sm}$) which form a monoclinic structure at room temperature.^[67] The monoclinic structure is isomorphic with $\text{Ca}_2\text{Nb}_2\text{O}_7$ and forms a layered perovskite.^[70,71] An orthorhombic modification of this system appears at temperatures above 800°C and is related to the monoclinic structure using the series of maximal subgroup relationships. Table 4 outlines the crystallographic information for the rare-earth di-titanates at room temperature and Figure 14 depicts the structures.

Similar to the polymorphic phase transformations in the rare-earth mono-titanates, little is known about the mechanisms and kinetics of transformation.

Table 4. Cell Parameters for the Rare-earth Di-Titanate Structures.[67]

$\text{Ln}_2\text{Ti}_2\text{O}_7$	a (Å)	b (Å)	c (Å)	β (°)	Space Group	Structure	Z
La-Sm	7.80	5.546	13.011	98.6	$P2_1$	Monoclinic	4
La-Sm	7.692	5.501	25.457	90	$Pn2_1a$	Orthorhombic	8
Eu-Lu	10.211	-	-	90	$Fd\bar{3}m$	Cubic	8

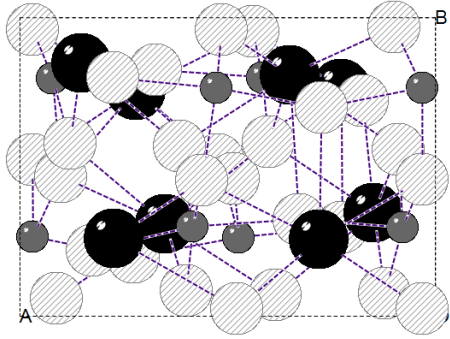


Figure 14(a) Crystallographic structure of the monoclinic phase for $\text{Dy}_2\text{Ti}_2\text{O}_7$ projected down the c-axis. Dy = solid black, Ti = solid gray, O = striped

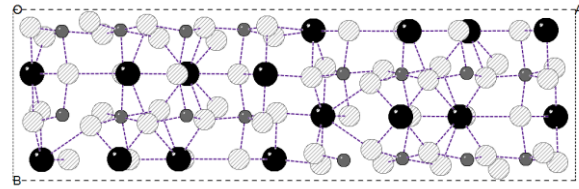


Figure 14(b) Crystallographic structure of the orthorhombic phase for $\text{Dy}_2\text{Ti}_2\text{O}_7$ projected down the c-axis. Dy = solid black, Ti = solid gray, O = striped

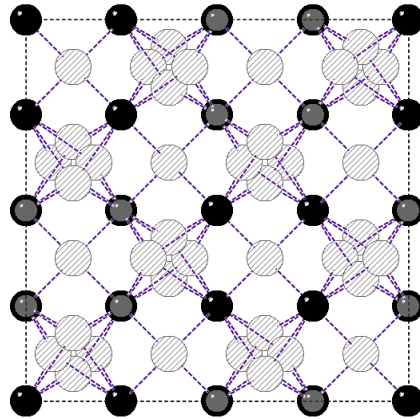


Figure 14(c) Crystallographic structure of the pyrochlore phase for $\text{Dy}_2\text{Ti}_2\text{O}_7$ projected down the c-axis. Dy = solid black, Ti = solid gray, O = striped

CHAPTER 3

SAMPLE SYNTHESIS

3.1 Powder Synthesis

Two different methods were employed to produce oxide powders in the Ln_2TiO_5 system: the inorganic-organic steric entrapment technique and the conventional solid-state route.

The resulting powder from both methods were examined by X-ray diffraction (XRD) with a Siemens D5000 diffractometer (Bruker AXS Inc., Madison, WI) using CuK_α radiation ($\lambda=1.5418$ Å, 40 kV, 30 mA). XRD patterns were acquired in reflection geometry between 5° and 65° 2θ at a scanning speed of $0.5^\circ/\text{min}$ and a step size of 0.02° . The orthorhombic crystalline phase was identified using the International Center for Diffraction Data PDF-4+ database (ICDD v. 2014, International Center for Diffraction Data, Newton Square, PA) accessed through program Jade 9.4.1 (Materials Data Inc., Livermore, CA). Powders produced from both methods were found to be very phase pure.

3.1.1 The Inorganic-Organic Steric Entrapment Method

This method, developed in the Kriven research group, has been used to form numerous (>50) compounds to date with high phase purity and small particle sizes.[72-101] The general process of the inorganic-organic steric entrapment method is outlined in Figure 15. At a fundamental level, the dissolved ions, usually nitrate salts, are surrounded by the steric entrapper, PVA or EG, to bring them into close proximity, illustrated in Figure 16. The solvent, either deionized water or ethanol, is evaporated, leaving behind a fluffy gel. This gel is then dried at 200°C for 2 hours and calcined to produce the desired phase (approximately 1200°C for the formation of the

orthorhombic phase [La-Y], and lower for the cubic phase [Dy-Lu]). An example process for powder synthesis using the inorganic-organic steric entrapment method is provided below in Figure 15 for Dy_2TiO_5 .

Stoichiometric amounts of dysprosium nitrate (99.9%, Sigma-Aldrich, St Louis, MO) and titanium (IV) isopropoxide (99.995%, Alfa Aesar, Ward Hill, MA) were combined in a 5 wt% ethylene glycol / isopropanol solution which was left to stir overnight. The isopropanol was then evaporated using a hot plate, producing a gel that was subsequently dried in a furnace at 200 °C for 2 hours. The dried gel was crushed using a mortar and pestle and then calcined at 1200 °C for 10 hours.

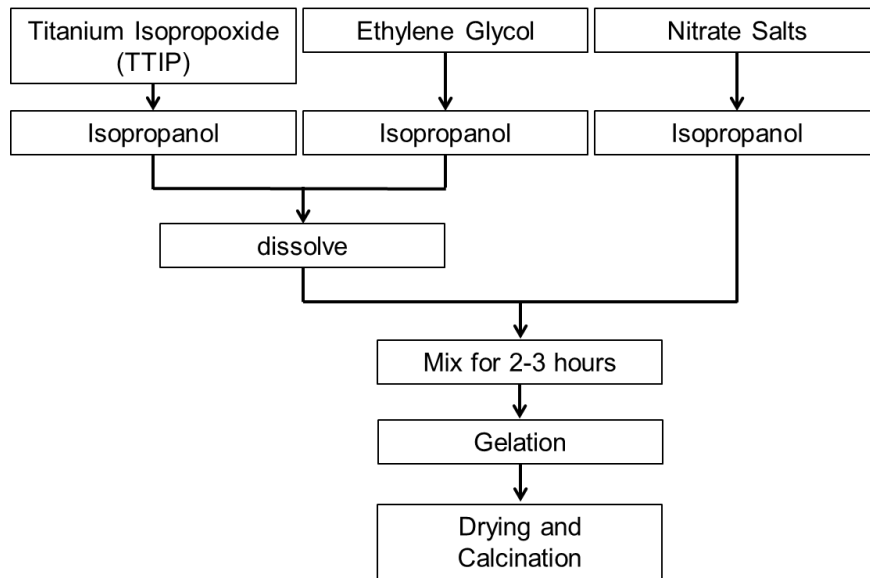


Figure 15. Schematic illustration of powder synthesis via the inorganic-organic steric entrapment method for the Ln_2TiO_5 system.

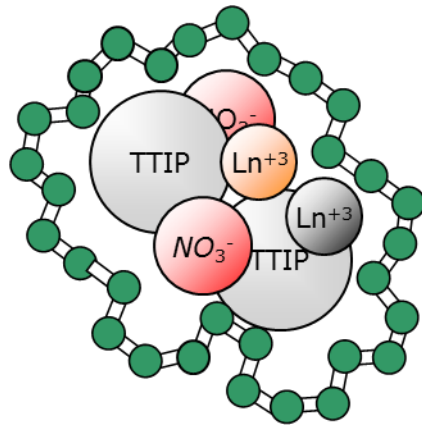


Figure 16. Proposed mechanism of the inorganic-organic steric entrapment method. The PVA/EG polymer surround constituent ions spatially confining them and separating them from others. TTIP is titanium isopropoxide.

3.1.2 Conventional Solid-State Reaction Method

The second and more commonly used method is calcination via the solid-state technique. This process is illustrated in Figure 17 and simply relies on the stoichiometric mixing and heating of the base oxides (Ln_2O_3 and TiO_2).

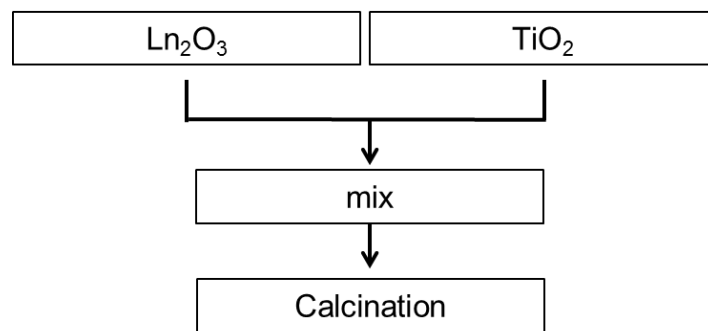


Figure 17. Illustration of the conventional method of powder synthesis via the solid-state process.

3.2 Sample Preparation

Each type of experiment described in this document required extensive processing of the synthesized powder in order to prepare samples for characterization. Listed below are the three main experiments and a description of the sample preparation for each.

3.2.1 Thermal Expansion Experiments

The custom nature of the experimental setup (see Chapter 4), also necessitated the need for a sample which was also custom. Samples for thermal expansion experiments need to be in powder form. This was desired to prevent/minimize any effects from strain in the sample which may arise from grain boundary impingement with nearby grains which complicated the analysis of thermal expansion from crystallographic parameters. In order to suspend the powder inside the quadrupole lamp furnace, whilst also positioning it in the X-ray beam path, the sample was mounted in the configuration schematically described in Figure 18. The powder was first mixed with approximately 5-10 wt. % platinum powder, sieved using a 325-mesh sieve (45 μm), and then “scooped” in a thin sapphire capillary. Packing of the powder in the capillary was critical. The powder must be able to freely roll when spinning; preventing particle interaction while ensuring minimal packing density which improved the resulting diffraction pattern (this was due to absorption from the sample caused by the use of heavy elements i.e. lanthanides). The powder was then secured in place, prevented from rolling out of the sapphire capillary, using smaller alumina capillary plugs. These plugs allowed air to enter and escape which helped minimize pressure build-up. The smaller sapphire capillary was then placed in a longer alumina rod and secured in place with zirconia paste. Finally, platinum paste was brushed on the sapphire capillary on either side of the powder which ended up in the beam path to help evenly distribute heat across the sample.

The resulting sample was then placed in a brass stub and inserted into the goniometer head on the diffractometer. The quadrupole lamp furnace was then centered over the sample.

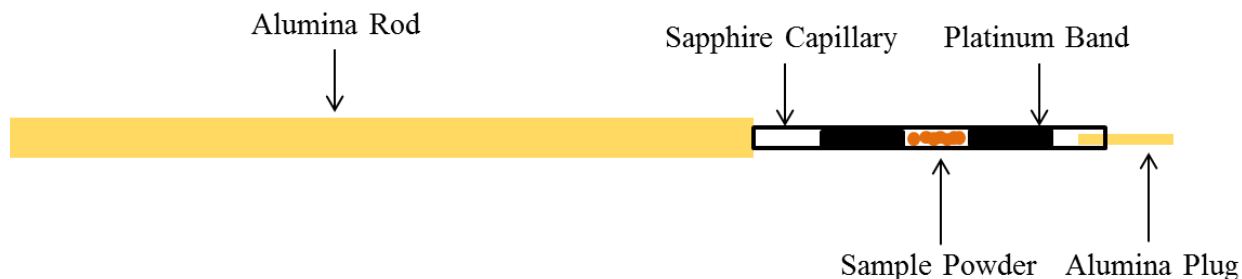


Figure 18. Design of the method to suspend powders in the center of the diffractometer and the quadrupole lamp furnace.

3.2.2 Phase Transformation Experiments via X-ray Diffraction

The sample preparation for the phase transformation experiments was very similar to that of the thermal expansion experiments with slight modification. Since it was only necessary to track the evolution of the largest hexagonal diffraction peak the sample need not be in powder form.

Instead, a sintered rod of the material was secured in a longer alumina rod using zirconia paste with bands of platinum paste brushed directly onto the sample as depicted in Figure 19. The diameter of the rod could be tailored, minimizing the effect of absorption from both the sample and sapphire capillary.



Figure 19. Design of the method to suspend sintered rods in the center of the diffractometer and the quadrupole lamp furnace.

3.2.3 Phase Transformation Experiments via Differential Scanning Calorimetry

Two different sample types were employed to characterize the phase transformation behavior via Differential Scanning Calorimetry (DSC). The first sample types were in powder form to ensure that microstrain effects were minimized. The second sample types used were sintered pellets, reverted back to the orthorhombic phase, and annealed to grown the grain size. There was no difference observed between the two sample types with regard to the transformation temperature and behavior, though the sintered pellets had a “cleaner” signal with respect to the powder samples, which is not too surprising. All of the DSC experiments were carried out with a Netzsch STA 409 CD simultaneous thermal analyzer (Netzsch Instruments, Selb, Germany). A picture of the instrument is provided in Figure 32 in Chapter 4.5.

CHAPTER 4

EXPERIMENTAL SETUP

4.1 Beamline Configuration

4.1.1 The National Synchrotron Light Source

The National Synchrotron Light Source (NSLS) is located at Brookhaven National Laboratory in Upton, NY. Although recently decommissioned and replaced by NSLS-II, all of the experiments in this study were performed at NSLS.

The NSLS is a source of synchrotron radiation, see Chapter 1.5. First commissioned in 1982, NSLS consisted of 65 experimental beamlines on two synchrotron storage rings producing light in the X-ray, ultraviolet, and infrared range. The characteristic energy of operation of NSLS was 2.8 GeV with a ring circumference of 170 m. A picture of the NSLS is provided in Figure 20.



Figure 20. Aerial view of the National Synchrotron Light Source at Brookhaven National Laboratory in Upton, NY.

Beamline X14-A was used for all of the experiments carried out at the NSLS. X14-A was equipped with a double Si monochromator and a single focusing mirror. The quadrupole lamp furnace would be located at the center of a Huber diffractometer. Diffracted X-ray radiation was collected with a Si strip position sensitive detector located 1432 mm away from the center of the diffractometer. The detector could record a range of approximately $2.5^\circ 2\theta$ while stationary and up to $45^\circ 2\theta$ when moving (limited by the opening of the furnace). The X-ray beam was focused to 0.75×0.5 mm onto the sample. A schematic representation of the beamline setup at X14-A is provided in Figure 21.

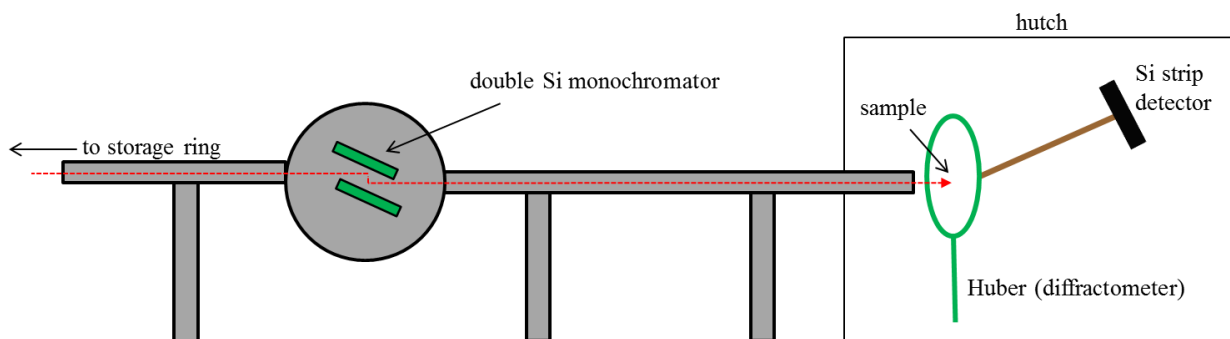


Figure 21. Schematic representation of the beamline setup at the National Synchrotron Light Source.

4.1.2 The Advanced Photon Source

The Advanced Photon Source (APS) is located at Argonne National Laboratory in Lemont, IL.

The APS is a source of synchrotron radiation, see Chapter 1.5. First commissioned in 1995, the APS currently has 35 sectors, with each sector typically having more than one experimental beamline. Additional sectors and beamlines are currently under construction. The APS mostly produces light in the X-ray range on a single synchrotron storage ring. The characteristic energy

of operation of APS was 7.0 GeV with a ring circumference of 1104 m. A picture of the APS is provided in Figure 22.



Figure 22. Aerial view of the Advanced Photon Source at Argonne National Laboratory in Lemont, IL.

Two separate beamlines were used at the APS for this study, 33BM-C and 11BM-B. Most of the work was carried out at 33BM-C which will be described here. The setup of 33BM-C is very similar to that of X14-A at NSLS. 33BM-C is equipped with a double Si monochromator and a single focusing mirror. The quadrupole lamp furnace would be located at the center of a Huber diffractometer. Diffracted X-ray radiation was collected with a Pilatus 100k detector located approximately 1040 mm away from the center of the diffractometer. The detector could record a range of approximately $4^\circ 2\theta$ while stationary and up to $45^\circ 2\theta$ when moving (limited by the

opening of the furnace). The X-ray beam was focused to 0.5 X 0.5 mm onto the sample. A schematic representation of the beamline setup at 33BM-C is provided in Figure 23.

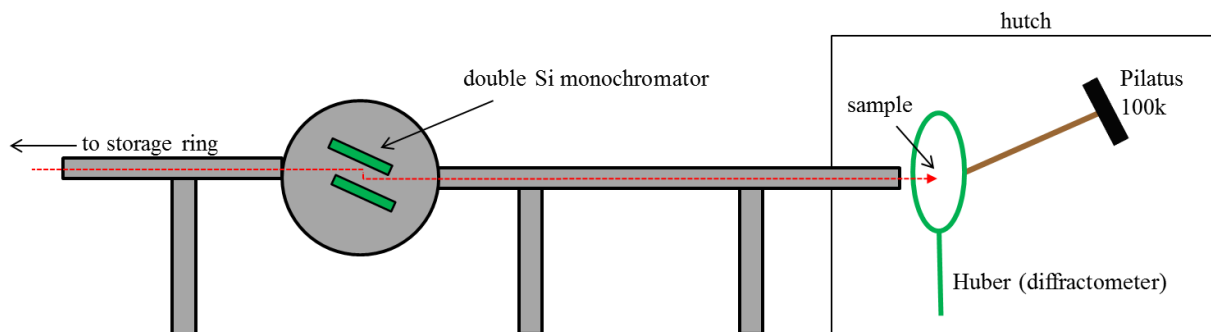


Figure 23. Schematic representation of the beamline setup at the Advanced Photon Source.

4.2 Spallation Neutron Source

The Spallation Neutron Source (SNS) is located at Oak Ridge National Laboratory in Oak Ridge, TN. One experiment was conducted at the powder diffractometer at beamline BL-11A (POWGEN) for the thermal expansion of Nd_2TO_5 in air using an ILL furnace. If all detector banks are used, five in total, data can be collected to $150^\circ 2\theta$, Figure 24 shows the detector setup. The sample to detector distance can be varied between 2.5-4.5 m depending on resolution needs. A picture of the SNS is provided in Figure 25.



Figure 24. The neutron detector banks at POWGEN located at the Spallation Neutron Source at Oak Ridge National Laboratory in Oak Ridge, TN.



Figure 25. Aerial view of the Spallation Neutron Source at Oak Ridge National Laboratory in Oak Ridge, TN.

4.3 The Quadrupole Lamp Furnace

Thermal-image furnaces have been a method for heating samples for many decades and have been employed in conjunction with X-ray diffraction for *in situ* measurement of samples at high temperature. Stecura, in 1968, was one of the first researchers to use a thermal-image furnace for high temperature X-ray diffraction.[102] In this setup two 1.52 m diameter parabolic mirrors focused the light from a carbon arc onto a sample. The sample could reach temperatures in excess of 2800 °C, but was limited to 1700 °C as thermal stability was an issue. Later designs for thermal-image furnaces included one by Wantanabe.[103] Wantanabe's design is similar to float zone techniques to synthesize single crystals, wherein a sample is placed at the intersection of two parabolic halogen lamps coated with a layer of gold. This design also incorporated a small linear slit for the diffracted radiation to escape without having to interact with the enclosure improving the quality of the collected pattern. Temperatures were recorded up to 1700 °C in air using a thermocouple inserted into the "hot zone". Wantanabe's design is reproduced in Figure 26.

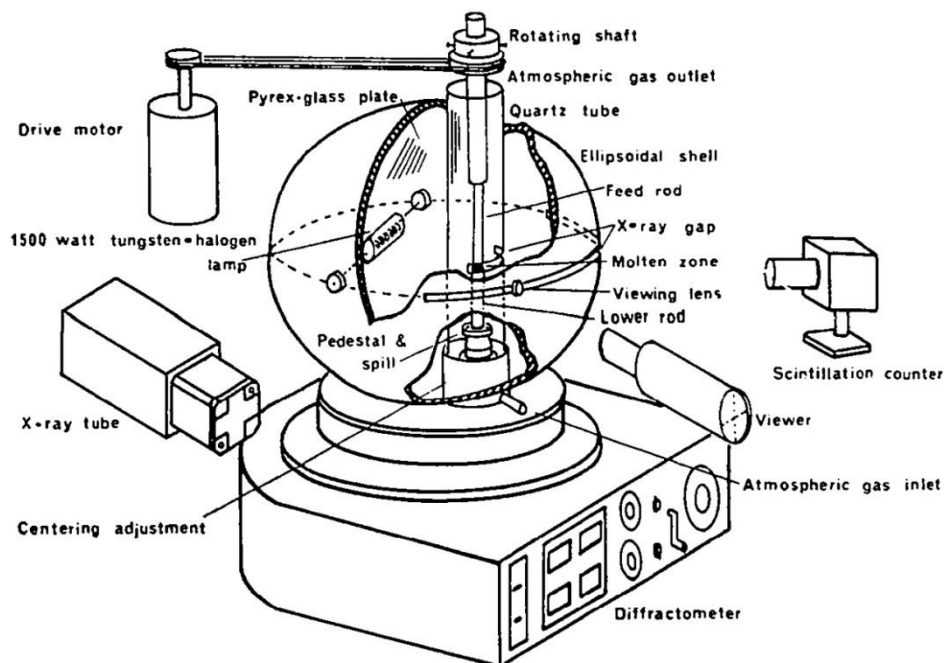


Figure 26. Wantanabe's design of a thermal image furnace paired with an X-ray diffractometer representing one of the first experimental setups to record diffraction patterns at temperature *in situ*.

A compact furnace was conceptualized at Ludwig Maximilians University in Munich, Germany. This furnace used two commercially available halogen IR-reflector lamps to heat the sample up to a maximum temperature of 1500 °C.[104] The ability of this furnace to reach intermediate to high temperatures, in conjunction with its small size and ability to be easily customized to a diffractometer, was recognized by Kriven while on sabbatical leave in 1997. A new furnace was envisioned with four halogen lamps, allowing for temperatures up to 2000 °C in air to be achieved which is necessary for studies of refractory and high temperature materials. The result of this work is the quadrupole lamp furnace.

The quadrupole lamp furnace consists of four IR halogen lamps (OSRAM Xenophot HLX64635, 15 V, 150 W). These lamps emit light in the range of 500-2500 nm with a maximum intensity at 800 nm. The light from the lamps is reflected off a gold-coated, parabolic reflector. The focal point of each lamp is located 19 mm away from the edge mirror in free space. All four lamps are positioned in such a way so that the real images of the lamp filaments converge to a single spot. Since the filaments themselves have a linear dimension, the convergence spot is shaped more like a disc, termed the “hot zone”.[105] The position of the lamps is depicted in Figure 27.

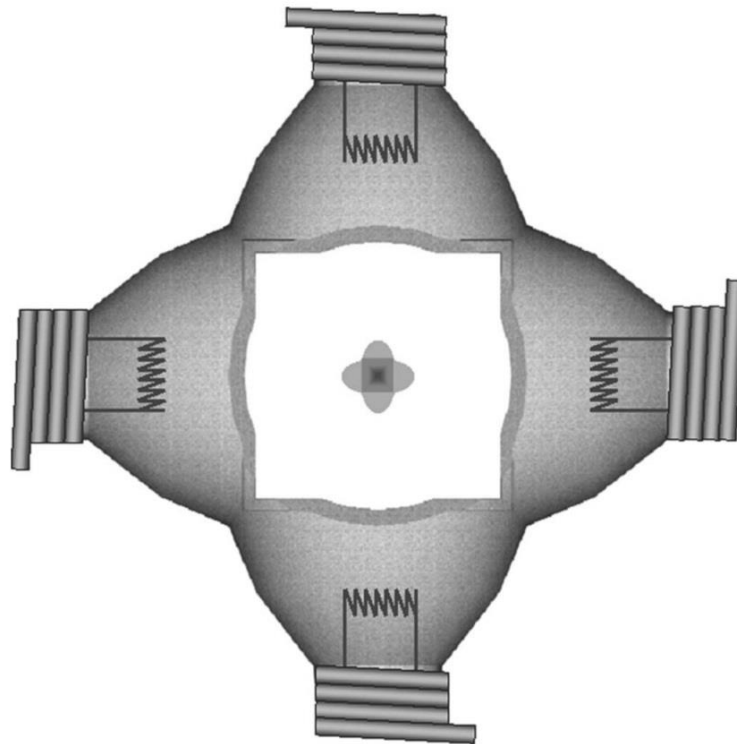


Figure 27. Orientation relationship of the halogen lamps in the quadrupole lamp furnace. At the intersection of the real images of the lamp filaments is an area termed the “hot zone”.

The lamps are housed in a rotated square brass holder and are connected in series to a proportional-integral-derivative (PID) controller (Omega Engineering, Inc) as seen in Figure 28.

The temperature distribution in the hot zone was measured using a B-type thermocouple and are provided in Figure 29.[105] The temperature variation over a disc 4 X 4 mm was less than 20 °C. High temperature X-ray diffraction patterns were collected to measure the thermal expansion of standard materials (CeO₂, MgO, and Pt) for comparison with literature values and were found to be in good agreement (+/- 3%), see Figure 30.[105]

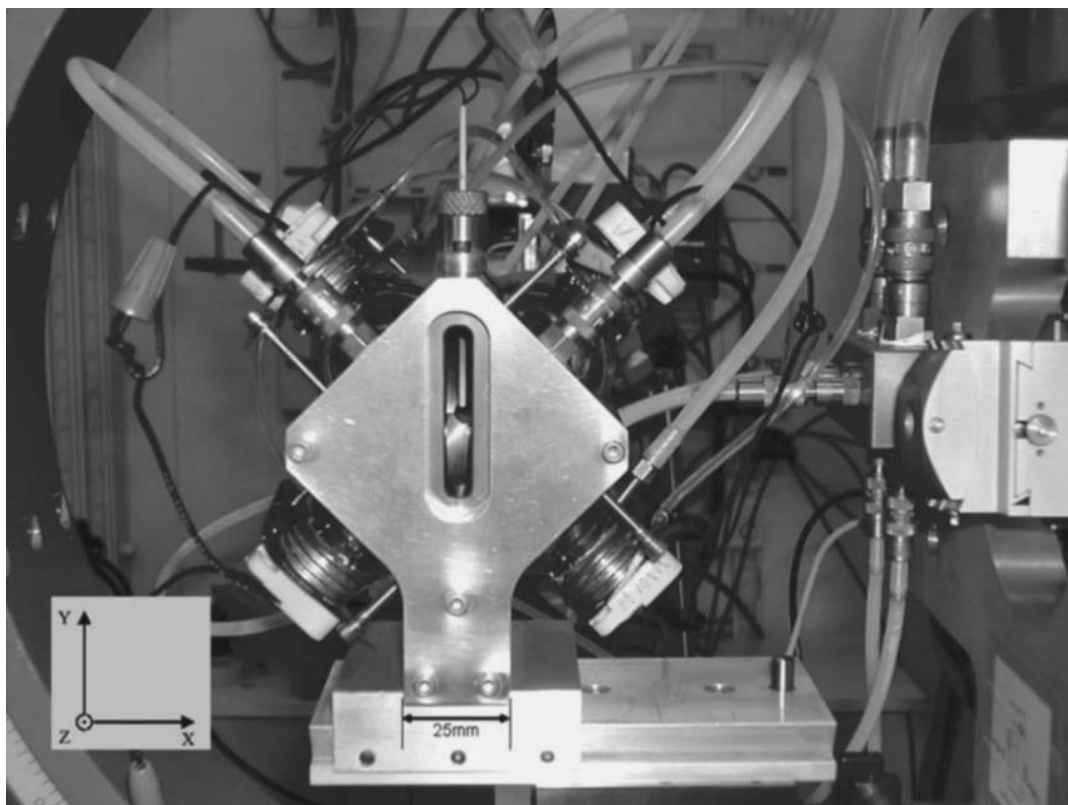


Figure 28. The quadrupole lamp furnace mounted at the beamline 33BM-C at the Advanced Photon Source.

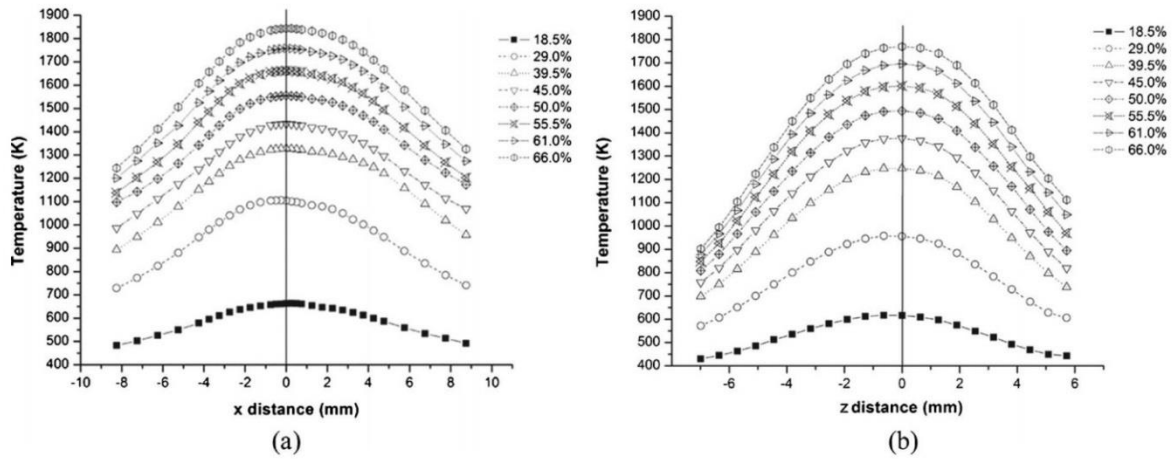


Figure 29. The temperature distribution in the “hot zone” of the quadrupole lamp furnace.[105]

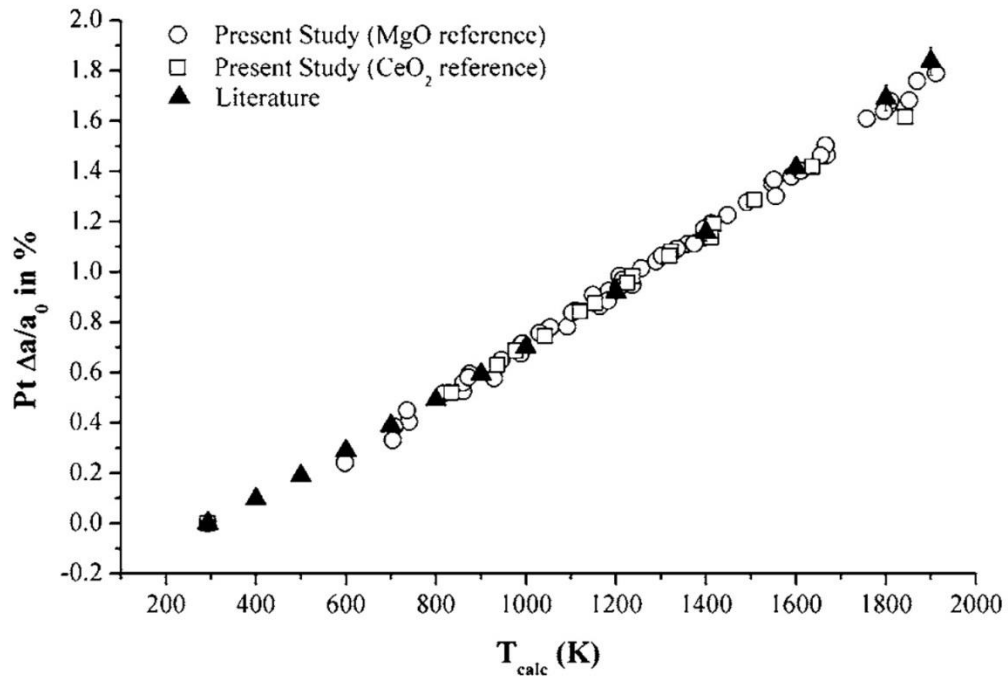


Figure 30. Thermal expansion values calculated for MgO and CeO₂. This information was used to validate the method used to determine the temperature of the sample when heated using the quadrupole lamp furnace.

4.4 Temperature Calibration

Although the thermocouple placed above the sample can give a rough approximation of the temperature, it is unable to accurately describe the temperature of the sample well enough for analysis. This difference can sometimes be up to 200 °C different from the actual temperature, particularly in the intermediate range, as illustrated in Figure 31. Little can be done to minimize this effect by changing the setup of the furnace.

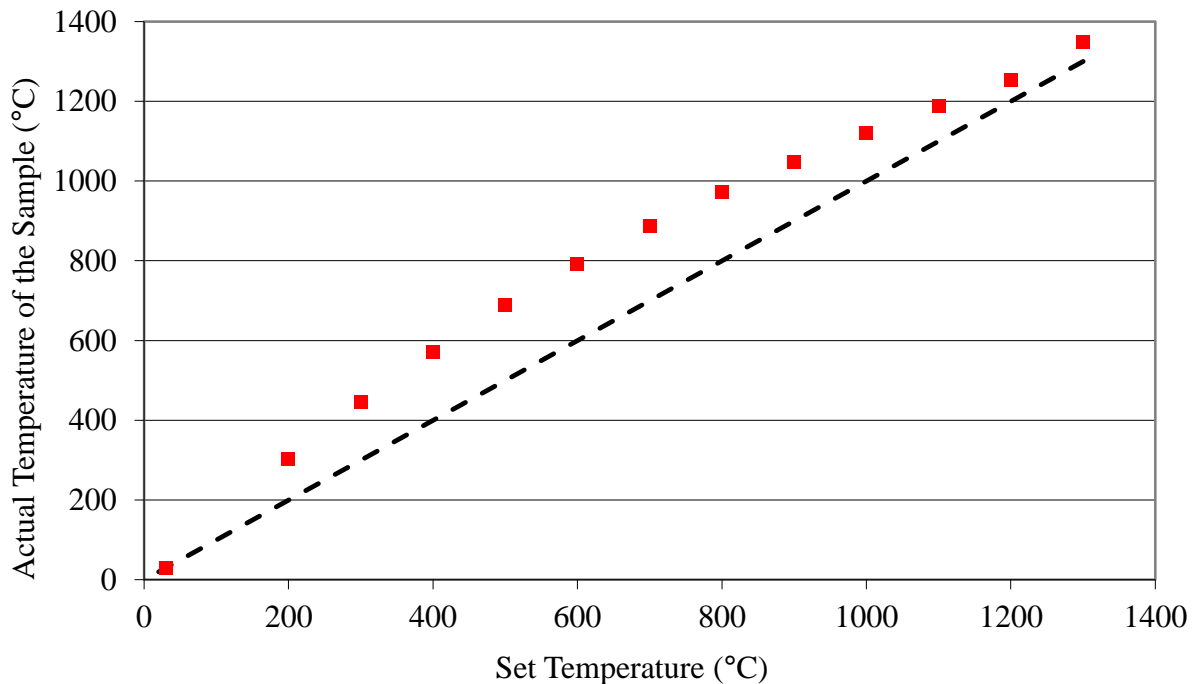


Figure 31. The real temperature of the sample plotted against the set temperature. Black line indicates when the set temperature is equal to the measured temperature. Generally, the real temperature of the sample is significantly higher than the set temperature, particularly in the lower temperature range.

In order to determine the temperature of the sample, platinum is mixed with the powder (or painted on the surface in the case of the sintered rods) in a 90:10 weight ratio. Platinum is used because it affords several advantages; 1) platinum is unlikely to react with the sample, 2) platinum will evenly distribute heat throughout the sample, and 3) platinum acts as a temperature standard. Using the well-known thermal expansion behavior of platinum, it is possible to calculate the temperature. Assuming the platinum powder is in thermal equilibrium with the sample, the temperature of the sample can be readily determined. The error in the calculation of the temperature of the sample in the hot zone was found to be approximately 4-6 °C, sufficient for thermal expansion characterization.

4.5 Differential Scanning Calorimetry

Based on the similar and complementary technique of differential thermal analysis (DTA), differential scanning calorimetry (DSC) was first developed by Watson in 1964 while working for Perkin-Elmer (Norwalk, CT).[106] DTA and DSC both measure the temperature of a sample under heating/cooling. Unlike DTA, the signal from a DSC can be converted into a heat-flux differential allowing for the determination of the heat of fusion/crystallization. DSC can be used for many different applications, most notably though, DSC is primarily used for the observation of transformations (melting/solidification, crystallization, and glass transitions). In certain situations, under isochronal and isothermal conditions, DSC may also be useful in the determination of kinetic parameters of phase transformations.

In this study, a Netzsch STA 409 CD simultaneous thermal analyzer (Netzsch Instruments, Selb, Germany), Figure 32, was used to determine the temperature of transformation and key kinetic parameters which define the time-temperature dependencies of the transformation.



Figure 32. The Netzsch STA 409 CD simultaneous thermal analyzer located in the Kriven research facilities used to make differential scanning calorimetry measurements.

4.6 Dilatometry

A dilatometer can be used to measure the change in volume of a material as a function of temperature. Dilatometry can be used to determine the onset of sintering in ceramics, linear/volume thermal expansion, and monitor phase transformations (glass transition temperatures, transformations with a change in volume, and kinetics).

The experiments in this study were performed with a Netzsch DIL 402 E dilatometer (Netzsch Instruments, Selb, Germany). The synthesized powder was pressed into a bar having dimensions of 25 x 6 x 6 mm and sintered. A background measurement was performed with a sapphire standard to remove the expansion of the instrument from the sample measurement.

CHAPTER 5

THERMAL EXPANSION IN THE RARE-EARTH TITANATES

5.1 Thermal Expansion in the Low Temperature Cubic Phase

The thermal expansion behavior in the cubic phase was determined for Lu_2TiO_5 , Er_2TiO_5 , Ho_2TiO_5 , Y_2TiO_5 , and Dy_2TiO_5 using X-ray diffraction to monitor the crystallographic changes in the structure as a function of temperature in air. Results will be presented in order of increasing rare-earth cation ion size (Lu, Er, Ho, Y, and Dy).

5.1.1 Results

Lu₂TiO₅

As described in Chapter 4, powder of Lu_2TiO_5 was mounted in a sapphire capillary and placed in the center of the quadrupole lamp furnace in alignment with the incident synchrotron X-ray radiation. An X-ray diffraction pattern was collected at each temperature from room temperature up to approximately 1600 °C in air. Using the programs GSAS and EXPGUI, the X-ray diffraction patterns were refined using the Rietveld method and the values for the lattice parameters, hkl , and corresponding d -spacings were extracted from the refined data. The lattice parameters as a function of temperature are plotted in Figure 33 and are listed in Table 5.

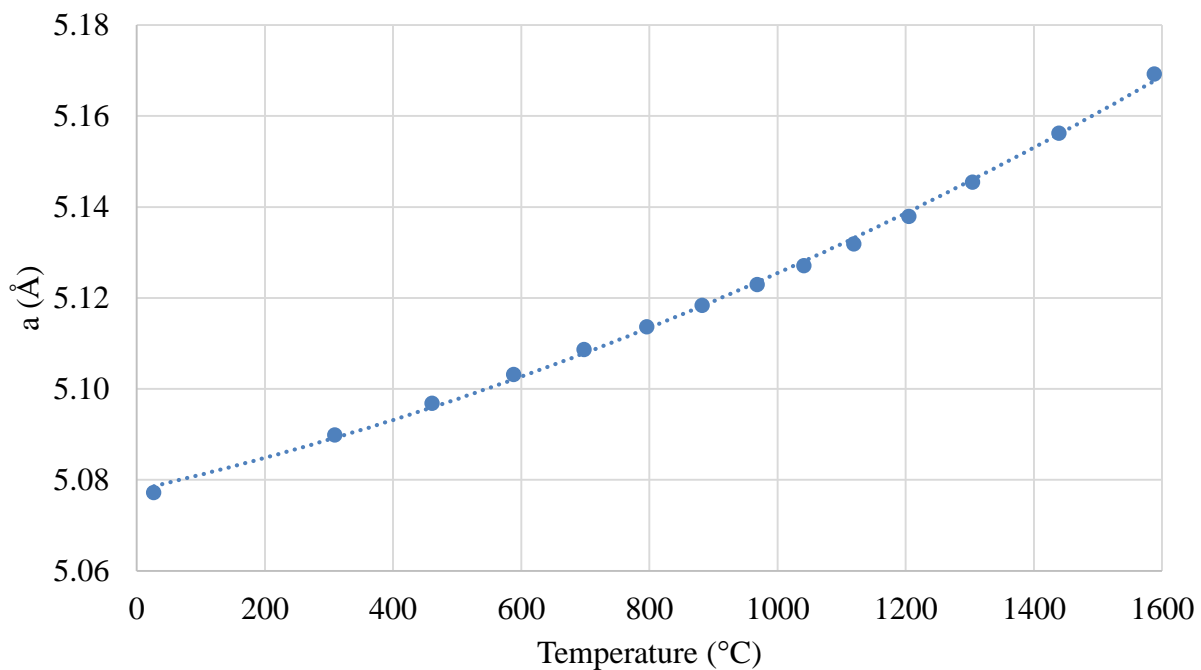


Figure 33. The lattice parameter measured via *in situ* X-ray diffraction for Lu₂TiO₅ in the cubic phase in air. Error bars lie within the symbols.

Table 5. The lattice parameter and volume of Lu₂TiO₅ in the cubic phase as a function of the measured temperature.

Temperature (°C) (± 6)	a (Å)	Volume (Å ³)
26.5	5.07724(2)	130.88
309	5.08991(2)	131.86
461	5.09686(2)	132.40
588	5.10314(2)	132.89
698	5.10868(2)	133.32
796	5.11369(2)	133.72
882	5.11837(2)	134.09
968	5.12295(2)	134.45
1041	5.12708(2)	134.77
1119	5.13188(2)	135.15
1205	5.13793(2)	135.63
1304	5.14544(2)	136.22
1439	5.15620(2)	137.08
1588	5.16925(2)	138.12

In addition to the determination of the lattice parameters, a CTEAS analysis was performed on the hkl listings and corresponding d-spacings as a function of temperature using a second-order polynomial fit. The results of the CTEAS analysis of the appropriate temperature range are listed in Table 6.

Table 6. The component of the thermal expansion tensor for Lu₂TiO₅ as a function of extrapolated temperature.

Temperature (°C)	α_{11} (x 10 ⁻⁶ /°C)	Error
25	6.51	0.51
50	6.66	0.49
75	6.81	0.48
100	6.95	0.46
125	7.10	0.44
150	7.25	0.43
175	7.40	0.41
200	7.55	0.40
225	7.69	0.38
250	7.84	0.37
275	7.99	0.36
300	8.14	0.34
325	8.29	0.33
350	8.43	0.32
375	8.58	0.31
400	8.73	0.30
425	8.88	0.29
450	9.02	0.28
475	9.17	0.27
500	9.32	0.26
525	9.47	0.25
550	9.62	0.25
575	9.76	0.24
600	9.91	0.23
625	10.06	0.23
650	10.21	0.22
675	10.36	0.22
700	10.50	0.22
725	10.65	0.21

750	10.80	0.21
775	10.95	0.21
800	11.09	0.20
825	11.24	0.20
850	11.39	0.20
875	11.54	0.20
900	11.69	0.20
925	11.83	0.20
950	11.98	0.20
975	12.13	0.21
1000	12.28	0.21
1025	12.42	0.21
1050	12.57	0.22
1075	12.72	0.22
1100	12.87	0.22
1125	13.02	0.23
1150	13.16	0.23
1175	13.31	0.24
1200	13.46	0.25
1225	13.61	0.25
1250	13.75	0.26
1275	13.90	0.27
1300	14.05	0.28
1325	14.20	0.29
1350	14.35	0.30
1375	14.49	0.31
1400	14.64	0.32
1425	14.79	0.33
1450	14.94	0.34
1475	15.09	0.36
1500	15.23	0.37
1525	15.38	0.38
1550	15.53	0.40
1575	15.68	0.41

The two-dimensional representation of the three-dimensional quadric surface looking down the [100] direction is presented in Figure 34.

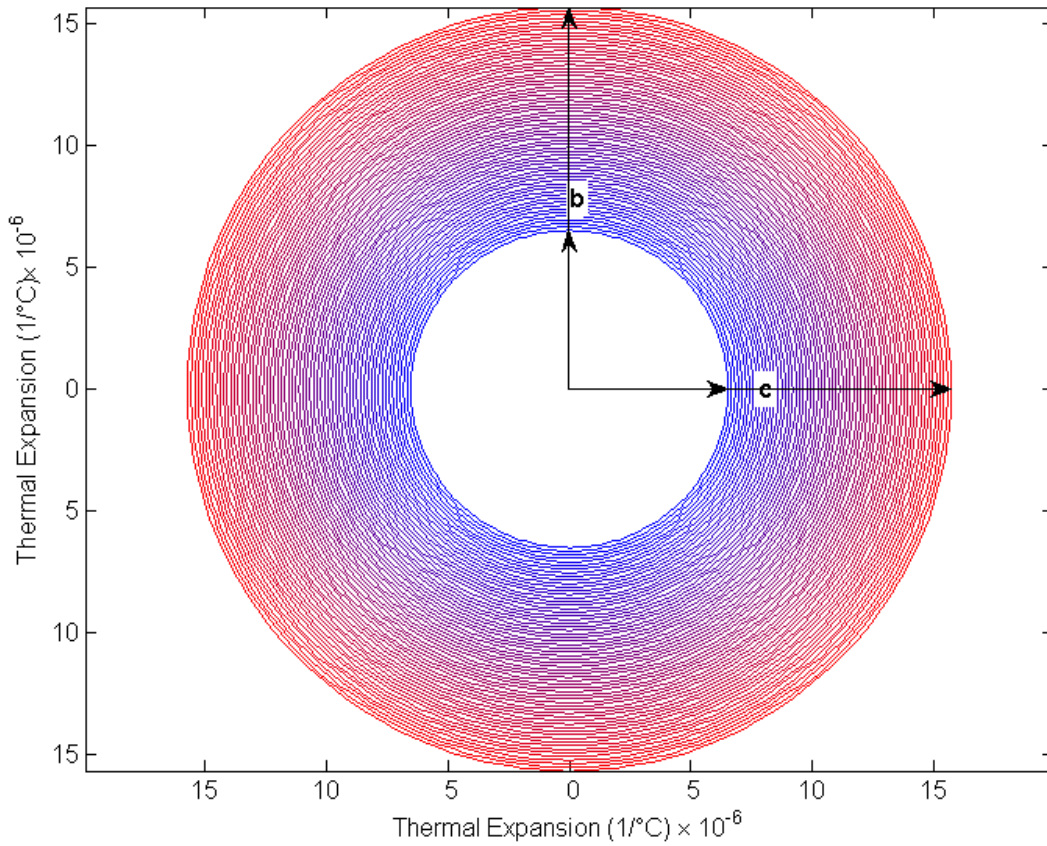


Figure 34. The two-dimensional projection of the three-dimensional representation of thermal expansion along the [100] for Lu_2TiO_5 in 25 °C steps from room temperature (inner circle) to 1575 °C (outer circle). Low temperature indicated with the color blue changing to red with increasing temperature.

Er_2TiO_5

As described in Chapter 4, powder of Er_2TiO_5 was mounted in a sapphire capillary and placed in the center of the quadrupole lamp furnace in alignment with the incident synchrotron X-ray radiation. An X-ray diffraction pattern was collected at each temperature from room temperature up to approximately 1275 °C in air. Using the programs GSAS and EXPGUI, the X-ray diffraction patterns were refined using the Rietveld method and the values for the lattice parameters, hkl, and corresponding d-spacings were extracted from the refined data. The lattice parameters as a function of temperature are plotted in Figure 35 and are listed in Table 7.

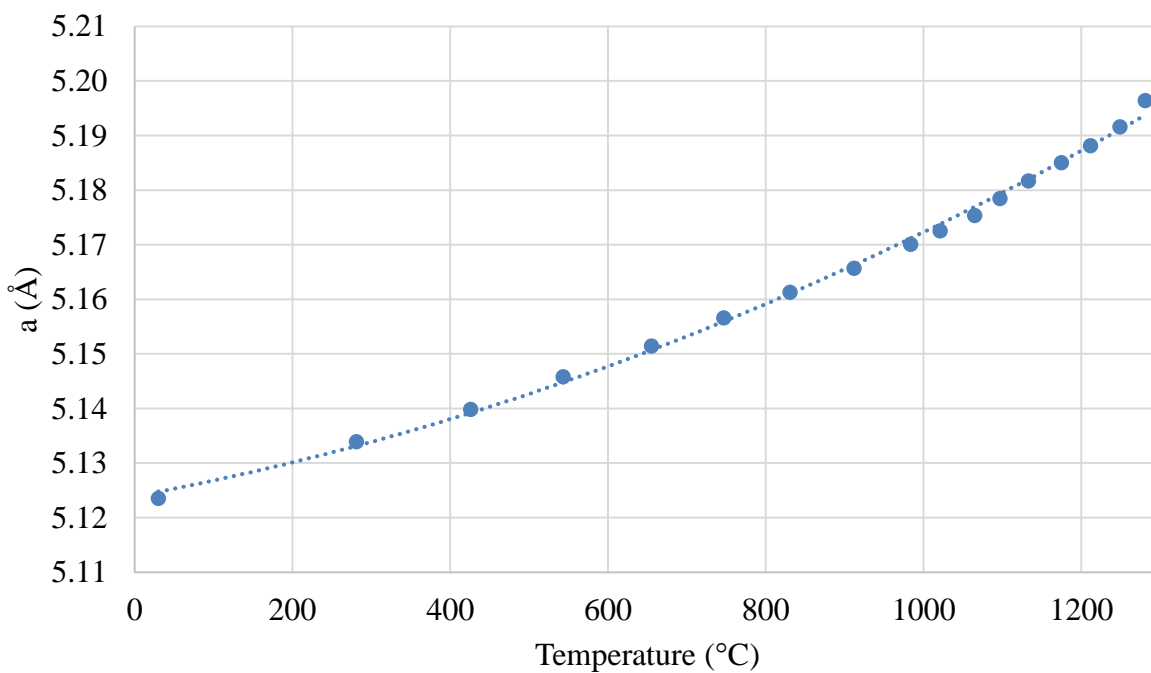


Figure 35. The lattice parameter measured via *in situ* X-ray diffraction for Er_2TiO_5 in the cubic phase in air. Error bars lie within the symbols.

Table 7. The lattice parameter and volume of Er₂TiO₅ in the cubic phase as a function of the measured temperature.

Temperature (°C) (±6)	a (Å)	Volume (Å ³)
29.9	5.12351(6)	134.49
281	5.13390(6)	135.31
426	5.13984(5)	135.78
543	5.14581(6)	136.25
655	5.15142(6)	136.70
747	5.15661(6)	137.11
831	5.16127(6)	137.48
912	5.16569(6)	137.84
984	5.17007(6)	138.19
1021	5.17255(6)	138.39
1065	5.17533(6)	138.61
1097	5.17847(6)	138.86
1133	5.18168(6)	139.12
1175	5.18499(6)	139.39
1212	5.18812(4)	139.64
1249	5.19161(4)	139.92
1281	5.19640(3)	140.31

In addition to the determination of the lattice parameters, a CTEAS analysis was performed on the hkl listings and corresponding d-spacings as a function of temperature using a second-order polynomial fit. The results of the CTEAS analysis of the appropriate temperature range are listed in Table 8.

Table 8. The component of the thermal expansion tensor for Er₂TiO₅ as a function of extrapolated temperature.

Temperature (°C)	α_{11} (x 10 ⁻⁶ /°C)	Error
25	5.48	0.54
50	5.69	0.52
75	5.89	0.50
100	6.10	0.48
125	6.31	0.46
150	6.51	0.44
175	6.72	0.43
200	6.93	0.41
225	7.13	0.39
250	7.34	0.38
275	7.55	0.36
300	7.75	0.35
325	7.96	0.34
350	8.17	0.32
375	8.37	0.31
400	8.58	0.30
425	8.78	0.29
450	8.99	0.28
475	9.20	0.27
500	9.40	0.26
525	9.61	0.25
550	9.81	0.24
575	10.02	0.24

600	10.23	0.23
625	10.43	0.22
650	10.64	0.22
675	10.84	0.21
700	11.05	0.21
725	11.26	0.20
750	11.46	0.20
775	11.67	0.20
800	11.87	0.20
825	12.08	0.20
850	12.29	0.19
875	12.49	0.19
900	12.70	0.20
925	12.90	0.20
950	13.11	0.20
975	13.31	0.20
1000	13.52	0.20
1025	13.72	0.21
1050	13.93	0.21
1075	14.14	0.22
1100	14.34	0.22
1125	14.55	0.23
1150	14.76	0.24
1175	14.96	0.24
1200	15.17	0.25
1225	15.37	0.26
1250	15.58	0.27
1275	15.79	0.28

The two-dimensional representation of the three-dimensional quadric surface looking down the [100] direction is presented in Figure 36.

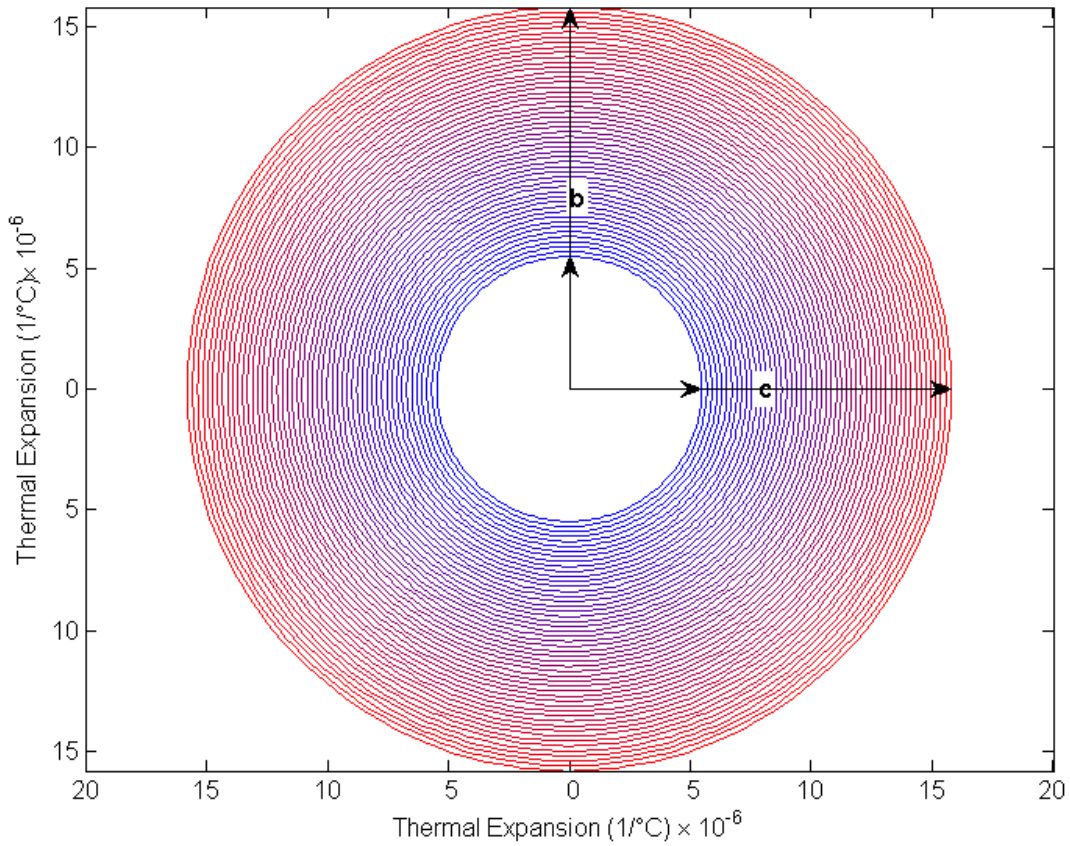


Figure 36. The two-dimensional projection of the three-dimensional representation of thermal expansion along the [100] for Er_2TiO_5 in 25 °C steps from room temperature (inner circle) to 1275 °C (outer circle). Low temperature indicated with the color blue changing to red with increasing temperature.

Ho_2TiO_5

As described in Chapter 4, powder of Ho_2TiO_5 was mounted in a sapphire capillary and placed in the center of the quadrupole lamp furnace in alignment with the incident synchrotron X-ray radiation. An X-ray diffraction pattern was collected at each temperature from room temperature up to approximately 1300 °C in air. Using the programs GSAS and EXPGUI, the X-ray diffraction patterns were refined using the Rietveld method and the values for the lattice parameters, hkl, and corresponding d-spacings were extracted from the refined data. The lattice parameters as a function of temperature are plotted in Figure 37 and are listed in Table 9.

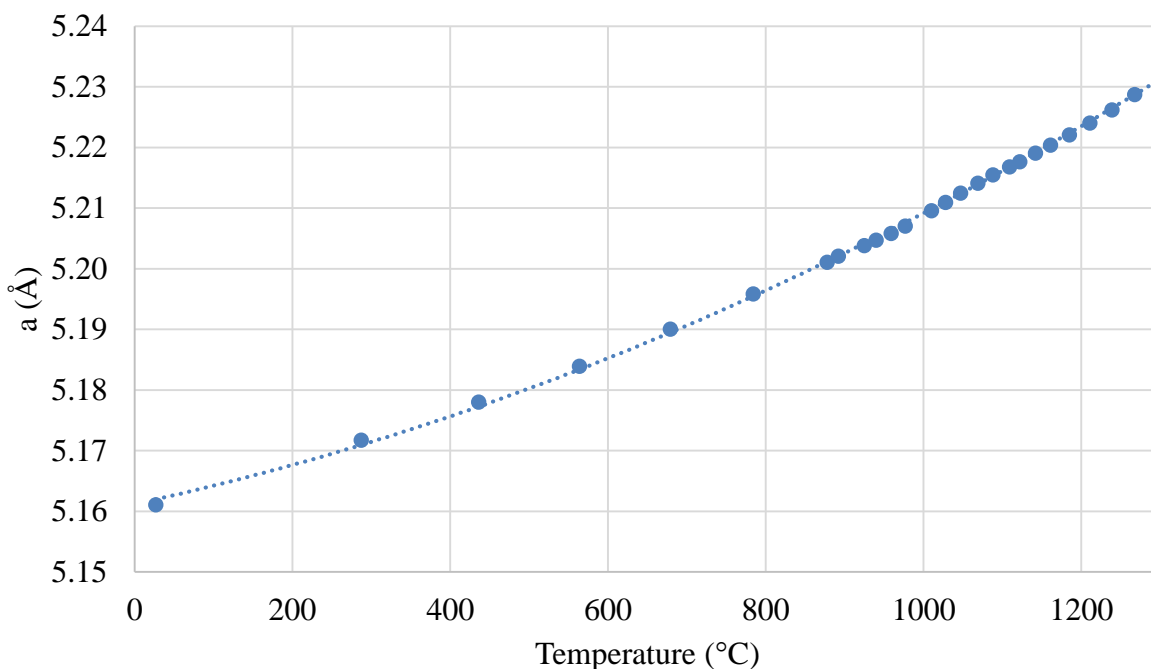


Figure 37. The lattice parameter measured via *in situ* X-ray diffraction for Ho_2TiO_5 in the cubic phase in air. Error bars lie within the symbols.

Table 9. The lattice parameter and volume of Ho_2TiO_5 in the cubic phase as a function of the measured temperature.

Temperature ($^{\circ}\text{C}$) (± 6)	a (\AA)	Volume (\AA^3)
26.5	5.16103(6)	137.47
287	5.17168(6)	138.32
436	5.17799(7)	138.82
564	5.18388(6)	139.30
679	5.19002(6)	139.79
784	5.19580(6)	140.26
878	5.20102(6)	140.69
892	5.20201(6)	140.77
925	5.20381(6)	140.91
940	5.20468(6)	140.98
959	5.20581(6)	141.07
977	5.20700(5)	141.17
1010	5.20955(5)	141.38
1028	5.21091(5)	141.49
1047	5.21244(4)	141.61
1069	5.21405(4)	141.75
1088	5.21545(4)	141.86
1109	5.21676(4)	141.97
1122	5.21760(4)	142.04
1142	5.21904(4)	142.15
1161	5.22037(4)	142.26
1185	5.22204(4)	142.40
1211	5.22397(4)	142.56
1239	5.22616(5)	142.74
1268	5.22871(6)	142.94
1301	5.23335(1)	143.33

In addition to the determination of the lattice parameters, a CTEAS analysis was performed on the hkl listings and corresponding d-spacings as a function of temperature using a second-order polynomial fit. The results of the CTEAS analysis of the appropriate temperature range are listed in Table 10.

Table 10. The component of the thermal expansion tensor for Ho_2TiO_5 as a function of extrapolated temperature.

Temperature (°C)	α_{11} ($\times 10^{-6}/^\circ\text{C}$)	Error
25	5.85	0.37
50	6.04	0.36
75	6.22	0.34
100	6.40	0.33
125	6.59	0.32
150	6.77	0.31
175	6.95	0.29
200	7.13	0.28
225	7.32	0.27
250	7.50	0.26
275	7.68	0.25
300	7.87	0.24
325	8.05	0.23
350	8.23	0.23
375	8.41	0.22
400	8.60	0.21
425	8.78	0.20
450	8.96	0.20
475	9.15	0.19
500	9.33	0.18
525	9.51	0.18
550	9.69	0.17
575	9.88	0.17
600	10.06	0.16

625	10.24	0.16
650	10.42	0.16
675	10.61	0.15
700	10.79	0.15
725	10.97	0.15
750	11.16	0.15
775	11.34	0.15
800	11.52	0.15
825	11.70	0.15
850	11.89	0.15
875	12.07	0.15
900	12.25	0.15
925	12.44	0.15
950	12.62	0.15
975	12.80	0.15
1000	12.98	0.16
1025	13.17	0.16
1050	13.35	0.16
1075	13.53	0.17
1100	13.71	0.17
1125	13.90	0.18
1150	14.08	0.18
1175	14.26	0.19
1200	14.45	0.19
1225	14.63	0.20
1250	14.81	0.21
1275	14.99	0.21
1300	15.18	0.22

The two-dimensional representation of the three-dimensional quadric surface looking down the [100] direction is presented in Figure 38.

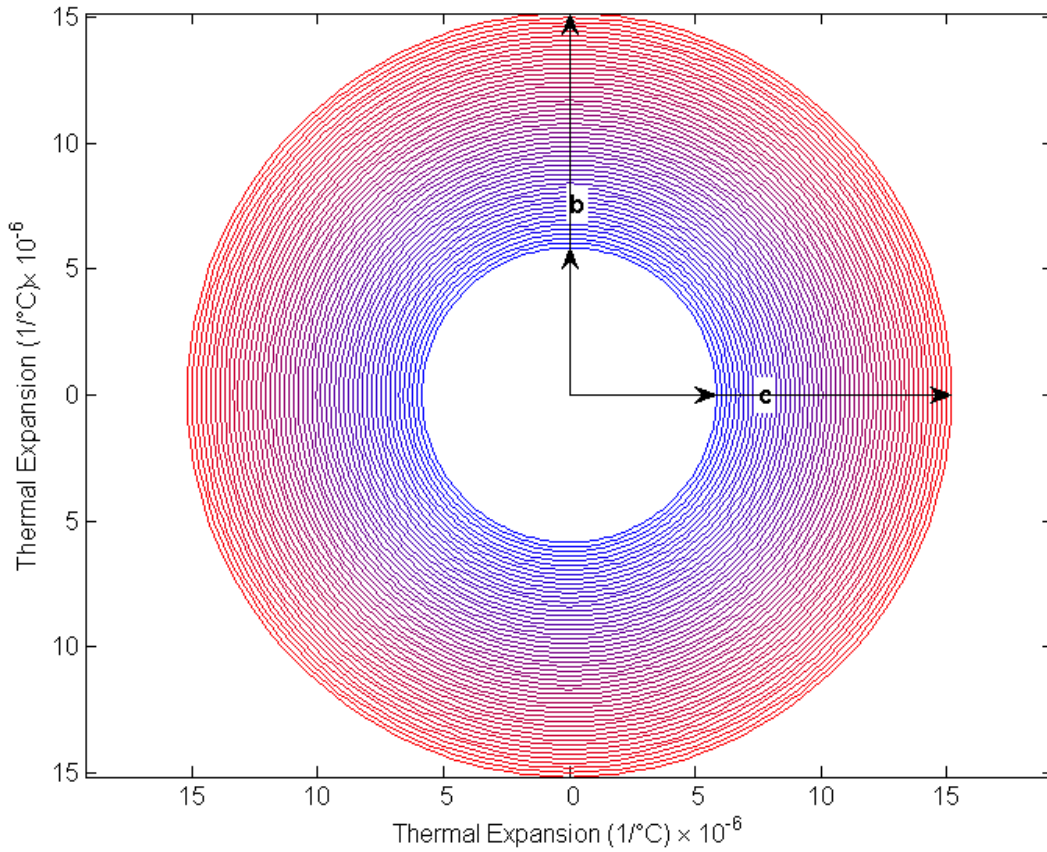


Figure 38. The two-dimensional projection of the three-dimensional representation of thermal expansion along the [100] for Ho_2TiO_5 in 25 °C steps from room temperature (inner circle) to 1300 °C (outer circle). Low temperature indicated with the color blue changing to red with increasing temperature.

Y_2TiO_5

As described in Chapter 4, powder of Y_2TiO_5 in the cubic phase (Y_2TiO_5 can exist in both the cubic and orthorhombic phase at room temperature) was mounted in a sapphire capillary and placed in the center of the quadrupole lamp furnace in alignment with the incident synchrotron X-ray radiation. An X-ray diffraction pattern was collected at each temperature from room temperature up to approximately 1275 °C in air. Using the programs GSAS and EXPGUI, the X-ray diffraction patterns were refined using the Rietveld method and the values for the lattice parameters, hkl, and corresponding d-spacings were extracted from the refined data. The lattice parameters as a function of temperature are plotted in Figure 39 and are listed in Table 11.

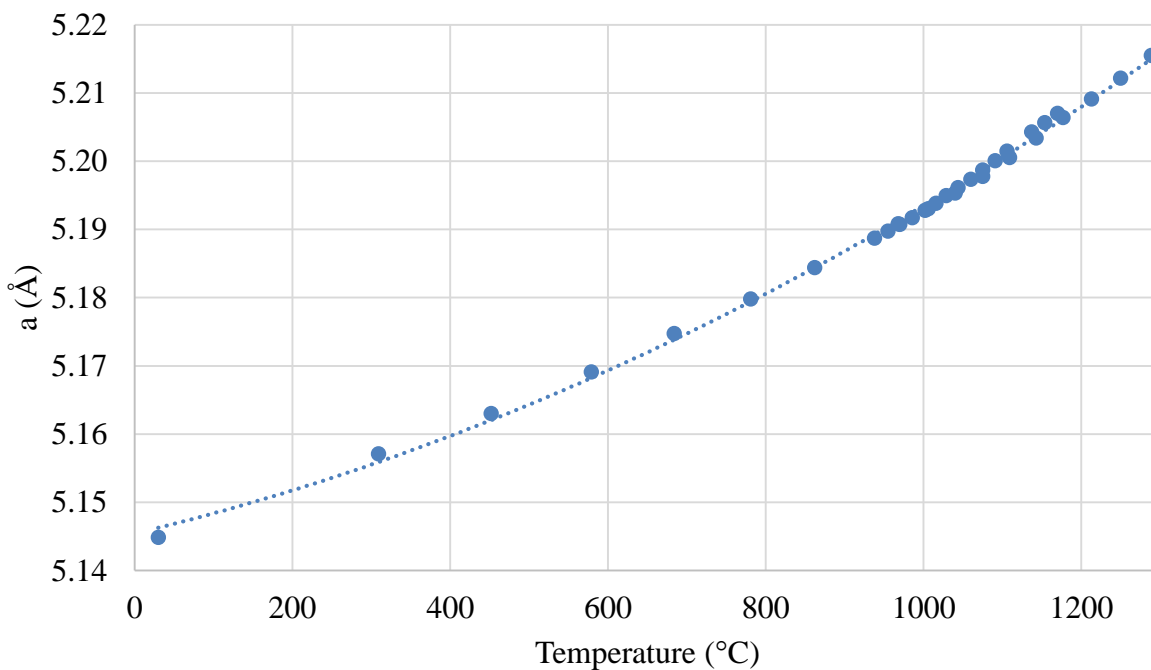


Figure 39. The lattice parameter measured via *in situ* X-ray diffraction for Y_2TiO_5 in the cubic phase in air. Error bars lie within the symbols.

Table 11. The lattice parameter and volume of Y_2TiO_5 in the cubic phase as a function of the measured temperature.

Temperature (°C) (± 6)	a (Å)	Volume (Å ³)
29.9	5.14488(3)	136.18
309	5.15713(5)	137.15
452	5.16304(3)	137.63
579	5.16913(3)	138.11
684	5.17479(3)	138.57
781	5.17982(3)	138.97
862	5.18445(3)	139.34
938	5.18877(3)	139.69
955	5.18976(3)	139.77
968	5.19083(3)	139.86
970	5.19078(3)	139.86
986	5.19174(3)	139.93
1002	5.19280(3)	140.02
1006	5.19306(3)	140.04
1016	5.19387(3)	140.11
1029	5.19497(3)	140.20
1040	5.19538(3)	140.23
1044	5.19614(3)	140.29
1060	5.19739(3)	140.39
1075	5.19781(3)	140.43
1091	5.20009(3)	140.61
1106	5.20151(3)	140.73
1109	5.20054(3)	140.65
1137	5.20433(3)	140.95
1143	5.20341(2)	140.88
1154	5.20566(2)	141.06
1170	5.20703(2)	141.17
1177	5.20644(3)	141.13
1213	5.20916(3)	141.35
1250	5.21219(3)	141.59
1289	5.21553(3)	141.87

In addition to the determination of the lattice parameters, a CTEAS analysis was performed on the hkl listings and corresponding d-spacings as a function of temperature using a second-order polynomial fit. The results of the CTEAS analysis of the appropriate temperature range are listed in Table 12.

Table 12. The component of the thermal expansion tensor for Y_2TiO_5 as a function of extrapolated temperature.

Temperature (°C)	α_{11} ($\times 10^{-6}/^{\circ}\text{C}$)	Error
25	5.98	0.39
50	6.16	0.38
75	6.35	0.36
100	6.53	0.35
125	6.71	0.33
150	6.89	0.32
175	7.08	0.31
200	7.26	0.29
225	7.44	0.28
250	7.62	0.27
275	7.80	0.26
300	7.98	0.25
325	8.16	0.24
350	8.34	0.23
375	8.53	0.22
400	8.71	0.21
425	8.89	0.20
450	9.07	0.19
475	9.25	0.19
500	9.43	0.18
525	9.61	0.17
550	9.79	0.17
575	9.97	0.16

600	10.15	0.16
625	10.33	0.15
650	10.51	0.15
675	10.69	0.14
700	10.87	0.14
725	11.05	0.14
750	11.23	0.13
775	11.41	0.13
800	11.59	0.13
825	11.76	0.13
850	11.94	0.13
875	12.12	0.13
900	12.30	0.13
925	12.48	0.13
950	12.66	0.13
975	12.84	0.13
1000	13.03	0.14
1025	13.21	0.14
1050	13.39	0.14
1075	13.58	0.15
1100	13.76	0.15
1125	13.94	0.16
1150	14.13	0.16
1175	14.31	0.17
1200	14.50	0.17
1225	14.68	0.18
1250	14.87	0.19
1275	15.05	0.19

The two-dimensional representation of the three-dimensional quadric surface looking down the [100] direction is presented in Figure 40.

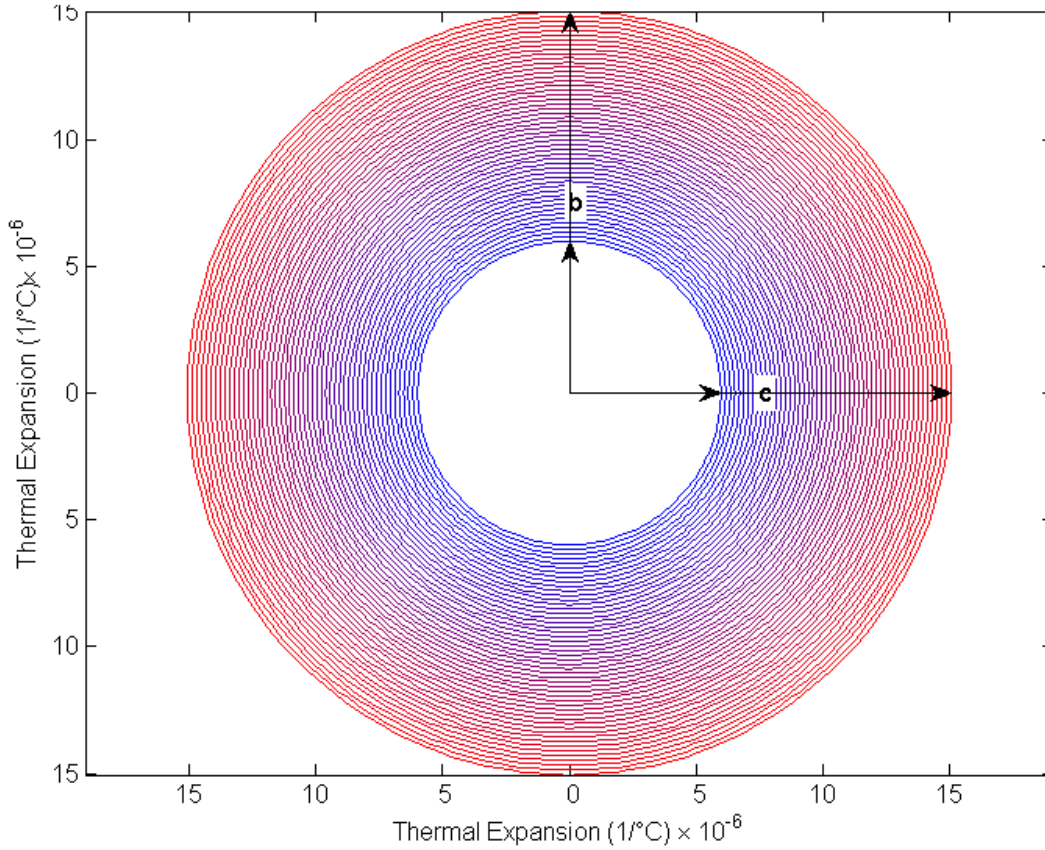


Figure 40. The two-dimensional projection of the three-dimensional representation of thermal expansion along the [100] for Y_2TiO_5 in 25 °C steps from room temperature (inner circle) to 1275 °C (outer circle). Low temperature indicated with the color blue changing to red with increasing temperature.

Dy_2TiO_5

As described in Chapter 4, powder of Dy_2TiO_5 in the cubic phase (Dy_2TiO_5 can exist in both the cubic and orthorhombic phase at room temperature) was mounted in a sapphire capillary and placed in the center of the quadrupole lamp furnace in alignment with the incident synchrotron X-ray radiation. An X-ray diffraction pattern was collected at each temperature from room temperature up to approximately 1150 °C in air. Using the programs GSAS and EXPGUI, the X-ray diffraction patterns were refined using the Rietveld method and the values for the lattice parameters, hkl, and corresponding d-spacings were extracted from the refined data. The lattice parameters as a function of temperature are plotted in Figure 41 and are listed in Table 13.

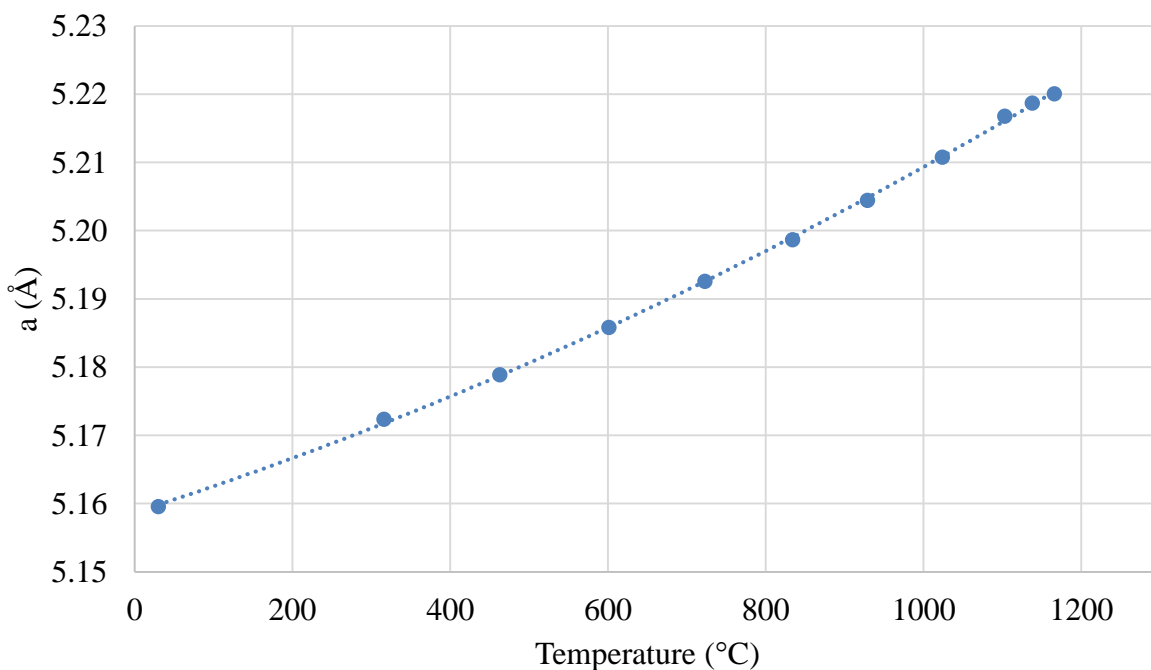


Figure 41. The lattice parameter measured via *in situ* X-ray diffraction for Dy_2TiO_5 in the cubic phase in air. Error bars lie within the symbols.

Table 13. The lattice parameter and volume of Dy₂TiO₅ in the cubic phase as a function of the measured temperature.

Temperature (°C) (±6)	a (Å)	Volume (Å ³)
29.9	5.15953(8)	137.35
316	5.17235(8)	138.37
463	5.17888(9)	138.90
601	5.18581(8)	139.46
723	5.19255(8)	140.00
834	5.19868(9)	140.50
929	5.2044(1)	140.96
1024	5.21075(9)	141.48
1103	5.2167(1)	141.97
1138	5.21870(9)	142.13
1166	5.2200(1)	142.23

In addition to the determination of the lattice parameters, a CTEAS analysis was performed on the hkl listings and corresponding d-spacings as a function of temperature using a second-order polynomial fit. The results of the CTEAS analysis of the appropriate temperature range are listed in Table 14.

Table 14. The component of the thermal expansion tensor for Dy₂TiO₅ as a function of extrapolated temperature.

Temperature (°C)	α_{11} (x 10 ⁻⁶ /°C)	Error
25	7.33	0.19
50	7.46	0.18
75	7.58	0.18
100	7.71	0.17
125	7.84	0.16
150	7.97	0.16
175	8.10	0.15
200	8.23	0.15
225	8.35	0.14
250	8.48	0.14
275	8.61	0.13
300	8.74	0.13
325	8.87	0.12
350	9.00	0.12
375	9.12	0.11
400	9.25	0.11
425	9.38	0.11
450	9.51	0.10
475	9.64	0.10
500	9.77	0.10
525	9.89	0.09
550	10.02	0.09

575	10.15	0.09
600	10.28	0.09
625	10.41	0.09
650	10.54	0.09
675	10.66	0.08
700	10.79	0.08
725	10.92	0.08
750	11.05	0.08
775	11.18	0.08
800	11.31	0.08
825	11.43	0.08
850	11.56	0.08
875	11.69	0.08
900	11.82	0.09
925	11.95	0.09
950	12.08	0.09
975	12.20	0.09
1000	12.33	0.09
1025	12.46	0.09
1050	12.59	0.10
1075	12.72	0.10
1100	12.85	0.10
1125	12.97	0.11
1150	13.10	0.11
1175	13.23	0.11

The two-dimensional representation of the three-dimensional quadric surface looking down the [100] direction is presented in Figure 42.

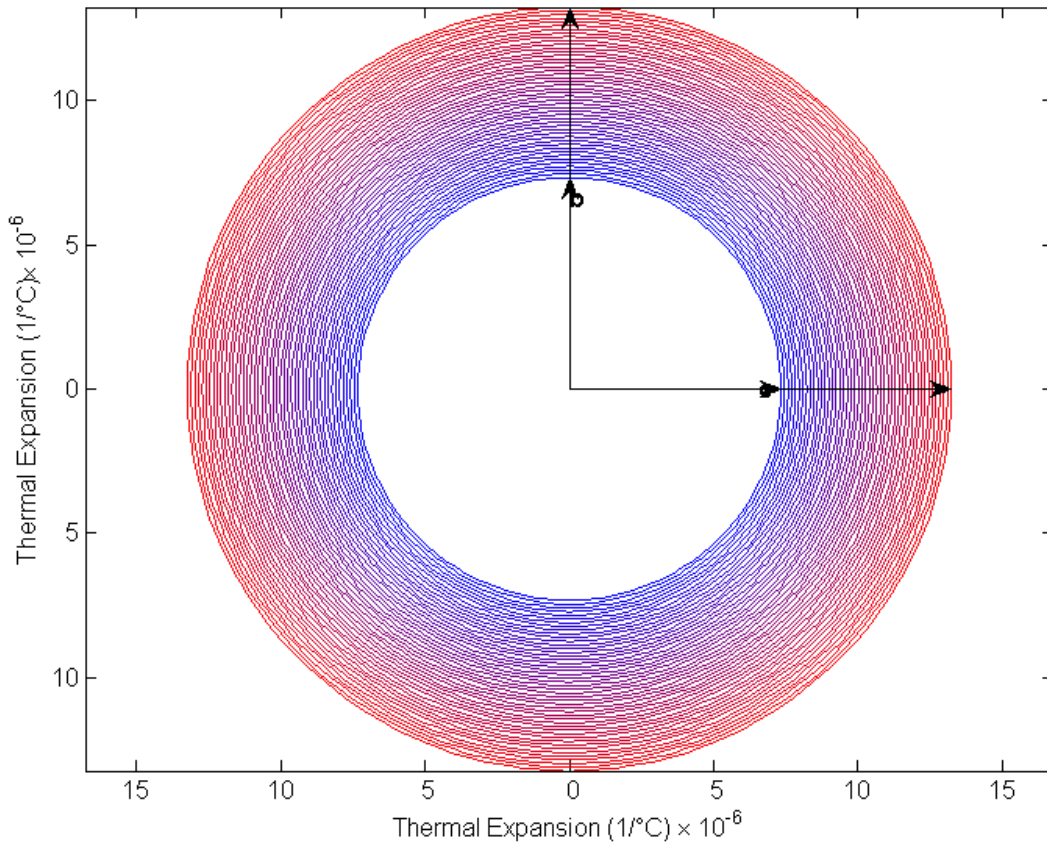


Figure 42. The two-dimensional projection of the three-dimensional representation of thermal expansion along the [100] for Dy_2TiO_5 in 25 °C steps from room temperature (inner circle) to 1175 °C (outer circle). Low temperature indicated with the color blue changing to red with increasing temperature.

5.1.2 Discussion and Mechanism of Thermal Expansion

As described above, the change in lattice parameter and values for thermal expansion follow an expected trend for a cubic system. As temperature is increased the distance between two neighboring atoms is increased resulting in an overall expansion of the cell.

Commonly, the thermal expansion of a cubic system is erroneously reported as a single value. This implies that the rate of expansion is constant over an entire temperature range which is almost never the case. Here we see a cell which is expanding at an increasing rate with temperature, as with most systems, which requires more than one value to describe. This is reflected in the data both provided above in Figures 33, 35, 37, 39, and 41, and in a combined form below in Figure 43.

Unlike the orthorhombic phase, there is no trend to be found in the thermal expansion behavior with respect to the size of the rare-earth cation. Generally, the coefficient of thermal expansion starts at a relatively moderate value of $5-7 \times 10^{-6}$ and increases linearly for each material till reaching a value of approximately $15-16 \times 10^{-6}$.

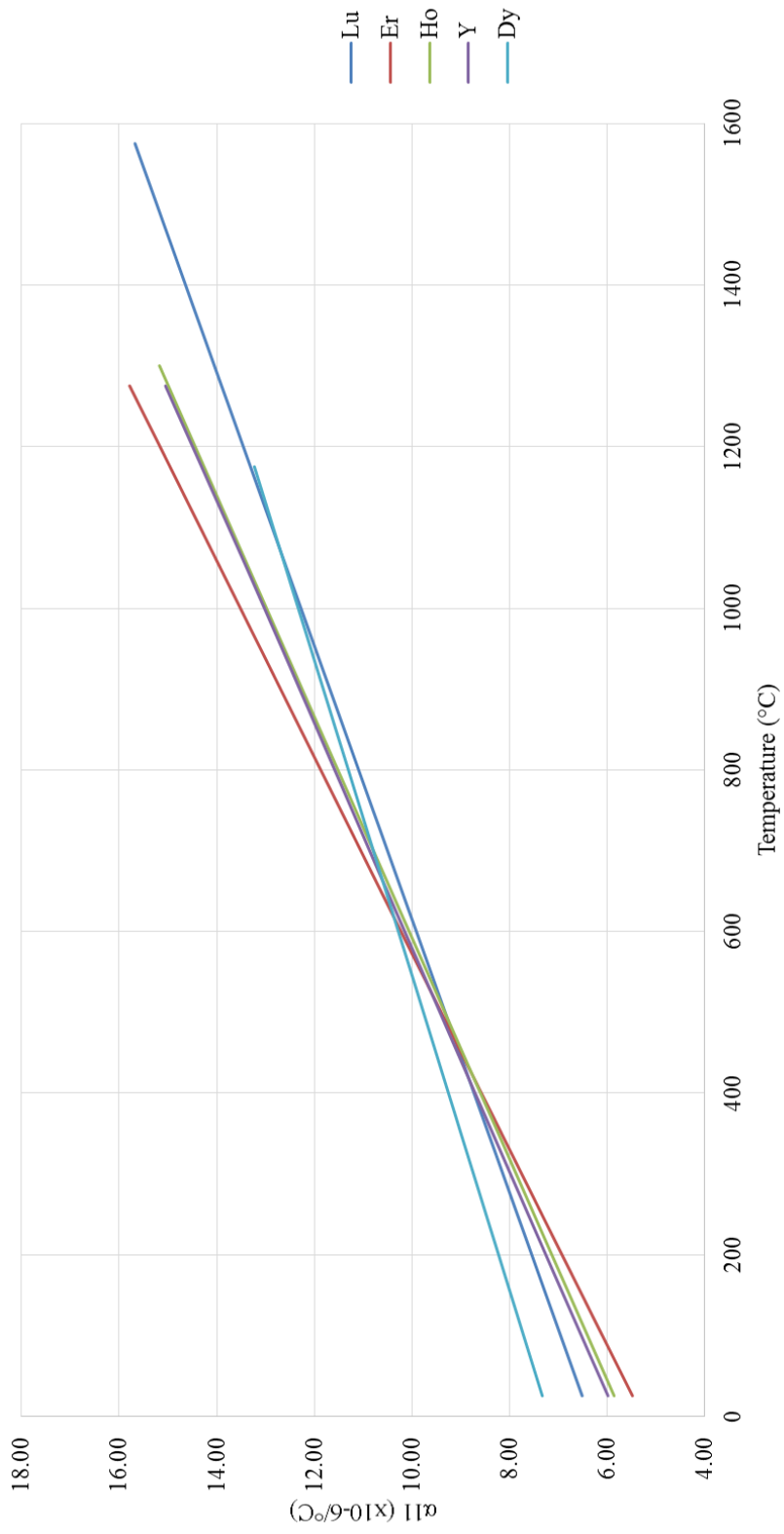


Figure 43. The combined thermal expansion behavior for all members of the Ln₂TiO₅ family which exist in the cubic phase.

The mechanism of thermal expansion in the cubic phase is relatively clear and simple. All of the atoms in the cubic phase are located at special positions. Each special position in the structure is fixed in its relative position in each cell meaning the x, y, and z coordinate of each atom does not change. Because of this, the mechanism of thermal expansion in the cubic phase is related to the interatomic distance between each of the ions.

The Lennard-Jones potential describes the interatomic distance as a balance between attractive and repulsive forces, the equation for which is reproduced below[107]

$$E(r) = 4\epsilon \left[\left(\frac{\sigma}{r} \right)^{12} - \left(\frac{\sigma}{r} \right)^6 \right]$$

where E is the intermolecular potential between the two atoms, ϵ the “well” depth, σ the potential when the distance between the atoms is zero, and r the separation. An illustration of this equation is provided in Figure 44. The potential “well” describes the distance where the repulsive forces are balanced by the attractive forces. If a material was cooled to 0 K, you would expect the atom to be at the bottom of this well (i.e. the minima of the curve). As energy is put into the system, in the form of thermal energy, the atom vibrates up the well, and the average distance between the two atoms increases as depicted in Figure 44. Since the shape of the well itself is not symmetric about its minima, the differential change in distance with temperature is not linear. As a result of this non-linearity, the change in lattice parameter observed as a function of temperature in this study is also non-linear. It should be noted that the Lennard-Jones potential was not used as a means to fit the thermal expansion data in the cubic phase, but only as a qualitative description of thermal expansion in general. This simple, yet sufficient, explanation of the nature of thermal expansion in cubic systems describes the underlying mechanism well.

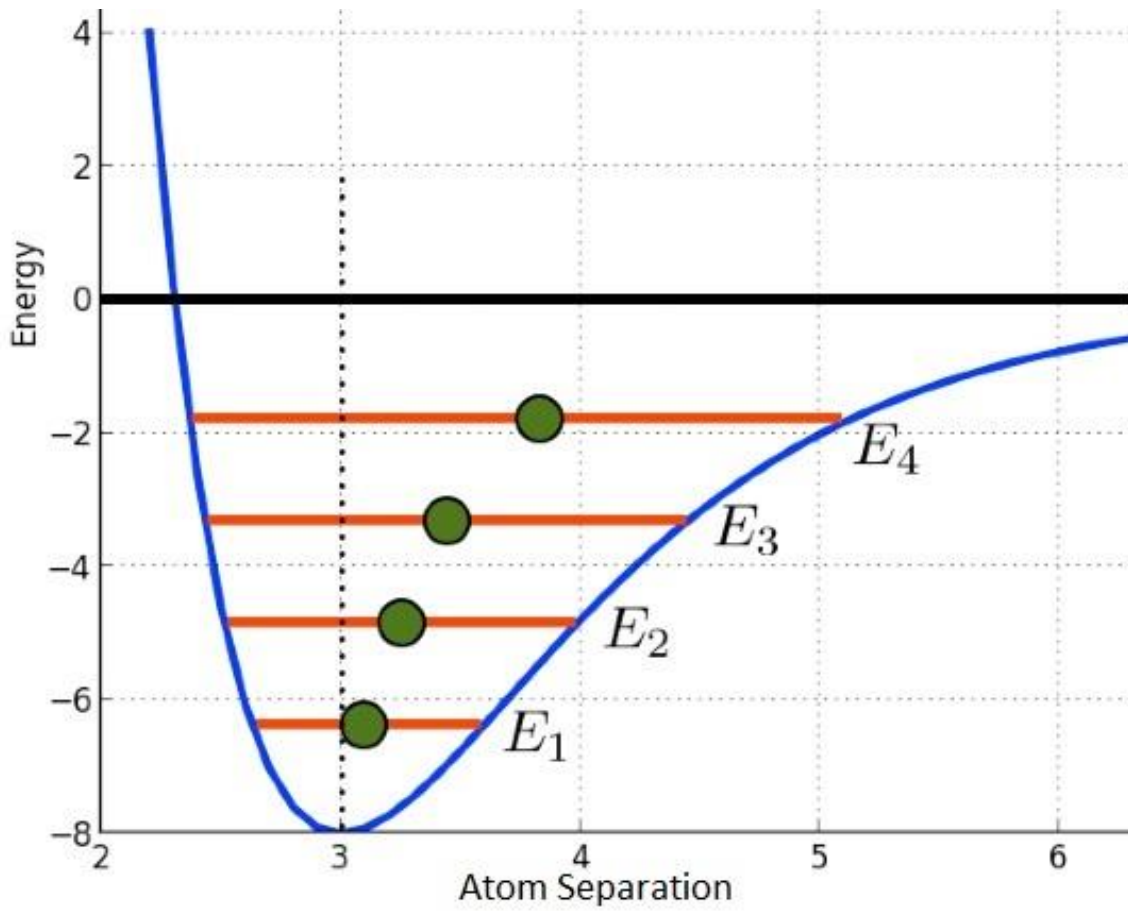


Figure 44. The Lennard-Jones potential for a generalized system. As thermal energy is added to a system, the average distance between atoms is increased.

5.1.3 Conclusions

The thermal expansion behavior of Lu_2TiO_5 , Er_2TiO_5 , Ho_2TiO_5 , Y_2TiO_5 , and Dy_2TiO_5 were evaluated. As a function of temperature the cubic phase expands at an increasing rate. This behavior is expected with an increase in thermal energy in the system as the distance between two atoms increases. This distance is related to the Lennard-Jones potential which describes the potential energy of bonding with the distance between two atoms. Since the well is not symmetric about its center, it is not expected that the increase in the expansion rate would be constant, and as such, agrees well with the observations made in this study.

5.2 Thermal Expansion in the Orthorhombic Phase

The thermal expansion behavior in the orthorhombic phase was determined for Y_2TiO_5 , Dy_2TiO_5 , Gd_2TiO_5 , Nd_2TiO_5 , and La_2TiO_5 using X-ray diffraction to monitor the crystallographic changes in the structure as a function of temperature in air. Results will be presented in order of increasing rare-earth cation ion size (Y, Dy, Gd, Nd, and La).

5.2.1 Results

Y₂TiO₅

As described in Chapter 4, powder of Y_2TiO_5 in the orthorhombic phase (where Y_2TiO_5 can exist in both the cubic and orthorhombic phase at room temperature) was mounted in a sapphire capillary and placed in the center of the quadrupole lamp furnace in alignment with the incident synchrotron X-ray radiation. An X-ray diffraction pattern was collected at each temperature from room temperature up to approximately 1400 °C in air. Using the programs GSAS and EXPGUI, the X-ray diffraction patterns were refined using the Rietveld method and the values for the lattice parameters, hkl, and corresponding d-spacings were extracted from the refined data. The lattice parameters as a function of temperature are plotted in Figures 45, 46, and 47 and are listed in Table 15.

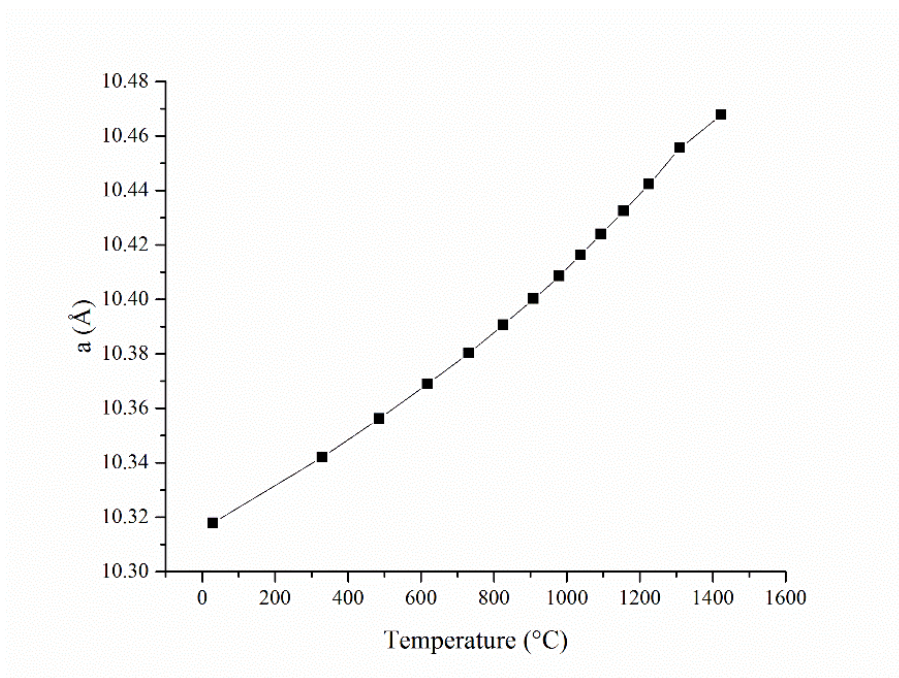


Figure 45. The lattice parameter of the a-axis in orthorhombic Y_2TiO_5 as a function of temperature. Error bars lie within the symbols.

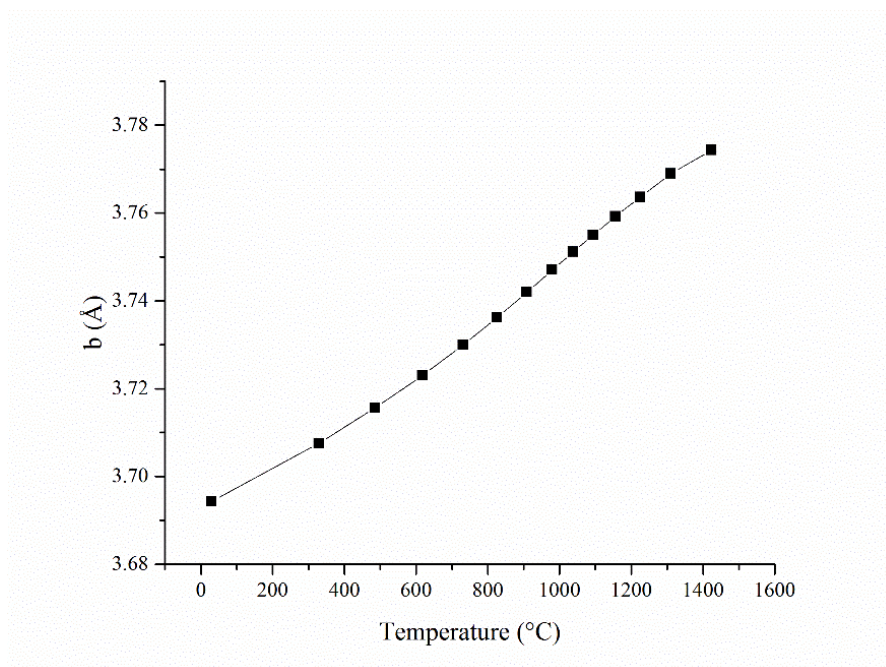


Figure 46. The lattice parameter of the b-axis in orthorhombic Y_2TiO_5 as a function of temperature. Error bars lie within the symbols.

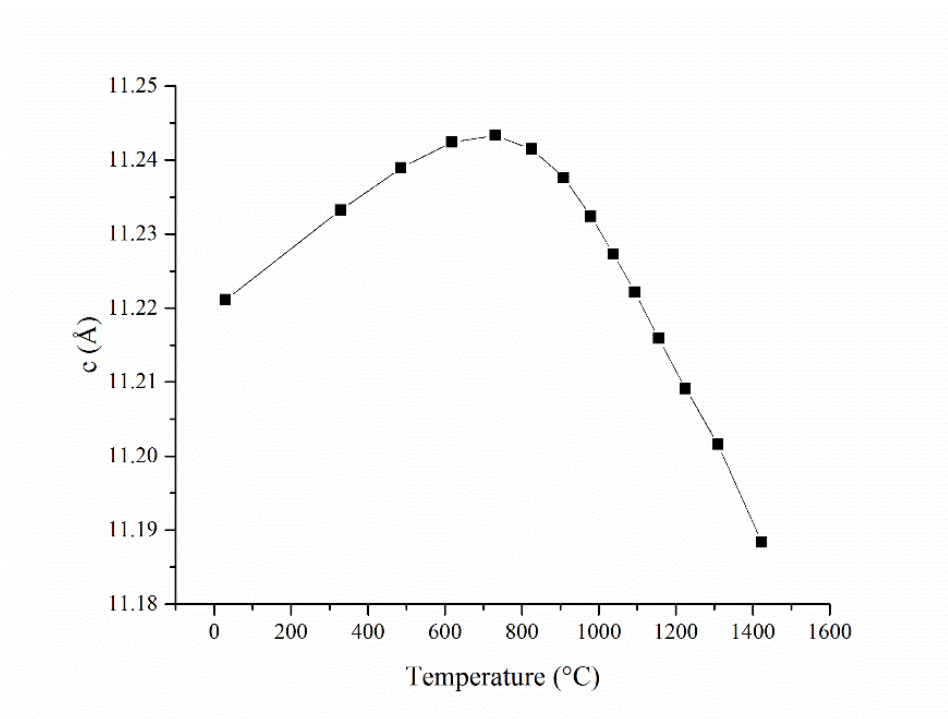


Figure 47. The lattice parameter of the c-axis in orthorhombic Y_2TiO_5 as a function of temperature. Error bars lie within the symbols.

Table 15. The lattice parameters of Y_2TiO_5 in the orthorhombic phase as a function of the measured temperature.

Temperature (°C) (± 6)	a (Å)	b (Å)	c (Å)
29	10.31788(8)	3.69431(2)	11.22110(8)
329	10.34200(8)	3.70756(2)	11.23322(7)
486	10.35622(8)	3.71563(2)	11.23894(7)
618	10.36899(8)	3.72305(2)	11.24239(7)
731	10.38022(8)	3.72993(2)	11.24329(7)
826	10.39063(8)	3.73619(2)	11.24147(7)
909	10.40013(8)	3.74200(2)	11.23758(9)
980	10.40855(8)	3.74707(3)	11.23233(9)
1038	10.41635(7)	3.75114(2)	11.22730(7)
1094	10.42392(8)	3.75501(2)	11.22214(7)
1156	10.43248(8)	3.75922(2)	11.21587(7)
1226	10.44231(8)	3.76364(2)	11.20906(7)
1310	10.45554(9)	3.76893(2)	11.20157(7)
1424	10.4678(5)	3.7743(1)	11.1883(4)

In addition to the determination of the lattice parameters, a CTEAS analysis was performed on the hkl listings and corresponding d-spacings as a function of temperature using a fourth-order polynomial fit. The results of the CTEAS analysis of the appropriate temperature range is depicted in Figure 48 and listed in Table 16.

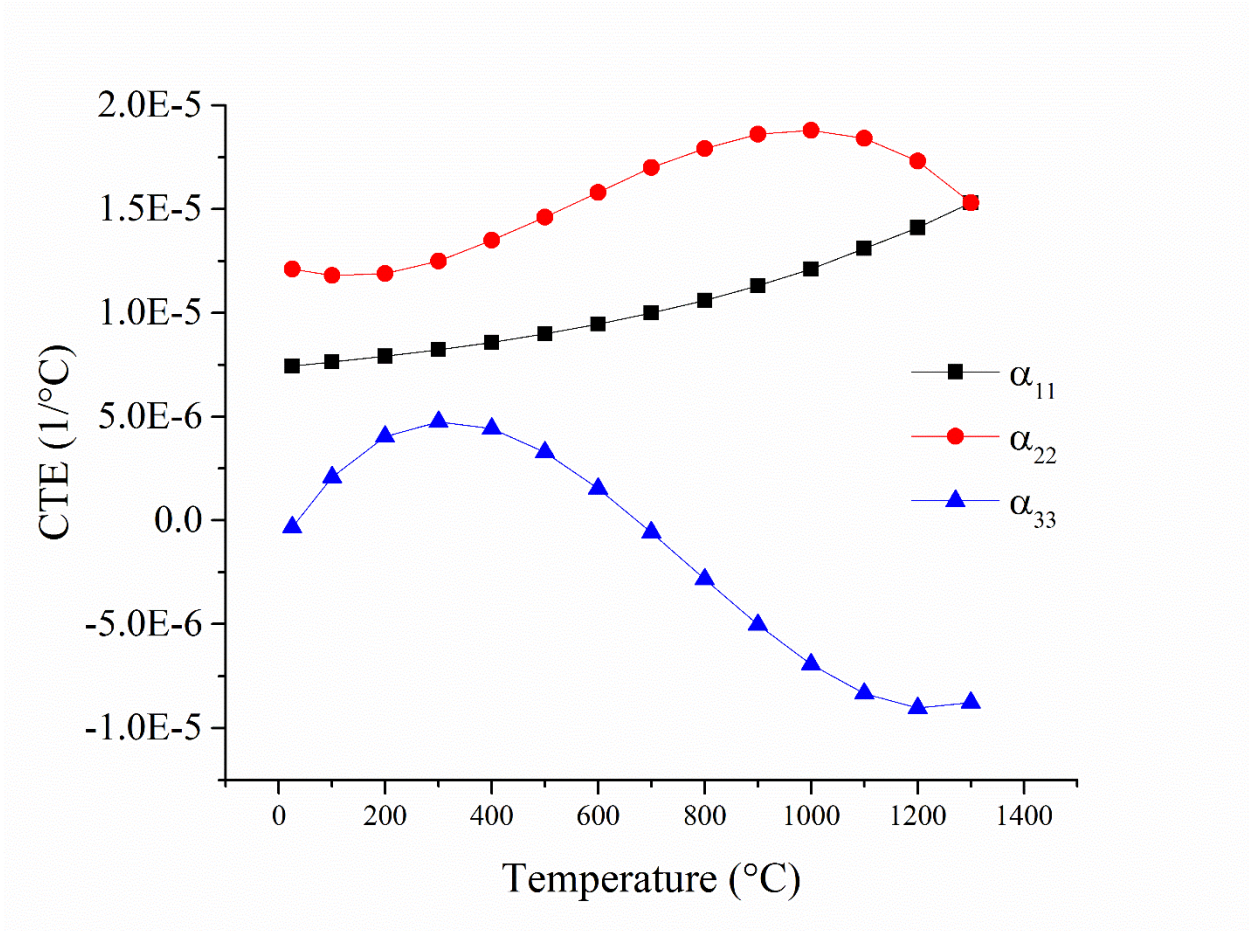


Figure 48. The coefficients of thermal expansion for Y₂TiO₅ in the orthorhombic phase as a function of temperature. Error bars lie within the symbols.

Table 16. The coefficients of thermal expansion for Y_2TiO_5 in the orthorhombic phase as a function of extrapolated temperature.

Temperature (°C)	α_{11}	α_{22}	α_{33}	Error
25	7.43	12.10	-0.33	0.17
100	7.63	11.80	2.08	0.15
200	7.91	11.90	4.04	0.14
300	8.22	12.50	4.75	0.13
400	8.58	13.50	4.42	0.12
500	8.99	14.60	3.28	0.11
600	9.46	15.80	1.54	0.10
700	10.00	17.00	-0.57	0.09
800	10.60	17.90	-2.83	0.09
900	11.30	18.60	-5.03	0.08
1000	12.10	18.80	-6.93	0.08
1100	13.10	18.40	-8.34	0.09
1200	14.10	17.30	-9.03	0.10
1300	15.30	15.30	-8.78	0.14

Dy₂TiO₅

As described in Chapter 4, powder of Dy_2TiO_5 in the orthorhombic phase (where Dy_2TiO_5 can exist in both the cubic and orthorhombic phase at room temperature) was mounted in a sapphire capillary and placed in the center of the quadrupole lamp furnace in alignment with the incident synchrotron X-ray radiation. An X-ray diffraction pattern was collected at each temperature from room temperature up to approximately 1400 °C in air. Using the programs GSAS and EXPGUI, the X-ray diffraction patterns were refined using the Rietveld method and the values for the lattice parameters, hkl, and corresponding d-spacings were extracted from the refined data. The lattice parameters as a function of temperature are plotted in Figures 49, 50, and 51 and are listed in Table 17.

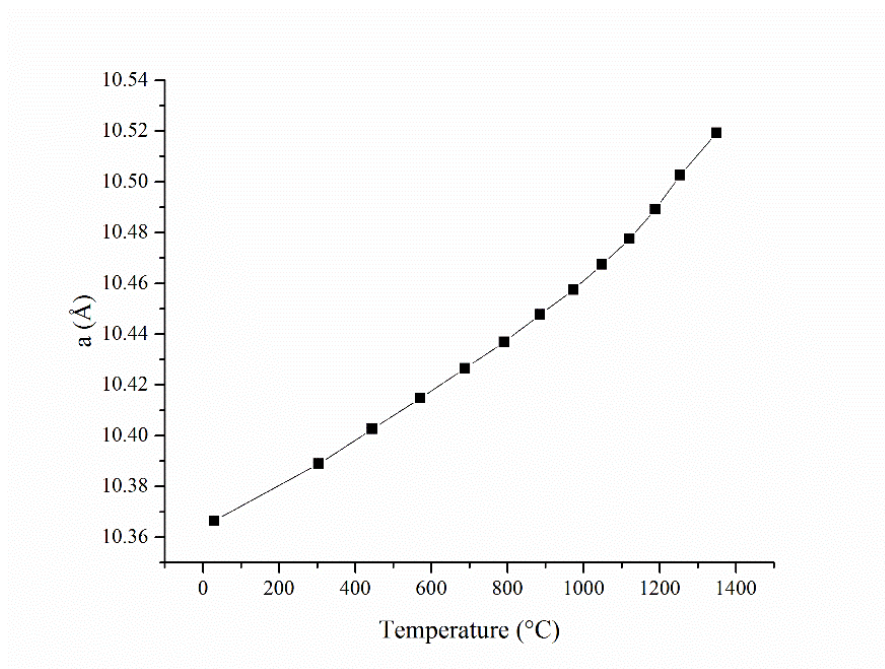


Figure 49. The lattice parameter of the a-axis in orthorhombic Dy_2TiO_5 as a function of temperature. Error bars lie within the symbols.

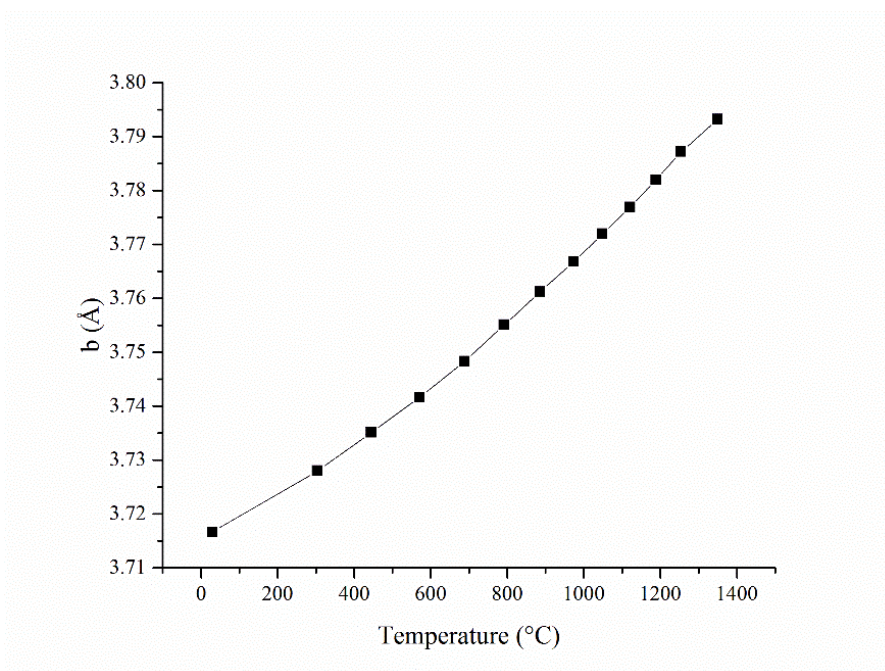


Figure 50. The lattice parameter of the b-axis in orthorhombic Dy_2TiO_5 as a function of temperature. Error bars lie within the symbols.

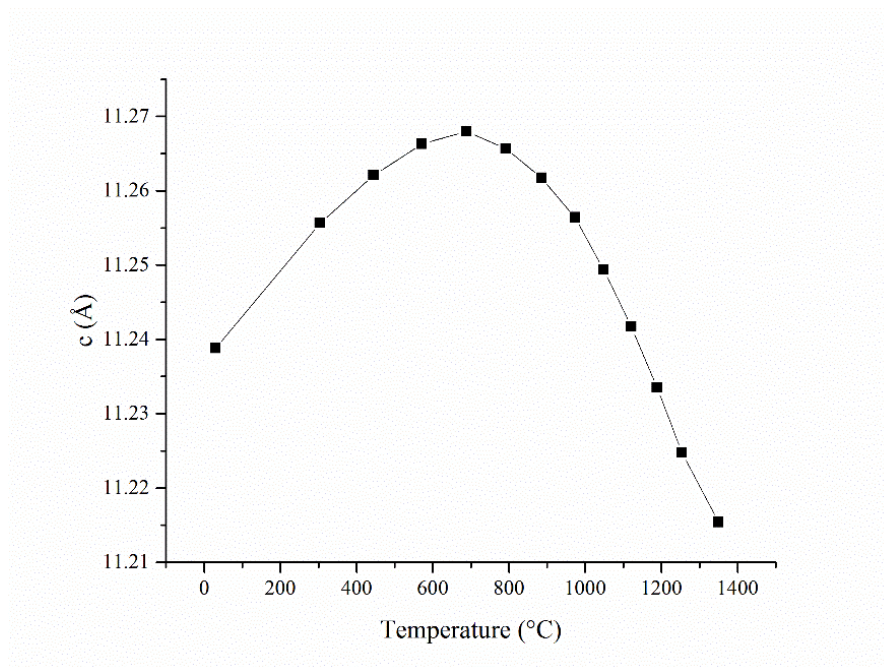


Figure 51. The lattice parameter of the c-axis in orthorhombic Dy_2TiO_5 as a function of temperature. Error bars lie within the symbols.

Table 17. The lattice parameters of Dy_2TiO_5 in the orthorhombic phase as a function of the measured temperature.

Temperature (°C) (± 6)	a (Å)	b (Å)	c (Å)
29	10.3663(1)	3.71667(4)	11.2388(1)
304	10.3888(1)	3.72798(3)	11.2556(1)
445	10.40253(9)	3.73509(3)	11.26210(9)
571	10.41467(9)	3.74166(2)	11.26628(9)
689	10.42652(8)	3.74830(2)	11.26799(9)
792	10.43687(8)	3.75508(3)	11.2656(1)
886	10.44768(8)	3.76121(2)	11.26174(8)
973	10.45737(8)	3.76674(2)	11.25642(7)
1049	10.46729(9)	3.77194(2)	11.24940(7)
1121	10.47750(9)	3.77692(2)	11.24175(8)
1189	10.4891(1)	3.78196(3)	11.23348(8)
1254	10.5025(1)	3.78713(3)	11.22477(9)
1350	10.5192(1)	3.79321(3)	11.21540(9)

In addition to the determination of the lattice parameters, a CTEAS analysis was performed on the hkl listings and corresponding d-spacings as a function of temperature using a fourth-order polynomial fit. The results of the CTEAS analysis of the appropriate temperature range is depicted in Figure 52 and listed in Table 18.

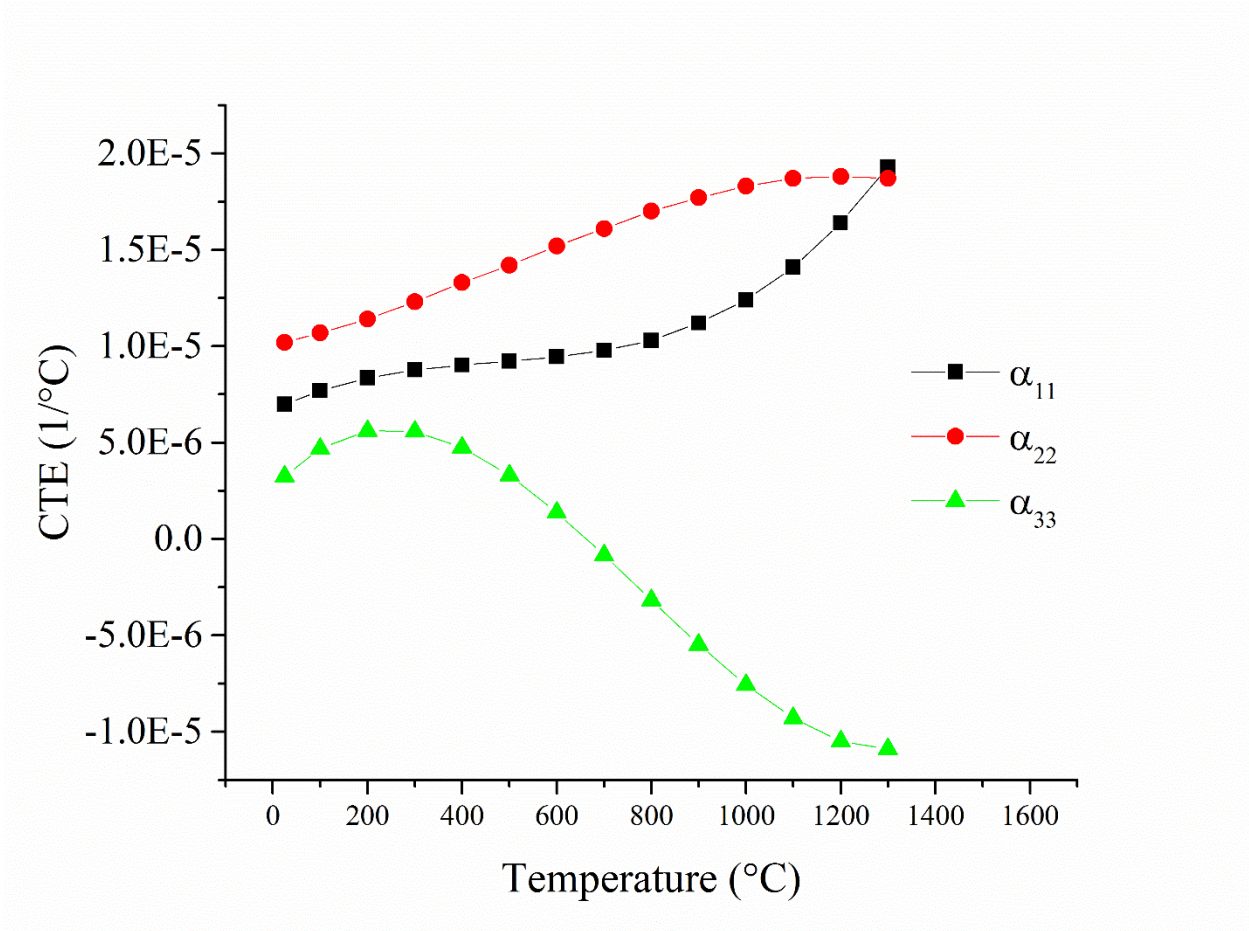


Figure 52. The coefficients of thermal expansion for Dy₂TiO₅ in the orthorhombic phase as a function of temperature. Error bars lie within the symbols.

Table 18. The coefficients of thermal expansion for Dy₂TiO₅ in the orthorhombic phase as a function of extrapolated temperature.

Temperature (°C)	α_{11}	α_{22}	α_{33}	Error
25	6.99	10.20	3.25	0.32
100	7.69	10.70	4.68	0.28
200	8.35	11.40	5.61	0.25
300	8.76	12.30	5.57	0.23
400	9.02	13.30	4.74	0.21
500	9.22	14.20	3.29	0.19
600	9.45	15.20	1.37	0.18
700	9.78	16.10	-0.85	0.17
800	10.30	17.00	-3.18	0.15
900	11.20	17.70	-5.48	0.14
1000	12.40	18.30	-7.57	0.14
1100	14.10	18.70	-9.29	0.15
1200	16.40	18.80	-10.50	0.18
1300	19.30	18.70	-10.90	0.23

Gd₂TiO₅

As described in Chapter 4, powder of Gd₂TiO₅ in the orthorhombic phase was mounted in a sapphire capillary and placed in the center of the quadrupole lamp furnace in alignment with the incident synchrotron X-ray radiation. An X-ray diffraction pattern was collected at each temperature from room temperature up to approximately 1550 °C in air. Using the programs GSAS and EXPGUI, the X-ray diffraction patterns were refined using the Rietveld method and the values for the lattice parameters, hkl, and corresponding d-spacings were extracted from the refined data. The lattice parameters as a function of temperature are plotted in Figures 53, 54, and 55 and are listed in Table 19.

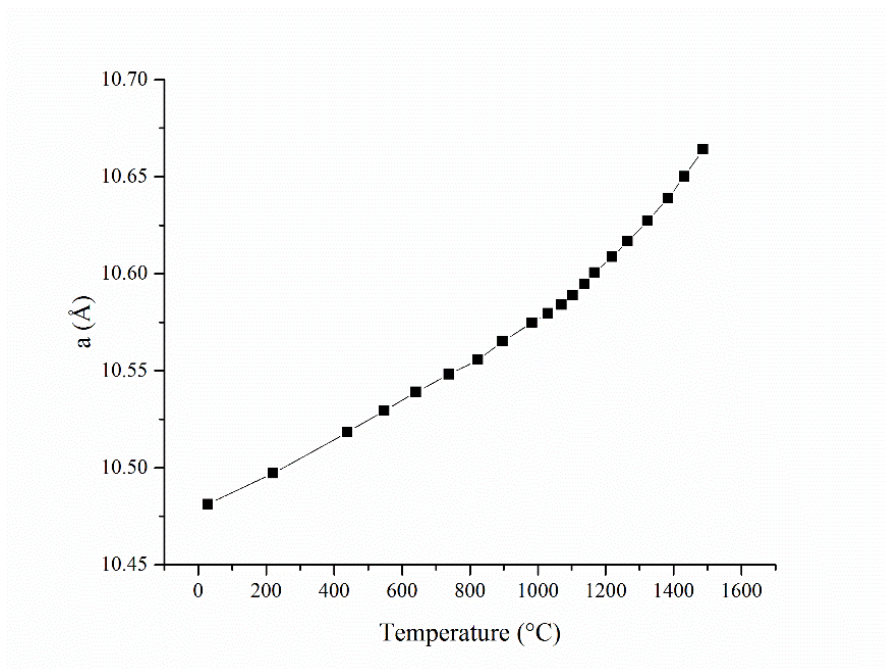


Figure 53. The lattice parameter of the a-axis in orthorhombic Gd_2TiO_5 as a function of temperature. Error bars lie within the symbols.

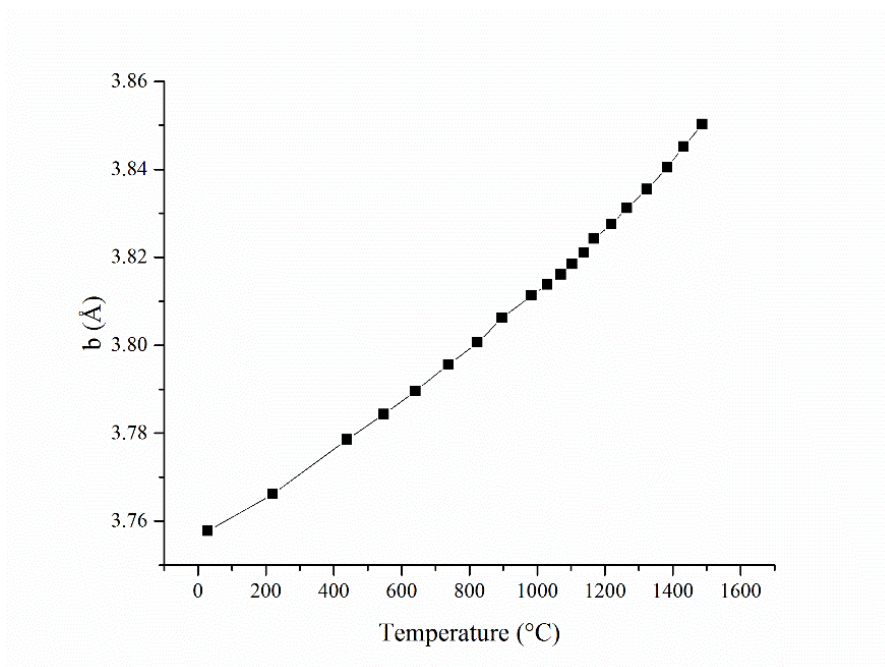


Figure 54. The lattice parameter of the b-axis in orthorhombic Gd_2TiO_5 as a function of temperature. Error bars lie within the symbols.

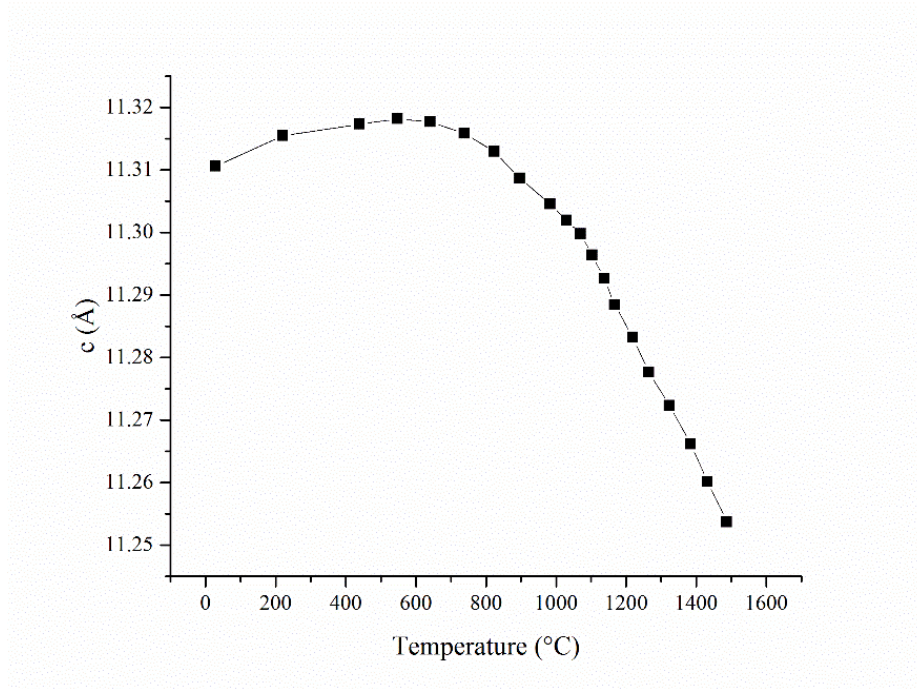


Figure 55. The lattice parameter of the c-axis in orthorhombic Gd_2TiO_5 as a function of temperature. Error bars lie within the symbols.

Table 19. The lattice parameters of Gd₂TiO₅ in the orthorhombic phase as a function of the measured temperature.

Temperature (°C) (± 6)	a (Å)	b (Å)	c (Å)
28	10.4812(1)	3.75776(6)	11.3105(1)
220	10.4971(2)	3.76616(7)	11.3154(2)
439	10.5183(1)	3.77853(6)	11.3172(2)
548	10.5293(1)	3.78435(5)	11.3181(1)
641	10.5389(2)	3.78961(7)	11.3176(2)
738	10.5481(1)	3.79560(4)	11.3158(1)
824	10.5554(1)	3.8006(4)	11.3129(1)
896	10.5652(1)	3.80618(4)	11.3086(1)
984	10.5747(1)	3.8113(3)	11.3045(1)
1030	10.5794(1)	3.81380(3)	11.3019(1)
1070	10.5839(1)	3.81601(3)	11.2997(1)
1103	10.5886(1)	3.81846(3)	11.2964(1)
1137	10.5945(1)	3.82106(3)	11.2926(1)
1167	10.6005(1)	3.82416(3)	11.2884(1)
1219	10.6085(1)	3.82752(4)	11.2832(1)
1265	10.6167(1)	3.83115(4)	11.2776(1)
1324	10.6270(2)	3.83549(6)	11.2722(1)
1384	10.6389(3)	3.84043(9)	11.2661(2)
1432	10.6501(5)	3.8451(1)	11.2601(3)
1487	10.6639(7)	3.85025(1)	11.2537(5)

In addition to the determination of the lattice parameters, a CTEAS analysis was performed on the hkl listings and corresponding d-spacings as a function of temperature using a fourth-order polynomial fit. The results of the CTEAS analysis of the appropriate temperature range is depicted in Figure 56 and listed in Table 20.

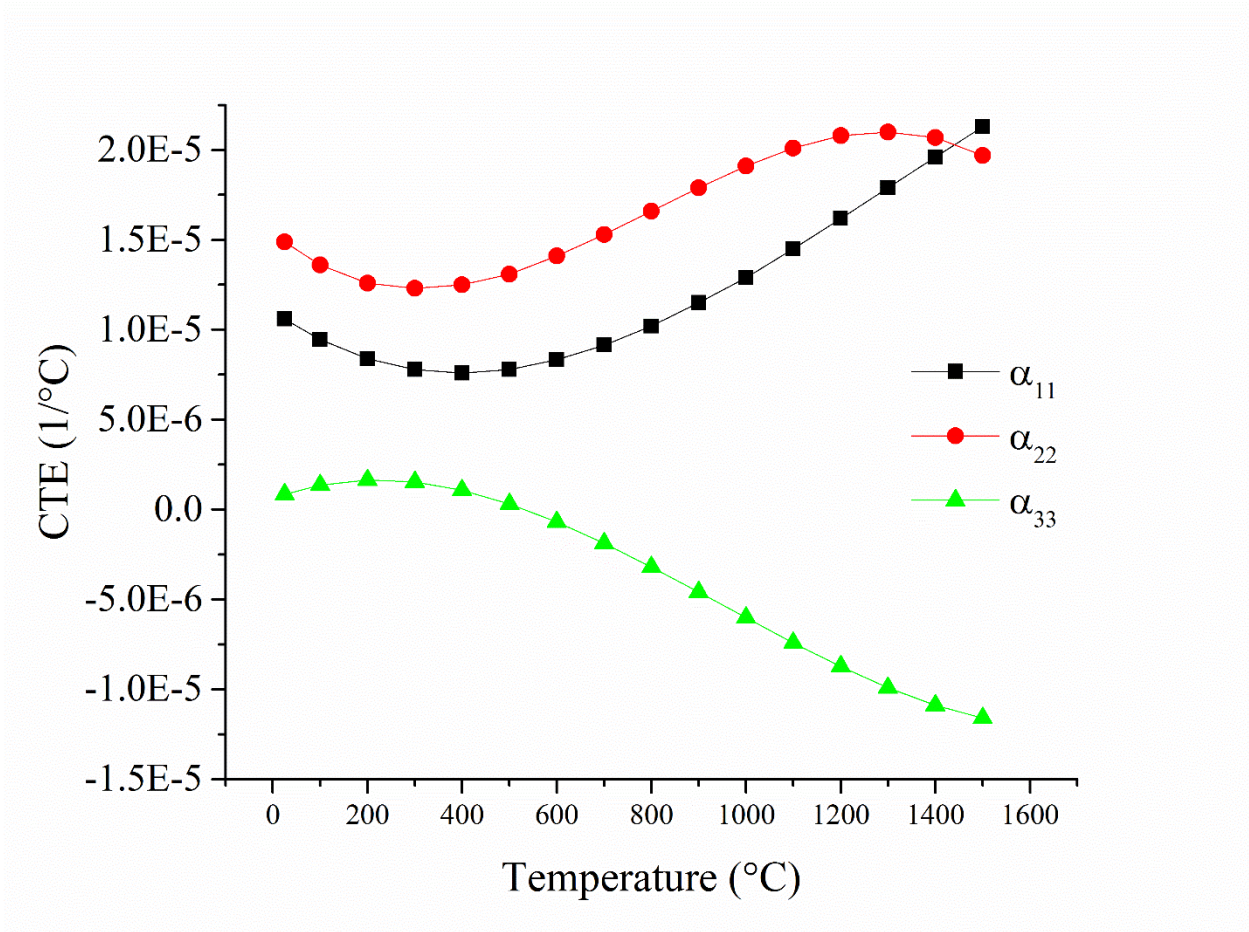


Figure 56. The coefficients of thermal expansion for Gd₂TiO₅ in the orthorhombic phase as a function of temperature. Error bars lie within the symbols.

Table 20. The coefficients of thermal expansion for Gd₂TiO₅ in the orthorhombic phase as a function of extrapolated temperature.

Temperature (°C)	α_{11}	α_{22}	α_{33}	Error
25	10.60	14.90	0.84	2.81
100	9.46	13.60	1.36	2.34
200	8.39	12.60	1.64	1.92
300	7.79	12.30	1.53	1.65
400	7.60	12.50	1.06	1.49
500	7.79	13.10	0.30	1.38
600	8.33	14.10	-0.70	1.30
700	9.15	15.30	-1.88	1.22
800	10.20	16.60	-3.20	1.14
900	11.50	17.90	-4.60	1.06
1000	12.90	19.10	-6.02	0.98
1100	14.50	20.10	-7.42	0.94
1200	16.20	20.80	-8.73	0.98
1300	17.90	21.00	-9.91	1.14
1400	19.60	20.70	-10.90	1.49
1500	21.30	19.70	-11.60	2.09

Nd₂TiO₅

As described in Chapter 4, powder of Nd₂TiO₅ in the orthorhombic phase was mounted in a sapphire capillary and placed in the center of the quadrupole lamp furnace in alignment with the incident synchrotron X-ray radiation. An X-ray diffraction pattern was collected at each temperature from room temperature up to approximately 1600 °C in air. Using the programs GSAS and EXPGUI, the X-ray diffraction patterns were refined using the Rietveld method and the values for the lattice parameters, hkl, and corresponding d-spacings were extracted from the refined data. The lattice parameters as a function of temperature are plotted in Figures 57, 58, and 59 and are listed in Table 21.

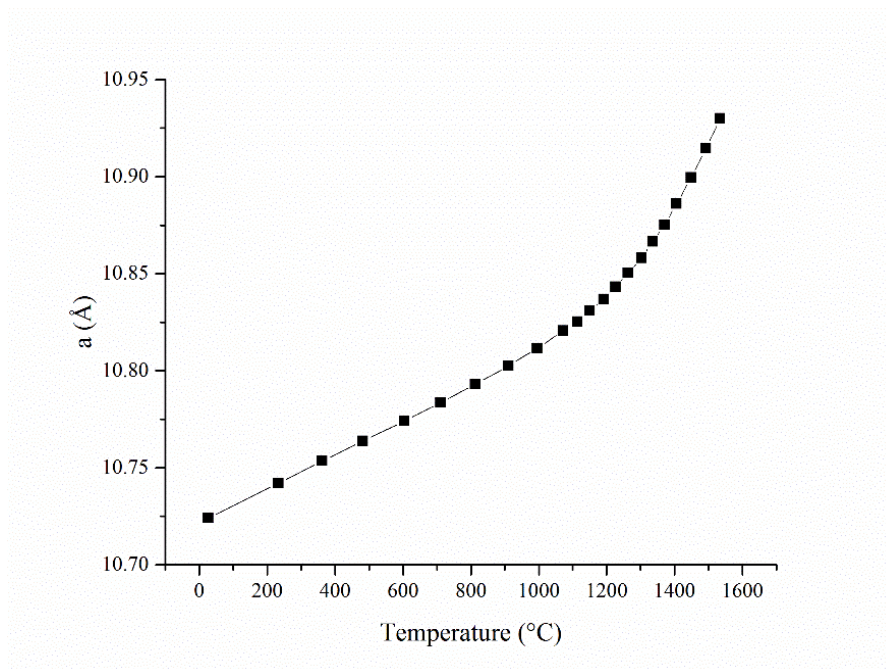


Figure 57. The lattice parameter of the a-axis in orthorhombic Nd_2TiO_5 as a function of temperature. Error bars lie within the symbols.

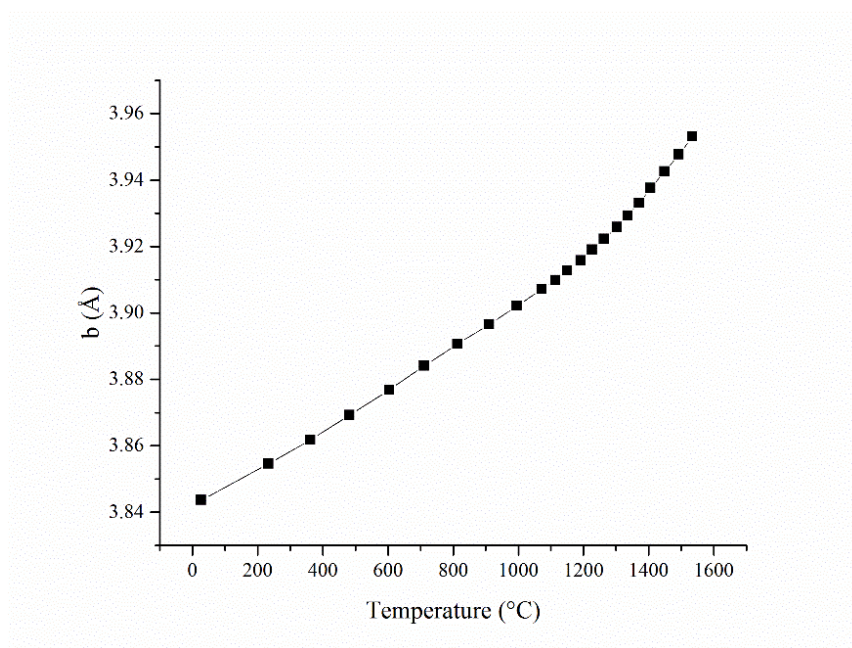


Figure 58. The lattice parameter of the b-axis in orthorhombic Nd_2TiO_5 as a function of temperature. Error bars lie within the symbols.

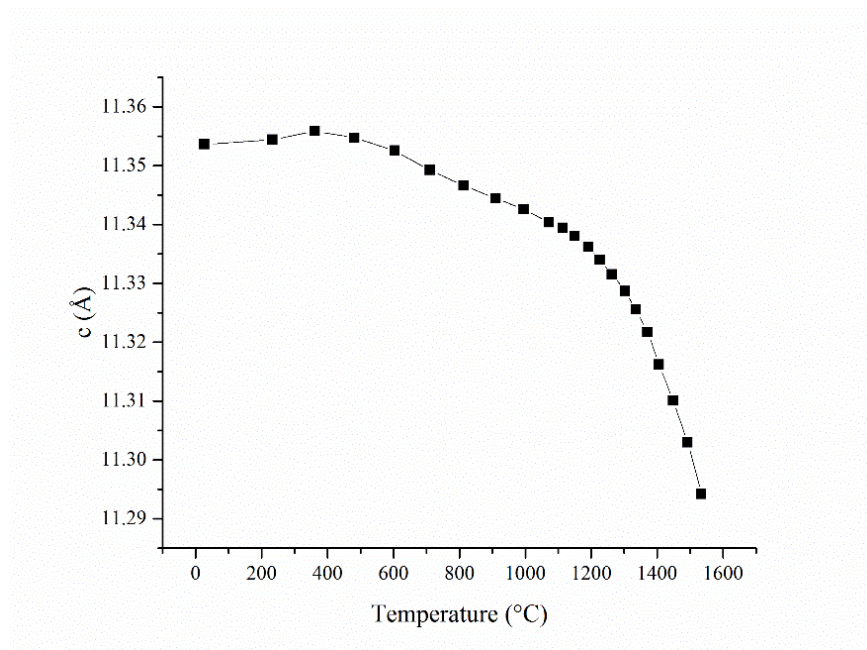


Figure 59. The lattice parameter of the c -axis in orthorhombic Nd_2TiO_5 as a function of temperature. Error bars lie within the symbols.

Table 21. The lattice parameters of Nd₂TiO₅ in the orthorhombic phase as a function of the measured temperature.

Temperature (°C) (±6)	a (Å)	b (Å)	c (Å)
27	10.7241(2)	3.84366(5)	11.3535(1)
233	10.7419(1)	3.85457(5)	11.3543(1)
362	10.7534(1)	3.86182(4)	11.3558(1)
482	10.7638(1)	3.86924(4)	11.3547(1)
604	10.7740(1)	3.87682(4)	11.3525(1)
711	10.7836(1)	3.88409(4)	11.3491(1)
813	10.7930(1)	3.89068(4)	11.3465(1)
911	10.8025(1)	3.89653(3)	11.3444(1)
996	10.8115(1)	3.90208(3)	11.34255(1)
1072	10.8206(1)	3.90716(3)	11.34030(9)
1114	10.8253(1)	3.90989(3)	11.33939(9)
1151	10.8308(1)	3.91282(3)	11.3379(1)
1191	10.8368(1)	3.91576(3)	11.3361(1)
1227	10.8432(1)	3.91904(3)	11.3339(1)
1263	10.8503(1)	3.92231(3)	11.3315(1)
1303	10.8579(1)	3.92583(4)	11.32869(5)
1335	10.8664(1)	3.92931(4)	11.3255(1)
1371	10.8751(1)	3.93311(4)	11.3216(1)
1406	10.8859(2)	3.93763(5)	11.31619(1)
1449	10.8995(2)	3.94256(6)	11.3100(1)
1493	10.9145(3)	3.94765(7)	11.3029(2)
1535	10.9299(2)	3.95312(7)	11.2941(2)

In addition to the determination of the lattice parameters, a CTEAS analysis was performed on the hkl listings and corresponding d-spacings as a function of temperature using a fourth-order polynomial fit. The results of the CTEAS analysis of the appropriate temperature range is depicted in Figure 60 and listed in Table 22.

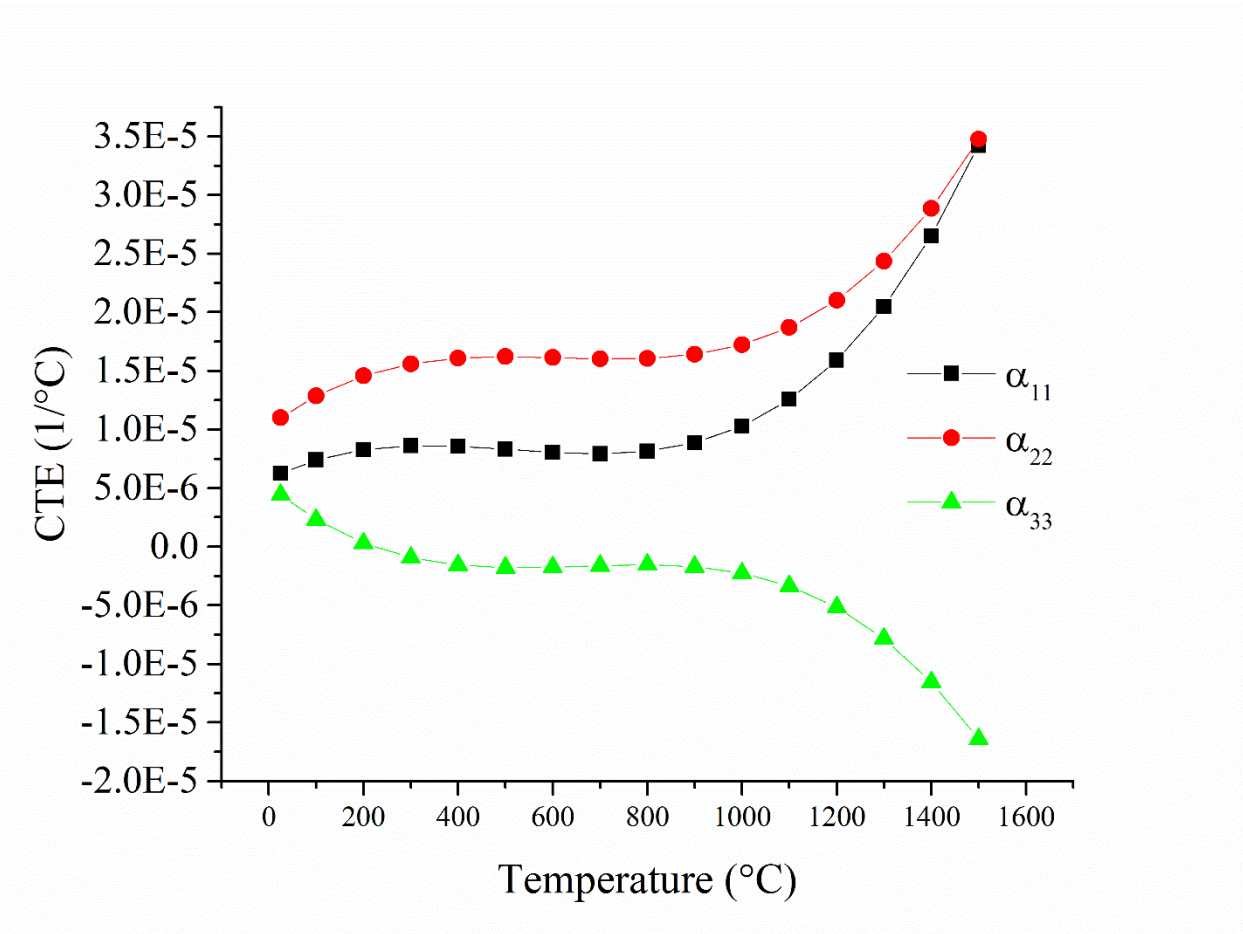


Figure 60. The coefficients of thermal expansion for Nd_2TiO_5 in the orthorhombic phase as a function of temperature. Error bars lie within the symbols.

Table 22. The coefficients of thermal expansion for Nd₂TiO₅ in the orthorhombic phase as a function of extrapolated temperature.

Temperature (°C)	α_{11}	α_{22}	α_{33}	Error
25	6.24	11.00	4.41	0.29
100	7.40	12.90	2.30	0.24
200	8.28	14.60	0.31	0.19
300	8.60	15.60	-0.92	0.17
400	8.56	16.10	-1.57	0.16
500	8.31	16.20	-1.79	0.15
600	8.05	16.10	-1.75	0.15
700	7.93	16.00	-1.62	0.14
800	8.14	16.10	-1.54	0.13
900	8.86	16.40	-1.70	0.12
1000	10.30	17.20	-2.25	0.11
1100	12.60	18.70	-3.35	0.10
1200	15.90	21.00	-5.16	0.09
1300	20.50	24.30	-7.84	0.10
1400	26.50	28.90	-11.50	0.12
1500	34.20	34.80	-16.40	0.17

La₂TiO₅

As described in Chapter 4, powder of La₂TiO₅ in the orthorhombic phase was mounted in a sapphire capillary and placed in the center of the quadrupole lamp furnace in alignment with the incident synchrotron X-ray radiation. An X-ray diffraction pattern was collected at each temperature from room temperature up to approximately 1400 °C in air. Using the programs GSAS and EXPGUI, the X-ray diffraction patterns were refined using the Rietveld method and the values for the lattice parameters, hkl, and corresponding d-spacings were extracted from the refined data. The lattice parameters as a function of temperature are plotted in Figures 61, 62, and 63 and are listed in Table 23.

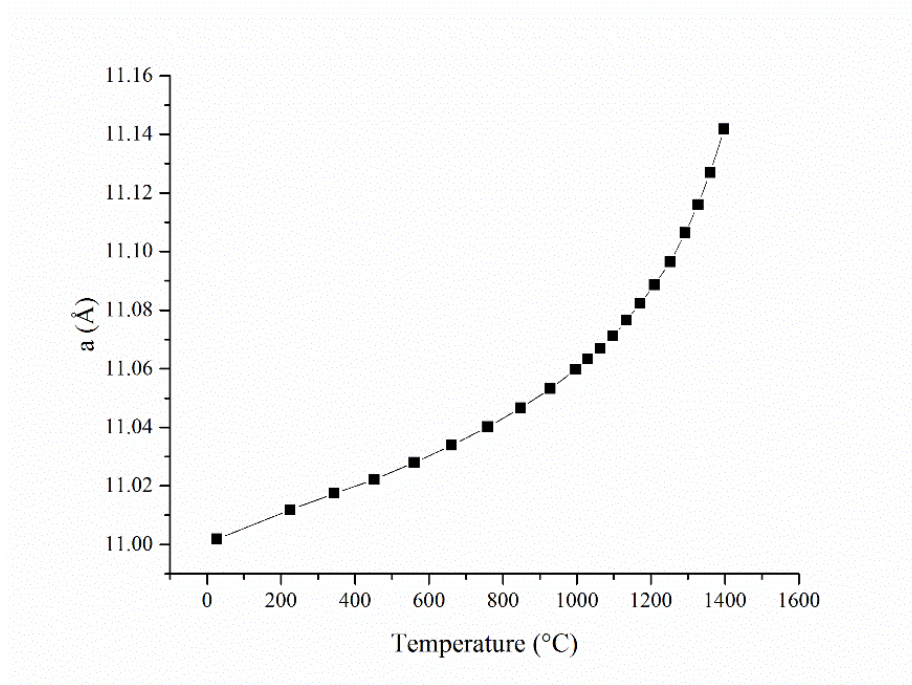


Figure 61. The lattice parameter of the a-axis in orthorhombic La_2TiO_5 as a function of temperature. Error bars lie within the symbols.

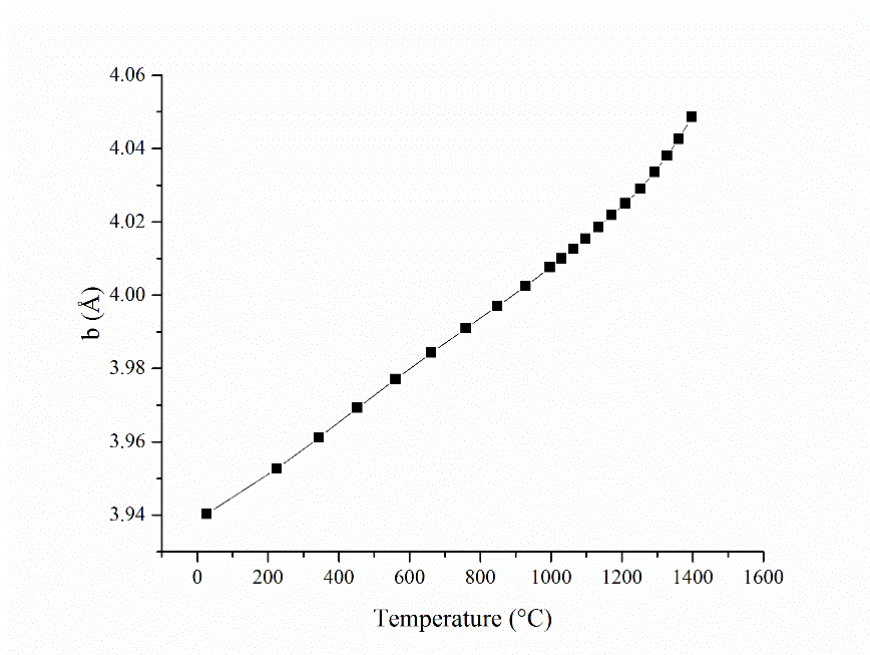


Figure 62. The lattice parameter of the b-axis in orthorhombic La_2TiO_5 as a function of temperature. Error bars lie within the symbols.

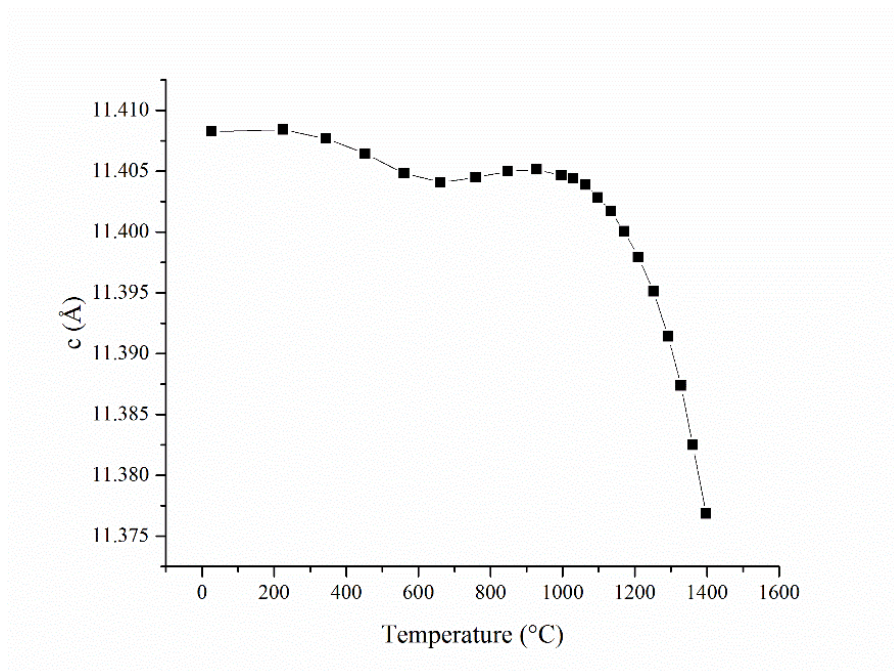


Figure 63. The lattice parameter of the c-axis in orthorhombic La_2TiO_5 as a function of temperature. Error bars lie within the symbols.

Table 23. The lattice parameters of La_2TiO_5 in the orthorhombic phase as a function of the measured temperature.

Temperature ($^{\circ}\text{C}$) (± 6)	a (\AA)	b (\AA)	c (\AA)
27	11.0019(2)	3.94031(5)	11.4082(1)
225	11.0118(1)	3.95274(3)	11.4084(1)
344	11.0174(1)	3.96119(4)	11.4076(1)
453	11.0222(1)	3.96925(4)	11.4064(1)
561	11.0280(1)	3.97709(3)	11.4048(1)
662	11.0338(1)	3.98436(3)	11.4040(1)
759	11.0401(1)	3.99091(4)	11.4044(1)
848	11.0466(1)	3.99702(4)	11.4049(1)
928	11.0531(1)	4.00247(4)	11.4051(1)
997	11.0597(1)	4.00754(4)	11.4046(1)
1029	11.0632(1)	4.01001(4)	11.4043(1)
1064	11.0669(1)	4.01261(4)	11.4038(1)
1098	11.0711(1)	4.01536(4)	11.4028(1)
1134	11.0764(1)	4.01848(4)	11.4016(1)
1171	11.0822(1)	4.02179(3)	11.40003(8)
1210	11.0885(1)	4.02503(3)	11.39792(9)
1252	11.0964(1)	4.02902(3)	11.39510(9)
1293	11.1063(1)	4.03357(3)	11.3914(1)
1328	11.1159(1)	4.03807(3)	11.3873(1)
1361	11.1268(1)	4.04255(4)	11.3824(1)
1398	11.1418(1)	4.04856(3)	11.3768(1)

In addition to the determination of the lattice parameters, a CTEAS analysis was performed on the hkl listings and corresponding d-spacings as a function of temperature using a fourth-order polynomial fit. The results of the CTEAS analysis of the appropriate temperature range is depicted in Figure 64 and listed in Table 24.

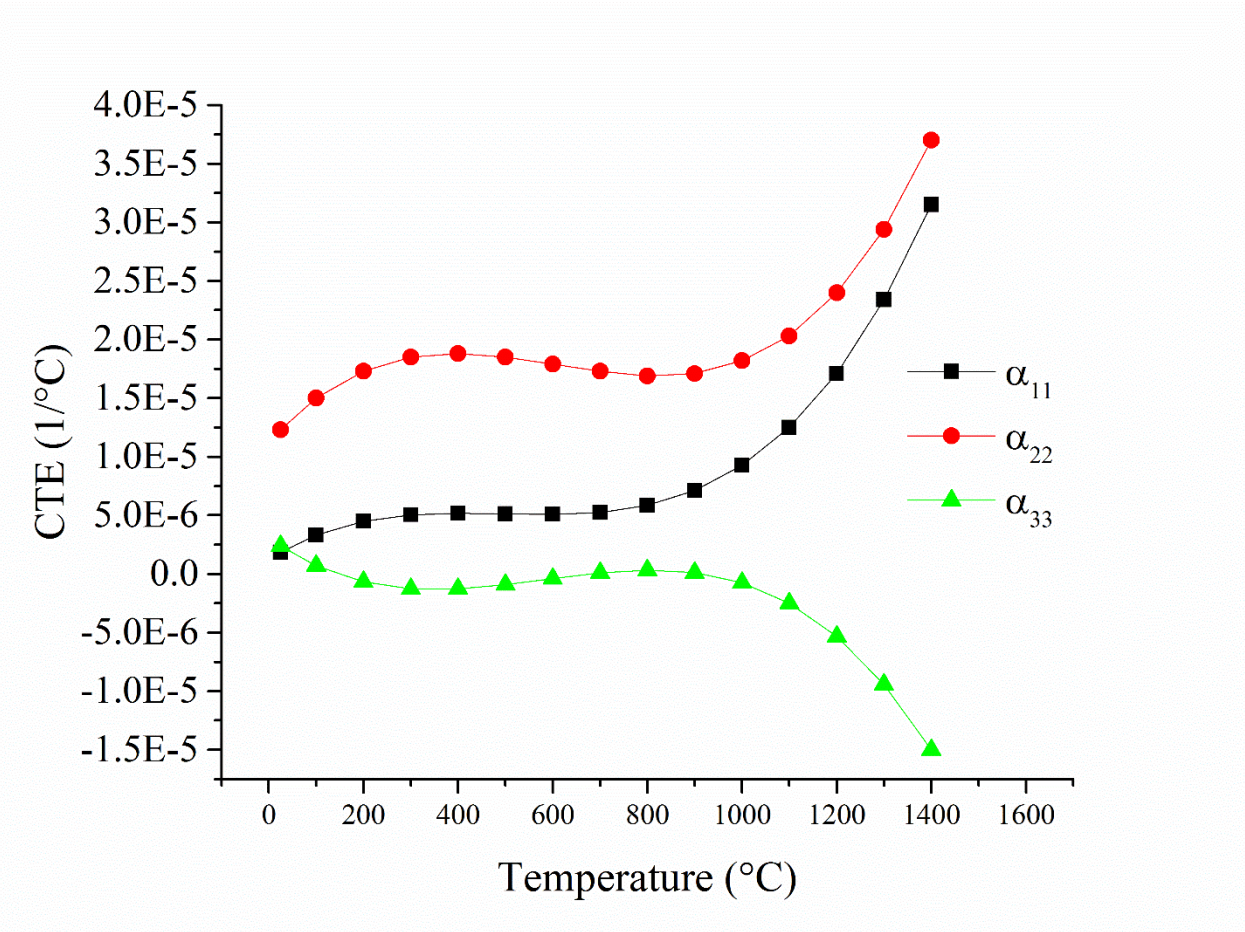


Figure 64. The coefficients of thermal expansion for La₂TiO₅ in the orthorhombic phase as a function of temperature. Error bars lie within the symbols.

Table 24. The coefficients of thermal expansion for La₂TiO₅ in the orthorhombic phase as a function of extrapolated temperature.

Temperature (°C)	α_{11}	α_{22}	α_{33}	Error
25	1.85	12.30	2.39	0.34
100	3.33	15.00	0.71	0.28
200	4.51	17.30	-0.67	0.22
300	5.05	18.50	-1.26	0.19
400	5.19	18.80	-1.27	0.18
500	5.12	18.50	-0.91	0.17
600	5.08	17.90	-0.39	0.17
700	5.24	17.30	0.10	0.16
800	5.85	16.90	0.33	0.15
900	7.12	17.10	0.12	0.13
1000	9.26	18.20	-0.76	0.12
1100	12.50	20.30	-2.50	0.12
1200	17.10	24.00	-5.32	0.12
1300	23.40	29.40	-9.41	0.15
1400	31.50	37.00	-15.00	0.22

5.2.2 Discussion and Mechanism of Thermal Expansion

The general structure for the orthorhombic phase of Ln₂TiO₅ is depicted in Figure 13. Among the rare-earth titanates that crystallize in the orthorhombic phase at room temperature, La, Nd, Gd, Dy, and Y were chosen because they provide the full range of cation sizes in this phase. The lattice parameters for each sample as a function of temperature are plotted in the Figures above and listed in Tables 15, 17, 19, 21, and 23 and combined in Figure 65.

As expected, the initial lattice parameters and volume follow a trend associated with the relative rare-earth cation size: smaller cations have cells with smaller lattice parameters and volumes, and larger cations have cells with larger lattice parameters and volumes. This information can be compared with the theoretical sizes of the rare-earth cations as published by Shannon and is in agreement.

Table 25. Combined coefficient of thermal expansion (CTE) tensor values.

T (°C)	La ₂ TiO ₅			Nd ₂ TiO ₅			Gd ₂ TiO ₅			Dy ₂ TiO ₅			Y ₂ TiO ₅			
	α_{11}	α_{22}	α_{33}	α_{11}	α_{22}	α_{33}										
25	1.85	12.30	2.39	6.24	11.00	4.41	10.60	14.90	0.84	6.99	10.20	3.25	7.43	12.10	-0.33	
100	3.33	15.00	0.71	7.40	12.90	2.30	9.46	13.60	1.36	7.69	10.70	4.68	7.63	11.80	2.08	
200	4.51	17.30	-0.67	8.28	14.60	0.31	8.39	12.60	1.64	8.35	11.40	5.61	7.91	11.90	4.04	
300	5.05	18.50	-1.26	8.60	15.60	-0.92	7.79	12.30	1.53	8.76	12.30	5.57	8.22	12.50	4.75	
400	5.19	18.80	-1.27	8.56	16.10	-1.57	7.60	12.50	1.06	9.02	13.30	4.74	8.58	13.50	4.42	
500	5.12	18.50	-0.91	8.31	16.20	-1.79	7.79	13.10	0.30	9.22	14.20	3.29	8.99	14.60	3.28	
600	5.08	17.90	-0.39	8.05	16.10	-1.75	8.33	14.10	-0.70	9.45	15.20	1.37	9.46	15.80	1.54	
700	5.24	17.30	0.10	7.93	16.00	-1.62	9.15	15.30	-1.88	9.78	16.10	-0.85	10.00	17.00	-0.57	
800	5.85	16.90	0.33	8.14	16.10	-1.54	10.20	16.60	-3.20	10.30	17.00	-3.18	10.60	17.90	-2.83	
900	7.12	17.10	0.12	8.86	16.40	-1.70	11.50	17.90	-4.60	11.20	17.70	-5.48	11.30	18.60	-5.03	
1000	9.26	18.20	-0.76	10.30	17.20	-2.25	12.90	19.10	-6.02	12.40	18.30	-7.57	12.10	18.80	-6.93	
1100	12.50	20.30	-2.50	12.60	18.70	-3.35	14.50	20.10	-7.42	14.10	18.70	-9.29	13.10	18.40	-8.34	
1200	17.10	24.00	-5.32	15.90	21.00	-5.16	16.20	20.80	-8.73	16.40	18.80	-10.50	14.10	17.30	-9.03	
1300	23.40	29.40	-9.41	20.50	24.30	-7.84	17.90	21.00	-9.91	19.30	18.70	-10.90	15.30	15.30	-8.78	
1400	31.50	37.00	-15.00	26.50	28.90	-11.50	19.60	20.70	-10.90	-	-	-	-	-	-	
1500	-	-	-	34.20	34.80	-16.40	21.30	19.70	-11.60	-	-	-	-	-	-	-

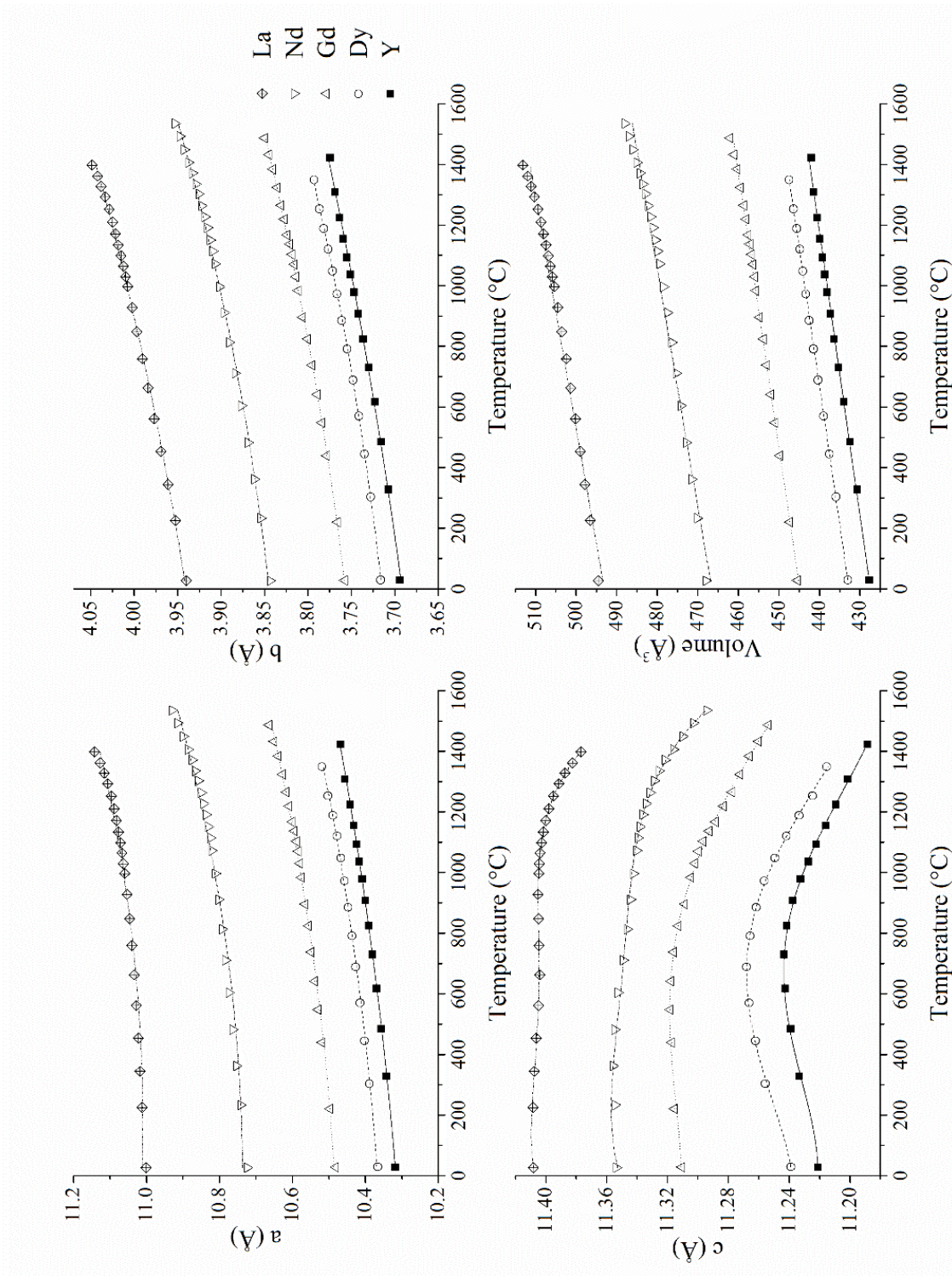


Figure 65. The combined lattice parameters and volume for La_2TiO_5 , Nd_2TiO_5 , Gd_2TiO_5 , Dy_2TiO_5 , and Y_2TiO_5 in the orthorhombic phase as a function of temperature. Error bars are smaller than data points.

Initially, the lattice parameters for each sample increased as a function of temperature. Upon continued heating, however, the lattice parameters for the c-axis reach a maximum and begins to decrease. This behavior was different from the findings in a similar study to characterize the thermal expansion behavior of Dy_2TiO_5 and Gd_2TiO_5 , where a study that was carried out in an argon atmosphere.[47,108]

In the argon study the thermal expansion along each of the primary crystallographic directions was both positive and increasing as a function of temperature. This would suggest that oxygen vacancies resulting from a lower oxygen partial pressure can have a significant impact on the thermal expansion behavior in this materials system. Depending on the intended operating conditions, this could result in undesirable thermophysical or mechanical behavior. The effect of oxygen vacancies on the thermal expansion warrants further exploration.

A CTEAS analysis was performed for each sample in terms of a fourth-order polynomial fit of each hkl and corresponding d-spacing. For an orthorhombic crystal system only three components of the thermal expansion tensor were needed to describe the system, and the results of the calculation are presented in Table 25 and Figure 66. A clear relationship existed between the size of the rare-earth cation and the thermal expansion behavior. For example, α_{33} began as a relatively small number, but upon heating this value increased with temperature until it reached a maximum value, after which it contracted. The temperature at which the onset of contraction began was related to the rare-earth cation size. For rare-earth cations which had smaller radii (i.e. Y and Dy) this transition occurred at higher temperatures, and for larger rare-earth cations (i.e. La and Nd) it occurred at lower temperatures. This relationship is depicted in Figure 66(d). Overall, the thermal expansion behavior was similar across the lanthanide series and shifted by temperature in relation to the size of the rare-earth cation.

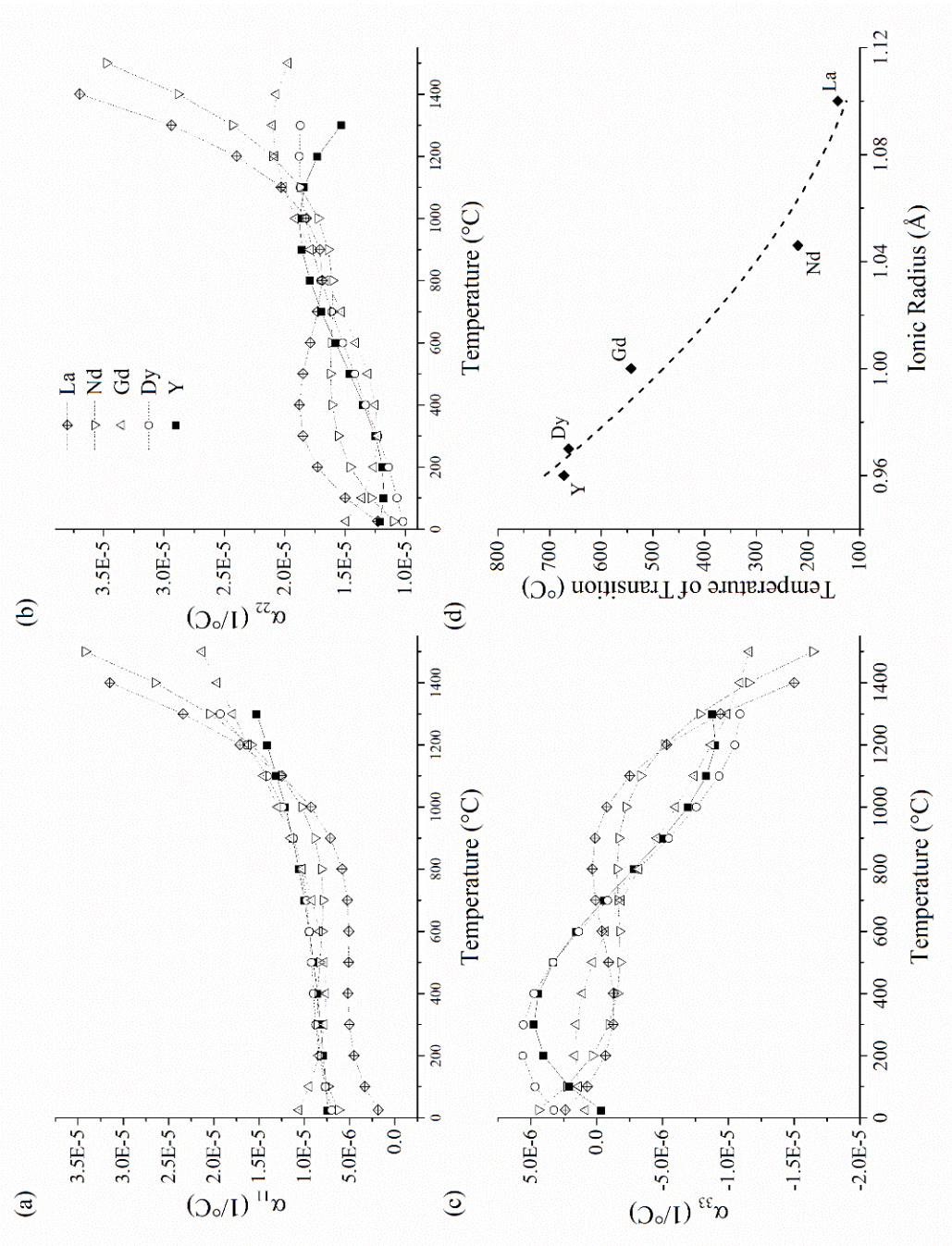


Figure 66. The combined coefficients of thermal expansion for La_2TiO_5 , Nd_2TiO_5 , Gd_2TiO_5 , Dy_2TiO_5 , and Y_2TiO_5 in the orthorhombic phase as a function of temperature. Also described is the relationship between the ionic size of the rare-earth cation with respect to the temperature where the c-axis transitions from expanding to contracting in length. Error bars are smaller than data points.

For comparison, the linear thermal expansion was measured for Nd_2TiO_5 and Dy_2TiO_5 by means of dilatometry. The results of this measurement, along with the average coefficient of thermal expansion calculated from the X-ray diffraction data, are provided in Figure 67. Generally, the linear thermal expansion behavior displays similar trends between measurements made via dilatometry versus those made through X-ray diffraction techniques. At first, both measurements showed an increase in the thermal expansion coefficient followed by a plateau of no change or a slight decrease in the thermal expansion coefficient. Then, at higher temperatures the coefficient of thermal expansion began to increase again. While the general behavior patterns observed through the two measurement techniques were similar, the values for the coefficient of thermal expansion were not. The difference in the overall value of the coefficient of thermal expansion could potentially be caused by strain and grain effects that may be present in a sintered sample but not in the relatively strain free powder samples. This strain was evident after a comparison of the room temperature lattice parameters was made via X-ray diffraction between the sintered and powder samples and was found to be up to 2.8% different.

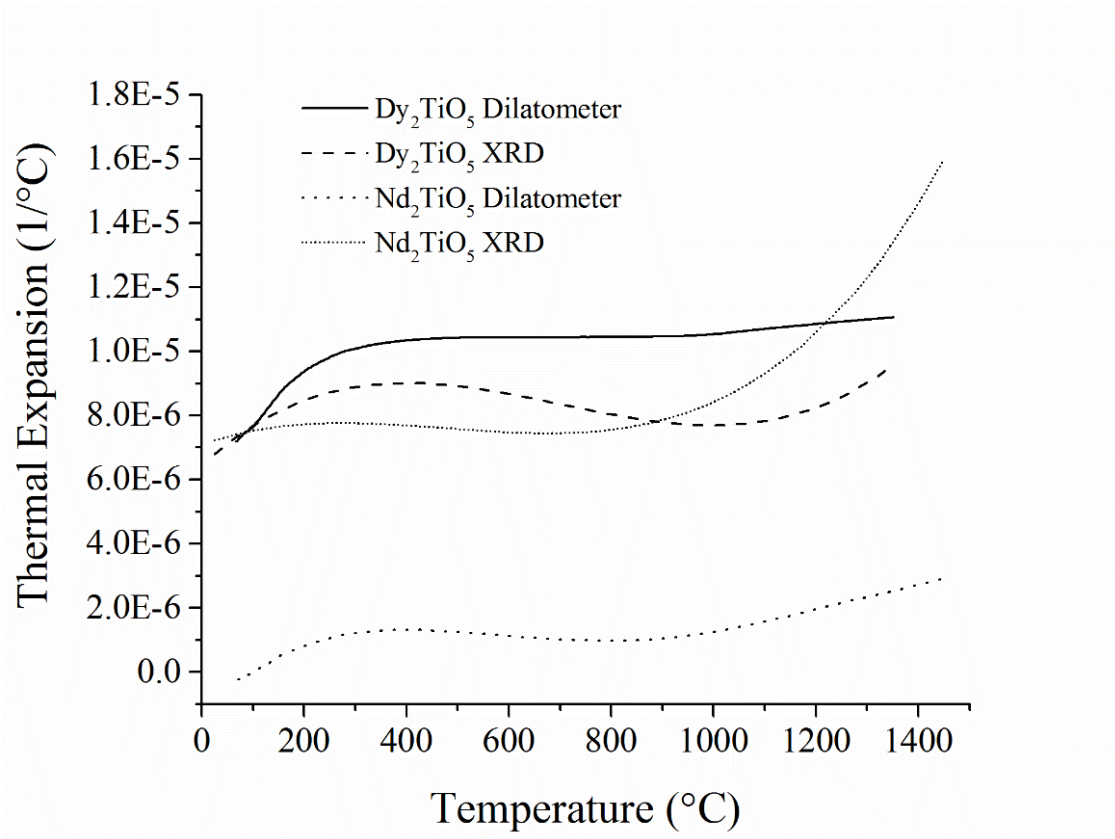


Figure 67. A comparison of the linear thermal expansion measured via dilatometry versus X-ray diffraction for orthorhombic Dy₂TiO₅ and Nd₂TiO₅.

When interpreting the mechanism behind the thermal expansion behavior in the Ln₂TiO₅ system, it is best to start at the end result. Upon heating, Y₂TiO₅, Dy₂TiO₅, and Gd₂TiO₅ will transform from the orthorhombic phase to the hexagonal phase at approximately 1300 °C, 1370 °C, and 1700 °C, respectively. This is to say that, as the size of the rare-earth cation increases, the transformation temperature also increases. In contrast, as the size of the rare-earth cation increases, the melting temperature decreases. In other words, although the orthorhombic forms of La-Eu did not transform into the hexagonal phase, it seems likely that they would have done so if they had not melted beforehand.

In both the hexagonal and orthorhombic phases the Ti cation is five-fold coordinated with surrounding oxygen atoms, forming a trigonal bipyramidal structure. In the hexagonal phase this structure is ideal, meaning the distances between the equatorial oxygen atoms and the central titanium atom are the same, as well as those between the central titanium atom and the axial oxygen atoms. The angles formed between the atoms are also ideal, where the angle formed between two oxygen atoms in the equatorial plane with the central titanium atom are all 120° , and the angle between the axial oxygen atoms with the central atom at 180° . The trigonal bipyramidal structure in the orthorhombic phase, on the other hand, is far from ideal and is highly distorted. In the orthorhombic phase the O1, O4, and O5 atoms form the triangular base of the trigonal bipyramidal structure, with the O3 atoms found in the axial positions. For clarity, Figure 68 describes this distortion for both the orthorhombic and the hexagonal phase. Due to the symmetry constraints of the space group, all of the atoms are found to reside in either a 0.25 or 0.75 y-position. Though the O1, O4, O5, and Ti atoms reside in the same plane, their movements are not restricted in the other two directions. They must, however, maintain an average angle between them of 120° .

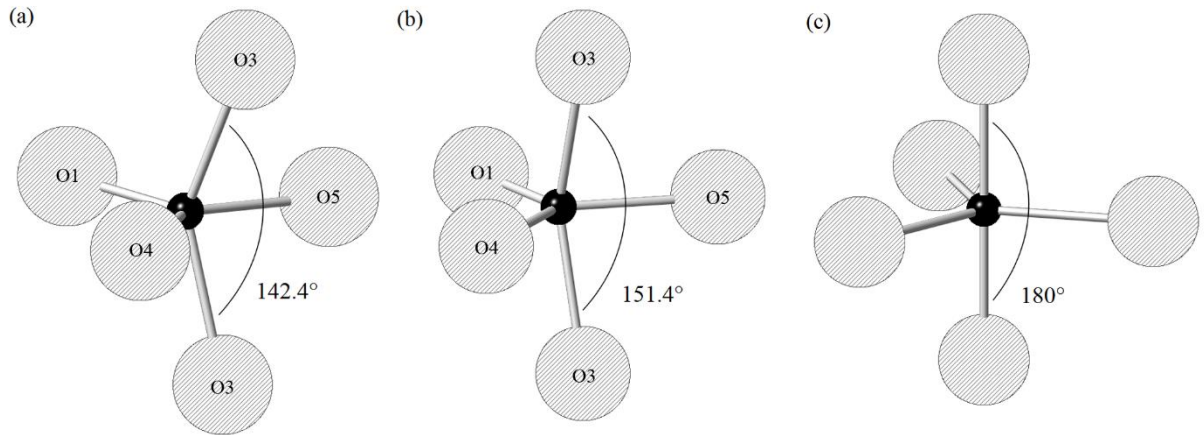


Figure 68. Trigonal bipyramidal structure at (a) room temperature, (b) 1310 °C, and (c) for the hexagonal phase.

At room temperature, there is a considerable amount of strain on the trigonal bipyramidal structure, and the struggle to become less distorted is the driving mechanism behind the interesting expansion behavior in the c-axis. The O1 and O5 anions are unequally bonded to the Y and Ti cations on one side, thereby manifesting a larger than expected angle between the O1-Ti and O5-Ti bonds with respect to the others in the equatorial plane as described in Figure 69 (a-b). In addition, the two O3 anions that make up the axial direction are also attracted to one side of the Ti cation to be nearer to the Y cation to negate charge effects. As the temperature is increased, the overall volume of the cell increases as well, lengthening bonds and allowing more and more free movement of the atoms. Relative to the a-axis, the O3 and O1 atoms would like to switch positions but are prevented from doing so as the energy barrier for two negatively charged anions to slide past one another is too large. Once the overall volume of the cell is sufficiently large enough, however, the O3 and O1 atoms quickly slide past each other and relax the structure. This behavior is exemplified in Figure 69(a), where a noticeable shift in bond lengths

and angles occurs after the transition of the c-axis from expanding to contracting for Y_2TiO_5 . Since neutron diffraction is more sensitive to oxygen atoms, a similar analysis was performed on Nd_2TiO_5 . Similar to Y_2TiO_5 , Nd_2TiO_5 also showed a significant structural change in bond lengths before and after the expanding/contracting transition in the c-axis. This data is illustrated in Figure 69(b). These same phenomena are seen across the lanthanide series; as cation size decreases so do the initial volume, and consequently the temperature where sufficient space is available for a shift of the O3 and O1 atoms to occur is pushed higher.

Additional analysis of the thermal expansion behavior further points to a shift from an orthorhombic cell to a hexagonal one. In an orthorhombic cell, the components of the thermal expansion tensor (α_{11} , α_{22} , and α_{33}) are independent of each other. Upon heating, two of the components, α_{11} and α_{22} , begin to converge to a similar number as described in Table 25. This convergence of two of the components is indicative of the orthorhombic to hexagonal phase transformation because only two independent components of the thermal expansion tensor are needed to describe the hexagonal system, α_{11} and α_{33} as $\alpha_{11} = \alpha_{22}$. This change is further illustrated in Figure 70, which shows the thermal expansion quadric surface at room temperature and near the transition for Y_2TiO_5 . The donut shape in the xy-plane is a result of having equivalent values for α_{11} and α_{22} , which is typical for hexagonal systems.

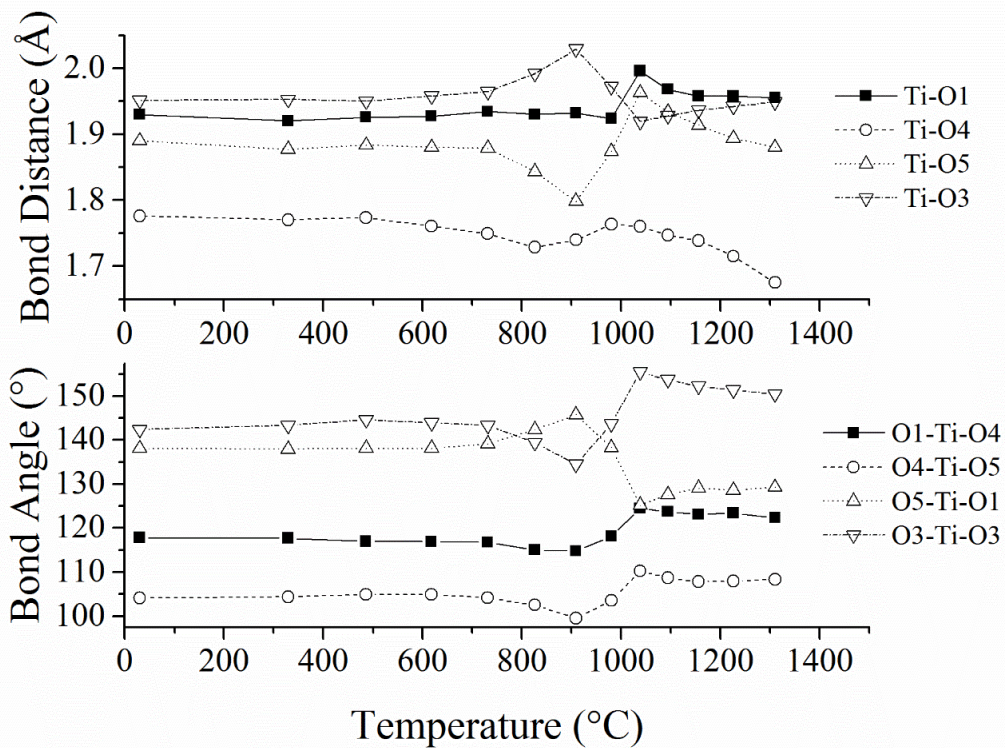


Figure 69(a). Bond lengths and angles as a function of temperature for Y_2TiO_5 collected using X-ray diffraction. Error bars are smaller than data points.

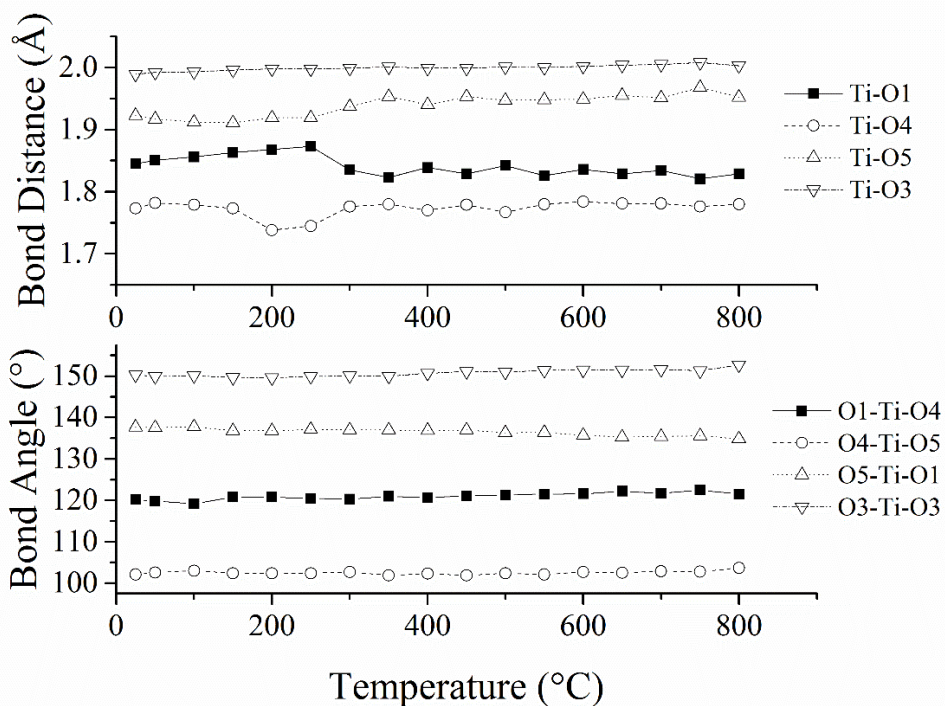


Figure 69(b). Bond lengths and angles as a function of temperature for Nd_2TiO_5 collected using neutron diffraction. Error bars are smaller than data points.

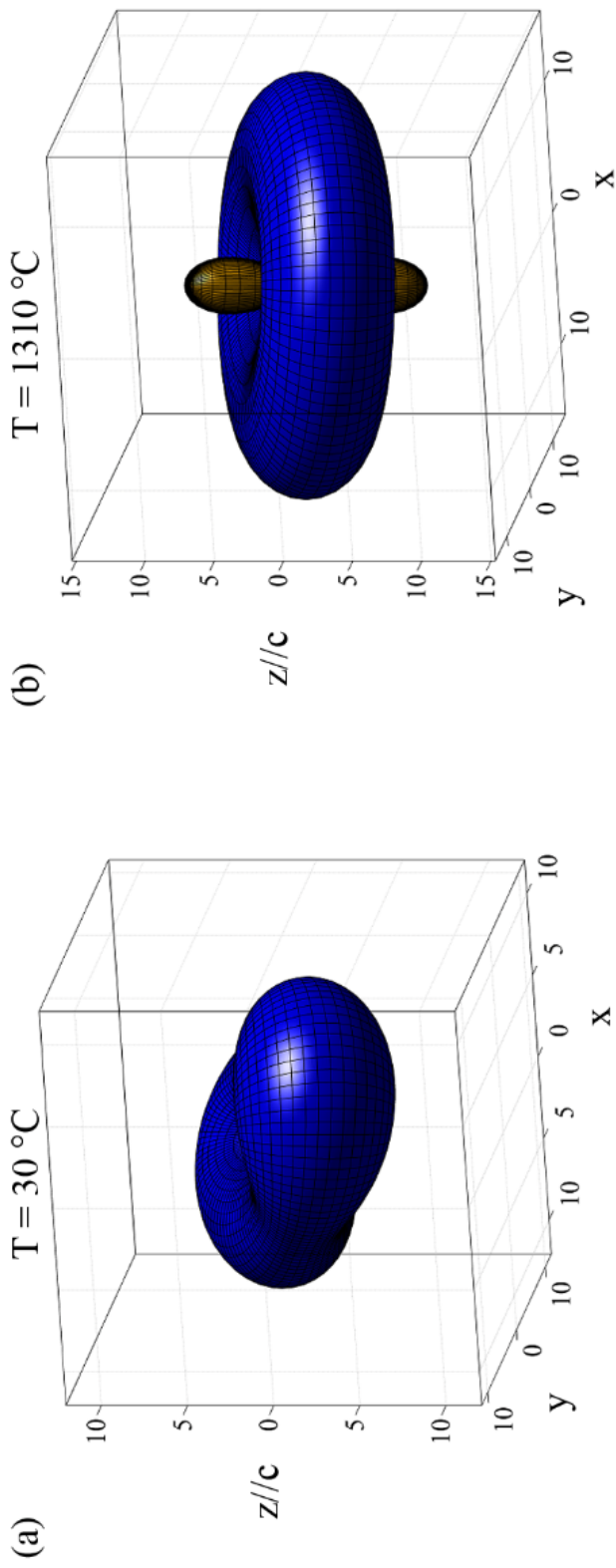


Figure 70. Quadric surface describing the thermal expansion in three-dimensions at (a) room temperature and (b) 1310 °C. Each axis is scaled by 10^{-6} ($1/^{\circ}\text{C}$).

5.2.3 Conclusions

The characterization of the thermal expansion in this materials system and comparison with studies performed in different atmospheric conditions is important for their use as engineered materials with applications in high temperature environments. It is evident that the atmosphere in which these experiments were carried out can have a significant impact on the observed thermal expansion behavior.

Unlike similar studies conducted in an argon atmosphere, the thermal expansion was found to have a very different behavior for the c-axis in which the lattice parameter increased until reaching a maximum, and then subsequently decreased as a function of temperature. This phenomenon was attributed to the inclination of this crystal system to become more hexagonal-like before the actual transformation took place or the material melted. The driving mechanism behind this was ascribed to a highly strained trigonal bipyramidal structure in the cell wanting to become more ideal, as is the case in the hexagonal phase. This shift from a strained to an ideal structure was hindered by nearby atoms preventing free atomic movement by repulsion between cations trying to pass each other. As the volume of the cell expanded the barrier for atoms in the trigonal bipyramidal structure to slide past nearby atoms was decreased and the structure could be relaxed. This was supported by a trend with the relative size of the rare-earth cation. Rare-earth cations having a relatively larger size, resulting in a larger cell volume, exhibited a major shift in the relaxation of the trigonal bipyramidal structure at a lower temperature as opposed to cells with smaller rare-earth cations.

5.3 Thermal Expansion in the Hexagonal Phase

5.3.1 Results

Dy₂TiO₅

As described in Chapter 4, powder of Dy₂TiO₅ was mounted in a sapphire capillary and placed in the center of the quadrupole lamp furnace in alignment with the incident synchrotron X-ray radiation. An X-ray diffraction pattern was collected at each temperature step from 1425 °C up to approximately 1650 °C in air. Using the programs GSAS and EXPGUI, the X-ray diffraction patterns were refined using the Rietveld method and the values for the lattice parameters, hkl, and corresponding d-spacings were extracted from the refined data. The lattice parameters as a function of temperature are plotted in Figures 71 and 72 and listed in Table 26.

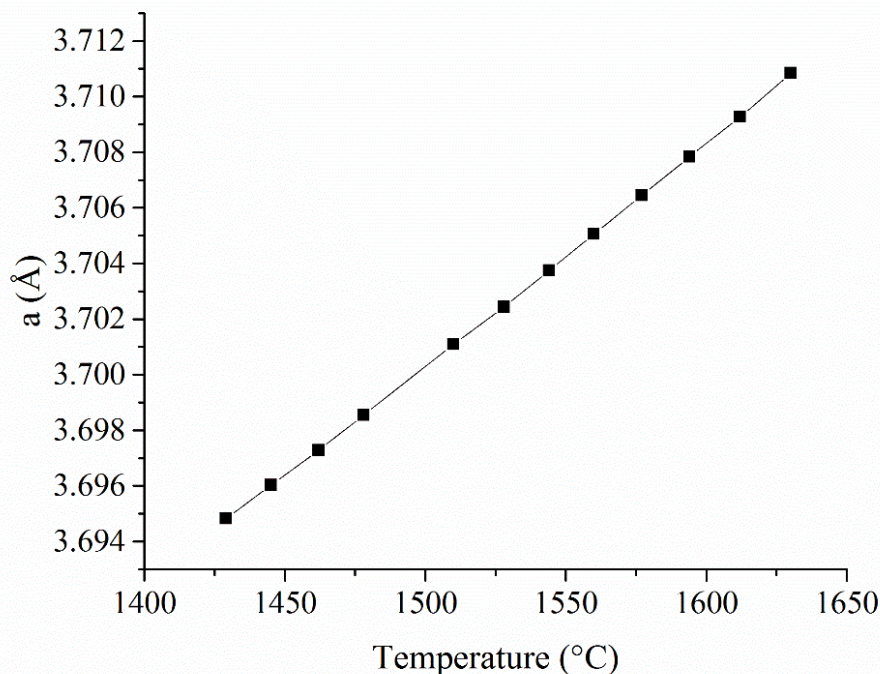


Figure 71. The lattice parameter for the a-axis of hexagonal Dy₂TiO₅ in the hexagonal phase as a function of temperature.

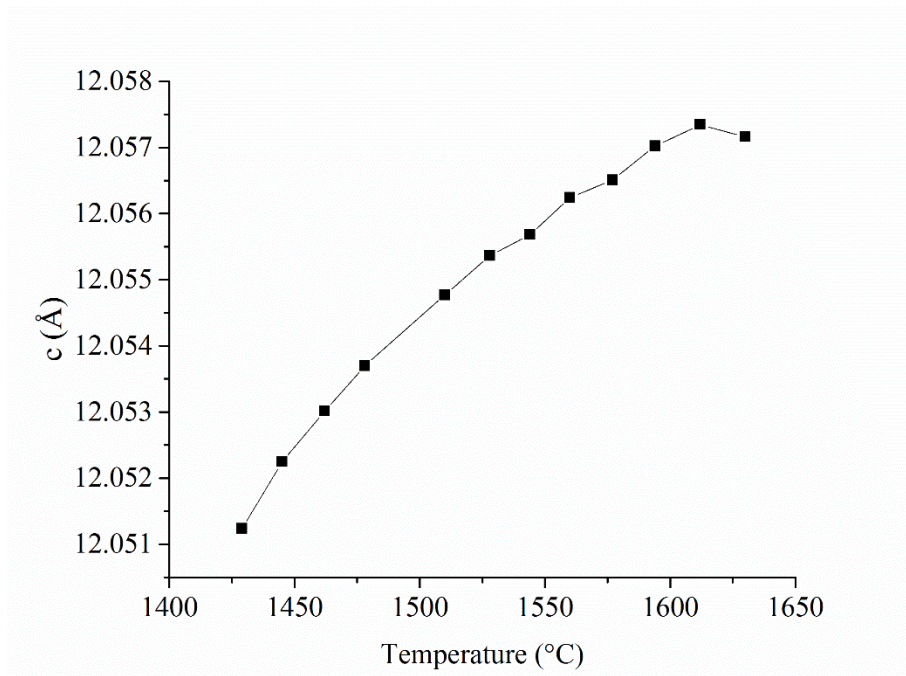


Figure 72. The lattice parameter for the c-axis of hexagonal Dy₂TiO₅ in the hexagonal phase as a function of temperature.

Table 26. The lattice parameters and volume for Dy₂TiO₅ in the hexagonal phase as a function of the measured temperature.

Temperature (°C)(±6)	a (Å)	c (Å)	Volume (Å ³)
1429	3.69484(2)	12.0512(1)	142.479
1445	3.69602(2)	12.0522(1)	142.583
1462	3.69728(2)	12.0530(1)	142.689
1478	3.69855(2)	12.0537(1)	142.794
1510	3.70109(2)	12.0547(1)	143.004
1528	3.70244(2)	12.0553(1)	143.115
1544	3.70375(2)	12.0556(1)	143.220
1560	3.70506(2)	12.0562(1)	143.328
1577	3.70644(2)	12.0565(1)	143.438
1594	3.70783(2)	12.0570(1)	143.5526
1612	3.70926(2)	12.0573(1)	143.6671
1630	3.71084(2)	12.0571(1)	143.7873
1649	3.71222(2)	12.0540(1)	143.8576

In addition to the determination of the lattice parameters, a CTEAS analysis was performed on the hkl listings and corresponding d-spacings as a function of temperature using a second-order polynomial fit. The results of the CTEAS analysis of the appropriate temperature range is depicted in Figure 73 and listed in Table 27.

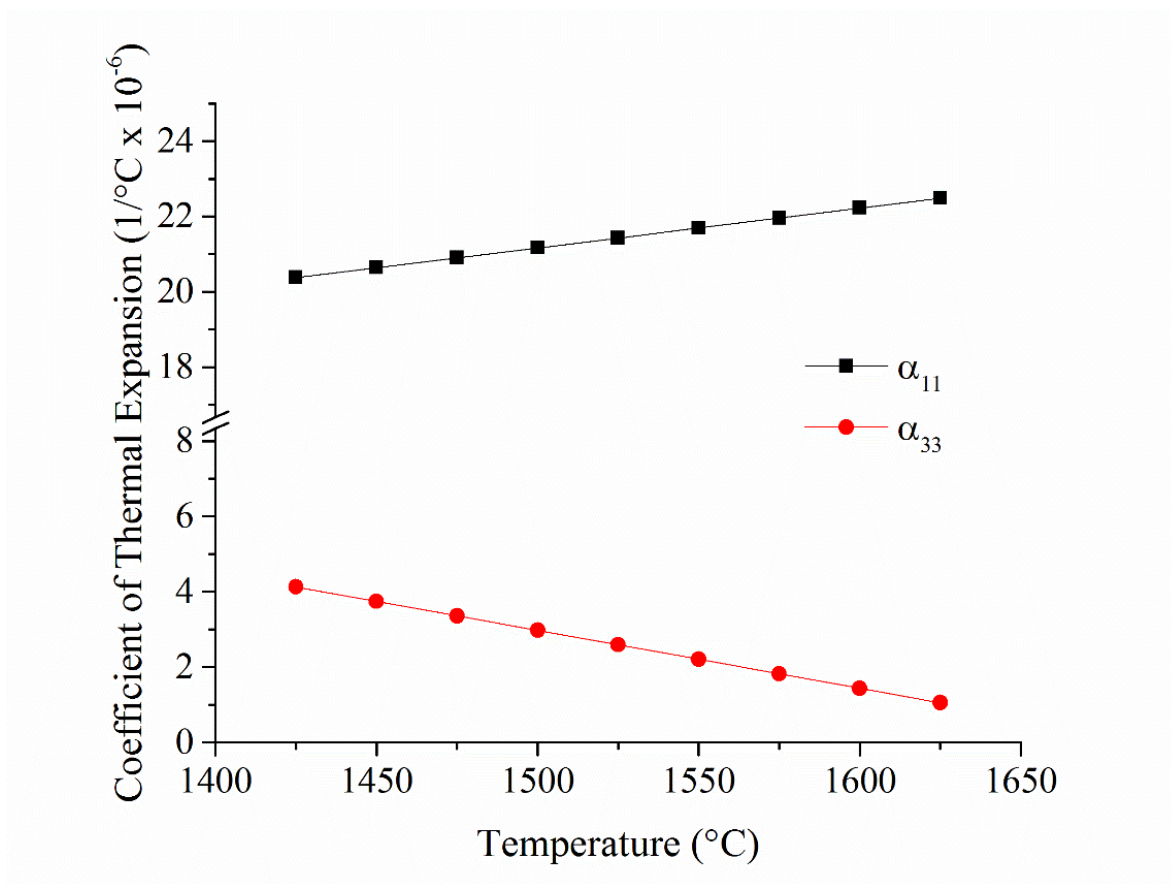


Figure 73. The coefficients of thermal expansion for Dy_2TiO_5 in the hexagonal phase as a function of temperature.

Table 27. The coefficients of thermal expansion for Dy₂TiO₅ in the hexagonal phase as a function of extrapolated temperature.

Temperature (°C)	α_{11}	α_{22}	Error
1425	20.38	4.13	188.68
1450	20.64	3.74	345.88
1475	20.90	3.36	188.64
1500	21.17	2.97	188.62
1525	21.43	2.59	4146.72
1550	21.69	2.21	4146.24
1575	21.96	1.82	0.03
1600	22.22	1.44	9119.55
1625	22.49	1.05	439.28

5.3.2 Discussion and Mechanism of Thermal Expansion

All of the atoms present in the hexagonal phase are found on special positions. Each atom, with the exception of the O1 anion on the $4f$ Wyckoff position, is fixed at its relative location in the cell. The $4f$ Wyckoff position is fixed in x and y at $1/3$ and $2/3$, respectively, but is free to change in z . As a function of temperature, the overall cell expands in each direction, but as indicated by the decreasing thermal expansion value for α_{33} , it is increasing at a decreasing rate. The overall expansion of the cell is related to the increase in interatomic distance with temperature which is related to the Lennard-Jones potential described in Chapter 5.1.2. The rate of decrease is caused by the movement of the O1 anion towards the Ti cation at the center of the trigonal bipyramidal structure centered on the $2c$ Wyckoff position. The combination of an increase in the overall cell with a minor contraction caused by the movement of the O1 anion towards the Ti cation results in a decreased expansion rate along the c -direction. This behavior is illustrated in Figure 74.

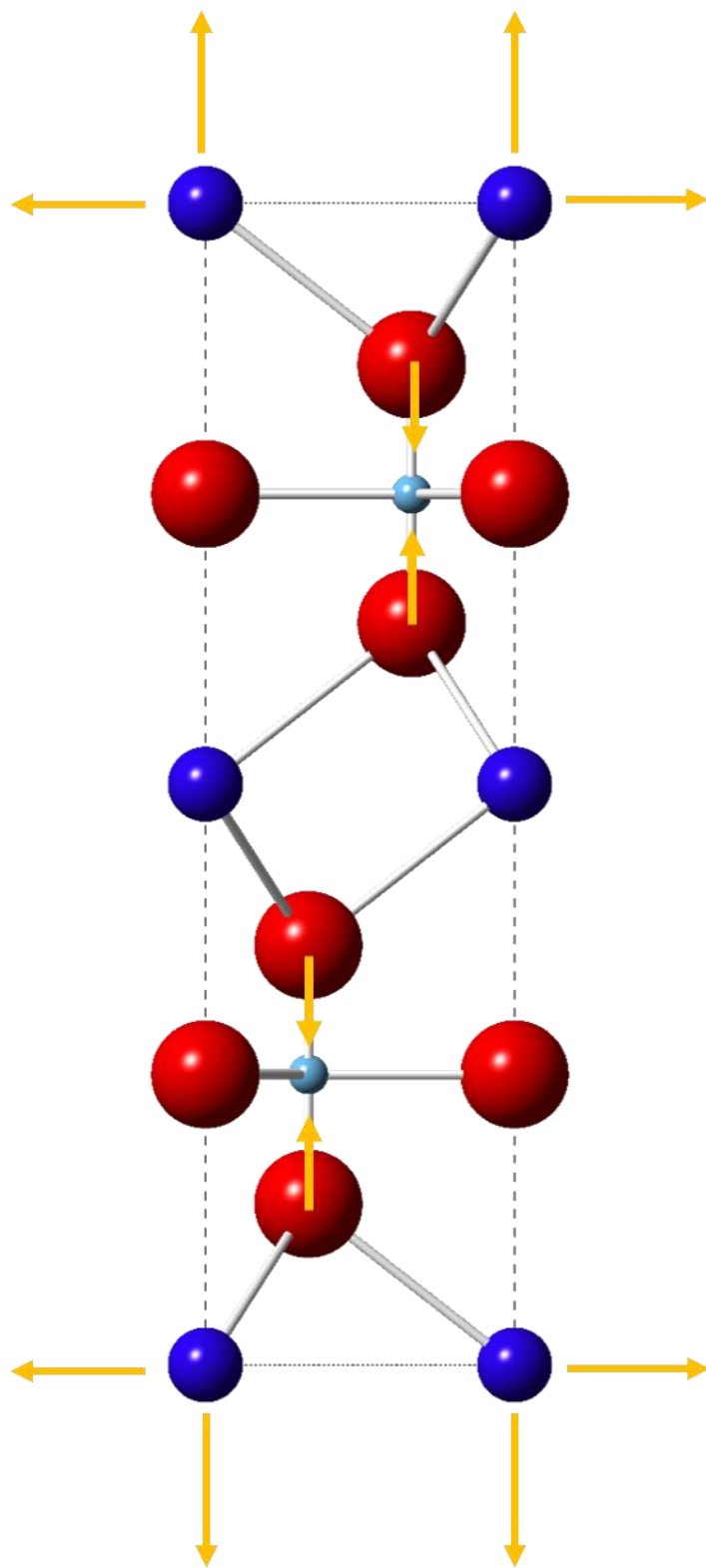


Figure 74. An illustration of the mechanism of thermal expansion in the hexagonal phase. The dark blue atoms are Dy, the light blue Ti, and the red atoms are the oxygen anions. Yellow arrows indicate relative movement of cell and atoms.

5.3.3 Conclusions

The lattice parameters in the hexagonal phase increase as a function of temperature. Although there is an increase in the lattice parameters, the analysis of the thermal expansion coefficients reveals that the hexagonal cell is expanding at a decreasing rate along the c-axis. The expansion along the a- and b-axes is related to an increase in interatomic spacing between atoms, which is expected with an increase in thermal energy. The decreasing rate along the c-axis is attributed to a single oxygen atom which may move in its relative atomic position with regard to the overall cell. This oxygen atom moves towards the Ti cation at the center of the trigonal bipyramidal structure which “pulls” both ends of the c-axis towards the center of the cell adding a retarding effect to the expansion of the c-axis, and thus, resulting in a decrease in the value of α_{33} .

CHAPTER 6

THE RELATIONSHIP BETWEEN THE ORTHORHOMBIC AND HEXAGONAL PHASES

6.1 The Relationship between the Orthorhombic and Hexagonal Phase

6.1.1 Results and Discussion

In order to better understand the relationship between the orthorhombic and hexagonal phases it may be worthwhile to inspect the thermal expansion behavior for clues.

Among the three members of the Ln_2TiO_5 family which can be found in the hexagonal phase at higher temperatures (Gd_2TiO_5 , Dy_2TiO_5 , and Y_2TiO_5), Dy_2TiO_5 was chosen for this investigation as it provided the largest temperature range in which the hexagonal phase can be observed (1380-1680 °C). The lattice parameters and volume of Dy_2TiO_5 as a function of the measured temperature are provided in Table 28 for both the orthorhombic and hexagonal phases. As previously described, the lattice parameters all initially increase in the orthorhombic phase till approximately 663 °C where the c-axis begins to contract. The lattice parameters in the hexagonal phase both increase with an increase in temperature and continue to do so until its transition to the high temperature cubic phase.

A CTEAS analysis was performed in terms of a second-order polynomial fit of each hkl and corresponding d-spacing for the hexagonal phase. As previously described, the hexagonal crystal system only requires two components of the thermal expansion tensor to be fully described (α_{11} and α_{22}). The results of the calculation for the thermal expansion tensor for the hexagonal phase are presented in Table 29 and illustrated in Figure 75 and 76 with thermal expansion coefficient values for the orthorhombic phase.

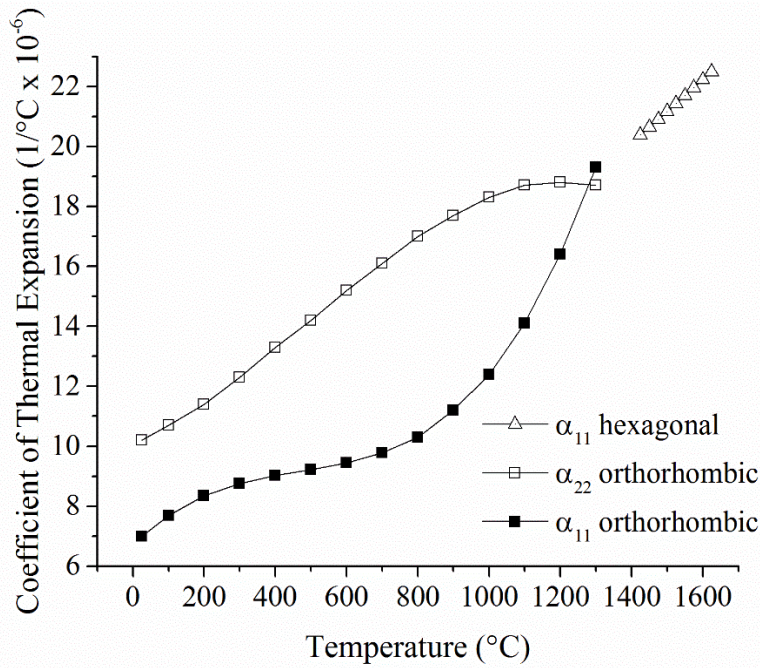


Figure 75. The combined coefficients of thermal expansion for the a- and b-axes in both the orthorhombic and hexagonal phases as a function of temperature in Dy_2TiO_5 .

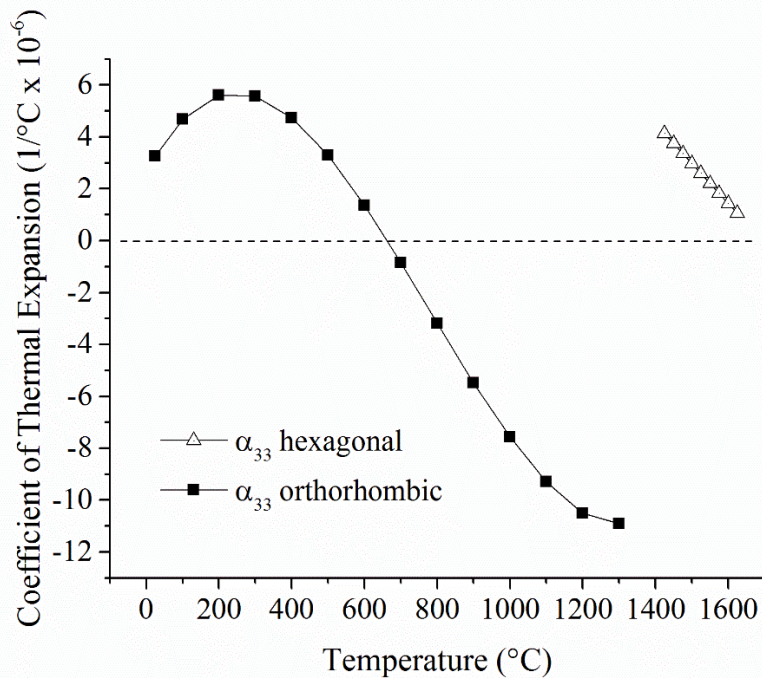


Figure 76. The coefficient of thermal expansion for the c-axis in both the orthorhombic and hexagonal phases as a function of temperature in Dy_2TiO_5 .

Table 28. Lattice parameters and volume as a function of the measured temperature.

Dy ₂ TiO ₅					
	Temperature (°C)	a (Å)	b (Å)	c (Å)	V (Å ³)
Orthorhombic	29	10.3663(1)	3.71667(4)	11.2388(1)	433.013
	304	10.3888(1)	3.72798(3)	11.2556(1)	435.923
	445	10.40253(9)	3.73509(3)	11.26210(9)	437.581
	571	10.41467(9)	3.74166(2)	11.26628(9)	439.026
	689	10.42652(8)	3.74830(2)	11.26799(9)	440.373
	792	10.43687(8)	3.75508(3)	11.2656(1)	441.515
	886	10.44768(8)	3.76121(2)	11.26174(8)	442.541
	973	10.45737(8)	3.76674(2)	11.25642(7)	443.393
	1049	10.46729(9)	3.77194(2)	11.24940(7)	444.149
	1121	10.47750(9)	3.77692(2)	11.24175(8)	444.866
	1189	10.4891(1)	3.78196(3)	11.23348(8)	445.629
	1254	10.5025(1)	3.78713(3)	11.22477(9)	446.458
	1350	10.5192(1)	3.79321(3)	11.21540(9)	447.515
Hexagonal	1429	3.69484(2)	3.69484(2)	12.0512(1)	142.480
	1445	3.69602(2)	3.69602(2)	12.0522(1)	142.583
	1462	3.69728(2)	3.69728(2)	12.0530(1)	142.689
	1478	3.69855(2)	3.69855(2)	12.0537(1)	142.795
	1510	3.70109(2)	3.70109(2)	12.0547(1)	143.004
	1528	3.70244(2)	3.70244(2)	12.0553(1)	143.116
	1544	3.70375(2)	3.70375(2)	12.0556(1)	143.221
	1560	3.70506(2)	3.70506(2)	12.0562(1)	143.329
	1577	3.70644(2)	3.70644(2)	12.0565(1)	143.439
	1594	3.70783(2)	3.70783(2)	12.0570(1)	143.553
	1612	3.70926(2)	3.70926(2)	12.0573(1)	143.667
	1630	3.71084(2)	3.71084(2)	12.0571(1)	143.787

Table 29. Coefficient of thermal expansion (CTE) tensor values for the orthorhombic and hexagonal phases as a function of the extrapolated temperature.

Dy ₂ TiO ₅				
	α_{11}	α_{22}	α_{33}	
Temperature (°C)	(x 10 ⁻⁶)			
Orthorhombic	25	6.99	10.20	3.25
	100	7.69	10.70	4.68
	200	8.35	11.40	5.61
	300	8.76	12.30	5.57
	400	9.02	13.30	4.74
	500	9.22	14.20	3.29
	600	9.45	15.20	1.37
	700	9.78	16.10	-0.85
	800	10.30	17.00	-3.18
	900	11.20	17.70	-5.48
	1000	12.40	18.30	-7.57
	1100	14.10	18.70	-9.29
	1200	16.40	18.80	-10.50
	1300	19.30	18.70	-10.90
Hexagonal	1425	20.38	20.38	4.13
	1450	20.64	20.64	3.74
	1475	20.90	20.90	3.36
	1500	21.17	21.17	2.97
	1525	21.43	21.43	2.59
	1550	21.69	21.69	2.21
	1575	21.96	21.96	1.82
	1600	22.22	22.22	1.44
	1625	22.49	22.49	1.05

There is no symmetry based group-subgroup relationship between the orthorhombic (*Pnma*) and the hexagonal (*P6₃/mmc*) phases. The transformation between the two is first-order and reconstructive in nature. This is confirmed by the presence of latent heat observed via DSC and by a fundamental comparison between the two crystallographic structures and symmetries.

Since the transformation is reconstructive, it is not possible to track the atomic movement of atoms as the transformation progresses due to the inherent lack of long range order. This makes the development of a crystallographic relationship between the two phases difficult. It is possible

to develop potential candidate pathways by finding similarities between the two structures just before and immediately after the transformation, but meaningless without supporting correlated experimental evidence.

As observed in several different systems with displacive transformations, the thermal expansion behavior, particularly around the transformation temperature, can provide insight into the crystallographic relationship between two phases.[31,109] Little information is found in the literature which employs thermal expansion in the same manner for reconstructive-type transformations (ones which involve the breaking and reforming of bonds coupled with diffusion). Logically though, in cases where few or minor changes would need to be made in the position of certain atoms to change one structure into another, it would be reasonable to correlate thermal expansion to a particular structural change. For example, a smooth transition in thermal expansion from one phase to another may suggest a close structural relationship between two phases along the corresponding axes. Conversely, a significant change in thermal expansion, such as a discontinuity, may suggest a significant change in structure along a different set of axes. This is not to say that a thermal expansion analysis in two different phases is a definitive indicator of how a reconstructive transformation may progress, but can be one piece of a puzzle, when looking at other evidence, to make a structural connection between two phases.

Figures 75 and 76 illustrate the change in the thermal expansion behavior in both the orthorhombic and hexagonal phases as a function of the extrapolated temperature. As described by Figure 75, α_{11} and α_{22} of the orthorhombic phase have different values at room temperature, approximately 6 and $10 \times 10^{-6}/^{\circ}\text{C}$, respectively. Upon heating, α_{11} and α_{22} converge to a similar value of $18 \times 10^{-6}/^{\circ}\text{C}$ just before the transition from orthorhombic to hexagonal phase. Just after the transformation, in the hexagonal phase, α_{11} is approximately $20 \times 10^{-6}/^{\circ}\text{C}$. It is apparent that

α_{11} and α_{22} of the orthorhombic phase and α_{11} of the hexagonal phase are potentially related when observing trends in the thermal expansion behavior, and consequently, the a- and b-axes of the orthorhombic phase and a-axis of the hexagonal are potentially related.

In comparison, the thermal expansion behavior in the c-axis, described by α_{33} , is illustrated in Figure 76 and listed in Table 29. The initial value of α_{33} in the orthorhombic phase is $3.25 \times 10^{-6} / ^\circ\text{C}$. As previously described in Chapter 5, this value initially increases with temperature. At approximately $663 \text{ }^\circ\text{C}$, the c-axis of Dy_2TiO_5 will begin to contract and continue to do so before the orthorhombic to hexagonal transformation. Just before the transformation the value of α_{33} in the orthorhombic phase is $-10.9 \times 10^{-6} / ^\circ\text{C}$, and just after in the hexagonal phase it is $4.13 \times 10^{-6} / ^\circ\text{C}$. Such a significant change, in the form of a discontinuity, in the coefficient of thermal expansion may be related to a significant structural change along the c-axis in the orthorhombic phase before the transformation to the hexagonal phase.

To further illustrate this behavior, Figure 77 shows the three-dimensional representation in Dy_2TiO_5 of thermal expansion as a quadric surface. Figure 77(a) and 77(b) show the thermal expansion in the orthorhombic phase, and Figure 77(c) for the hexagonal. The change in shape between Figure 77(a) and 77(b), as described in Chapter 5, is indicative of a shift in thermal expansion from an orthorhombic to hexagonal cell (the same general “donut” shape indicates the coefficients α_{11} and α_{22} are equal). Again, a significant change between Figures 77(b) and 77(c) is exhibited in the α_{33} direction, corresponding to the c-axis switching from a relatively large negative number to a smaller positive one (so small that it is hidden inside of the “donut” shape).

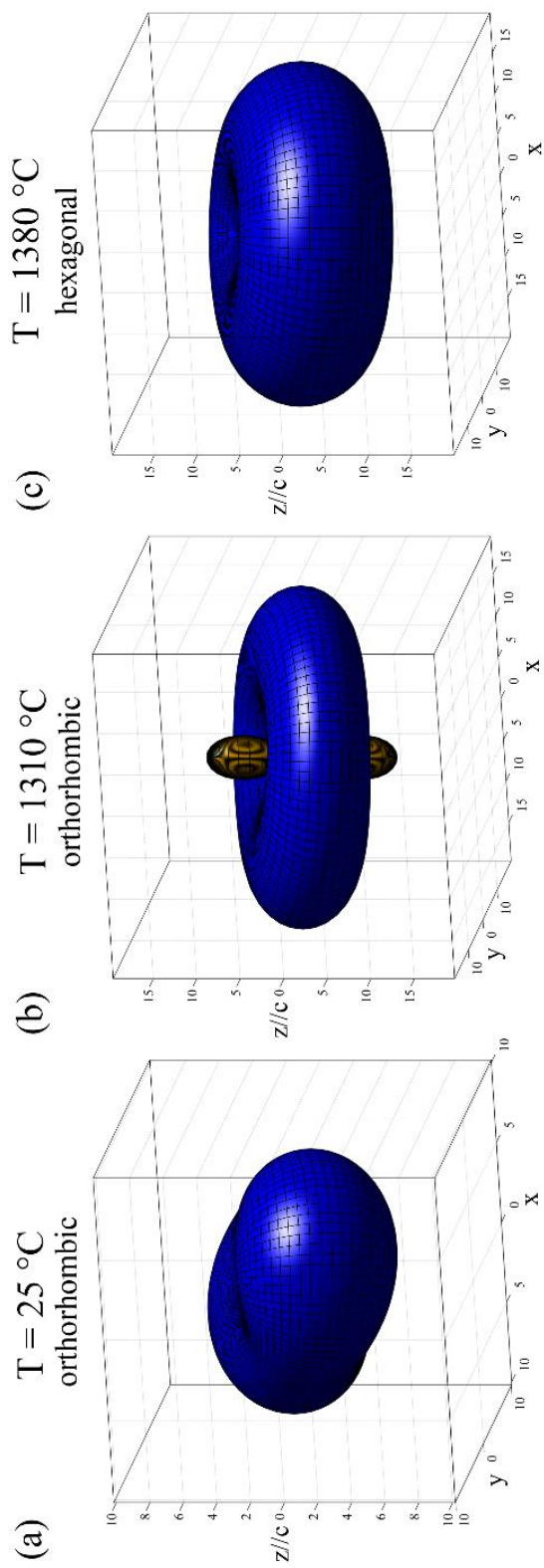


Figure 77. Quadric surface describing the thermal expansion in three-dimensions at (a) room temperature (orthorhombic), (b) $1310\text{ }^{\circ}\text{C}$ (orthorhombic), and (c) $1380\text{ }^{\circ}\text{C}$ (hexagonal). Each axis is scaled by 10^{-6} ($1/^{\circ}\text{C}$).

An additional clue which can aid in the analysis of this reconstructive transformation is how the volume changes between the two phases. Figure 78 plots the volume of both the orthorhombic and hexagonal cells as a function of temperature and is normalized by the number of formula units in each cell. In the region of coexistence, the hexagonal cell is found to be approximately 6.07% larger as compared to the orthorhombic cell, a relatively large value change compared to other transforming ceramic systems.

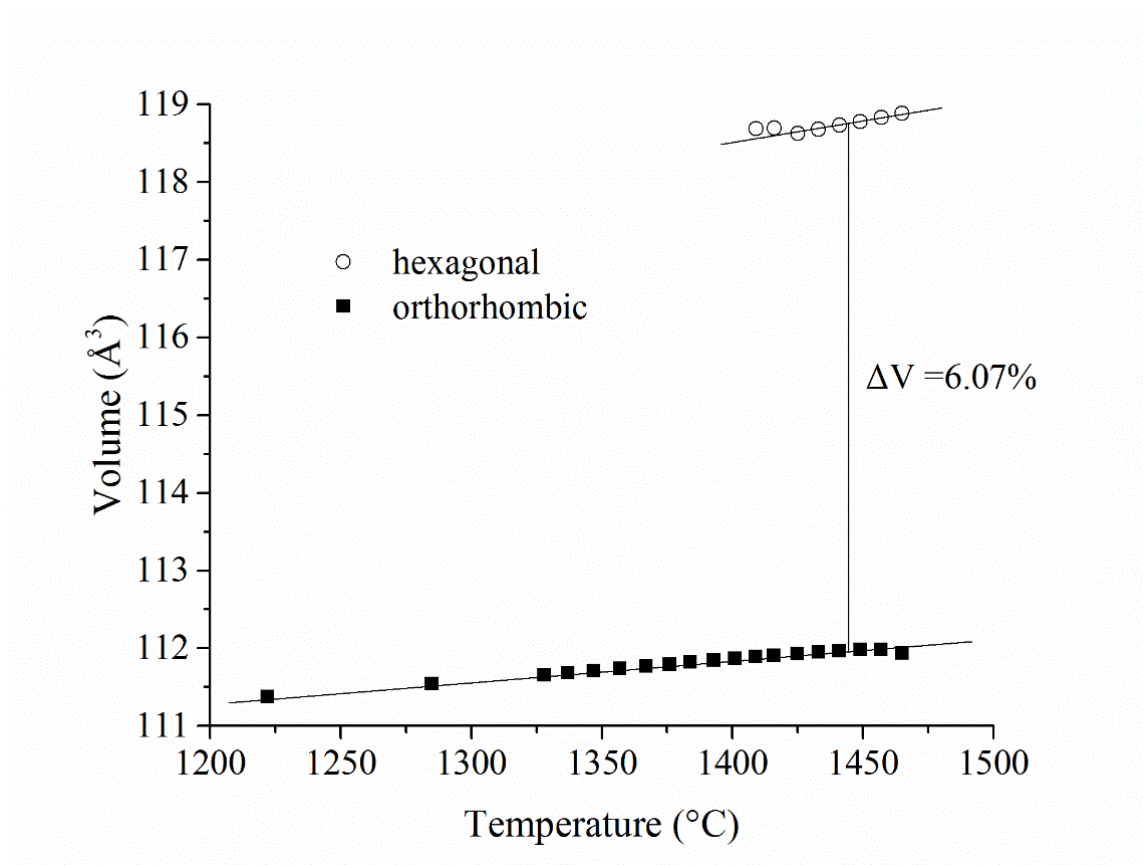


Figure 78. The normalized molar volume of the orthorhombic and hexagonal phases around the transformation temperature with its associated volume change.

Looking for a hexagonal cell, in the orthorhombic structure, which has similar lattice parameters, position of atoms, angle between atoms, and polyhedron, combined with knowledge related to

the lattice correspondence developed from the thermal expansion analysis and information on the volume change, it is only possible to find one potential solution. Figure 79 illustrates the closest approximation of the hexagonal unit which can be found in the orthorhombic cell just before its transformation.

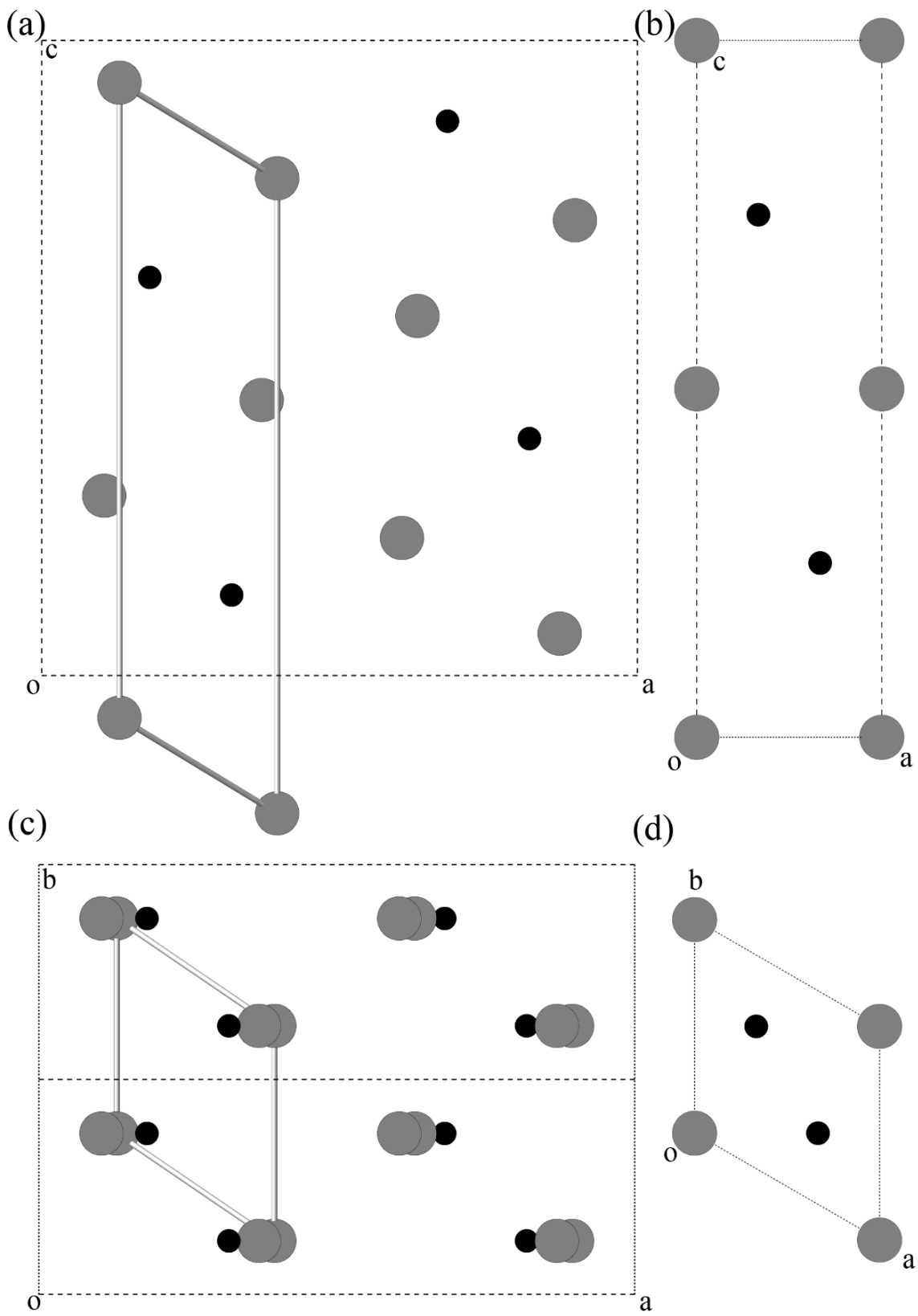


Figure 79. The proposed relationship between the orthorhombic and hexagonal phases in Dy_2TiO_5 . Oxygen anions removed for simplification.

This proposed hexagonal cell in the orthorhombic setting (hence referred to as the proposed cell) has several defining features which make this a promising candidate. Along the a- and b-axes of the proposed cell, similar lengths in lattice parameter are observed which correlate well with the hexagonal phase just after the transformation, 3.769 Å and 3.793 Å for a and b, respectively, in the proposed cell, and 3.695 Å in the hexagonal. In addition, the proposed angle γ of 120.215°, is very close to the constraint of 120° in a hexagonal cell. Along the c-axis this difference is larger, the proposed cell having a lattice parameter of 11.215 Å and the hexagonal cell just after the phase transformation having a lattice parameter of 12.051 Å. Furthermore, an α angle of 63.373° is very different from the 90° needed for a hexagonal cell. The β angle is 90° in both the proposed and hexagonal cells.

Moreover, from the experimentally determined volumetric information, the proposed cell should not only have a similar volume to the hexagonal cell but should also represent a significant positive expansion of the orthorhombic cell. The proposed cell has a volume of 118.4 Å³. The hexagonal cell in the orthorhombic setting, if ideal (a and b are equal and $\gamma = 120^\circ$), would have a volume of 137.9 Å³. The difference between the two is approximately 16%, a reasonable value in comparison to the expected expansion of 6.07% determined experimentally, considering the positive nature of both and the overall diffusion and relaxation of atoms which still must occur.

Considering the above, paired with information regarding the thermal expansion behavior and volume expansion, the proposed cell is a reasonable choice. To summarize, the “continuity” of α_{11} and α_{22} between the orthorhombic and hexagonal phases suggests only minor changes would need to occur along the a- and b-axes. Very similar lattice parameters are observed along these same directions in both the proposed and hexagonal cell. In addition, α_{33} has a large discontinuity between the orthorhombic and hexagonal cells suggesting a significant change in structure.

Along the c-axis a large difference in lattice parameters is observed between the proposed and hexagonal cells in agreement to what is expected. Finally, the volume change between the proposed cell and that of the ideal cell must be a large positive number to be consistent with experimental observations. The proposed cell meets this requirement.

6.1.2 Conclusion

There is no group-subgroup relationship between the orthorhombic and hexagonal phases making the development of a structural relationship difficult. Utilizing information regarding the thermal expansion behavior, structural form (i.e. lattice parameters, angles, polyhedra, etc.), and volume it is possible to develop a candidate relationship between the two dissimilar phases. This candidate, the proposed hexagonal cell in the orthorhombic setting, is illustrated in Figure 79, and is the best approximation with regard to experimental evidence and logical associations.

CHAPTER 7

PHASE TRANSFORMATION KINETICS BETWEEN THE ORTHORHOMBIC AND HEXAGONAL PHASES

7.1 Phase Transformations Kinetics

7.1.1 Results and Discussion

Differential scanning calorimetry (DSC) has been a popular method for the study of phase transformation kinetics. Chapter 4 describes the process by which DSC works. Two experimental methods may be employed to collect relevant data, these being isochronal (constant heating rate) and isothermal (constant temperature) experiments. The latent heat evolved during a phase transformation generally is measured as a symmetric Gaussian peak. By determining the partial area underneath the curve as a function of time, with the appropriately applied background function, it is possible to describe the fraction of phase transformed with increasing time or temperature. The fraction of phase transformed between the orthorhombic and hexagonal phases during isochronal experiments under different heating conditions is provided in Figure 80 below. The sigmoidal shape of the curve is typical for these types of experiments.

The relationship observed in the data is relatively straightforward. The completion of the phase transformation occurs at lower temperatures for experiments with slower heating rates. Although the heating rate is slow, it spends more time above the transformation temperature with minimal rate increases, which shifts the curve to lower temperatures.

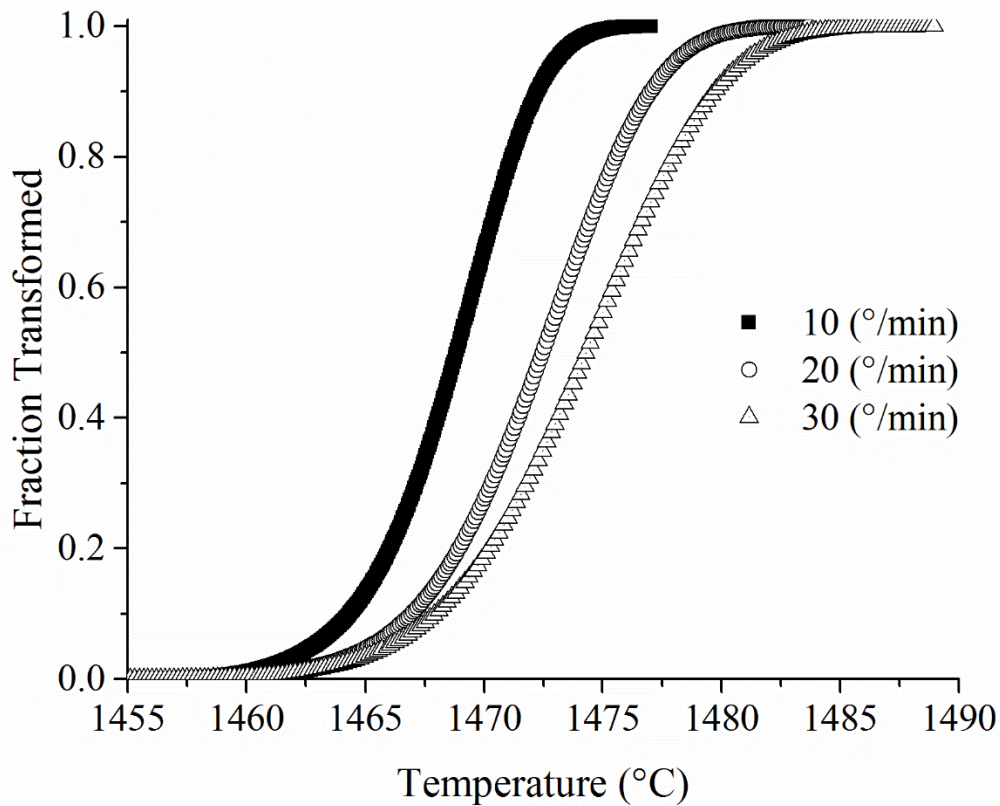


Figure 80. The fraction of the orthorhombic phase transformed to hexagonal at different heating rate for an isochronal experiment.

Although the data is “textbook”, there are several problems which arise during the analysis of the data. A simple Kissinger analysis of the data, wherein the slope of the line multiplied by Boltzmann’s constant which best fits the data points, can reveal the activation energy for the transformation. Figure 81 illustrates this analysis method.

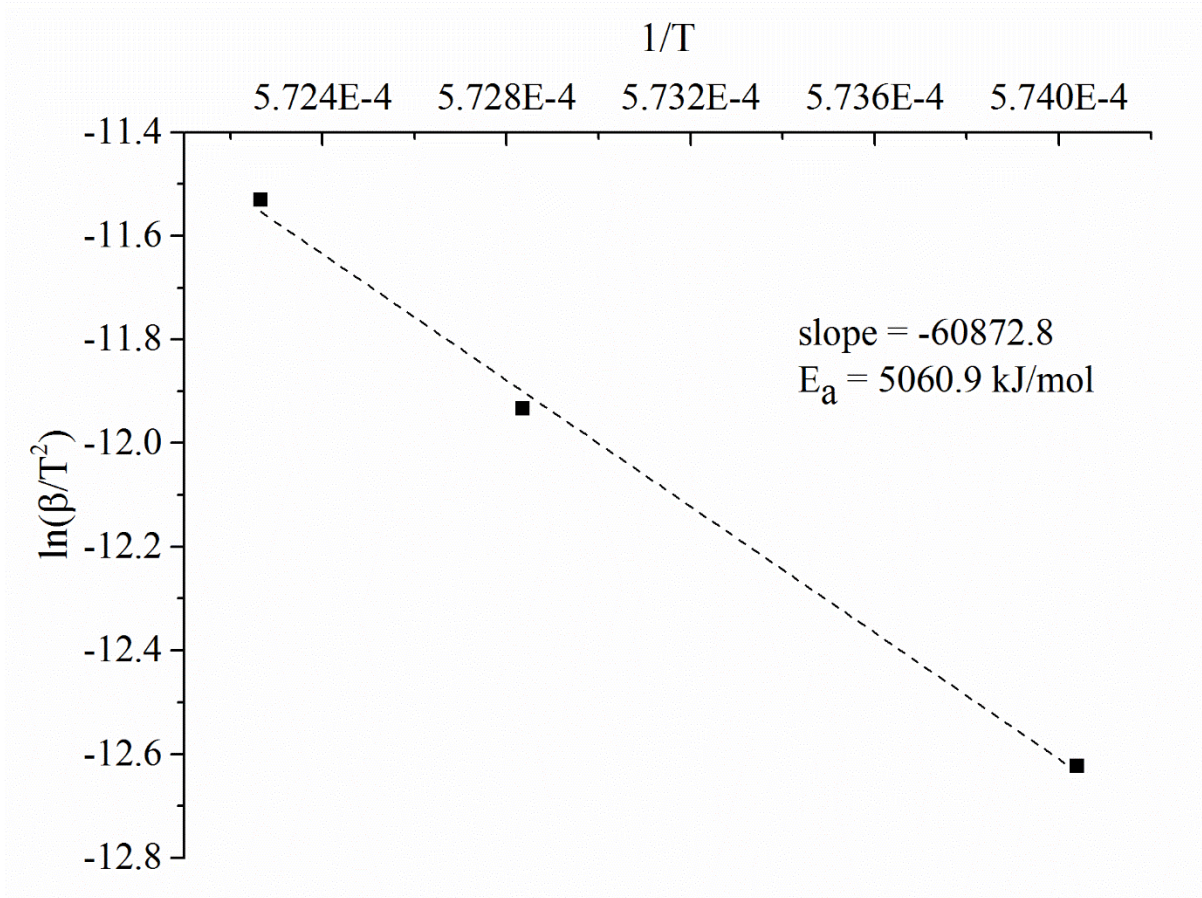


Figure 81. A Kissinger analysis of isochronal data to determine the activation energy of transformation.

The calculated activation energy from the analysis is 5060.9 kJ/mol. Most activation energies for reconstructive transformations in ceramic system fall between 50-800 kJ/mol. In comparison the activation energy found using DSC is far above an expected value by an order of magnitude.

Baumann, Leineweber, and Mittenmeijer discuss the failure of this method in describing the kinetic behavior in a transforming system from the standpoint of the driving force, particularly at high temperatures.[110] Just above the transformation the driving force for nucleation is weak. This is attributed to the critical particle size of the new phase which must exist for it to be stable

and grow uninhibited (not transform back to its original phase). This concept is described in Figure 82. With minimal overheating, it is difficult to nucleate a new phase due to this factor, particularly when the transformation process is complex, as is the case for the orthorhombic to hexagonal transformation in Dy_2TiO_5 . In order to solve this this problem a significant amount of overheating should be used to avoid the driving force issue. Baumann provides two examples in which a phase transformation was probed, the first around the transition temperature and the other far away. After applying a Kissinger analysis on the data near the transformation temperature the activation energy was found to be 12600 kJ/mol, a nonsensical value, see Figure 82. When performing the same experiment further away from the transformation temperature the activation energy was found to be 161 kJ/mol, a much more reasonable value, see Figure 84.

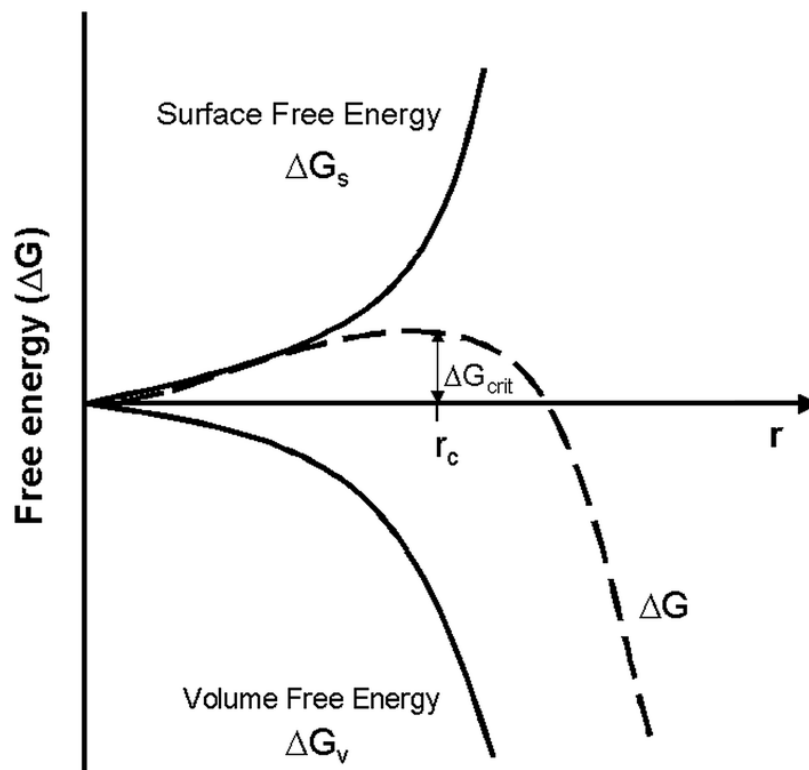


Figure 82. Free energy and radius of particle describing a critical size needed in order for a nucleated particle to be stabilized in the new phase and begin to grow.[111]

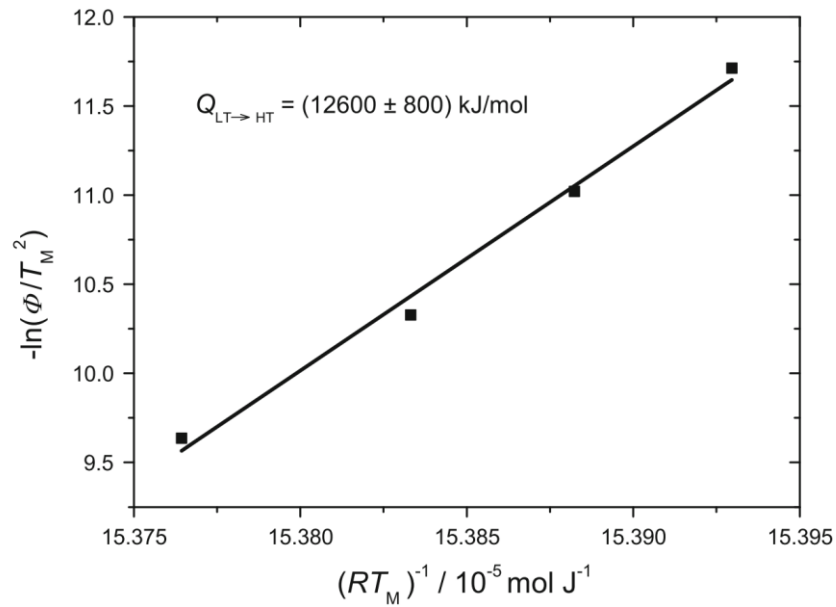


Figure 83. A Kissinger analysis performed on data from a transforming sample near the temperature of transformation.

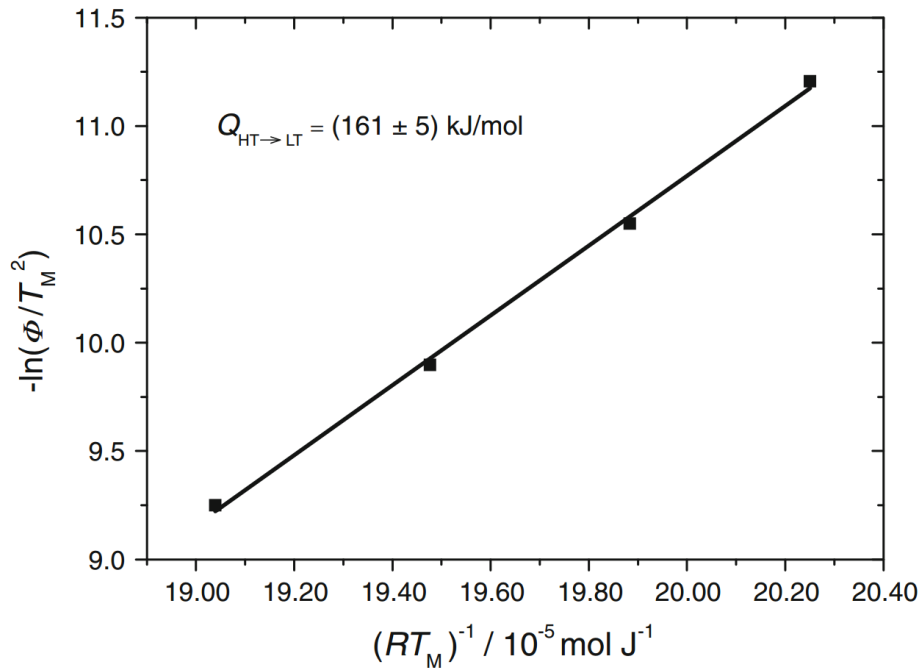


Figure 84. A Kissinger analysis performed on data from a transforming sample far the temperature of transformation.

Isoconversional analysis, pioneered by Vyazovkin, can be used to further illustrate the problem with the driving force.[112-116] The Isoconversional method is a model-free technique used to analyze the change in activation energy as a function of the fraction of the phase transformed with time. A flat line as a function of fraction transformed would suggest the activation energy for nucleation is equal to that of growth. An increasing line suggests that growth is more difficult than nucleation, and a decreasing line suggesting nucleation is more difficult than growth. This method was applied to the same data on Dy_2TiO_5 using DSC for both isothermal and isochronal data, the result of which is provided in Figures 85 and 86. Although both the isothermal and isochronal data result in different values for the activation energy (also nonsensical), the trend in slope is the same. Since both lines decrease as a function of temperature it suggests that the nucleation event is the limiting factor in the transformation, supporting the result from the Kissinger analysis.

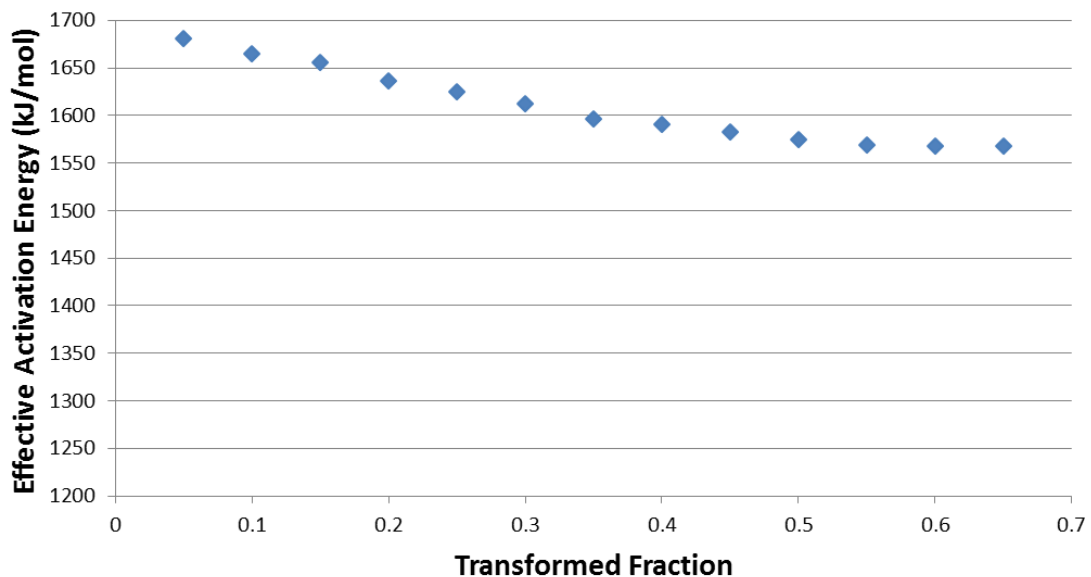


Figure 85. Isoconversional analysis performed on isothermal data from Dy_2TiO_5 using DSC to calculate the effective activation energy as a function of phase fraction transformed.

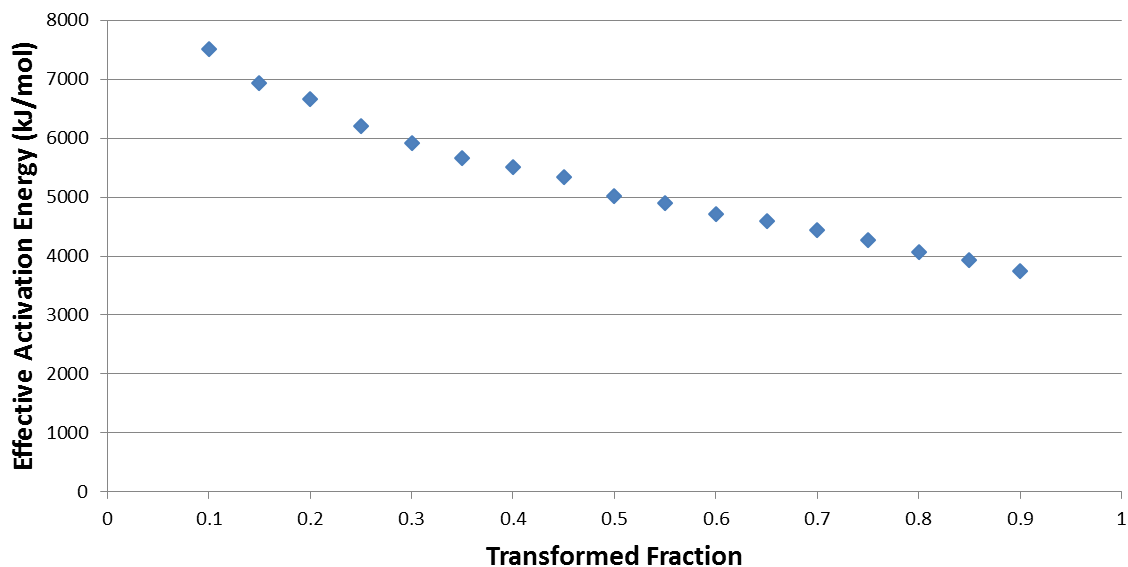


Figure 86. Isoconversional analysis performed on isochronal data from Dy_2TiO_5 using DSC to calculate the effective activation energy as a function of phase fraction transformed.

As Baumann describes, the best way to avoid the problem with the driving force is to overheat the sample. By overheating, sufficient energy is provided that the barrier to forming a particle of sufficient size is no longer a factor. Unfortunately, the DSC experimental setup in the Kriven research lab is not able to overheat to the degree needed in a short enough time to achieve this. Instead, the quadrupole lamp furnace, which has a very high rate of heating (several hundred degrees per second), can be used to overheat the sample in a short time frame.

Kinetic experiments also require the quick collection of diffraction patterns in order to have sufficient time resolution in the data. The Pilatus 100k detector mounted at the beamline at the Advanced Photon Source can cover a range of approximately $4^\circ 2\theta$ and can be refreshed at a rate of 1000 Hz. Though the refresh rate on the detector is large, enough intensity must be collected

from the sample that the time resolution of the experiment is on the order of seconds (sufficient for this study).

Raw images collected from a sample transforming from the orthorhombic to hexagonal phase as a function of time from the Pilatus 100k detector are provided in Figure 87. Figure 87 depicts the partial rings associated with a powder sample. As a function of time the main partial rings associated with the orthorhombic phase decrease in intensity while the partial rings belonging to the hexagonal phase increase. As observed in the images of Figure 87, it would seem that a slight amount of texturing may be occurring in the sample during the phase transformation process (seen as an unequal distribution of intensity along a powder diffraction ring). A relationship between the amount of texturing for a particular plane and the way in which the transformation progresses could be potentially made, but would require the observation of the total ring. For future work, this experiment could potentially be redone at beamline 17BM at the Advanced Photon Source which is equipped with a detector able to collect the entire powder ring.

Summation of each powder ring, along the same value of Q , results in a traditional 1D diffraction pattern. Each pattern can be stacked as a function of time, the result of which is illustrated in Figure 88. Figure 88 depicts the main peaks of the orthorhombic phase decreasing in intensity with time and peaks associated with the hexagonal phase increasing. Another way to visualize these data, as a 2D contour plot, is provided in Figure 89.

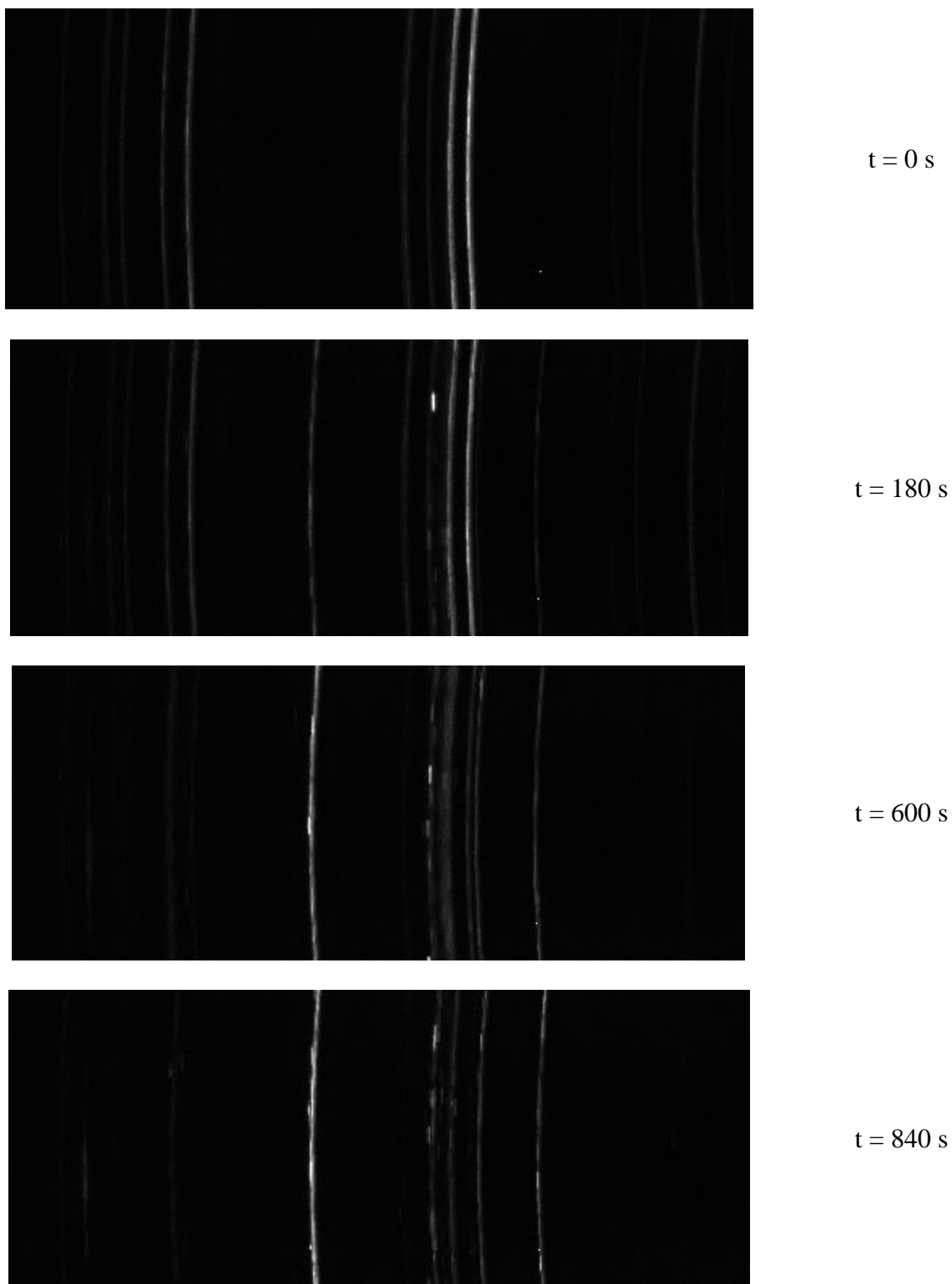


Figure 87. The raw images collected by the Pilatus 100k detector during an isothermal experiment. From top to bottom is increasing time.

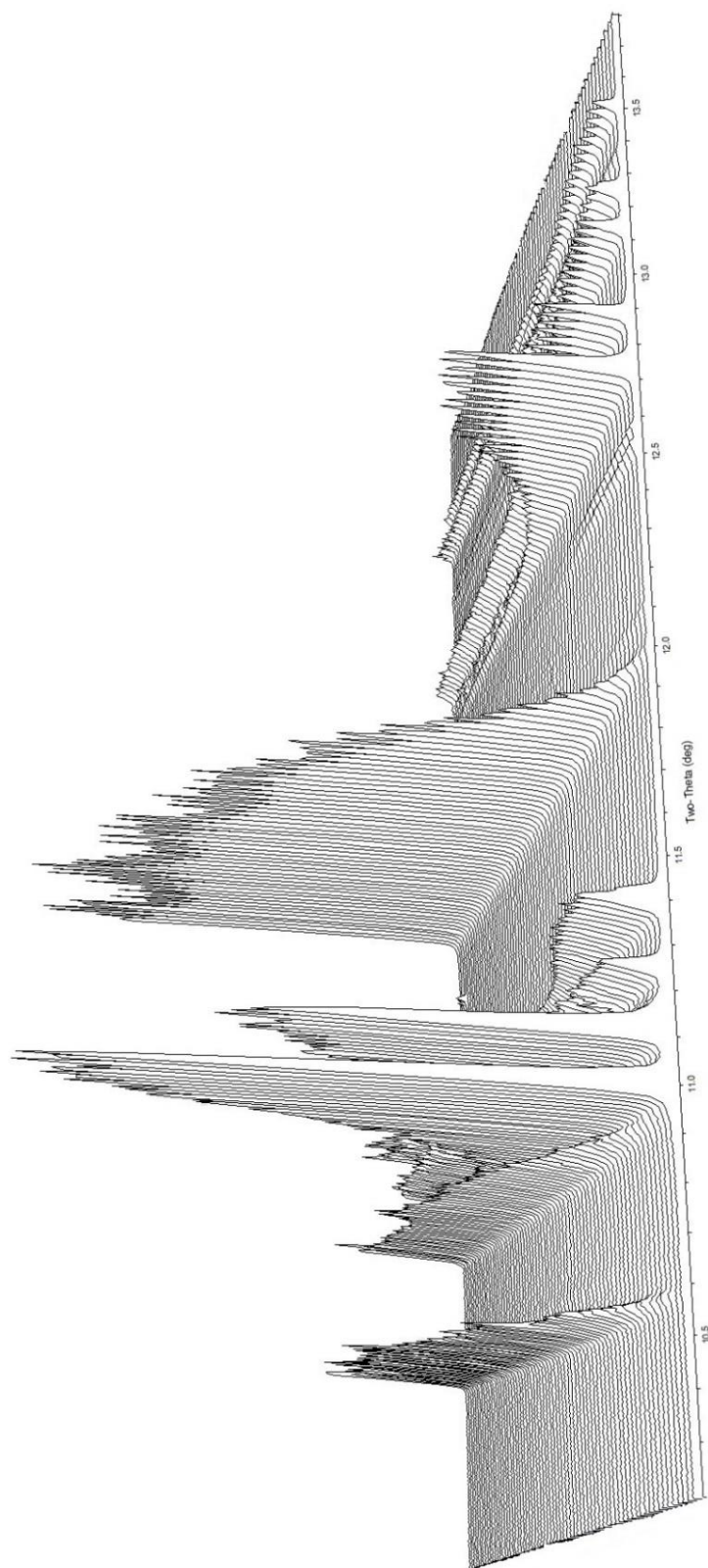


Figure 88. The evolution of peak intensity between the orthorhombic and hexagonal phases as a function of time in Dy₂TiO₅ during an isothermal experiment.

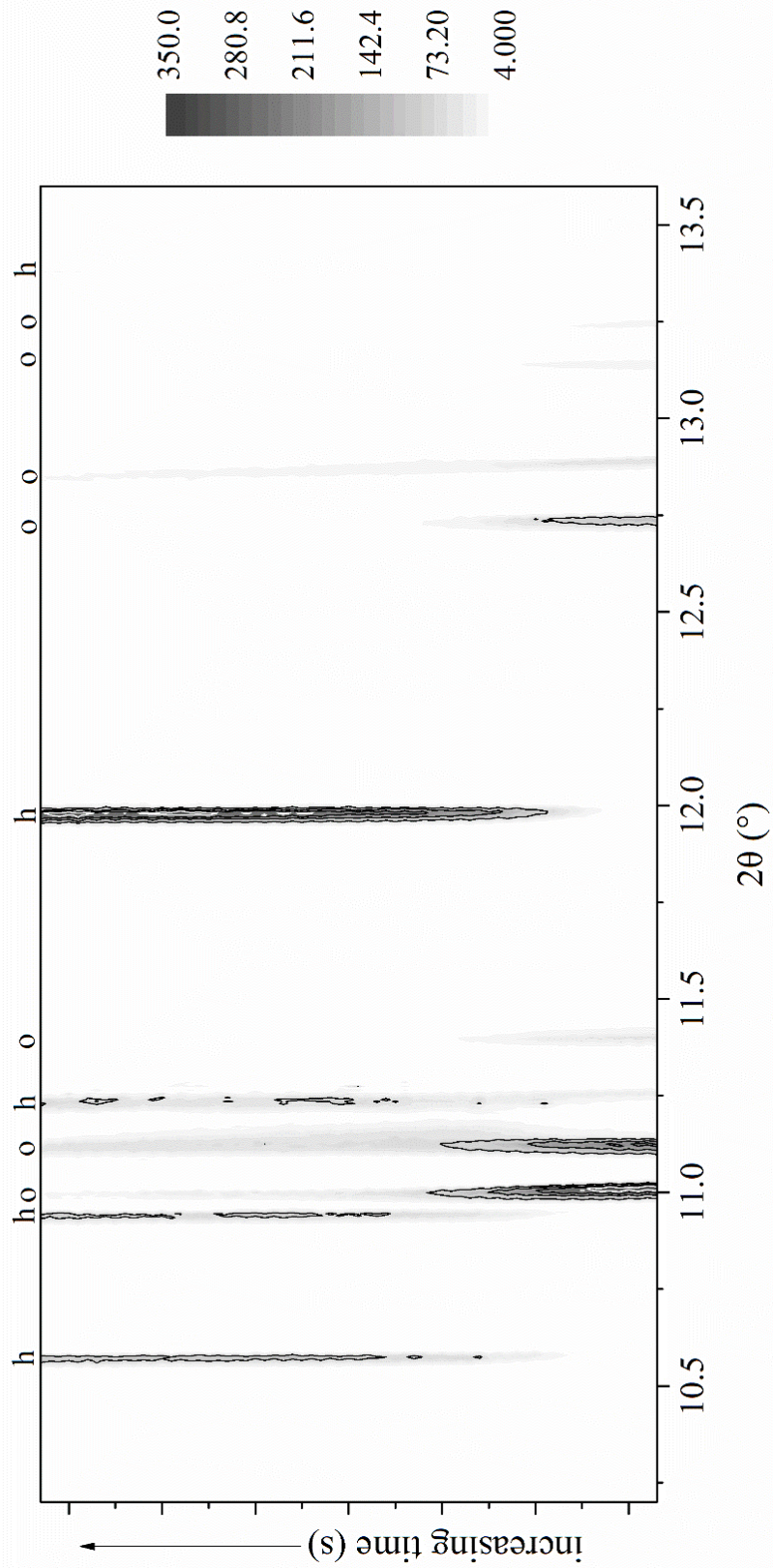


Figure 89. The evolution of peak intensity between the orthorhombic and hexagonal phases in Dy_2TiO_5 as a function of time during an isothermal experiment.

In order to fit each independent isothermal experiment globally, the data were combined into a single set and imported into OriginPro 9.1. A custom, non-linear equation was implemented to fit these data based on the functional form of the Avrami equation reproduced below.

$$F = 1 - \exp \left[- \left[k_0 * \exp \left(- \frac{E_a \frac{kJ}{mol}}{k_b T} \right) \right] * t^n \right]$$

Where, F is the fraction of the initial phase transformed into the new phase, k_0 , the rate constant, E_a , the activation energy, and n, the Avrami constant (dimensional growth parameter). The thermal energy was set for each isotherm to its value of $k_b T$, while k_0 , E_a , and n were allowed to globally fit by minimization. Initial parameters were set which centered on reasonable values, but bounds were set to a wide range to allow a significant amount of freedom. Initial fitting was performed using the OriginPro simplex function. A simplex function is an optimization technique which uses a response surface in n-dimensional space to find a minimum. After an initial minimum was found, a least-squares function was used to further minimize differences from the observed data to those of the model. The least-squares fitting was performed until convergence. Figure 90 plots each isothermal experiment for a phase fraction transformed as a function of time along with the globally fit curve for each individual data set.

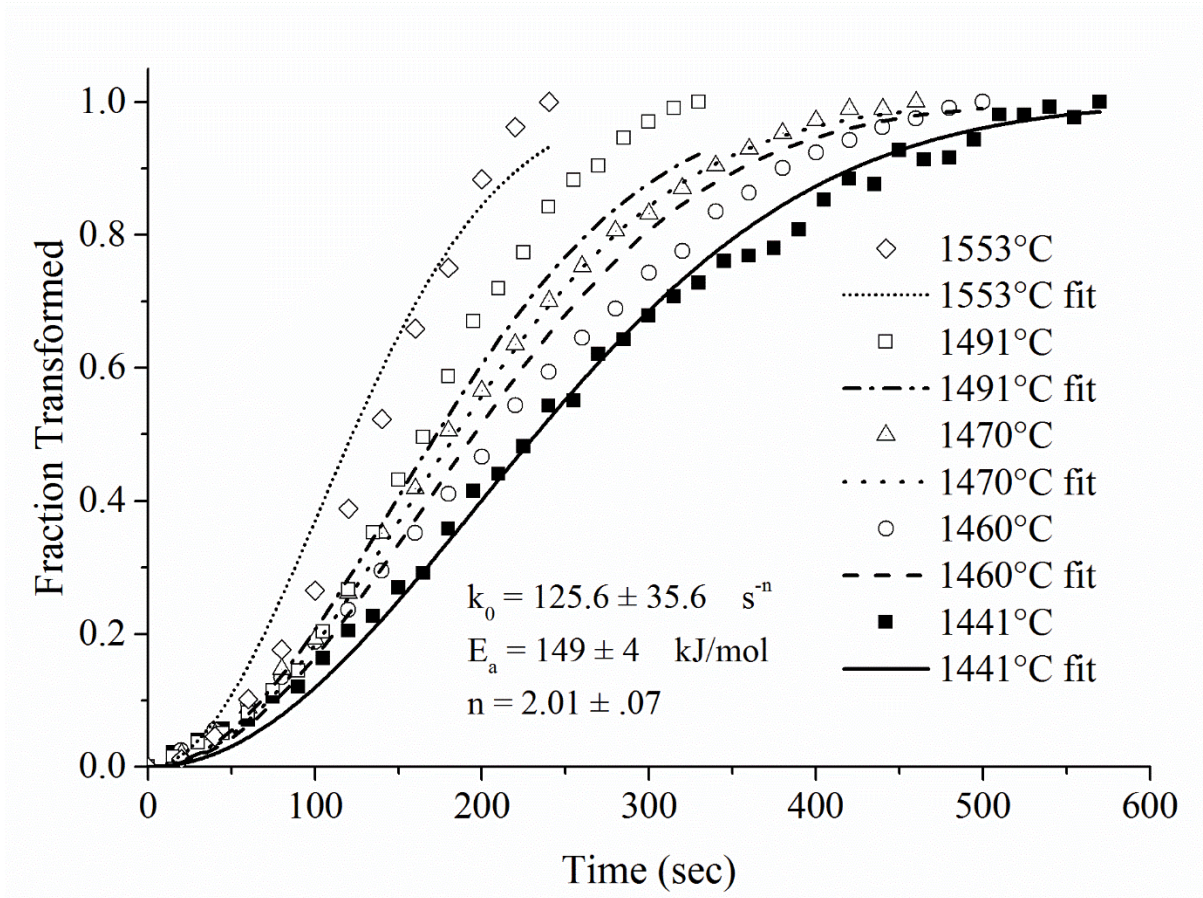


Figure 90. The fraction of the orthorhombic phase transformed to hexagonal in Dy_2TiO_5 at different temperatures as a function of time for an isothermal experiment.

The globally fit Avrami equation to the data is given below for all temperatures and time.

$$F = 1 - \exp \left[- \left[125.6 * \exp \left(- \frac{149 \frac{\text{kJ}}{\text{mol}}}{k_b T} \right) \right] * t^{2.01} \right]$$

$$E_a = 149 \pm 4 \text{ kJ/mol}$$

$$k_0 = 126.6 \pm 35.6 \text{ s}^{-n}$$

$$n = 2.01 \pm 0.07$$

Several interesting observations may be made based on the data and fitted curves. First, unlike the previous Kissinger and isconversional analysis, the value determined here for the activation energy is 149 kJ/mol. Not only is this value a much more reasonable approximation for the activation energy, it is also on par with activation energies found in other transforming ceramic systems (50-800 kJ/mol). It should be noted that the activation energy for the Avrami equation is an “effective” activation energy, meaning it is the combination of two separate events having their own associated activation energies, these being nucleation and growth.

Additionally, the value of the Avrami exponent is very close to 2. If all of the assumptions involving the simplification to the Avrami equation are valid, then the Avrami exponent represents the dimensional manner in which the particles of the new phase grow (1 for a line, 2 for a disc, and 3 for a sphere). A value of 2 would indicate that after nucleation, the growth of the phase progresses two-dimensionally. This behavior is very interesting, particularly when correlated with the crystallographic phase relationship developed in Chapter 6. It was previously found that only minor structural changes would be necessary along the a- and b-axes as opposed to the c-axis. Since the transformation is less hindered in two directions out of the three, an Avrami growth exponent of two is consistent with previous experimental data.

7.1.2 Conclusions

X-ray diffraction was employed to monitor the transformation between the orthorhombic and hexagonal phases as a function of time and temperature. Several isothermal data sets were collected and fit globally to a simplified kinetic model to determine the effective activation energy of the transformation, the nature of particle growth, and rate constant. Overall, the Avrami model fit well with the data but exhibited slight deviations for several isothermal data

sets. This may be attributed to the use of an over simplified model which may not capture the true transformation behavior.

7.2 Comparison with Similar X-ray Diffraction Experiments to Investigate Transformation Kinetics

Direct comparison between this research and similar experiments in literature can be difficult as every experiment has large variability in setup, analysis, and materials investigated. Observations relating to the quality of the data collected and certainty in fitted parameters will be discussed in the context of new method development for the determination of transformation kinetics at high temperature.

7.2.1 Advantages of Described Methods

There are several advantages in characterizing the transformation kinetics using the method described in this dissertation (pairing of a thermal image furnace, X-ray synchrotron radiation, and state-of-the-art detectors).

1. Synchrotron radiation sources, as described in Chapter 1, have a significantly higher photon flux when compared with traditional sources (X-ray tubes). This allows for the collection of data in a short amount of time which is critical for improved time resolution.
2. The wavelength, by means of a monochromator, from synchrotron radiation can be varied. Different materials absorb X-rays differently. The ability to adjust the wavelength is important to avoid such complications.
3. The X-ray detector (Pilatus 100k) can simultaneously measure a relatively large range of 2θ with a high refresh rate. This allows for the observation of several diffraction peaks

simultaneously which minimizes errors associated with fitting of individual peaks (preferred orientation and phase fraction transformed).

4. The Quadrupole Lamp Furnace's ability to reach approximately 2000 °C in air. Platinum heating strips can only reach temperatures around 1600 °C.
5. Stability at temperature using the Quadrupole Lamp Furnace.
6. Internal standard for temperature determination as opposed to external calibration. The thermal mass of the material being investigated does not affect the determination of the temperature allowing for greater consistency between samples and accuracy in temperature determination.
7. Statistical distribution of crystallite orientations in transmission geometry. Preferred orientation is not present allowing for improved determination of phase fraction transformed. Also, allows for potential mechanism of transformation to be elucidated.

7.2.2 Comparisons with Similar Work

Two main comparisons will be made with respect to similar research. First, whether or not the calculated value for activation energy for the orthorhombic to hexagonal transformation in Dy_2TiO_5 is reasonable compared with other reconstructive transforming ceramic systems. Second, a comparison between the quality of data collected and the Avrami fit in this work compared with similar studies which result in the calculation of activation energy will be made.

Range of Activation Energies for Transformations in Ceramic Systems

In order to contextualize this work it is important to draw comparison with other research in the open literature. As discussed previously in this chapter, measurements made using thermal analysis methods such as DSC result in dubious values for activation energy. Table 30 provides

several examples of activation energies determined using the Avrami equation on data collected by *ex situ* and *in situ* X-ray diffraction experiments.

Table 30. Activation energies for reconstructive transformations in other ceramic systems.

Transforming System	Fit Activation Energy (kJ/mol)	Error (kJ/mol)	Comments	Reference
quartz-cristobalite	193	73	particle size relationship with activation energy (small particles), combined in situ ex situ	Pagliari[117]
quartz-cristobalite	181	78	particle size relationship with activation energy (intermediate particles), combined in situ ex situ	Pagliari[117]
quartz-cristobalite	234	191	particle size relationship with activation energy (large particles), combined in situ ex situ	Pagliari[117]
quartz-cristobalite	555	24	seeding effect on transformation, ex situ	Breneman[118]
quartz-coesite	163	23	pressure and temperature, synchrotron radiation, EDS detector	Perrillat [119]
geopolymer crystallization	31.5	6	crystallization from amorphous phase	Provis [120]
geopolymer crystallization	36.4	2	crystallization from amorphous phase, zeolite	Gualtieri [121]
titania	210	40	crystallization kinetics of mesoporous titania films, surface nucleation mechanism	Kirsch [122]
titania	140	30	crystallization kinetics of mesoporous titania films, nanoscale restructuring	Kirsch [122]
UO ₂	46	-	oxidation of uranium metal	Zhang [123]
cristobalite crystallization	674	53	crystallization from amorphous powder	Bae [124]

Generally, the range in values for the activation energy for other transforming systems as described by Table 30 is approximately 30-675 kJ/mol with an average value of 177 kJ/mol.

With respect to other activation energies in ceramics, the value determined in this study for the activation energy between the orthorhombic and hexagonal phases of 149 kJ/mol is reasonable and tends towards the average. In addition, the value determined in this work, when compared with other literature values, has a much smaller error in certainty (± 4 kJ/mol). The smaller value in the error is likely due to better time resolution and/or improved fitting techniques. This will be discussed in more detail in the next section.

It should be noted when surveying the literature for reasonable values for activation energies that the potential for these data to suffer from the same pitfall of erroneously high activation energies exists. Therefore, the activation energies listed in Table 30 should be regarded as the potential upper limit of the real activation energy.

Comparison of Data Collected and Avrami Fit to Similar Works

Compared with the quality of data collected in other studies, and the method used to fit to the Avrami equation, the data in this study is of much higher quality. As described in Chapter 7.2.1, the combined use of synchrotron X-ray radiation with advanced detectors allows for an increase in the number of data points collected over similar time periods compared with other studies which rely on conventional X-ray sources and detectors. To illustrate this, Figures 91-93 reproduce the data collected in other research published in the literature which employed these conventional methods.

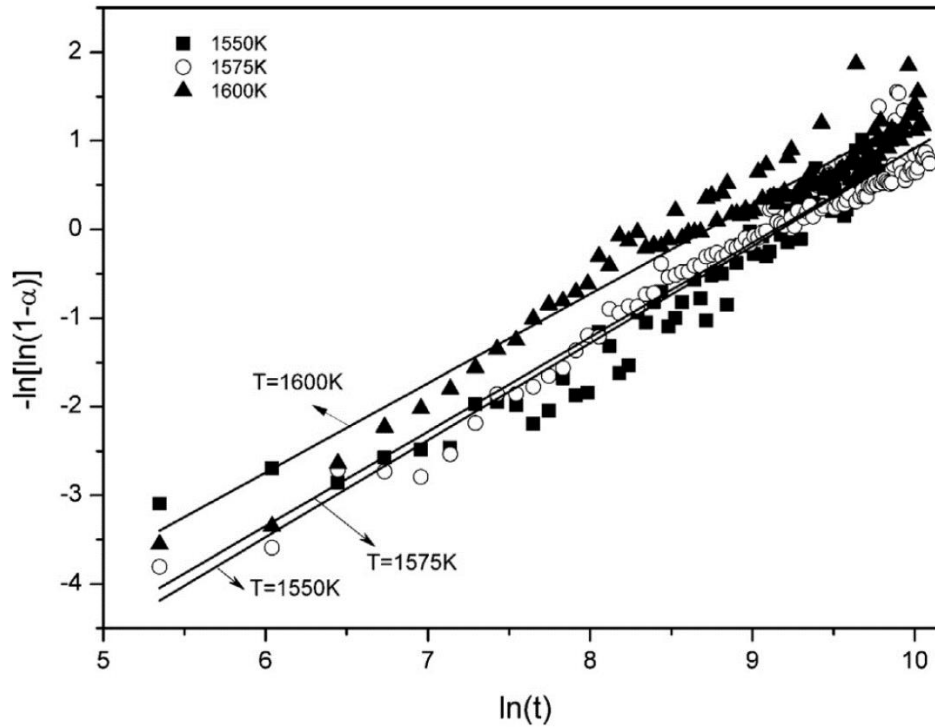


Figure 91. Linearized *in situ* data of phase fraction transformed with respect to time for three separate isothermal holds (quartz to cristobalite). Data collected with Philips X' Pert diffractometer equipped with an Anton-Paar heating chamber (HTK 16 MSW) and a Pt heating strip. 4 min collection time for each point.[117]

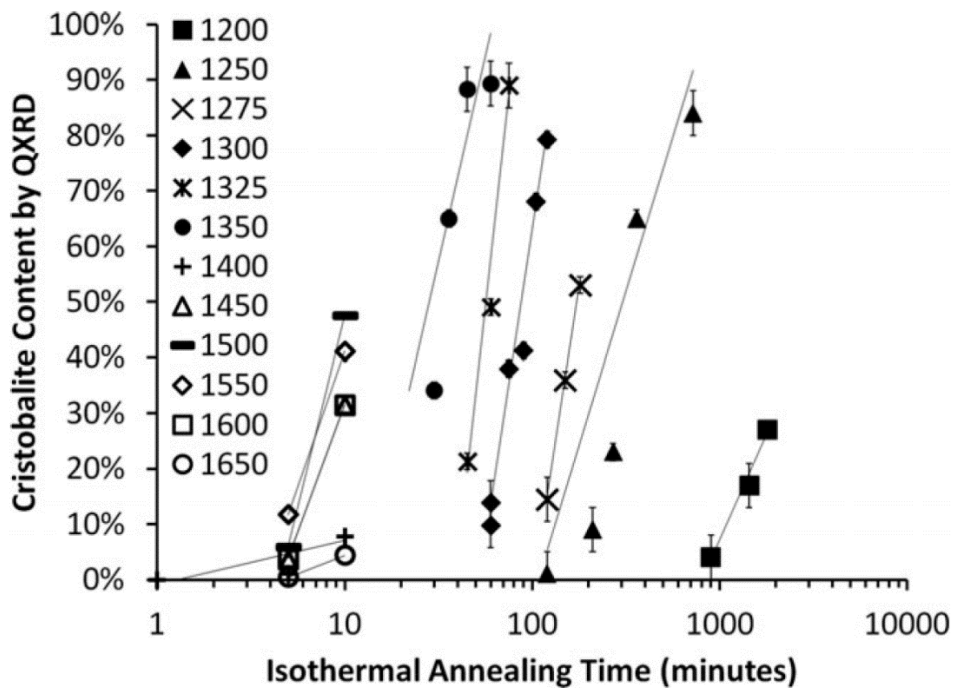


Figure 92. *Ex situ* data of phase fraction transformed after thermal annealing at various temperatures with respect to time (amorphous silica to cristobalite). Data collected with Rigaku Rotaflex.[118]

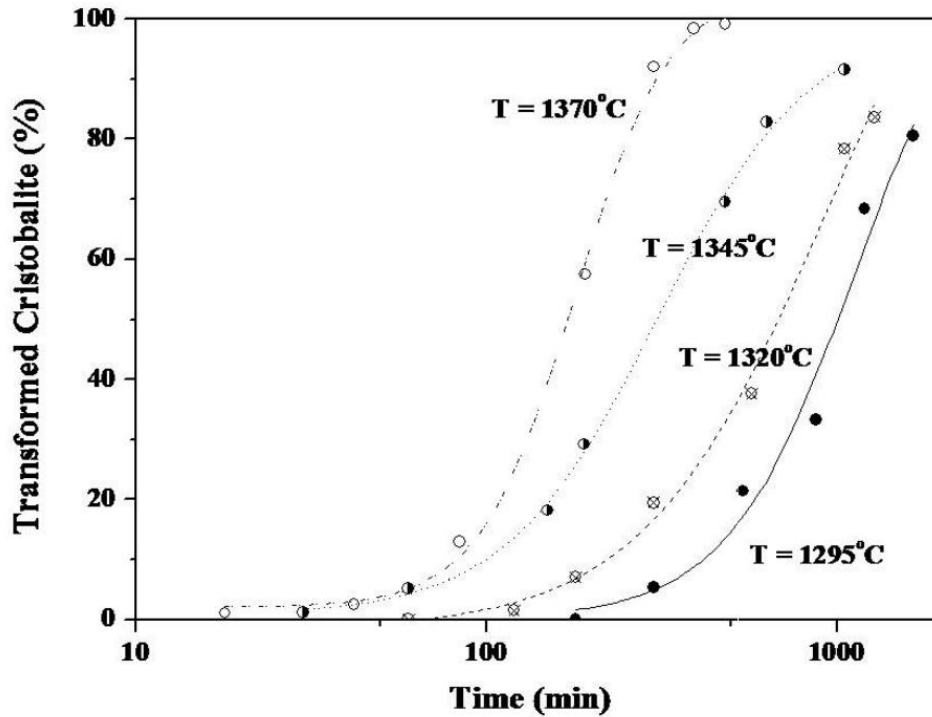


Figure 93. *Ex situ* data of phase fraction transformed after thermal annealing at various temperatures with respect to time (amorphous silica to cristobalite). Data collected with Rigaku MiniFlex.[124]

The lack of data is obvious from inspection of Figures 91-93. The feasibility in collecting more data is likely not justified or possible for experimental techniques used in the collection of these data (taken with conventional laboratory equipment). For example, Figure 91 depicts the linearized data fit to the Avrami equation for the transition between quartz and cristobalite *in situ*. While this study collected many more data points as compared to the depicted *ex situ* work in Figures 92 and 93, it lacks the time resolution towards the beginning of the transformation as each data point represents 4 minutes of time. As discussed later in this chapter, time resolution towards the beginning of the transformation is far more valuable than data at the end, and as such, may have a significant impact on the analysis and calculation of the effective activation energy.

Comparisons with other work which employed the use of synchrotron radiation can also be made. Figures 94-100 show the raw data collected, and/or analysis of these data, for experiments using synchrotron radiation.

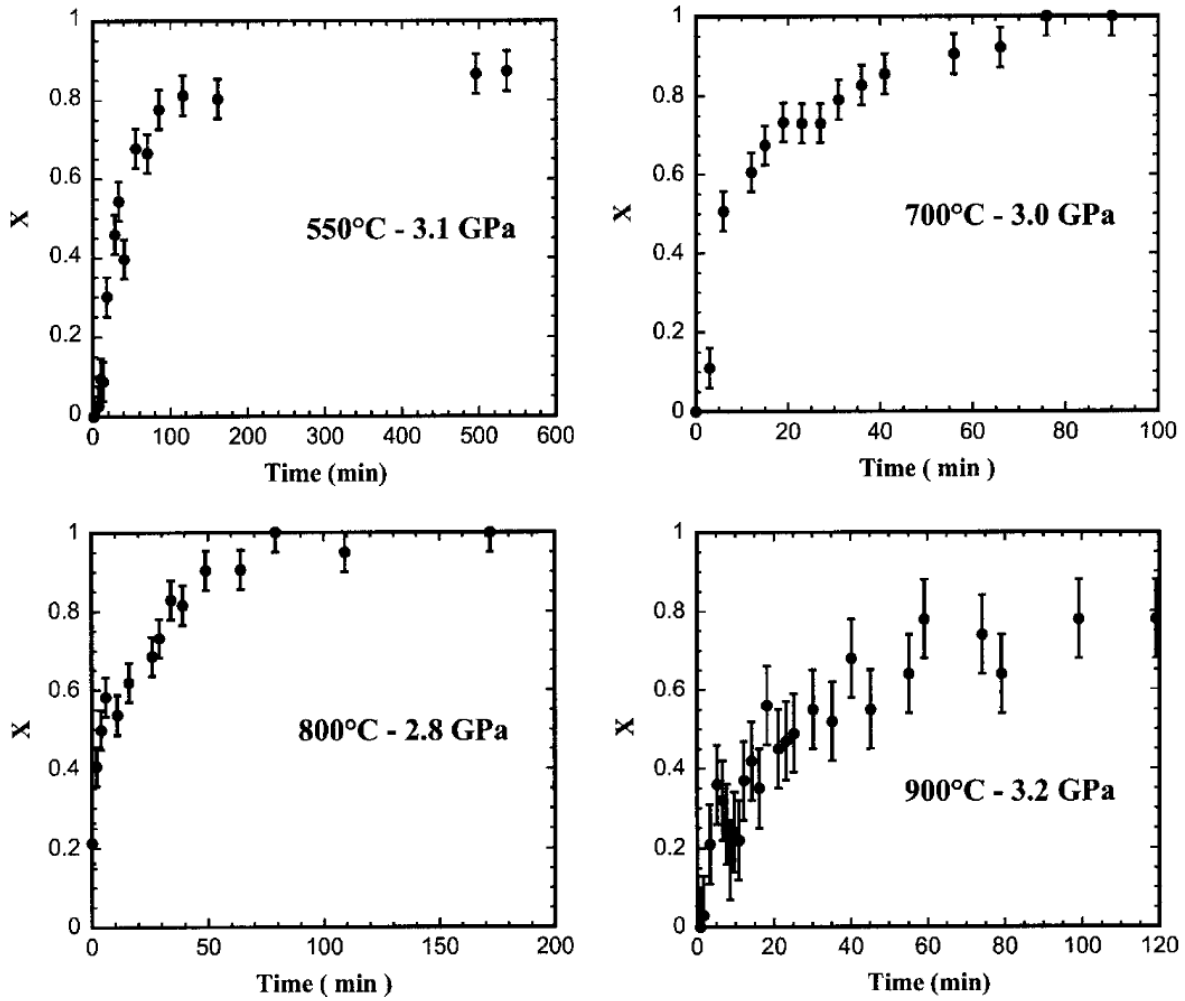


Figure 94. *In situ* data of phase fraction transformed during isothermal/isobaric hold with respect to time (quartz to coesite). Data collected at DW11 Laboratoire pour l'Utilisation du Rayonnement Electromagnetique using an energy dispersive detector.[119]

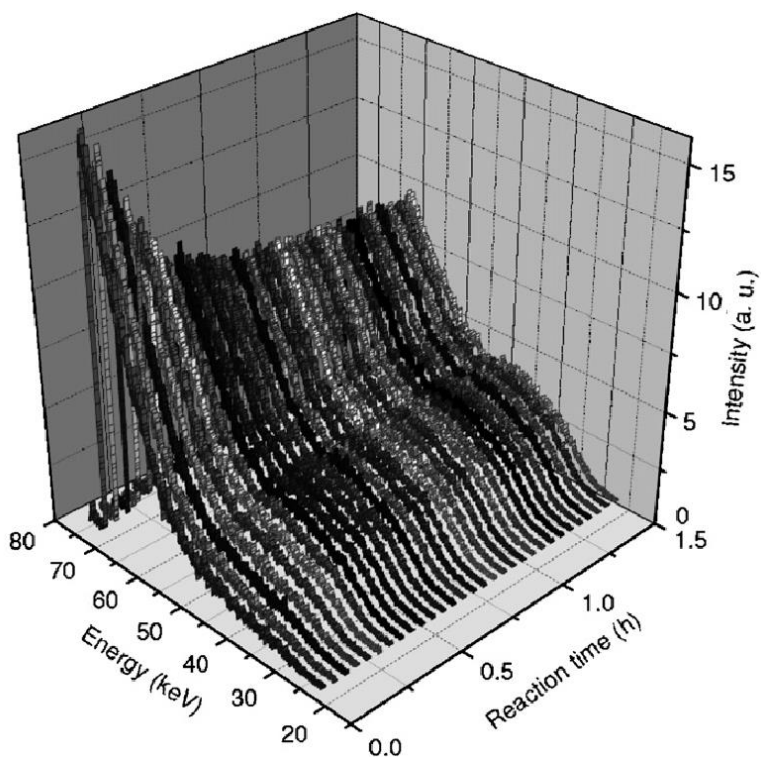


Figure 95. *In situ* data of phase fraction transformed during isothermal hold with respect to time (amorphous geopolymer to crystalline). Data collected at X17C at NSLS using an energy dispersive detector.[120]

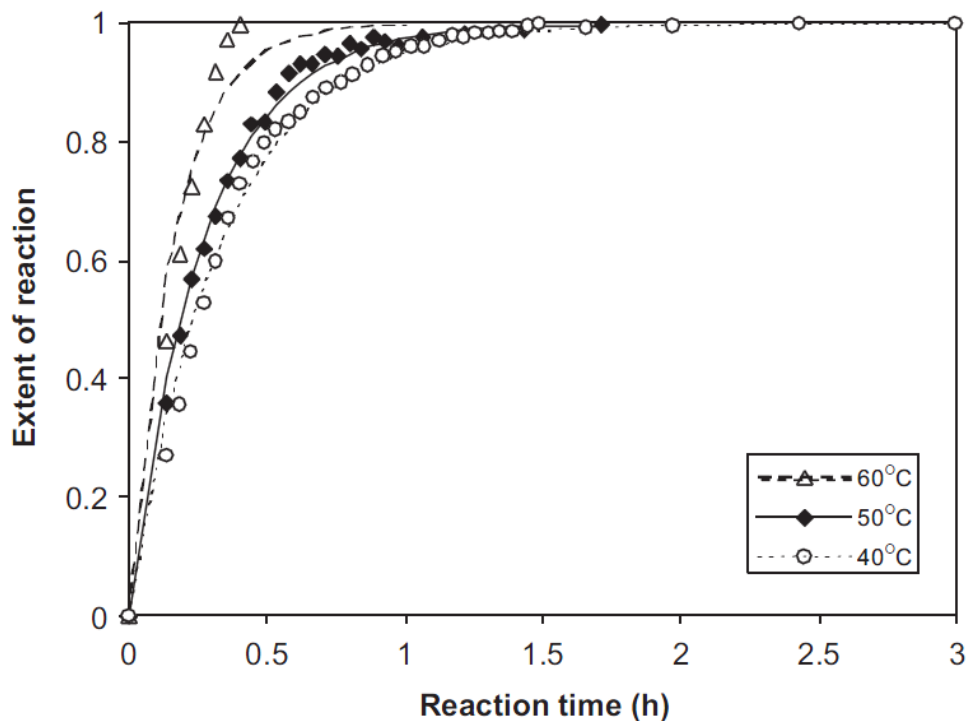


Figure 96. Analysis of *in situ* data of phase fraction transformed of various isothermal temperatures with respect to time (amorphous geopolymer to crystalline). Data collected at X17C at NSLS using an energy dispersive detector.[120]

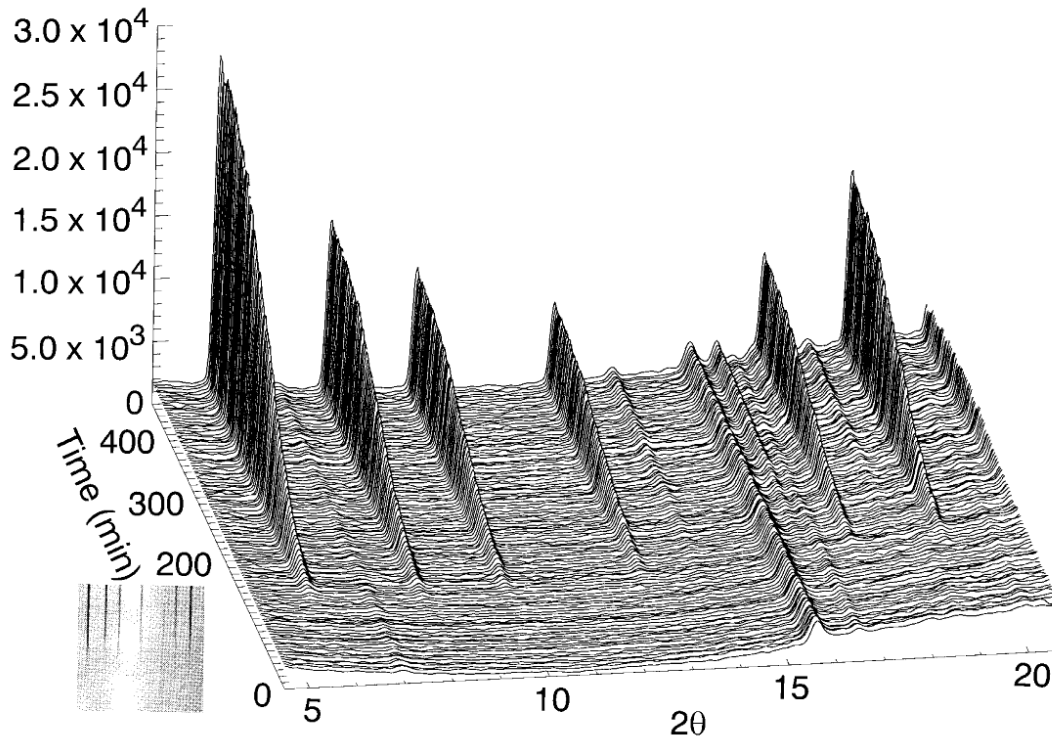


Figure 97. *In situ* data of phase fraction transformed during isothermal hold with respect to time (crystallization of amorphous geopolymer). Data collected at X7B at NSLS using a translating image plate system.[121]

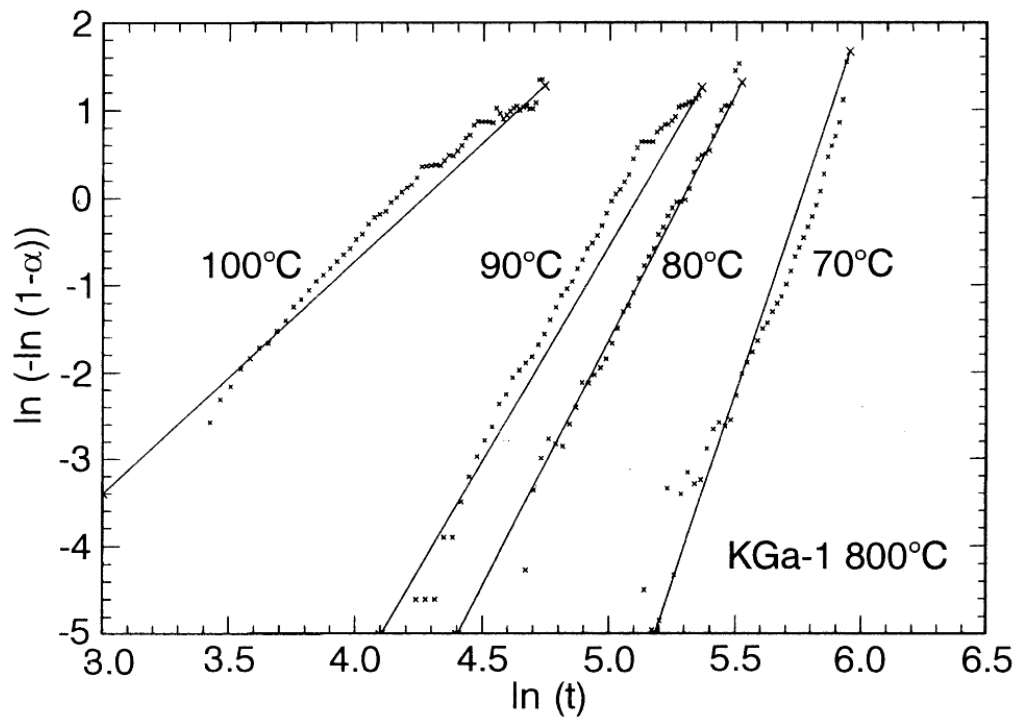


Figure 98. Analysis of *in situ* data of phase fraction transformed of various isothermal temperatures with respect to time (crystallization of amorphous geopolymer). Data collected at X7B at NSLS using a translating image plate system.[121]

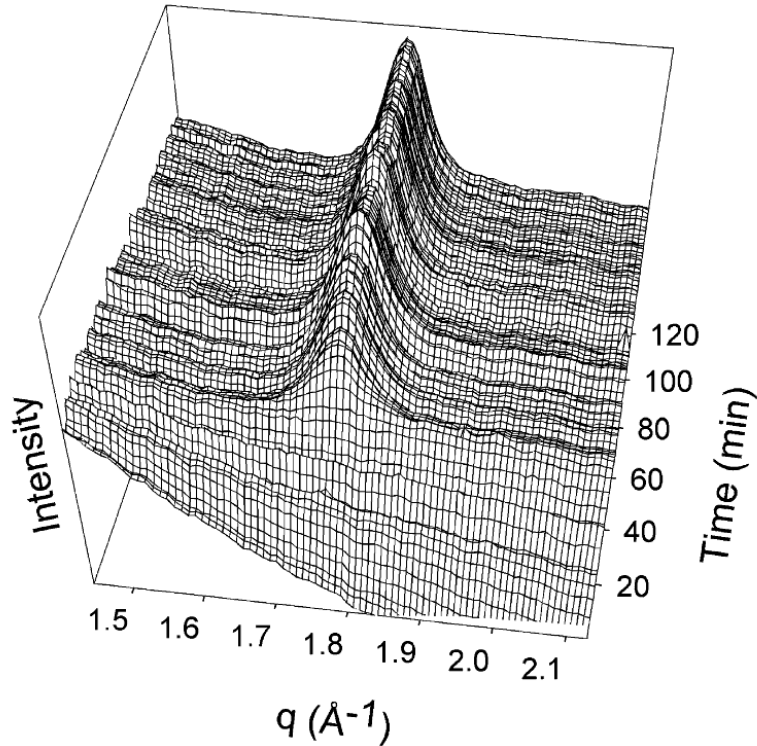


Figure 99. *In situ* data of phase fraction transformed during isothermal hold with respect to time (crystallization of amorphous titania). Data collected at 6-2 at the Stanford Synchrotron Radiation Laboratory using a CCD camera with 60-90 sec exposure times.[122]

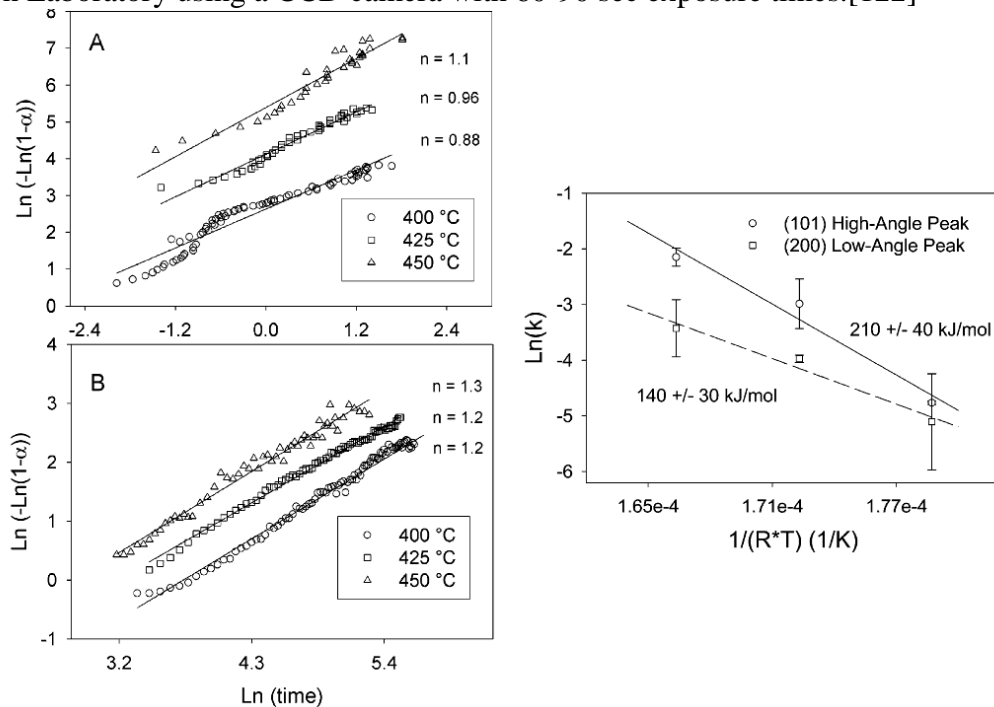


Figure 100. Analysis of *in situ* data of phase fraction transformed of various isothermal temperatures with respect to time (crystallization of amorphous titania). A) high angle B) low angle data. Data collected at 6-2 at the Stanford Synchrotron Radiation Laboratory using a CCD camera with 60-90 sec exposure times.[122]

While the data in the figures above are of much higher quality, relative to data collected via conventional means, it suffers from several similar drawbacks. The first is the lack of time resolution (on the order of minutes). Although the number of photons used in the collection of these data was significantly higher, the use of energy dispersive detectors and image plates in the experiments conducted by Perrillat, Provis, and Gualtieri significantly limited any potential benefit of increased time resolution. The use of a CCD camera in the Kirsch experiment may have been capable of increasing the time resolution, but the exposure time was set between 60 and 90 seconds (i.e. 4 to 6 times longer than the exposure time in this work).

In addition, the method of fitting of some of these data to the Avrami equation and subsequent analysis is antiquated. The linearization of the data using logarithms to fit to a simple line for individual isothermal data sets and averaging of the information is not only cumbersome to do, but also subject to error from averaging between data sets with differing amount of points. More advanced fitting with the aid of computer programs can avoid such problems.

7.2.3 Future Method Development

Other than major changes to the experimental setup (furnaces, sources, and detectors), the simplest modification that can be made with the most impact falls in the realm of automation. Currently every measurement is performed manually. A researcher must physically be present throughout the experiment and manually start each measurement (the push of a button at 10-20 second time intervals). As discussed later in this chapter, one factor which can result in a better fit of the Avrami equation to the data is time resolution. The current detector, the Pilatus 100k, has a refresh rate of 10,000 frames/second. Though this is the theoretical maximum of the number of data points which can be acquired, it is not practical. The refresh rate, which for the purposes here is equivalent to the exposure time, must be balanced with the quality of the pattern

collected, where more time would result in a better diffraction pattern. Under current conditions, this balance is approximately 1 to 2 seconds, a 10 to 20X improvement in resolution. With respect to the current manual method to collect these data, a 1 second exposure time is not practical, and as such, automation in the process would be required. This can be achieved through simple scripting in the form of a macro which can be run in SPEC and EPICS programming language which control beamline functions.

In addition to improved time resolution with automation, data analysis can become more streamlined with the use of batch processing of data. A full Rietveld refinement is not necessary to determine the ratio between two different phases, although desired. This can be achieved using relative peak intensities or areas. If there is an increase in time resolution in data collection by 10X, then there will be 10X the data to process, thus necessitating the use of batch processing. This can be accomplished by means of several different commercial programs on the market today.

7.2.4 Conclusions

With respect to other research which study phase transformation kinetics using X-ray diffraction, the method described in this work has several significant comparative advantages. These include increased photon flux by using synchrotron radiation, a furnace which can quickly overheat a sample to avoid complications with nucleation, and a detector which can collect excellent data in a relatively short amount of time. When combined, these improve the time resolution of the data which has a significant impact on the determination of the effective activation energy for a reconstructive transformation.

Relative to other work in the literature, a value of 149 kJ/mol for the activation energy required for the transformation between the orthorhombic and hexagonal phase in Dy₂TiO₅ is very reasonable. Additionally, the method used to collect the data in this work is a significant improvement to conventional methods both in time and in the quality of data collected.

In conclusion, the method described here is an excellent and accurate way to determine the activation energy for a reconstructive transformation, particularly those which occur on relatively shorter time scales.

7.3 Improving the Kinetic Model

For an initial experiment using the quadrupole lamp furnace to investigate the kinetic parameters of the transformation between the orthorhombic and hexagonal phases in Dy₂TiO₅, the global Avrami equation fit to the data is excellent. Slight deviations between the fit and the data is to be expected, but for several of the isothermal data the deviation can be quite significant. For example, the fit of the isothermal data for 1441 and 1470 °C are good, but the fits for 1460, 1491, and 1553 °C have much larger deviations as observed in Figure 90. This deviation is indicative of either poor experimental conditions or a poor model. Assuming the experiment was properly performed, the implications of a poor model will be discussed.

As described in Chapter 1, the Avrami model assumes several things about the transformation and the material system in general. The Avrami model assumes an infinitely sized system, uniform but random nucleation, that impingement ends growth, that spherical particles form, and that growth is interfacially controlled. The assumptions of infinitely sized system and that growth ends at impingement are likely to be valid for this experiment. The size of the region probed by the X-ray beam is relatively small compared to the size of the sample. In addition, the slowing

rate of transformation as a function of time, paired with the observed conversion of the orthorhombic to hexagonal phase via XRD, suggests that growth of the particles was inhibited by interaction with other particles of the same phase.

7.3.1 Sensitivity Analysis with Time

A sensitivity analysis was performed on the Avrami equation by determining the differential change in the result when a particular variable was adjusted. This analysis was performed in two different time regimes. The first time regime was one in which less than 50% of the phase had transformed and the other where more than 50% had transformed. This analysis would then be able to show the sensitivity of a particular variable within a particular time regime.

Figures 101-103 describe the sensitivity in the activation energy, rate constant, and Avrami exponent in the two different time regimes.

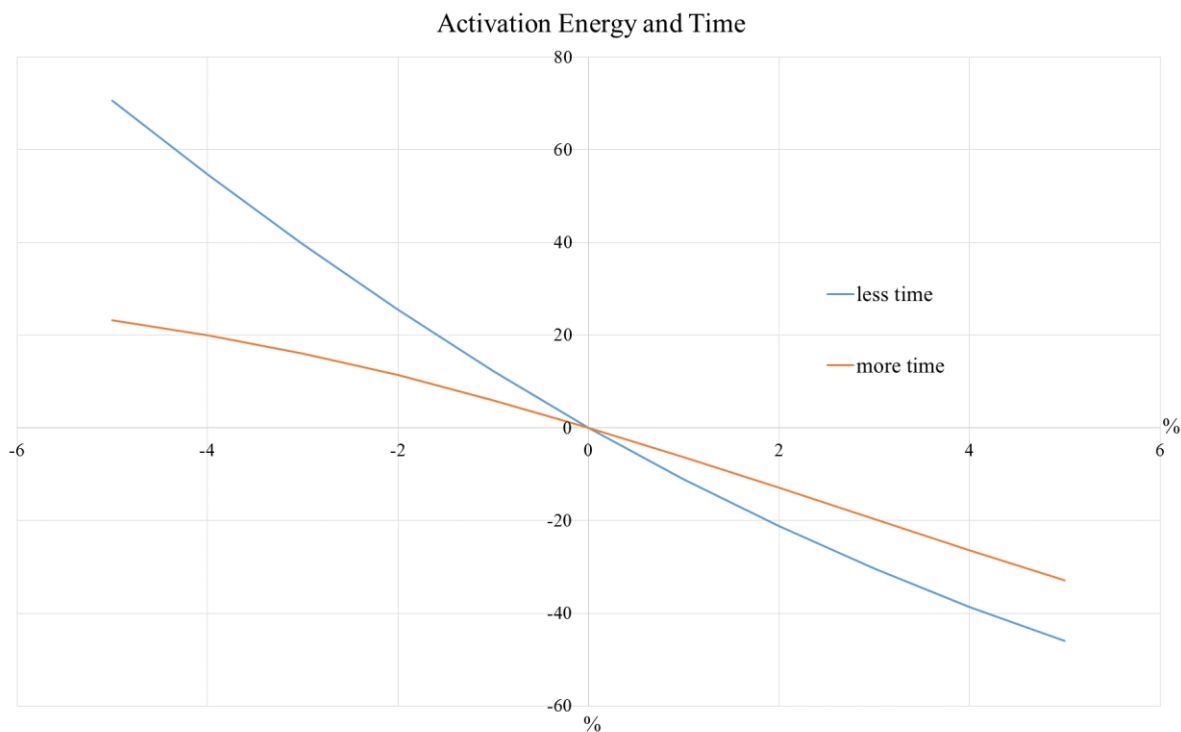


Figure 101. The differential change in the overall fitting result with a differential change in activation energy in two separate time regimes.

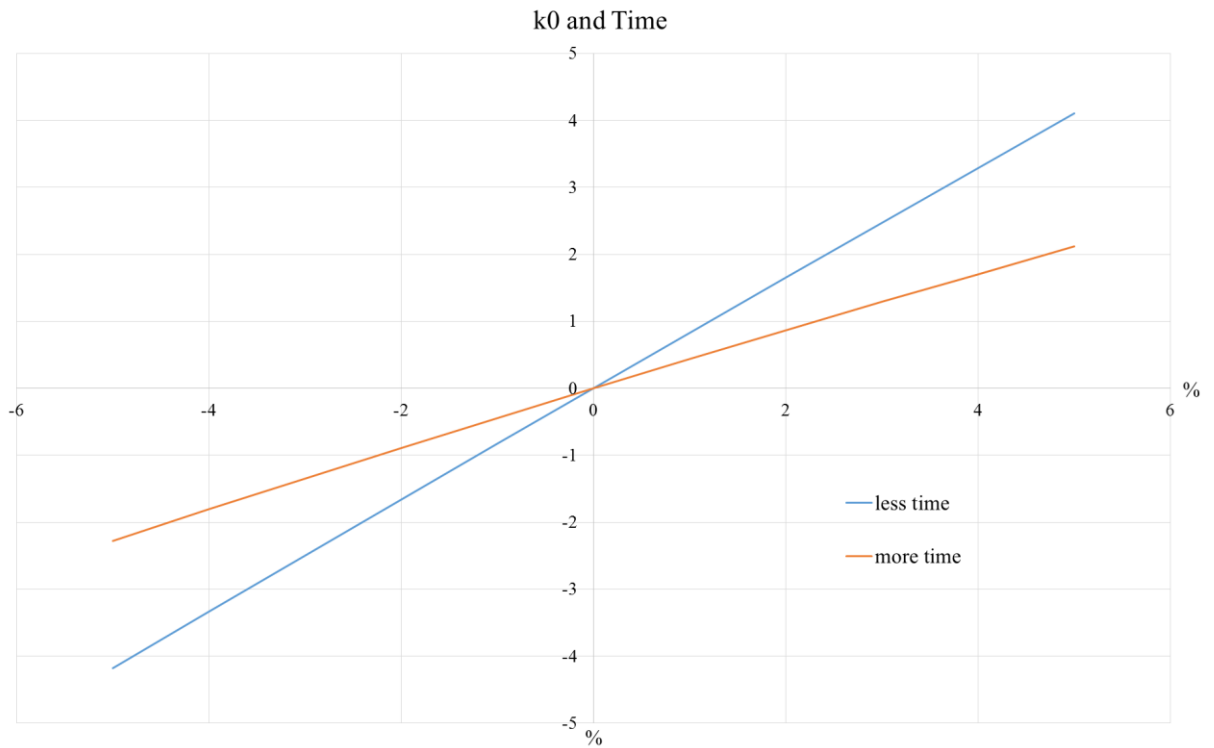


Figure 102. The differential change in the overall fitting result with a differential change in the rate constant in two separate time regimes.

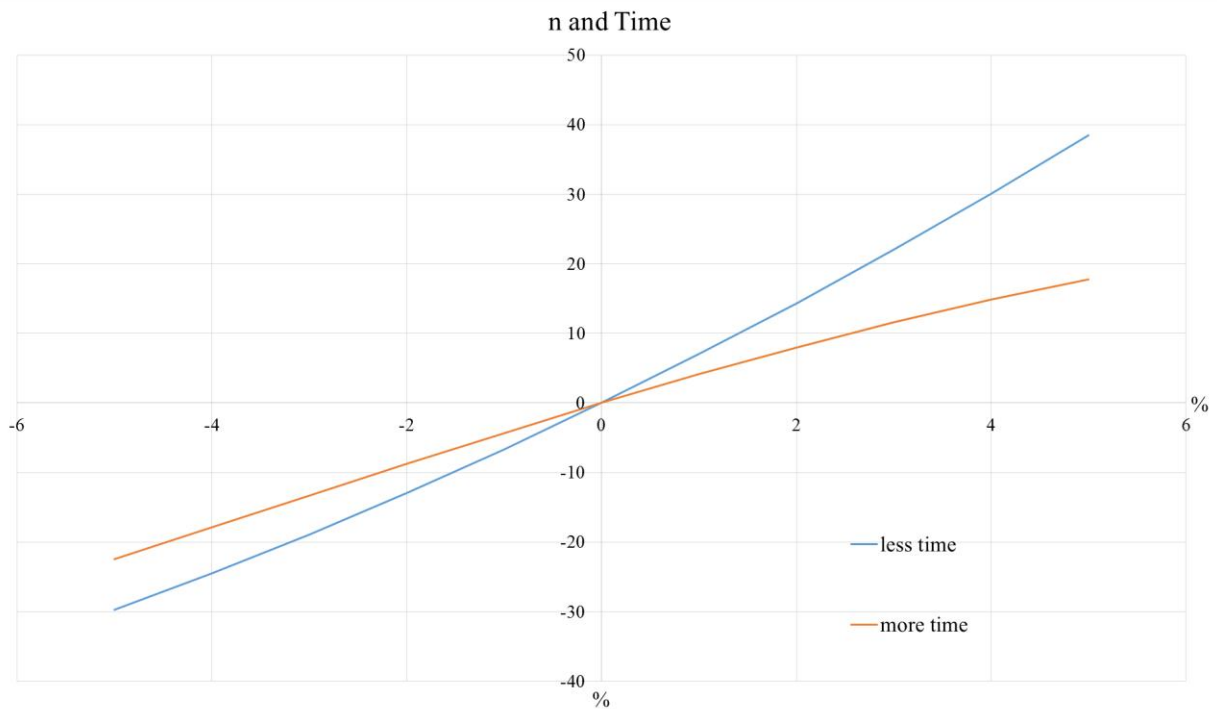


Figure 103. The differential change in the overall fitting result with a differential change in the Avrami exponent in two separate time regimes.

From Figures 101-103 two main relationships are apparent. First, that the activation energy has the largest impact on the result, followed by the Avrami exponent and rate constant. Second, uncertainties in the data at lower time intervals have the largest impact on the overall result. The implications of these findings will be discussed in the discussion section.

7.3.2 Sensitivity Analysis with Temperature

Uncertainty in the ability to determine the temperature of the set of data collected during an isothermal experiment may have an effect on the overall fit. A sensitivity analysis was performed which investigated this effect. The uncertainty in the temperature in this range was approximately ± 6 °C. This parameter was used as a static change in the input while the activation energy, rate constant, and Avrami exponent were differentially changed. The results of the sensitivity analysis are provided in Figures 104-106.

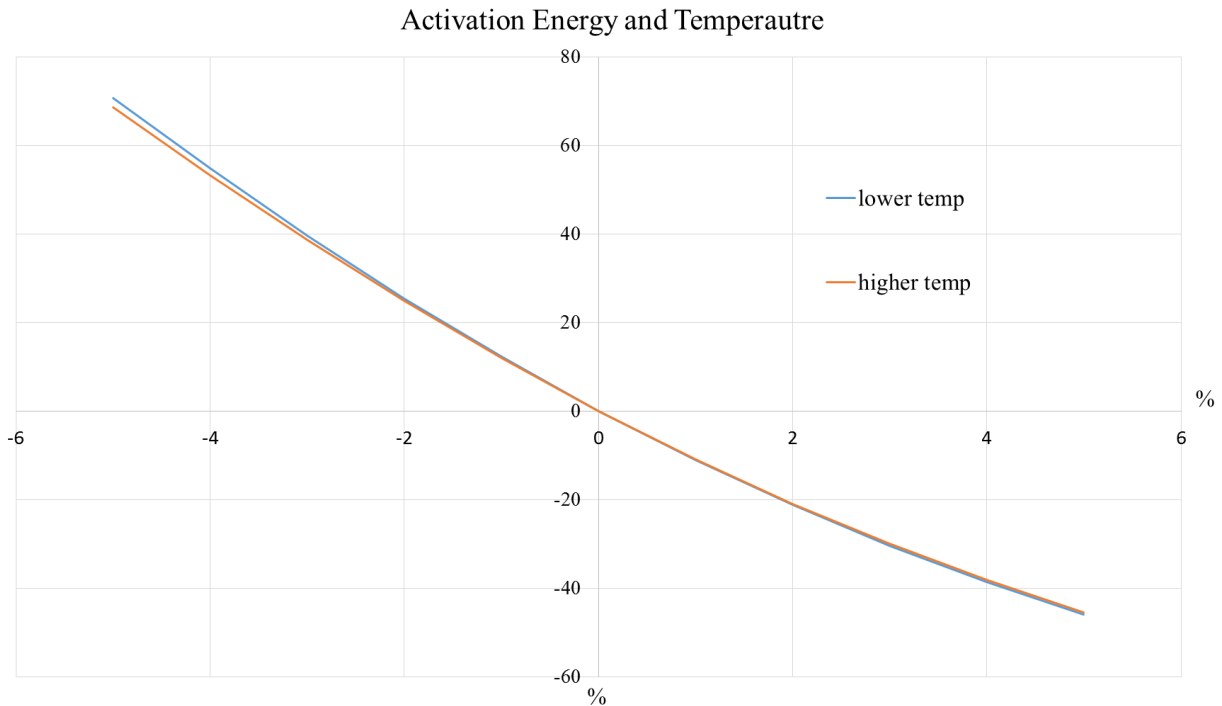


Figure 104. The differential change in the overall fitting result with a differential change in activation energy between two different temperatures.

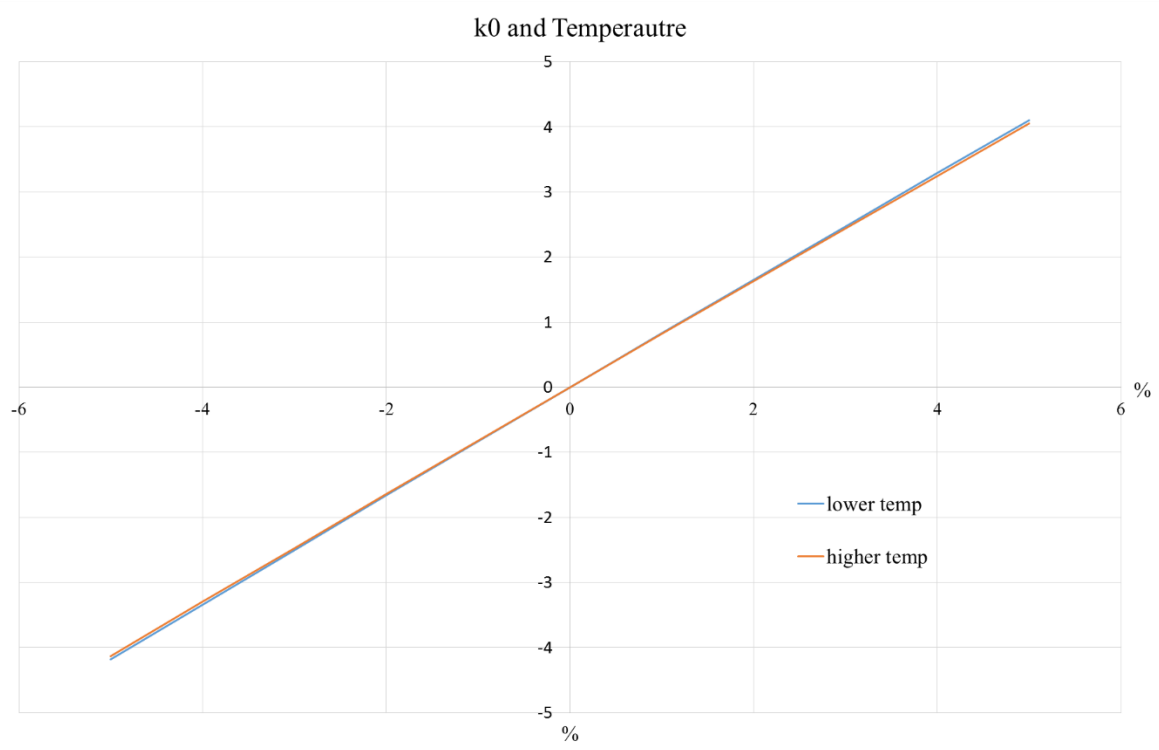


Figure 105. The differential change in the overall fitting result with a differential change in the rate constant between two different temperatures.

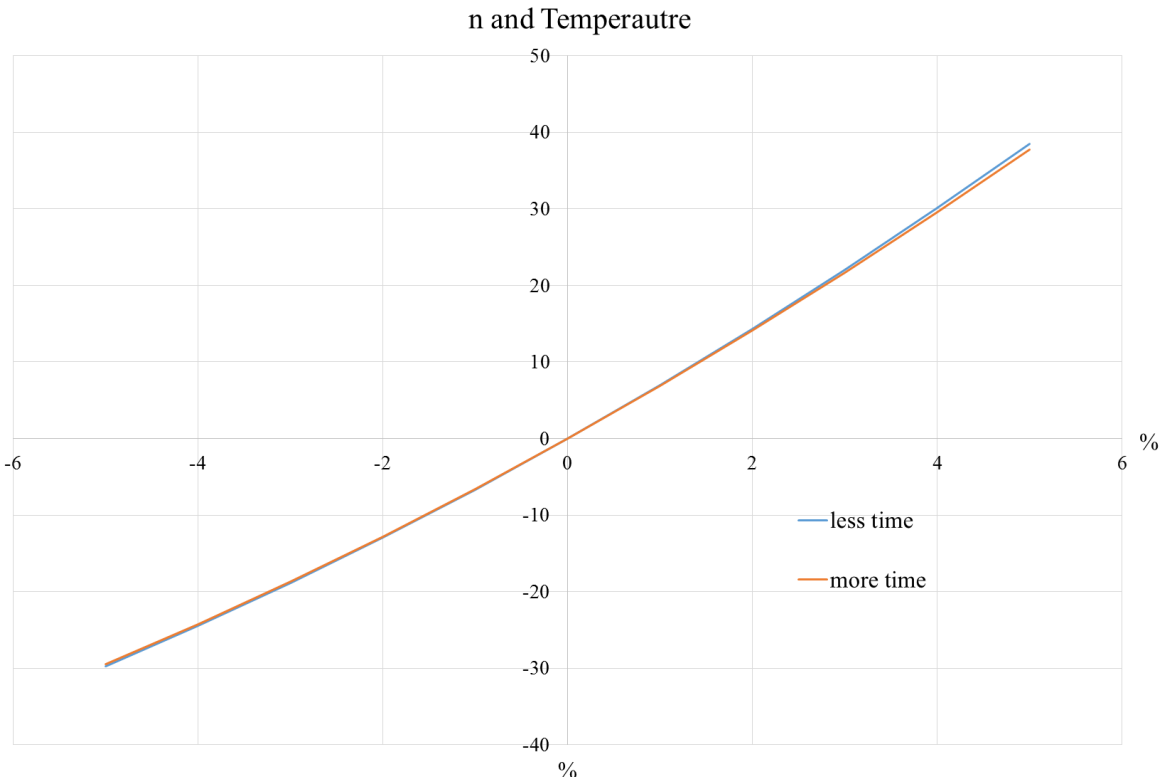


Figure 106. The differential change in the overall fitting result with a differential change in the Avrami exponent between two different temperatures.

Overall, as indicated by the results of the sensitivity analysis, the result of an uncertain temperature determination from the data has very little effect on the overall fitting result. This will be discussed in more detail in the discussion section.

7.3.3 Sensitivity with Variable Type

Relative to each other, the parameters used for the global fitting routine were also subjected to a sensitivity analysis. The results of this analysis are provided in Figure 107.

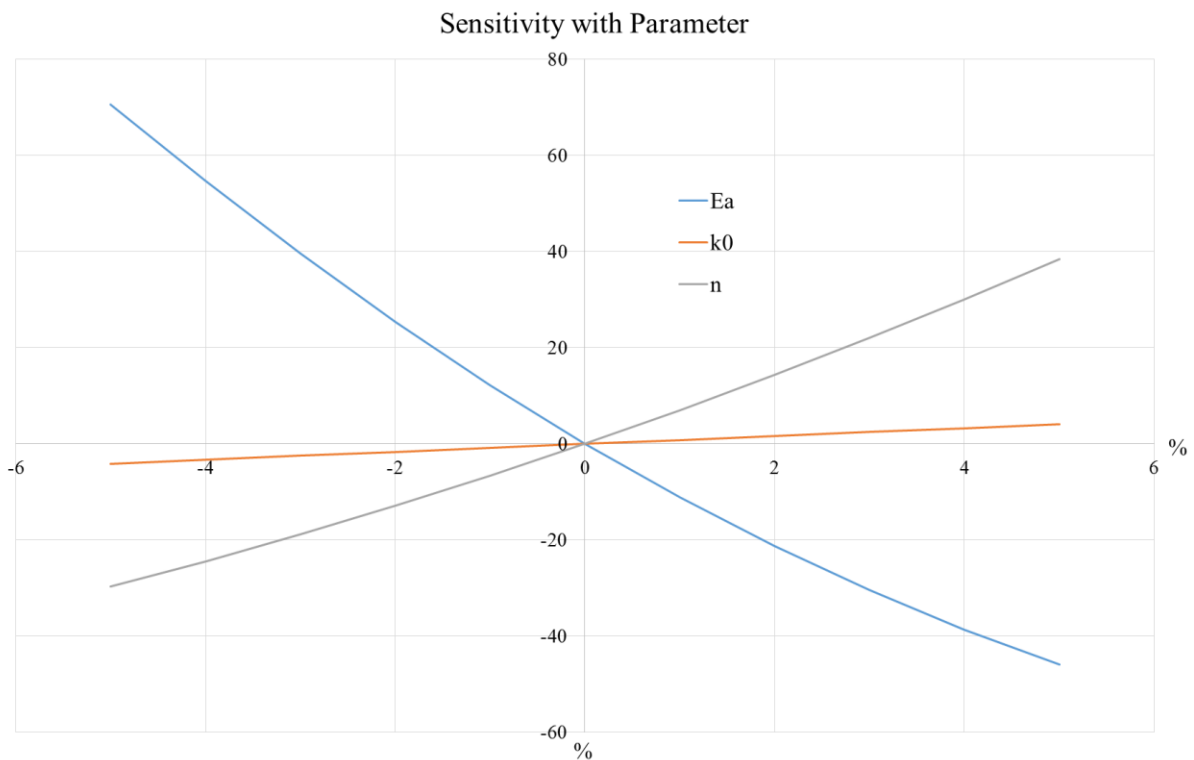


Figure 107. The relative differential change in the overall fitting result with a differential change in activation energy, rate constant, and Avrami exponent.

It is clear from the data that a 1% change in the activation energy affects the overall function more severely as opposed to the Avrami exponent and rate constant. The implications of this will be discussed in a later section.

7.3.4 Analysis of Data

Each individual isothermal data set can be independently fit to the Avrami equation to determine its activation energy, rate constant, and Avrami exponent. The results of this independent fitting are provided in Figure 108 and the equation variables of each are listed in Table 31. The results of this analysis are discussed in the next section.

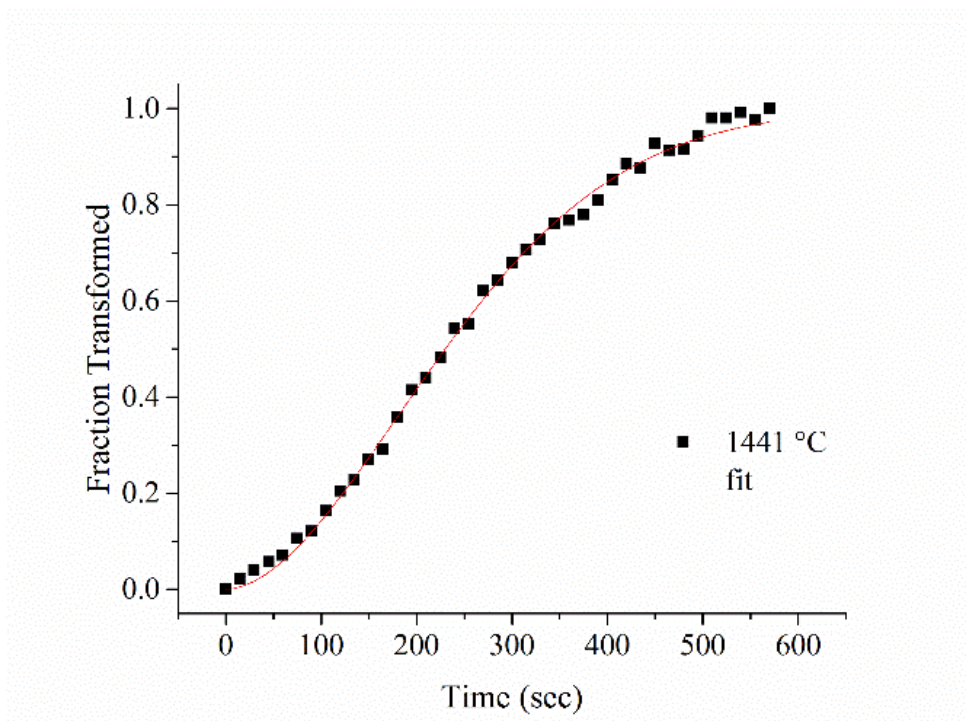


Figure 108(a). Individual fit the Avrami equation for isothermal data collected at 1441 °C for Dy_2TiO_5 .

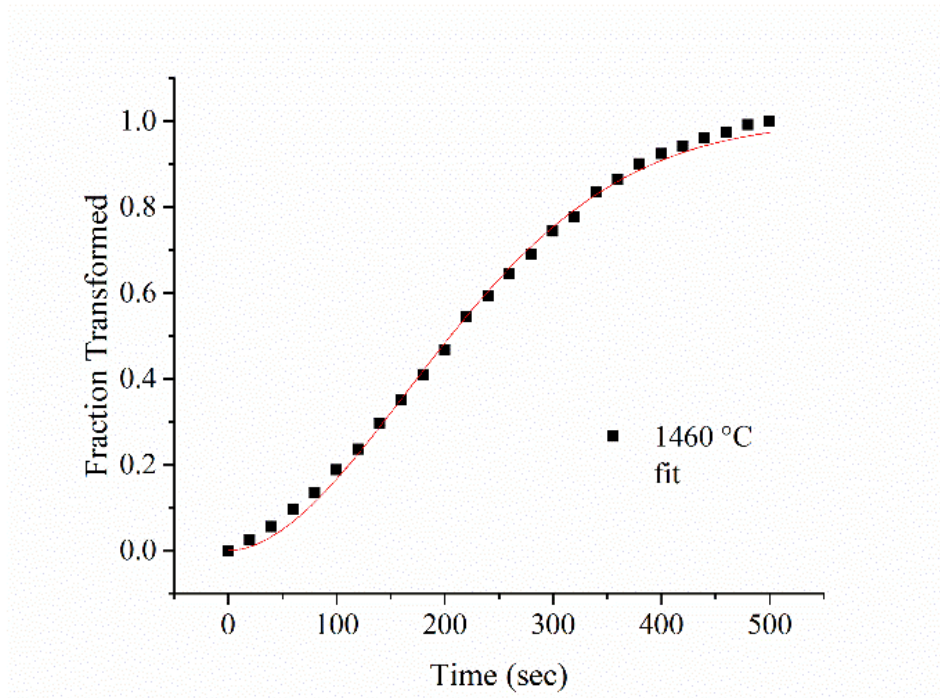


Figure 108(b). Individual fit the Avrami equation for isothermal data collected at 1460 °C for Dy_2TiO_5 .

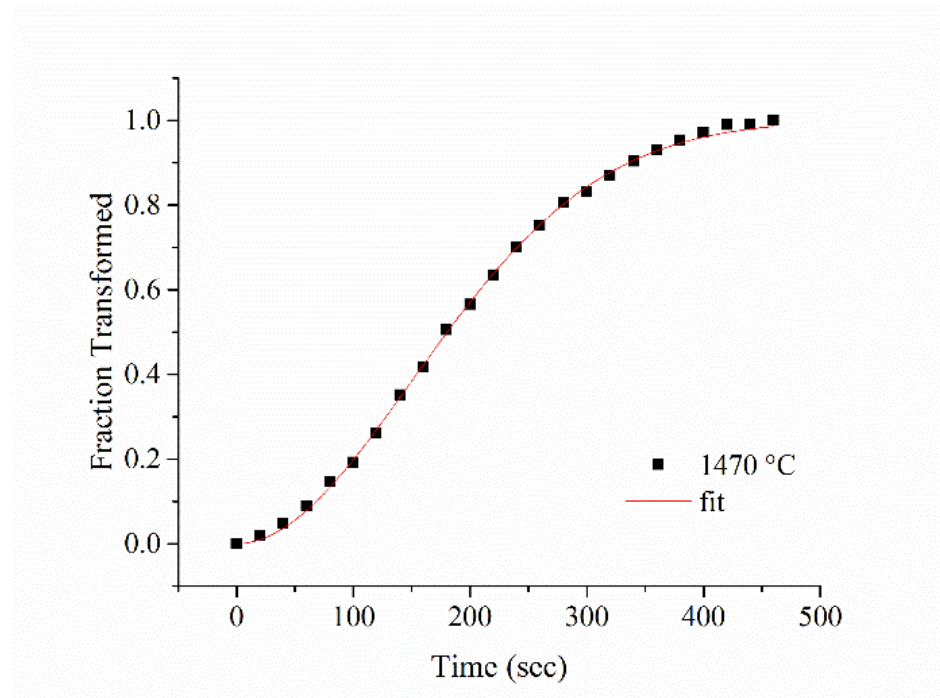


Figure 108(c). Individual fit the Avrami equation for isothermal data collected at 1470 °C for Dy_2TiO_5 .

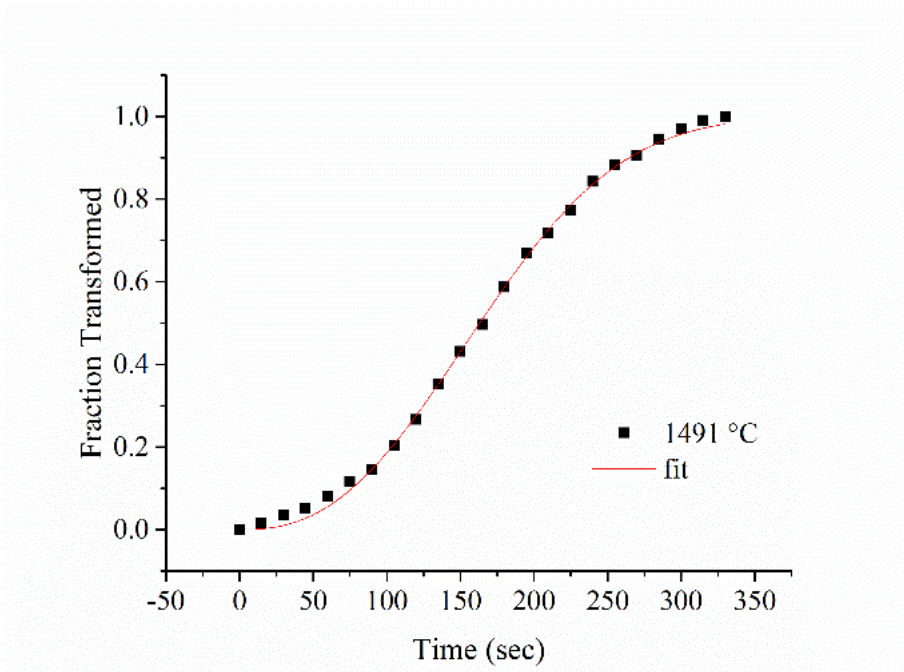


Figure 108(d). Individual fit the Avrami equation for isothermal data collected at 1491 °C for Dy₂TiO₅.

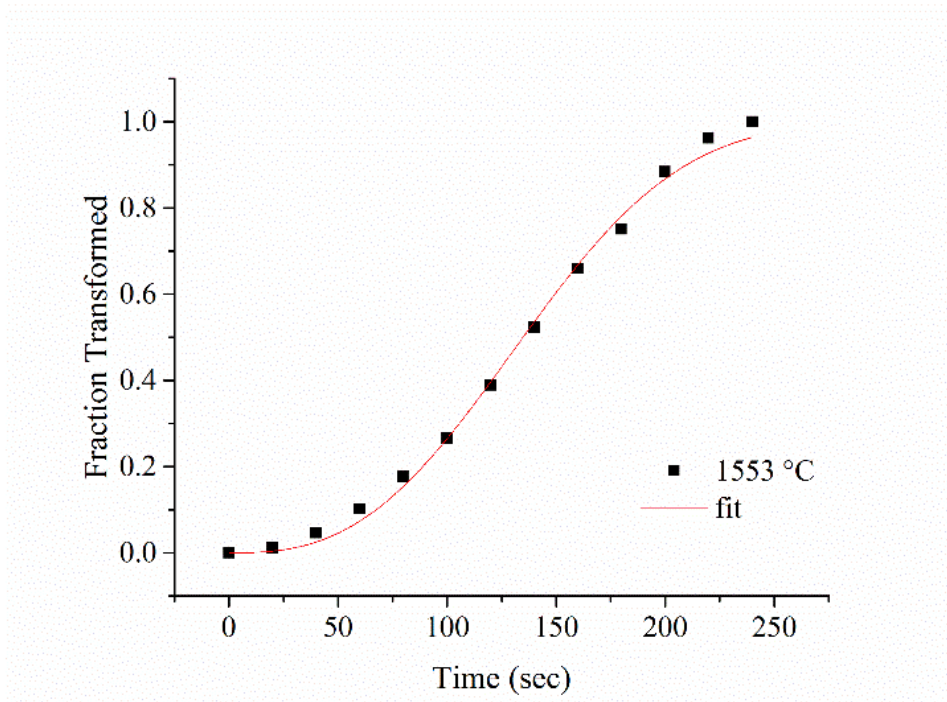


Figure 108(e). Individual fit the Avrami equation for isothermal data collected at 1553 °C for Dy₂TiO₅.

Table 31. Parameters calculated from the individual fits of the isothermal data.

Temp (°C)	E _a (kJ/mol)	k ₀ (1/s ⁿ)	n
1441	142.2	73.88	1.81
1460	125.18	112.85	1.86
1470	140.64	71.51	1.93
1491	134.5	51.08	2.48
1553	140.14	66.47	2.72



Figure 109. Plot of parameters calculated from the individual fits of the isothermal data.

7.3.5 Discussion

There are several important findings when interpreting the results of the sensitivity analysis.

First, in the temperature range the experiment is carried out, the uncertainty in the ability to determine the temperature from the refined lattice constant of platinum has a negligible effect on the results of the fitting. This finding supports the assumption that experimental errors have only a minor impact on the overall result.

Second, time resolution plays a major role when it comes to accurately fitting the data. It was observed that data in the time regime lower than 50% conversion of the new phase differentially have a much larger impact on the overall ability to determine the equation parameters accurately. This finding suggests that more data points should be collected at the beginning of the transformation process relative to those near the end of the transformation to decrease uncertainty.

Third, as expected from the functional form of the Avrami equation, the uncertainty in the ability to determine the overall activation energy has the most impact on the overall fit. Since the activation energy is part of an exponential function, inside of another exponential, this makes sense. Additionally, the Avrami constant, which describes the overall growth mechanism during transformation has the second largest impact followed by the rate constant.

Finally, when fitting each isothermal data set independently, connections may be made with the overall parameter trends across the series. With the exception of 1460 °C, which seems to be an outlier, the general value for the activation energy and rate constant seem to be the same across the various temperatures. On the other hand, the Avrami exponent seems to become larger with an increase in temperature, a 50% increase in value compared with a 5% increase between the

extremes of the activation energy and a 43% change with the rate constant. This monotonic increase as described by Table 31 and Figure 109 of the Avrami exponent is expected. With an increase in temperature, the barrier to growth in the third dimension should decrease, thus a shift from an Avrami exponent of two to three is makes sense.

Although a differential change in the activation energy has a larger impact on the overall fit, a crude comparison will reveal that when combined with its uncertainty it has the least impact on the overall fit, while the Avrami exponent and rate constant are potential sources of greater uncertainty.

These data can be re-fitted assuming the data from 1460 °C is an outlier. The new fit is provided in Figure 110 and the equation listed below.

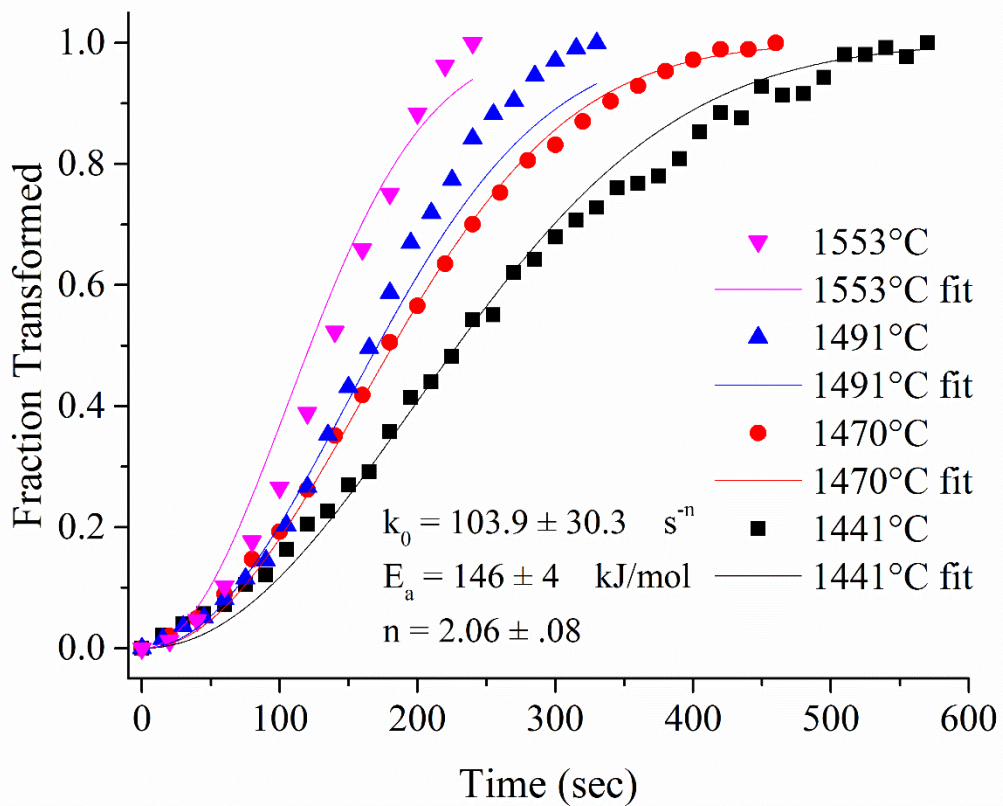


Figure 110. The fraction of the orthorhombic phase transformed to hexagonal in Dy_2TiO_5 at different temperatures as a function of time for an isothermal experiment with the 1460 °C data set removed.

$$F = 1 - \exp \left[- \left[103.9 * \exp \left(- \frac{146 \frac{\text{kJ}}{\text{mol}}}{k_b T} \right) \right] * t^{2.06} \right]$$

$$E_a = 146 \pm 4 \text{ kJ/mol}$$

$$k_0 = 103.9 \pm 30.3 \text{ s}^{-n}$$

$$n = 2.06 \pm 0.08$$

Although the new fit is an improvement over the previous one, it still suffers from many of the same problems. An overall investigation into the sensitivity of the model reveals that particular assumptions made about the rate constant and Avrami exponent can be improved upon.

There are three main simplifications in the Avrami model which are potential sources of uncertainty. The largest of these are the assumptions that the Avrami exponent and rate constant are not temperature/time dependent, and that nucleation and growth can be combined into a single term (assuming nucleation and growth are a combined event). Mittemeijer details this problem in several of his papers, most notably in the one referenced here.[33] Significantly more advanced fitting algorithms may be employed to deconvolute these assumptions which can lead to a better understanding of the phase transformation itself and provide a better fit. This equation can potentially include the influence of homogeneous and heterogeneous nucleation, weighed Avrami nucleation, the difference between interfacial and diffusion controlled growth, and the separation of activation energies associated with nucleation and growth. This equation is reproduced below.

$$F = 1 - \exp \left[- \left[k_0 * \exp \left(- \frac{Q \frac{kJ}{mol}}{k_b T} \right) \right] * t^n \right]$$

Which is broken down into the modular components provided here for isothermal and isochronal experiments,

Mixed nuc	Isothermal	Isochronal
n	$\frac{1}{\frac{d}{m} + \frac{1}{1 + (r_2/r_1)^{-1}}}$	$\frac{1}{\frac{d}{m} + \frac{1}{1 + (r_2/r_1)^{-1}}}$
Q	$\frac{\frac{d}{m} Q_G + \left(n - \frac{d}{m}\right) Q_N}{n}$	$\frac{\frac{d}{m} Q_G + \left(n - \frac{d}{m}\right) Q_N}{n}$
K_0^n	$\frac{g\nu_0^{d/m}}{\left(\frac{d}{m} + 1\right) \frac{1}{1 + (r_2/r_1)^{-1}}} \left[\frac{N_1^* \left(1 + \frac{r_2}{r_1}\right)^{\frac{1}{1 + \frac{r_2}{r_1}}}}{\left(N_{01} \left(1 + \left(\frac{r_2}{r_1}\right)^{-1}\right)\right)^{\frac{1}{1 + \left(\frac{r_2}{r_1}\right)^{-1}}}} \right]$	$\frac{g\nu_0^{d/m}}{\left(\frac{d}{m} + 1\right) \frac{1}{1 + (r_2/r_1)^{-1}}} \left[\frac{N_1^* \left(1 + \frac{r_2}{r_1}\right)^{\frac{1}{1 + \frac{r_2}{r_1}}}}{\left(C_c N_{01} \left(1 + \left(\frac{r_2}{r_1}\right)^{-1}\right)\right)^{\frac{1}{1 + \left(\frac{r_2}{r_1}\right)^{-1}}}} \right]$
r_2/r_1	$\frac{1}{\frac{d}{m} + 1} \frac{N_{01}^t \exp\left(-\frac{Q_N}{RT}\right)}{N_1^*}$	$\frac{C_c Q_G^{d/m} N_{01} \exp\left(-\frac{Q_N}{RT}\right)}{\left(\frac{d}{m} + 1\right) N_1^*} \left(\frac{RT^2}{\Phi}\right)$

where, d is the dimensionality of the growth ($d = 1, 2, \text{ or } 3$), m the growth parameter ($m = 1$ or 2 for interfacial or diffusion controlled growth, respectively), r_2/r_1 which is equal to the extended volume which is V_c/V_s (the ratio between pure continuous nucleation and site saturation) which has its own dependence on the number of sites per unit volume of nuclei formed, N , Q the effective activation energy which has contributions from both nucleation and growth with different functional dependencies, g the particle geometry factor, and v_0 the interface growth velocity.

Obviously, a fitting approach which has more than 10 different interrelated variable functions is not appropriate in the given circumstances. With an increased number of variables a better fit would be expected, but meaningless without additional information regarding the nature of the transformation.

7.3.6 Proposed Experiments

The equation described in the previous section can be trimmed down to a more manageable and meaningful size when particular variables become known. Under the current experimental conditions using X-ray diffraction to monitor the phase transformation behavior, it is not possible to determine the nature of nucleation, a major variable limitation in the Mittemeijer equation.

The simplest way to determine this would be to directly observe the transformation. This can be achieved by hot stage transmission electron microscopy or by hot stage optical microscopy *in situ*. The resources to carry out this work are available both in the Kriven research lab and in the Materials Research Laboratory. By employing these characterization techniques it may be possible to observe whether nuclei are formed randomly or preferentially at pores, grain boundaries, or other defects (the difference between homogenous and heterogeneous nucleation). Also, the number of nucleation sites can be monitored for a given volume. In addition, it may be

possible to observe the dimensionality of growth which would provide valuable insight. With this information many of the variables in the equation become known, such as N , d , and m , and the fitting much simpler.

7.3.7 Conclusions

As a first approximation of the transformation kinetics, the Avrami model seems to be sufficient and as described in Chapter 7.2, reasonable. It is apparent that some of the assumptions which are imbedded in this model are not correct. Unfortunately, more advanced modeling requires knowledge on the nature of the transformation and X-ray diffraction is not sufficient in providing this information. It is proposed that transmission electron microscopy and/or optical microscopy are employed *in situ* to directly observe the transformation process, allowing for the simplification in fitting of a more complex model.

CHAPTER 8

SUGGESTIONS FOR FUTURE WORK

8.1 Suggestions for Future Work

8.1.1 The Rare-Earth Di-Titanates

The rare-earth titanates can be found in two different compounds, the mono-titanates and di-titanates, Ln_2TiO_5 and $\text{Ln}_2\text{Ti}_2\text{O}_7$, respectively. This work focused on the thermal expansion behavior and kinetics of the transformation between the orthorhombic and hexagonal phases in the mono-titanates. It has been reported that $\text{La}_2\text{Ti}_2\text{O}_7$ and $\text{Nd}_2\text{Ti}_2\text{O}_7$, found in the di-titanates, transformation from a low temperature monoclinic phase to a high temperature orthorhombic phase in a displacive manner but this has not yet been verified. In addition, the rare-earth di-titanates from Sm to Lu are found in a cubic pyrochlore phase at room temperature. This cubic phase has been studied as the prototypical example of a magnetically frustrated material known as a spin-ice. Much work has been done in the low temperature regime for spin-ice materials but none at higher temperatures. Other researchers are interested in this phase as a potential thermal barrier coating material. To fully understand the entirety of this material system, research needs to be performed on the di-titanates to complement this work.

8.1.2 Research into Other Reconstructive Systems

This work proposed a new way to investigate the phase transformation behavior between two phases that have no group-subgroup relationship (reconstructive transformations) from the perspective of the thermal expansion behavior and structural changes as a function of temperature. In order to validate this perspective it is necessary to find other examples where this same method can be applied. Both the rare-earth mono-silicates and Ta_2O_5 undergo a

reconstructive transformation and may be excellent materials for such investigations. SiO₂ also undergoes several reconstructive transformations and may be beneficial to study to draw comparisons to other work in the literature.

8.1.3 Improving the Kinetic Model

As discussed extensively in Chapter 7, the Avrami model may be too simple to describe the phase transformation kinetics between the orthorhombic and hexagonal phases in the rare-earth titanate system (and many other systems as well). More advanced modeling requires much more background information on the nature of the transformation itself before proper application of more advanced models can be made. *In situ* observation of the transformation using hot stage transmission electron microscopy as well as hot stage optical microscopy may shed light on the nucleation and growth behavior during transformation and can simplify the process when fitting with a more advanced model.

REFERENCES

- ¹D. J. Green, R. H. J. Hannink, and M. V. Swain, "Transformation Toughening of Ceramics," CRC Press, (1989).
- ²R. C. Garvie, R. H. J. Hannink, and R. T. Pascoe, "Ceramic Steel?," *Nature*, **258**, [5537] 703-4 (1975).
- ³W. M. Kriven, "Possible Alternative Transformation Tougheners to Zirconia: Crystallographic Aspects," *Journal of the American Ceramic Society*, **71**, [12] 1021-30 (1988).
- ⁴F. F. Lange, "Transformation Toughening," *J Mater Sci*, **17**, [1] 225-34 (1982).
- ⁵X. Zhong, H. Zhao, C. Liu, L. Wang, F. Shao, X. Zhou, S. Tao, and C. Ding, "Improvement in Thermal Shock Resistance of Gadolinium Zirconate Coating by Addition of Nanostructured Yttria Partially-Stabilized Zirconia," *Ceramics International*, **41**, [6] 7318-24 (2015).
- ⁶P. Mohapatra, S. Rawat, N. Mahato, and K. Balani, "Restriction of Phase Transformation in Carbon Nanotube-Reinforced Yttria-Stabilized Zirconia," *Metall and Mat Trans A*, **46**, [7] 2965-74 (2015).
- ⁷S.-H. Guan, X.-J. Zhang, and Z.-P. Liu, "Energy Landscape of Zirconia Phase Transitions," *Journal of the American Chemical Society*, **137**, [25] 8010-13 (2015).
- ⁸X.-J. Jin, "Martensitic Transformation in Zirconia Containing Ceramics and its Applications," *Solid State and Materials Science*, **9**, [6] 313-18 (2005).
- ⁹B. Basu, "Toughening of Yttria-Stabilised Tetragonal Zirconia Ceramics," *International Materials Reviews*, **50**, [4] 239-56 (2005).
- ¹⁰A. H. Heuer, N. Claussen, W. M. Kriven, and M. Rühle, "Stability of Tetragonal ZrO₂ Particles in Ceramic Matrices," *Journal of the American Ceramic Society*, **65**, [12] 642-50 (1982).
- ¹¹G. Brunauer, H. Boysen, F. Frey, T. Hansen, and W. M. Kriven, "High Temperature Crystal Structure of a 3:2 Mullite from Neutron Diffraction Data," *Zeitschrift für Kristallographie*, **216**, 284 (2001).
- ¹²W. M. Kriven, J. W. Palko, S. Sinogeikin, J. D. Bass, A. Sayir, G. Brunauer, H. Boysen, F. Frey, and J. Schneider, "High Temperature Single Crystal Properties of Mullite," *Journal of the European Ceramic Society*, **19**, [13] 2529-41 (1999).
- ¹³J. Als-Nielsen and D. McMorrow, "Sources," pp. 29-67. in *Elements of Modern X-ray Physics*. John Wiley & Sons, Inc., 2011.
- ¹⁴F. R. Elder, A. M. Gurewitsch, R. V. Langmuir, and H. C. Pollock, "Radiation from Electrons in a Synchrotron," *Physical Review*, **71**, [11] 829-30 (1947).
- ¹⁵J. Als-Nielsen and D. McMorrow, "X-rays and their Interaction with Matter," pp. 1-28. in *Elements of Modern X-ray Physics*. John Wiley & Sons, Inc., 2011.
- ¹⁶N. E. Brown, S. M. Swapp, C. L. Bennett, and A. Navrotsky, "High-temperature X-ray Diffraction: Solutions to Uncertainties in Temperature and Sample Position," *Journal of Applied Crystallography*, **26**, [1] 77-81 (1993).
- ¹⁷J. H. Hubbell and S. M. Seltzer, "Tables of X-Ray Mass Attenuation Coefficients and Mass Energy-Absorption Coefficients from 1 keV to 20 MeV for Elements Z = 1 to 92 and 48 Additional Substances of Dosimetric Interest," *Radiation Physics Division, PML, NIST*, (1996).
- ¹⁸H. Rietveld, "Line Profiles of Neutron Powder-Diffraction Peaks for Structure Refinement," *Acta Crystallographica*, **22**, [1] 151-52 (1967).

- ¹⁹H. M. Rietveld, "A Profile Refinement Method for Nuclear and Magnetic Structures," *Journal of Applied Crystallography*, **2**, 65-71 (1969).
- ²⁰W. Dollase, "Correction of Intensities for Preferred Orientation in Powder Diffractometry: Application of the March Model," *Journal of Applied Crystallography*, **19**, [4] 267-72 (1986).
- ²¹E. Jansen, W. Schafer, and G. Will, "R Values in Analysis of Powder Diffraction Data Using Rietveld Refinement," *Journal of Applied Crystallography*, **27**, [4] 492-96 (1994).
- ²²J. C. Taylor and I. Hinczak, "Rietveld Made Easy," pp. 201. Sietronics Pty Limited, (2001).
- ²³E. Kisi, "Rietveld Analysis of Powder Diffraction Patterns," *Australian Journal of Physics*, **18**, 135-53 (1994).
- ²⁴L. W. Finger, D. E. Cox, and A. P. Jephcoat, "A Correction for Powder Diffraction Peak Asymmetry due to Axial Divergence," *Journal of Applied Crystallography*, **27**, [6] 892-900 (1994).
- ²⁵R. A. Young and D. B. Wiles, "Profile Shape Functions in Rietveld Refinements," *Journal of Applied Crystallography*, **15**, [4] 430-38 (1982).
- ²⁶D. Cox, "The Rietveld Method," *Journal of Applied Crystallography*, **27**, [3] 440-41 (1994).
- ²⁷A. C. Larson and R. B. Von Dreele, "General Structure Analysis System (GSAS)," *Los Alamos National Laboratory Report LAUR 86-748*, (2000).
- ²⁸B. H. Toby, "EXPGUI, A Graphical User Interface for GSAS," *Journal of Applied Crystallography*, **34**, 210-13 (2001).
- ²⁹R. E. Taylor, "Thermal Expansion of Solids," pp. 293. ASM International, (1998).
- ³⁰Z. A. Jones, P. Sarin, R. P. Haggerty, and W. M. Kriven, "CTEAS: A Graphical-User-Interface-Based Program to Determine Thermal Expansion from High-Temperature X-ray Diffraction," *Journal of Applied Crystallography*, **46**, [2] 550-53 (2013).
- ³¹R. P. Haggerty, P. Sarin, and W. M. Kriven, "In situ Studies of the Monoclinic to Tetragonal Phase Transformations in Hafnia and Comparison with Zirconia," *Journal of the American Ceramic Society*, (2014).
- ³²R. Balluffi, S. Allen, and W. C. Carter, "Kinetics of Materials," pp. 672. Wiley, (2005).
- ³³F. Liu, F. Sommer, C. Bos, and E. J. Mittemeijer, "Analysis of Solid State Phase Transformation Kinetics: Models and Recipes," *International Materials Reviews*, **52**, [4] 193-212 (2007).
- ³⁴J. W. Christian, "The Theory of Transformations in Metals and Alloys." Pergamon: Oxford, (2002).
- ³⁵A. N. Kolmogorov, "A Statistical Theory for the Recrystallisation of Metals," *Akad Nauk SSSR*, **3**, (1937).
- ³⁶M. Avrami, "Kinetics of Phase Change. I General Theory," *The Journal of Chemical Physics*, **7**, [12] 1103-12 (1939).
- ³⁷M. Avrami, "Kinetics of Phase Change. II Transformation-Time Relations for Random Distribution of Nuclei," *The Journal of Chemical Physics*, **8**, [2] 212-24 (1940).
- ³⁸M. Avrami, "Granulation, Phase Change, and Microstructure Kinetics of Phase Change. III," *The Journal of Chemical Physics*, **9**, [2] 177-84 (1941).
- ³⁹M. C. Weinberg, D. P. Birnie Iii, and V. A. Shneidman, "Crystallization Kinetics and the JMAK Equation," *Journal of Non-Crystalline Solids*, **219**, [0] 89-99 (1997).
- ⁴⁰A. K. Jena and C. Chaturvedi, "Phase Transformation in Materials." Prentice Hall, (1992).
- ⁴¹J. W. Cahn, "Transformation Kinetics During Continuous Cooling," *Acta Metallurgica*, **4**, [6] 572-75 (1956).

- ⁴²F. Thévenot, "Boron Carbide—A Comprehensive Review," *Journal of the European Ceramic Society*, **6**, [4] 205-25 (1990).
- ⁴³C.-H. Jung, C.-J. Kim, and S.-J. Lee, "Synthesis and Sintering Studies on Dy₂TiO₅ Prepared by Polymer Carrier Chemical Process," *Journal of Nuclear Materials*, **354**, [1–3] 137-42 (2006).
- ⁴⁴V. D. Risovanyi, E. P. Klochkov, and E. E. Varlashova, "Hafnium and Dysprosium Titanate Based Control Rods for Thermal Water-Cooled Reactors," *At Energy*, **81**, [5] 764-69 (1996).
- ⁴⁵V. D. Risovany, E. E. Varlashova, and D. N. Suslov, "Dysprosium Titanate as an Absorber Material for Control Rods," *Journal of Nuclear Materials*, **281**, [1] 84-89 (2000).
- ⁴⁶A. Sinha and B. P. Sharma, "Development of Dysprosium Titanate Based Ceramics," *Journal of the American Ceramic Society*, **88**, [4] 1064-66 (2005).
- ⁴⁷G. Panneerselvam, R. Venkata Krishnan, M. P. Antony, K. Nagarajan, T. Vasudevan, and P. R. Vasudeva Rao, "Thermophysical Measurements on Dysprosium and Gadolinium Titanates," *Journal of Nuclear Materials*, **327**, [2–3] 220-25 (2004).
- ⁴⁸R. B. van Dover, "Amorphous Lanthanide-Doped TiO_x Dielectric Films," *Applied Physics Letters*, **74**, [20] 3041-43 (1999).
- ⁴⁹T. Pan, J. Lin, M. Wu, and C. Lai, "Structural Properties and Sensing Performance of High-k Nd₂TiO₅ Thin Layer-Based Electrolyte–Insulator–Semiconductor for pH Detection and Urea Biosensing," *Biosensors and Bioelectronics*, **24**, [9] 2864-70 (2009).
- ⁵⁰P. Bergveld, "Thirty Years of ISFETOLOGY: What Happened in the Past 30 Years and What May Happen in the Next 30 Years," *Sensors and Actuators B: Chemical*, **88**, [1] 1-20 (2003).
- ⁵¹M. Petrova, A. Novikova, and R. Grebenschikov, "Polymorphism of Rare Earth Titanates of the Composition Ln₂TiO₅," *Inorg. Mater.*, **18**, [2] 236-40 (1982).
- ⁵²N. Mizutani, Y. O. Tajima, and M. Kato, "Phase Relations in the System Y₂O₃-TiO₂," *Journal of the American Ceramic Society*, **59**, [3-4] 168-68 (1976).
- ⁵³G. V. Shamrai, R. L. Magunov, I. V. Stasenko, and A. P. Zhirnova, "The Dy₂O₃-TiO₂ System," *Inorg. Mater.*, **25**, [2] 233-35 (1989).
- ⁵⁴W. G. Mumme and A. D. Wadsley, "The Structure of Orthorhombic Y₂TiO₅, an Example of Mixed Seven- and Fivefold Coordination," *Acta Crystallographica Section B*, **24**, [10] 1327-33 (1968).
- ⁵⁵L. G. Shcherbakova, L. G. Mamsurova, and G. E. Sukhanova, "Lanthanide Titanates," *Russian Chemical Reviews*, **48**, [3] 228 (1979).
- ⁵⁶P. Tiedemann and H. Mullerbuschbaum, "About the Structure of The High-Temperature Form of Dy₂TiO₅," *Z. Anorg. Allg. Chem.*, **520**, [1] 71-74 (1985).
- ⁵⁷M. A. Petrova, A. S. Novikova, and R. G. Grebenschikov, "Phase Relations in the Pseudobinary Systems La₂TiO₅-Lu₂TiO₅ and Gd₂TiO₅-Tb₂TiO₅," *Inorg. Mater.*, **39**, [5] 509-13 (2003).
- ⁵⁸Y. Shepelev and M. Petrova, "Structures of Two High-Temperature Dy₂TiO₅ Modifications," *Russian Journal of Inorganic Chemistry*, **51**, [10] 1636-40 (2006).
- ⁵⁹Y. F. Shepelev and M. A. Petrova, "Crystal Structures of Ln₂TiO₅ (Ln = Gd, Dy) Polymorphs," *Inorg. Mater.*, **44**, [12] 1354-61 (2008).
- ⁶⁰Y. F. Shepelev, M. A. Petrova, and A. S. Novikova, "Crystal Structure of the Hexagonal Modification of Lutetium-Stabilized Gadolinium Titanate Gd_{1.8}Lu_{0.2}TiO₅," *Glass Physics and Chemistry*, **30**, [4] 342-44 (2004).

- ⁶¹L. Shcherbakova, V. Glushkova, K. Guseva, L. Mamsurova, L. Sazonova, and G. Sukhanova, "The TiO₂-Tb₂O₃ System at High Temperatures," *Inorg. Mater.*, **16**, [8] 1445-49 (1980).
- ⁶²K. G. GE Sukhanova, AV Kolesnikov, LG Shcherbakova, "Phase Equilibria in the TiO₂-Ho₂O₃ System," *Inorg. Mater.*, **18**, [12] 2014-17 (1982).
- ⁶³H. Müller-Buschbaum and K. Scheunemann, "Zur Kenntnis von Nd₂TiO₅," *Journal of Inorganic and Nuclear Chemistry*, **35**, [4] 1091-98 (1973).
- ⁶⁴G. C. Lau, R. S. Freitas, B. G. Ueland, M. L. Dahlberg, Q. Huang, H. W. Zandbergen, P. Schiffer, and R. J. Cava, "Structural Disorder and Properties of the Stuffed Pyrochlore Ho₂TiO₅," *Physical Review B*, **76**, [5] 054430 (2007).
- ⁶⁵G. C. Lau, T. M. McQueen, Q. Huang, H. W. Zandbergen, and R. J. Cava, "Long- and Short-Range Order in Stuffed Titanate Pyrochlores," *Journal of Solid State Chemistry*, **181**, [1] 45-50 (2008).
- ⁶⁶L. P. Lyashenko, I. V. Kolbanev, L. G. Shcherbakova, E. I. Knerelman, and G. I. Davydova, "Effect of a Nonequilibrium State on Phase Relations in the System TiO₂-Sc₂O₃ (40-50 mol% Sc₂O₃)," *Inorg. Mater.*, **40**, [8] 833-39 (2004).
- ⁶⁷A. Preuss and R. Gruehn, "Preparation and Structure of Cerium Titanates Ce₂TiO₅, Ce₂Ti₂O₇, and Ce₄Ti₉O₂₄," *Journal of Solid State Chemistry*, **110**, [2] 363-69 (1994).
- ⁶⁸S. Bramwell and M. Gingras, "Spin Ice State in Frustrated Magnetic Pyrochlore Materials," *Science*, **294**, [5546] 1495-501 (2001).
- ⁶⁹S. T. Bramwell, S. R. Giblin, S. Calder, R. Aldus, D. Prabhakaran, and T. Fennell, "Measurement of the Charge and Current of Magnetic Monopoles in Spin Ice," *Nature*, **461**, [7266] 956-59 (2009).
- ⁷⁰J. K. Brandon and H. Megaw, "On the Crystal Structure and Properties of Ca₂Nb₂O₇, "calcium pyroniobate"," *Philosophical Magazine*, **21**, [169] 5 (1970).
- ⁷¹A. Jones, W. Frances, and C. Williams, "Rare Earth Minerals: Chemistry, Origin and Ore Deposits," pp. 372. Springer, (1996).
- ⁷²M. A. Gulgun and W. M. Kriven, "A Simple Solution-Polymerization Route for Oxide Powder Synthesis," *Ceramic Transactions* **62**, 57-66 (1995).
- ⁷³S. J. Lee and W. M. Kriven, "Crystallization and Densification of Nano-size, Amorphous Cordierite Powder Prepared by a Solution-Polymerization Route," *Journal of the American Ceramic Society*, **81**, [10] 2605-12 (1998).
- ⁷⁴M. H. Nguyen, S. Lee, and W. M. Kriven, "Synthesis of Oxide Powders by way of a Polymeric Steric Entrapment Precursor Route," *Journal of Materials Research*, **14**, [08] 3417-26 (1999).
- ⁷⁵S. J. Lee and W. M. Kriven, "Preparation of Ceramic Powders by a Solution-Polymerization Route Employing PVA Solution," *Cer. Eng. and Sci. Proc.*, **19**, [4] 469-76 (1998).
- ⁷⁶E. A. Benson, S. J. Lee, and W. M. Kriven, "Preparation of Portland Cement Components by PVA Solution Polymerization," *Journal of the American Ceramic Society*, **82**, [8] 2049-55 (1999).
- ⁷⁷S. J. Lee, M. D. Biegalski, and W. M. Kriven, "Barium Titanate and Barium Orthotitanate Powders Through an Ethylene Glycol Polymerization Route," *Cer. Eng. and Sci. Proc.*, **20**, [3] 11-18 (1999).
- ⁷⁸S. J. Lee and W. M. Kriven, "A Submicron-Scale Duplex Zirconia and Alumina Composite by Polymer Complexation Processing," *Cer. Eng. and Sci. Proc.*, **20**, [3] 69-76 (1999).

- ⁷⁹S. J. Lee, M D. Biegalsk, and W. M. Kriven, "Powder Synthesis of Barium Titanate and Barium Orthotitanate via an Ethylene Glycol Polymerization Route," *Mater. Res.*, **14**, [7] 3001-06 (1999).
- ⁸⁰W. M. Kriven, S. J. Lee, M. A. Gülgün, M. H. Nguyen, and D. K. Kim, "Synthesis of Oxide via Polymeric Steric Entrapment," *Ceramic Transactions*, **108**, 99-110 (2000).
- ⁸¹S. J. Lee, C. H. Lee, and W. M. Kriven, "Synthesis of Low-firing Anorthite Powder by the Steric Entrapment Route," *Ceram. Eng. and Sci. Proc.*, **23**, [3] 33-40 (2002).
- ⁸²M. A. Gülgün, W. M. Kriven, and M. H. Nguyen, "Processes for Preparing Mixed-Oxide Powders " US Patent 6,482,387, 2002. [patent]
- ⁸³S. J. Lee and W. M. Kriven, "Synthesis and Hydration Study of Portland Cement Components Prepared by the Organic Steric Entrapment Method," *Mat. Struct.*, **38**, [1] 87-92 (2005).
- ⁸⁴B. R. Rosczyk, W. M. Kriven, and T. O. Mason, "Solid Oxide Fuel Cell Materials Synthesized by an Organic Steric Entrapment Method," *Cer. Eng. and Sci. Proc.*, **24**, [3] 287-92 (2003).
- ⁸⁵K. Jurkschat, P. Sarin, L. F. Siah, and W. M. Kriven, "In situ High Temperature Phase Transformations in Rare Earth Niobates," *Advances in X-Ray Analysis*, **47**, 357-62 (2004).
- ⁸⁶W. M. Kriven and B. R. Rosczyk, "SOFC Powder Synthesis by the Organic Steric Entrapment Method." Kluwer Academic Publishers, (2005).
- ⁸⁷M. Gordon, J. Bell, and W. M. Kriven, "Comparison of Naturally and Synthetically-Derived, Potassium-Based Geopolymers," *Ceramic Transactions*, **165**, 95-106 (2005).
- ⁸⁸D. Kim and W. M. Kriven, "Processing and Characterization of Multiphase Ceramic Composites. Part I: Duplex Composites Formed In-Situ," *Journal of the American Ceramic Society*, **91**, [3] 784-92 (2007).
- ⁸⁹D. K. Kim and W. M. Kriven, "Processing and Characterization of Multiphase Ceramic Composites. Part II: Triplex Composites with a Wide Sintering Temperature Range," *Journal of the American Ceramic Society*, **91**, [3] 793-98 (2008).
- ⁹⁰D. K. Kim and W. M. Kriven, "Processing and Characterization of Multiphase Ceramic Composites. Part III: Strong, Hard and Tough, High Temperature, Quadruplex and Quintuplex Composites," *Journal of the American Ceramic Society*, **91**, [793-798] (2008).
- ⁹¹D. Jia, D. K. Kim, and W. M. Kriven, "Preparation of a Pore Self-Forming Macro-/Mesoporous Gehlenite Ceramic by the Organic Steric Entrapment (PVA) Technique, in Developments in Porous, Biological and Geopolymer Ceramics," **Vol. 28**. John Wiley & Sons, Inc., (2007).
- ⁹²D. Jia, D. Kim, and W. M. Kriven, "Sintering Behavior of Gehlenite. Part I. Self-forming, Macro-/Mesoporous Gehlenite – Pore Forming Mechanism, Microstructure, Mechanical and Physical Properties," *Journal of the American Ceramic Society*, **90**, [6] 1760-73 (2007).
- ⁹³D. Jia and W. M. Kriven, "Sintering Behavior of Gehlenite. Part II. Microstructure and Mechanical Properties," *Journal of the American Ceramic Society*, **90**, [8] 2766-70 (2007).
- ⁹⁴C. Jung, S. Lee, W. M. Kriven, J. P. and, and W. Ryu, "A Polymer Solution Technique for the Synthesis of Nano-sized Li_2TiO_3 Ceramic Breeder powders," *Journal of Nuclear Materials*, **373**, [194-198] (2007).

- ⁹⁵S. Lee, J. Kwak, and W. M. Kriven, "Effect of Polymer Addition on the Crystallite Size and Sinterability of Hydroxyapatite Prepared with CaO Powder and Phosphoric Acid," *J. Ceramic Processing Research* **13**, [3] 243-47 (2012).
- ⁹⁶A. Ozer, W. M. Kriven, and Y. K. Tür, "The Effect of $3Y_2O_3$ - ZrO_2 Produced by the Steric Entrapment Method on the Mechanical and Sintering Properties of Cr_3C_2 Based Cermets," *Mater. Sci. and Eng. A*, **556**, 878-84 (2012).
- ⁹⁷O. Garcia-Moreno, W. M. Kriven, J. S. Moya, and R. Torrecillas, "Alumina Region of the Lithium Aluminosilicate System: a New Window for Temperature Ultrastable Materials Design," *Journal of the American Ceramic Society Communication*, **96**, [7] 2039-41 (2013).
- ⁹⁸R. Uvic, K. Tolman, K. Chan, N. Lundy, S. Letourneau, and W. M. Kriven, "The Effective Size of Vacancies in Aliovalently Doped $SrTiO_3$ Perovskites," *J. Alloys and Compounds*, **575**, [239-245] (2013).
- ⁹⁹K. C. Seymour and W. M. Kriven, "Synthesis and Thermal Expansion of β -Eucryptite Powders Produced by the Inorganic-Organic Steric Entrapment Method," *Journal of the American Ceramic Society*, **97**, [10] 3087-91 (2014).
- ¹⁰⁰D. Ribero and W. M. Kriven, "Synthesis of Phosphate Materials Prepared by a Polymeric Steric Entrapment Precursor Route. Part I: $LiFePO_4$ Cathode Material," *Journal of the American Ceramic Society*, (2014).
- ¹⁰¹B. R. Rosczyk, S. Lee, and W. M. Kriven, "Synthesis of Highly Reactive Titanate Powders via an Ethylene Glycol, Steric Entrapment Route," *Journal of the American Ceramic Society*, (2013).
- ¹⁰²S. Stecura, "Evaluation of Imaging Furnace as Heat Source for X-ray Diffractometry," *Review of Scientific Instruments*, **39**, [5] 760-65 (1968).
- ¹⁰³A. Watanabe and M. Shimazu, "High-Temperature X-ray Diffraction Furnace Using a Thermal-Image Technique," *Journal of Applied Crystallography*, **9**, [pt.6] 466-9 (1976).
- ¹⁰⁴J. Schneider, "Mirror Heaters for High Temperature X-ray Diffraction," *Advances in X-Ray Analysis*, **36**, 397-402 (1993).
- ¹⁰⁵P. Sarin, W. Yoon, K. Jurkschat, P. Zschack, and W. M. Kriven, "Quadrupole Lamp Furnace for High Temperature (up to 2050 K) Synchrotron Powder X-ray Diffraction Studies in Air in Reflection Geometry," *Review of Scientific Instruments*, **77**, [9] (2006).
- ¹⁰⁶E. S. Watson, M. J. O'Neill, J. Justin, and N. Brenner, "A Differential Scanning Calorimeter for Quantitative Differential Thermal Analysis," *Analytical Chemistry*, **36**, [7] 1233-38 (1964).
- ¹⁰⁷J. E. Lennard-Jones, "Cohesion," *Proceedings of the Physical Society*, **43**, [5] 461 (1931).
- ¹⁰⁸G. Panneerselvam, R. Venkata Krishnan, K. Nagarajan, and M. P. Antony, "Heat Capacity and Thermal Expansion of Samarium Titanate," *Materials Letters*, **65**, [12] 1778-80 (2011).
- ¹⁰⁹P. Sarin, R. W. Hughes, D. R. Lowry, Z. D. Apostolov, and W. M. Kriven, "High Temperature Properties and Ferroelastic Phase Transitions in Rare-Earth Niobates ($LnNbO_4$)," *Journal of the American Ceramic Society*, **97**, [10] 3307-19 (2014).
- ¹¹⁰W. Baumann, A. Leineweber, and E. Mittemeijer, "Failure of Kissinger(-like) Methods for Determination of the Activation Energy of Phase Transformations in the Vicinity of the Equilibrium Phase-Transformation Temperature," *J Mater Sci*, **45**, [22] 6075-82 (2010).
- ¹¹¹M. Fine, "Introduction to Phase Transformations in Condensed Systems." Macmillan Materials Science Series, (1964).

- ¹¹²S. Vyazovkin, A. K. Burnham, J. M. Criado, L. A. Perez-Maqueda, C. Popescu, and N. Sbirrazzuoli, "ICTAC Kinetics Committee Recommendations for Performing Kinetic Computations on Thermal Analysis Data," *Thermochimica Acta*, **520**, [1-2] 1-19 (2011).
- ¹¹³S. Vyazovkin, "Thermal Analysis," *Analytical Chemistry*, **82**, [12] 4936-49 (2010).
- ¹¹⁴S. Vyazovkin and N. Sbirrazzuoli, "Isoconversional Kinetic Analysis of Thermally Stimulated Processes in Polymers," *Macromolecular Rapid Communications*, **27**, [18] 1515-32 (2006).
- ¹¹⁵D. L. Zhou, E. A. Schmitt, G. G. Zhang, D. Law, S. Vyazovkin, C. A. Wight, and D. J. W. Grant, "Crystallization Kinetics of Amorphous Nifedipine Studied by Model-Fitting and Model-Free Approaches," *Journal of Pharmaceutical Sciences*, **92**, [9] 1779-92 (2003).
- ¹¹⁶S. Vyazovkin, "Modification of the Integral Isoconversional Method to Account for Variation in the Activation Energy," *Journal of Computational Chemistry*, **22**, [2] 178-83 (2001).
- ¹¹⁷L. Pagliari, M. Dapiaggi, A. Pavese, and F. Francescon, "A Kinetic Study of the Quartz–Cristobalite Phase Transition," *Journal of the European Ceramic Society*, **33**, [15–16] 3403-10 (2013).
- ¹¹⁸R. C. Breneman and J. W. Halloran, "Kinetics of Cristobalite Formation in Sintered Silica," *Journal of the American Ceramic Society*, **97**, [7] 2272-78 (2014).
- ¹¹⁹J. P. Perrillat, I. Daniel, J. M. Lardeaux, and H. Cardon, "Kinetics of the Coesite–Quartz Transition: Application to the Exhumation of Ultrahigh-Pressure Rocks," *Journal of Petrology*, **44**, [4] 773-88 (2003).
- ¹²⁰J. L. Provis and J. S. J. van Deventer, "Geopolymerisation Kinetics. 1. In Situ Energy-Dispersive X-Ray Diffractometry," *Chemical Engineering Science*, **62**, [9] 2309-17 (2007).
- ¹²¹A. Gualtieri, P. Norby, G. Artioli, and J. Hanson, "Kinetics of Formation of Zeolite Na-A [LTA] from Natural Kaolinites," *Phys Chem Min*, **24**, [3] 191-99 (1997).
- ¹²²B. L. Kirsch, E. K. Richman, A. E. Riley, and S. H. Tolbert, "In-Situ X-ray Diffraction Study of the Crystallization Kinetics of Mesoporous Titania Films," *The Journal of Physical Chemistry B*, **108**, [34] 12698-706 (2004).
- ¹²³Z. Yanzhi, G. Weijun, W. Qinguo, W. Xiaolin, L. Xinchun, and S. Maobing, "Study the Oxidation Kinetics of Uranium using XRD and Rietveld Method," *IOP Conference Series: Materials Science and Engineering*, **9**, [1] 012019 (2010).
- ¹²⁴C.-B. Bae, "Integrally Cored Ceramic Investment Casting Mold Fabricated by Ceramic Sterolithography." in Materials Science and Engineering. University of Michigan, 2008.